The Electronic Properties of Thin Film $YBa_2Cu_3O_7$ Low Angle Grain Boundaries

Michael James Hogg

St. Catharine's College
Cambridge

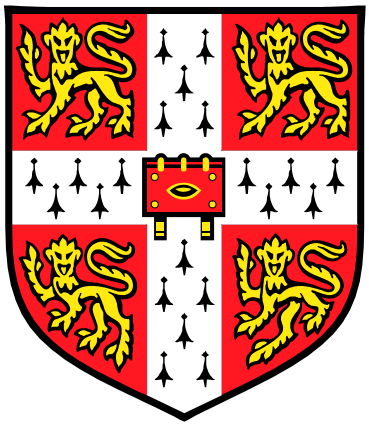

A dissertation submitted for the degree of Doctor of Philosophy
at the University of Cambridge

July 2002

Summary

Critical currents in the latest biaxially textured 'coated conductors' are now limited by 2D networks of *low angle grain boundaries* (LAGBs) with misorientation θ_m = 1 - 10°. In order to understand and optimise current transfer in these materials it is essential to elucidate the electromagnetic behaviour of the LAGB. This work presents an investigation into the transport properties of [001]-tilt LAGBs formed by the thin film deposition of $YBa_2Cu_3O_7$ onto bicrystalline substrates. Through the use of a precision two-axis goniometer, measurements of the *V-I* characteristic and critical current density were made as magnetic field was rotated in angles θ and ϕ relative to the LAGB defect.

It is found that for fields applied parallel to the LAGB defect plane, dissipation is dominated by the viscous flux flow of vortices along the boundary. Clear evidence for this is found in the *V-I* characteristic, which displays an increased linearity indicative of the viscous regime. It is shown that the number of vortex rows involved in the flow process can discontinuously switch, leading to a *V-I* characteristic made up of straight segments of different gradient.

For fields applied away from the LAGB defect plane a kinked vortex structure develops and the boundary critical current density, J_c^{GB}, is determined by the channelling of vortex segments still lying within the LAGB. The channelling regime is seen in angular measurements as a marked decrease in $J_c^{GB}(\theta,\phi)$ as field becomes aligned to within critical angles ϕ_K or θ_K of the LAGB. The aligned vortices experience a reduction in dimensionality that is manifest in a reduced temperature dependence of $J_c^{GB}(T)$. For fields applied at a sufficiently large angle from the defect plane the deleterious effects of the LAGB on current transport are mitigated considerably. In this regime a collinear vortex structure is regained and transport is controlled by the intragranular (IG) sections of the LAGB track; $J_c^{GB} = \delta J_c^{IG}$ where $\delta \sim 0.8$, a result that is independent of field, temperature and angle for a 4.9° LAGB.

For rotation of the applied field *within* the LAGB defect plane, the presence of a pinning peak in J_c^{GB} for field aligned to the dislocation array is confirmed and modelled. The peak is found to be absent in IG track measurements and increases relative to the intrinsic peak with both increasing field and temperature. In addition, a pronounced angular hysteresis is presented, which is directly linked to a corresponding 'static' hysteresis in $J_c^{GB}(B)$ with field. Magneto-optic measurements confirm that this effect is controlled by the flux density profile in the IG regions of the LAGB track.

Finally, above a temperature, angle and sample dependent merging field, B^*, the LAGB is found to be effectively transparent, as $\delta \sim 1$. This is due to the irreversibility line, above which dissipation occurs across the whole LAGB track.

Preface

I declare that, except where otherwise stated, this dissertation is the result of my own work and includes nothing which is the outcome of work done in collaboration. No part of this dissertation has been submitted at Cambridge or any other University for a degree, diploma or other qualification. This dissertation does not exceed 60,000 words.

Michael Hogg
July 2002

Acknowledgements

This thesis could not have been completed without the help of a number of people. First and foremost, I would like to thank my supervisor, Professor Jan Evetts, for his support and guidance over the years. Many thanks to Frank Kahlmann and Vassilka Tsaneva; when I needed samples, they were always willing to help out. Thanks also to Mark Blamire and Zoe Barber, for the provision of clean room and thin film facilities.

I am very grateful for informative talks with Edward Tarte, Bartek Glowacki, Alistair Bradley, James Ransley and Bernhard Zeimetz regarding grain boundaries and current transport. Particular thanks go to Andres Diaz, for his helpful correspondence. Also, I am indebted to a number of people who performed useful measurements that added to this work; Christian Jooss (Magneto-Optics), Sibe Mennema and Henny Zandbergen (TEM) and Garry Perkins (Hall Probe). Thanks also to Dae-Joon Kang for performing FIB milling.

I am very grateful to the Engineering and Physical Sciences Research Council, St. Catharine's College, the Department of Materials Science and the Cambridge Philosophical Society for financial assistance provided throughout my studies.

For help with the measurement rig, thanks to Peter Berghuis and John Durrell. Many thanks to Yee Cheng, Moon-Ho Jo, Noel Rutter and John Leake for help with X-ray techniques and interpretation. For giving their time to teach clean room techniques thanks to Phil McBrien, Richard Moseley and Peter Berghuis, and for solving software nightmares to John Durrell and Gavin Burnell. For stimulating highbrow office conversation, I am indebted to Yee, Ashishi, Cliff and Moon-Ho. For proof reading, thanks to Sibe, Dae-Joon and James. I am also grateful to many others in the lab, including Jose Prieto, Nadia Stelmashenko, Ahmed Kuršumović, Chris Bell and Dave Ansell.

Thanks to Emily, for sharing in the good times and steering me through the bad - Never ever give up. And finally, thanks to my parents, who have always given me amazing support, and without whom this work would most certainly not have happened.

Contents

Chapter 1. Introduction 1

1.1 Motivation and Background 1
1.2 Project Aims and Objectives 1
1.3 Thesis Overview 2
1.4 References 3

Chapter 2. Flux Vortices and Critical Currents 4

2.1 $YBa_2Cu_3O_7$ 4
2.2 Elementary Phenomenological Theory 5
2.2.1 The Ideal Phase Transition 5
2.2.2 London Theory 6
2.2.3 GL Theory 6
2.2.4 Type I and Type II Superconductivity7
2.3 The Flux Vortex 8
2.4 Flux Flow and Flux Pinning 9
2.4.1 Flux Lines and Transport Currents 9
2.4.2 Viscous Flux Flow Theory 9
2.4.3 J_c and Flux Pinning 10
2.4.4 Pinning Sites in $YBa_2Cu_3O_7$ 11
2.4.5 Flux Flow in HTS 12
2.5 The Critical State 13
2.6 The Effect of Anisotropy 14
2.6.1 Anisotropic GL Theory 14
2.6.2 Vortex Structure 14
2.7 J_c with angle of Applied Field 15
2.8 The Irreversibility Line 16
2.9 Demagnetising Effects 16
2.10 References 17

Chapter 3. Low Angle Grain Boundaries in $YBa_2Cu_3O_7$ 18

3.1 Critical Current with Misorientation Angle – The Grain Boundary Problem 18
3.2 The Dislocation Array 22
3.3 Dislocation Properties 24
3.3.1 Structure and Strain 24
3.3.2 Carrier Depletion 26
3.3.3 Band Bending 26
3.4 GB Heterogeneity 27
3.4.1 GB Meandering 27
3.4.2 GB Faceting 28
3.4.3 Substrate Defects29
3.5 The Channel Model of Transport 30
3.6 High Angle $J_c(\theta_m)$ Dependence 33
3.7 Low Angle $J_c(\theta_m)$ Dependence 34
3.8 The Vortex-GB Interaction - Flux Channelling and Pinning 34
3.8.1 Vortices At Grain Boundaries 35
3.8.2 LAGB Flux channelling 35
3.8.3 Flux Pinning 37
3.8.4 Magneto-Optic Investigations 39
3.9 GB Resistance Measurements 40
3.10 References 40

Chapter 4. Experimental Method 44

4.1 Sample Preparation 44
4.1.1 Sample Sources and Deposition 44
4.1.2 Sample Cleaning 45
4.1.3 Deposition of Contacts 45
4.1.4 Removal of the Underside Layer of YBCO 46
4.1.5 Revealing the Grain Boundary 46
4.1.6 Patterning of Tracks 47
4.1.7 Artificial FIB Channel 48
4.2 Electrical Measurement System 50
4.2.1 Two-Axis Goniometer 50
4.2.2 Sample Mounting 51
4.2.3 Temperature Control and the Cryostat 52
4.2.4 Measurement Rig 53
4.2.5 Voltage Criteria and Track Comparison 54
4.3 Additional Sample Characterisation Techniques 55
4.3.1 Optical and Atomic Force Microscopy 56
4.3.2 X-ray Diffraction 56
4.3.3 SQUID Measurements 56
4.3.4 Transmission Electron Microscopy 56
4.3.5 Magneto-Optical Flux Imaging 56
4.4 References 56

Chapter 5. Initial Characterisation 57

5.1 Misorientation Measurement 57
5.1.1 Substrate 58
5.1.2 Film 60
5.2 LAGB Morphology 61
5.2.1 AFM Imaging 61
5.2.1.1 Substrates *61*
5.2.1.2 Films *62*
5.2.2 TEM Imaging 65
5.3 Magneto-Optic Imaging 66
5.4 *R-T* Measurement 69
5.5 Summary 71
5.6 References 71

Chapter 6. The *V-I* Characteristic 72

6.1 Previous Measurements 72
6.2 LAGB Vortex Channelling 74
6.3 Mechanisms Predicting *V-I* Linearity 75
6.3.1 Viscous Flux Flow 75
6.3.2 Non Viscous Channelling 76
6.3.3 Long Josephson Junction Behaviour 77
6.4 LAGB *V-I* Kinking 78
6.4.1 Experimental Observation 78
6.4.2 Flux Flow Model 81
6.5 *V-I* Heterogeneity 83
6.5.1 Experimental Observation 83
6.5.2 The Flow of Partial Vortex Rows 85
6.5.3 *V-I* Noise 86
6.6 LAGB *V-I* Curvature 88

6.7 Flux Flow with Applied Magnetic Field 92
6.7.1 Flux Flow Resistivity 93
6.7.2 Non-Viscous Channelling 96
6.8 Summary 97
6.9 References 98

Chapter 7. J_c(B,T) Measurements 99

7.1 $J_c(B)$: Field Dependence 99
7.1.1 Previous Measurements 99
7.1.2 $J_c^{GB}(B)$ Limitation by $J_c^{IG}(B)$ 102
7.1.3 $J_c^{GB}(B)$ with Temperature 104
7.1.4 $\delta(B) = J_c^{GB}/J_c^{IG}$: Comparison of GB to IG Properties 107
7.1.5 $J_c^{GB}(B)$ with Angle of Applied Field 109
7.1.6 Static $J_c(B)$ Hysteresis 110
7.2 $J_c(T)$: Temperature Dependence 112
7.2.1 Previous Measurements 112
7.2.2 $J_c^{GB}(T)$ Limitation by $J_c^{IG}(T)$ 113
7.2.3 $\delta(T) = J_c^{GB}/J_c^{IG}$: Comparison of GB to IG Properties 115
7.3 Discussion 117
7.4 References 118

Chapter 8. LAGB $J_c(\phi)$ Measurements 119

8.1 Previous Work 119
8.1.1 Vortex Accommodation 120
8.1.2 Twin Plane Channelling and Pinning 121
8.2 Lorentz Force Variation 123
8.3 The LAGB Vortex Channelling Dip 125
8.3.1 Experimental Observation 125
8.3.2 LAGB ϕ Channelling Model 126
8.3.3 Temperature Dependence 128
8.3.4 Field Dependence 132
8.3.5 Track Variability 133
8.4 Scaling of Channelling Data – the Dependence of ϕ_K on J_c 134
8.5 The *V-I* Characteristic and LAGB Channelling 138
8.6 Channelling for Field directed Out of the *ab*-plane 143
8.7 Vortex Channelling at an Artificial Channel 144
8.8 Summary and Discussion 147
8.9 References 148

Chapter 9. LAGB $J_c(\theta)$ Measurements 150

9.1 Introduction 150
9.2 Previous Work 151
9.3 Scanning Field Within the GB Plane: $J_c^{GB}(\theta, \phi = 0°)$ 153
9.3.1 The LAGB Pinning Peak 153
9.3.2 Sample Dependence 155
9.3.3 Field Dependence 156
9.3.3.1 Observation 156
9.3.3.2 $J_c^{GB}(\theta)$ Limitation by $J_c^{IG}(\theta)$ 159
9.3.3.3 Field Dependence Mechanisms: $\Delta J_c(B)$ 160
9.3.4 Temperature Dependence 162
9.3.4.1 Observation 162
9.3.4.2 LAGB Pinning Model 165

9.3.5 LAGB Angular Hysteresis 167
9.3.5.1 Observation *167*
9.3.5.2 Angular Hysteresis Model *169*
9.3.6 The *V-I* Characteristic 173
9.4 Scanning Field Out of the GB Plane: $J_c^{GB}(\theta, \phi = 90°)$ 175
9.4.1 Vortex Channelling 175
9.4.2 Field Dependence 177
9.4.3 The *V-I* Characteristic 178
9.5 Summary 180
9.6 References 181

Chapter 10. Conclusions and Further Work 182

10.1 Conclusions 182
10.2 Further Work 184
10.3 References 185

Appendix A: Misorientation Types 186

Appendix B: List of Samples Investigated 187

Appendix C: Partial Vortex Row Modification to the VFF Model 188

Appendix D: Publications 190

List of Symbols

a,b,c	Unit cell dimensions of YBCO
a_o	Vortex spacing
B	Magnetic flux density
B_{app}	Applied magnetic flux density
B_{GB}	Net flux density, as measured by MO at the LAGB
B_{rev}	History dependent *additional* flux component at the LAGB
B_c	Thermodynamic critical field
B_{c1}	Lower critical field
B_{c2}	Upper critical field
B_{irr}	Irreversibility field
B_z	Measured flux density in the *c*-direction
$B_\perp$	Component of applied flux density perpendicular to *ab*-plane (the *c*-direction)
B^+,B^-	Denote increasing and decreasing applied flux magnitudes respectively
d_{eff}	Width of dissipation across the LAGB, in the direction of current flow
D	Dislocation spacing
D_m	Demagnetising factor
E	Electric field
F_L	Lorentz force density in N/m^2
F_p	Pinning force density in N/m^2
$f_{p,L}$	Pinning force and Lorentz forces per unit vortex length in N/m
$f_{n,s}$	Helmoltz free energies per unit volume of the normal and superconducting states
H_{app}	Applied magnetic field
J_c	Critical current density
J^A	Average track current density
J_b	Boundary depairing current
J_d	Intragranular depairing current
l	Extended vortex core length along an LAGB
l_p	Length over which vortices are perpendicular to a sample surface
L	Track length
L_d	General ‘defect’ length
Q	Track length ratio $Q = (L_{IG}/L_{GB})$
T_c	Critical temperature
t	Reduced temperature $t = T/T_c$
t_f	Film thickness
t_d	Damage depth of FIB artificial vortex channel
U	Pinning potential

V_c	Voltage criterion used to determine J_c
V_c^{GB}	Voltage criterion used to determine J_c^{GB}
V_c^{IG}	Voltage criterion used to determine J_c^{IG}
v_f	Vortex velocity
w	Track width
s	Number of vortex rows flowing along the LAGB
Δ_R	Relative decrease in $J_c^{GB}(\phi)$
δ	Measured transparency ratio $\delta = J_c^{GB}/J_c^{GB}$
δ_c	Calculated transparency ratio using channel model cross sectional reduction
ε	Anisotropy parameter, $\varepsilon = 1/\Gamma$
ε_θ	Angle dependent anisotropy parameter
ϕ	Angle between the component of applied field parallel to the *ab*-plane and the normal to the current direction in the *ab*-plane
Φ_o	Magnetic flux quantum
Γ	Anisotropy parameter, $\Gamma = 1/\varepsilon$
γ_f	Flux flow resistance-area product, giving the dV/dJ step size within the VFF model
η	Viscous drag coefficient
λ	Magnetic penetration depth
λ_{ab}	Magnetic penetration depth for current decay parallel to the *ab*-plane
λ_c	Magnetic penetration depth for current decay parallel to the *c*-axis
θ	Angle between the film normal and the direction of applied magnetic field
θ^+,θ^-	Rotation in positive and negative θ respectively
$\Delta\theta^+,\Delta\theta^-$	Shift in the intrinsic peak position for rotation in θ^+ and θ^- respectively
ρ_f	Flux flow resistivity
ρ_n	Normal state resistivity
ω_o	Characteristic frequency of vortex vibration
ξ	Ginzburg Landau Coherence length
ξ_{ab}	Coherence length parallel to the *ab*-plane
ξ_c	Coherence length parallel to the *c*-axis
Ψ	Order parameter

List of Abbreviations

AFM	Atomic Force Microscopy
FT	Flux Trapping
GB	Grain Boundary
HAGB	High Angle Grain Boundary
HREM	High Resolution Electron Microscopy
IG	Intragranular
LAGB	Low Angle Grain Boundary
MO	Magneto-Optic
STEM	Scanning Tunnelling Electron Microscopy
TEM	Transmission Electron Microscopy
VFF	Viscous Flux Flow
YBCO	$YBa_2Cu_3O_7$

1 Introduction

1.1 Motivation and Background

The advent of high temperature superconductivity (HTS) in 1986 held forth the promise of widespread, practical applications of the phenomenon. However, for many years the *high current* application of HTS technology has been hampered by the presence of high angle grain boundaries (HAGBs) in 'first generation' wires and tapes. Weak coupling of superconductivity across HAGBs results in a low critical current density, J_c, and an extreme sensitivity to magnetic field - a problem found to be common to all HTS. In the latest $YBa_2Cu_3O_7$ (YBCO) 'coated conductors', fabrication techniques focus on increased biaxial alignment by achieving both greater in-plane and out-of plane granular texturing. The result is that critical currents in these new materials are now limited by networks of low angle grain boundaries (LAGBs) of [001]-tilt misorientation $\theta_m \sim 1 - 10°$ and achieve J_c (77 K, 0 T) of up to $1\text{-}2 \times 10^6$ Acm^{-2} [1].

Unlike the vast body of work focussing on HAGB research, the electronic behaviour of the LAGB has yet to be as fully elucidated. Lying between the Josephson coupled regime found at large misorientation, and the intragranular regime found for nominally zero misorientation, the transport properties of LAGBs are both fundamentally important and interesting. They are found to display both strong coupling, in contrast to HAGBs, and localised dissipation, in contrast to intragranular material.

1.2 Project Aims and Objectives

The prime objective of this work is to elucidate the transport properties of YBCO low angle grain boundaries. The grain boundaries (GBs) to be investigated are nominally 4° [001]-tilt misoriented, and formed by epitaxial thin film deposition onto bicrystalline $SrTiO_3$ substrates.

The channelling and pinning properties of the LAGB are to be evaluated through an investigation of (a) the form of the *V-I* characteristic, and (b) the critical current density, J_c, as a function of applied field and temperature. Pivotal to this work will be precision angular measurements of J_c and *V-I* in which the external magnetic field is applied at various angles to the sample.

Previous reports that the LAGB *V-I* displays a linear nature [2] are to be confirmed and significantly built upon. In addition, the observation of a pronounced peak in J_c associated

with LAGB vortex pinning [3] is to be investigated over a much wider range of field and temperature. Novel experimental geometries involving field sweeps rotating applied field out of the LAGB defect plane are to be pioneered. Possible hysteretic effects are also to be investigated in the LAGB transport properties, as they are commonly found in bulk polycrystalline material and are associated with the GB matrix [4].

As far as is possible, all GB properties are to be compared directly to *in situ* measurements made on intragranular (IG) tracks. This will enable an important contrast in behaviour to be drawn, particularly through use of the transparency ratio of *intergranular* to *intragranular* critical current density, $\delta = J_c^{GB}/J_c^{IG}$.

1.3 Thesis Overview

This dissertation is organised in the following manner:

- Chapter 2 provides an introduction to the basic concepts of superconductivity including the effects of flux flow and flux pinning.
- Chapter 3 presents a review of LAGBs and the structural and electronic mechanisms thought to influence their behaviour.
- Chapter 4 discusses the experimental methods used in this investigation.
- Chapter 5 presents the results of initial LAGB characterisation, including atomic force and transmission electron microscopy, X-ray and resistance measurement.
- Chapter 6 investigates the nature of the LAGB *V-I* characteristic. Strong evidence is given for an analysis based on a viscous flux flow (VFF) model.
- Chapter 7 presents measurements of J_c as a function of field magnitude. Such scans involve incrementing the applied field at a given angle of field orientation.
- Chapter 8 presents measurements of $J_c(\phi)$, where field is rotated in angle ϕ, primarily in the *ab*-plane of the current track. Pronounced channelling minima in $J_c(\phi)$ are found for field aligned to the GB plane.
- Chapter 9 presents measurements of $J_c(\theta)$, where field is rotated in angle θ, away from the *c*-axis of the current track and towards the *ab*-plane. The occurrence of a LAGB pinning peak and angular hysteresis are presented scanning within the GB plane. The occurrence of a broad channelling dip similar to that in chapter 8 is presented scanning out of the GB plane.
- Chapter 10 summarises this work and highlights areas for future research.

1.4 References

[1] D.M. Feldmann, J.L. Reeves, A.A. Polyanskii, G. Kozlowski, R.R. Biggers, R.M. Nekkanti, I. Maartense, M. Tomsic, P. Barnes, C.E. Oberly, T.L. Peterson, S.E. Babcock and D.C. Larbalestier, *Appl. Phys. Lett.* **77**, 2960 (2000)

[2] A. Díaz, L. Méchin, P. Berghuis, and J. E. Evetts, *Phys. Rev. B* **58**, R2960 (1998)

[3] A. Díaz, L. Méchin, P. Berghuis, and J. E. Evetts, *Phys. Rev. Lett.* **80**, 3855 (1998)

[4] J.E. Evetts and B.A. Glowacki, *Cryogenics* **28**, 641 (1988)

2 Flux Vortices and Critical Currents

This Chapter introduces the basic phenomenological theories of superconductivity, and the general properties of the high temperature superconductor $YBa_2Cu_3O_7$. Also discussed are the concepts of flux flow and flux pinning and how they are manifest in J_c and the *V-I* characteristic.

2.1 $YBa_2Cu_3O_7$

The discovery of high T_c cuprates by Bednorz and Muller [1] soon lead to the detection of superconductivity in YBCO at 93 K. Superconductivity became accessible at liquid nitrogen temperatures (77 K), a cheaper and easier cryogen to work with than liquid helium.

The orthorhombic unit cell of YBCO is shown in figure 2.1 and displays a layered structure characteristic of all cuprate compounds. Consisting loosely of three perovskite cells stacked in the crystallographic *c* direction, the structure contains double layers of copper oxide planes separated by copper oxide chains [2].

The critical temperature, T_c, depends sensitively upon the level of oxygen doping in the material [3]. This dependence is shown in figure 2.2 and is associated with a structural transition between a tetragonal (lower oxygen) and orthorhombic (higher oxygen) phase. Optimally doped superconducting $YBa_2Cu_3O_{7-\delta}$ is orthorhombic and has a $T_c \approx 93$ K, with

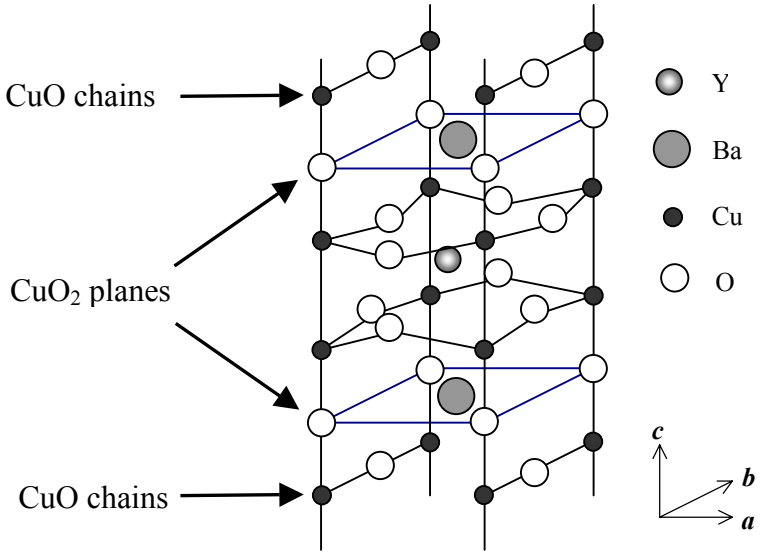

Figure 2.1. The unit cell of the orthorhombic phase of $YBa_2Cu_3O_{7-\delta}$, ($\delta \leq 0.5$). Optimally doped YBCO corresponds to $\delta \approx 0.03$. The orthorhombic structure consists of CuO chains and weakly coupled superconducting CuO_2 planes [2].

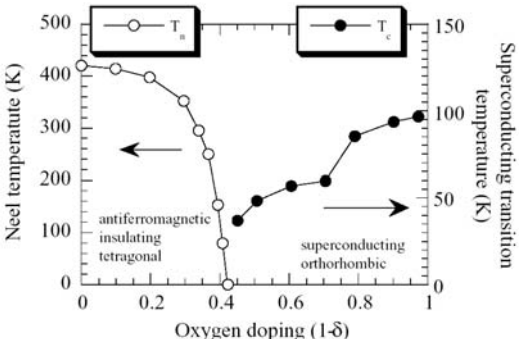

Figure 2.2. The oxygen doping phase diagram for YBCO (the Neel temperature, T_n, marks the onset of antiferromagnetic ordering) [3].

$\delta \approx 0.03$. The orthorhombic phase exists for $\delta \leq \sim 0.5$. For $\delta > 0.5$, YBCO becomes tetragonal and insulating antiferromagnetic. The dimensions of the YBCO orthorhombic unit cell, as found by Datta *et al* [4] for $\delta \approx 0.09$, are $a \approx 0.382$ nm, $b \approx 0.388$ nm and $c \approx 1.168$ nm.

Superconductivity is thought to be extremely localised to the copper oxide planes. The effect of oxygen doping is to introduce O^{2-}, creating CuO chains that strongly modify the macroscopic electronic properties of the superconductor. In order to maintain charge balance the CuO chains remove electrons from the CuO_2 planes. The remaining holes are mobile and by forming 'Cooper pairs' cause the planes to become superconducting.

The electrical properties of YBCO are also very anisotropic. In particular, J_c (section 2.4) is lower, and resistivity higher, for current transport in the *c* direction when compared to that in the *ab* direction [5]. This is because the coupling *between* CuO_2 planes is weak in comparison to that within the planes - the superconducting planes are isolated by less conductive chains.

Thin films of YBCO are deposited on substrates ideally possessing the same lattice constant and thermal contraction to enable good epitaxial growth. As YBCO is based loosely on the perovskite structure, obvious substrate choices tend also to be perovskite. Strontium titanate, $SrTiO_3$ was used for this study - the lattice mismatch with YBCO being only 1.2%.

2.2 Elementary Phenomenological Theory

2.2.1 The Ideal Phase Transition

The most fundamental property a superconductor exhibits is perfect diamagnetism - the Meissner effect [6]. Expulsion of magnetic field is achieved by the flow of circulating screening currents which require perfect conductivity, the phenomenon that provides the name 'superconductivity'. Perfect diamagnetism shows that superconductivity is a true thermodynamic state and that in switching from the normal to the superconducting state the superconductor undergoes a thermodynamic phase transition to a state with lower energy.

Superconductivity will be destroyed by applying a sufficiently large magnetic field, which for a uniform type I conductor with negligible demagnetising effects is B_c, the thermodynamic critical field. $B_c(T)$ gives the difference in free energy (the condensation energy) between the normal and the superconducting state. That is,

$$f_n(T) - f_s(T) = \frac{B_c^2(T)}{2\mu_o} \tag{2.1}$$

Where f_n and f_s are the Helmoltz free energies per unit volume of the normal and superconducting states respectively. Empirically, the from of $B_c(T)$ is approximated by the parabolic function, $B_c(T) \approx B_c(0)[1 - t^2]$, where $t = T/T_c$ [7].

In order to expel any magnetic field present, the superconductor must do work against a back EMF. A normal metal would trap this magnetic flux but the superconductor finds the energy required by making a phase transition to a state of lower energy.

2.2.2 London Theory

In 1935 Fritz and Heinz London [8] proposed two equations in an attempt to describe the electrodynamical properties of superconductors. The equations they derived, by assuming a density n_s of superelectrons with mass m_e, described the microscopic electric field, E, and magnetic flux density, B, within the superconductor,

$$\boldsymbol{E} = \frac{\partial}{\partial t}(\Lambda \boldsymbol{J}_s) \tag{2.2}$$

$$\boldsymbol{B} = -\nabla \times (\Lambda \boldsymbol{J}_s) \tag{2.3}$$

$$\text{where} \quad \Lambda = \mu_o \lambda_L^2 = m_e / n_s e^2 \tag{2.4}$$

Equation (2.2) replaces Ohms law ($\boldsymbol{E}=\rho\boldsymbol{J}$) as the relationship between electric field and current density and is an acceleration equation. The presence of an electric field accelerates the superelectrons, a short pulse of field being sufficient to leave the system with a supercurrent that will not decay. Equation (2.3) shows that a steady supercurrent is a function of the magnetic field (not the electric field as given by Ohms law for normal metals). Combining equation 2.3 with the Maxwell relation $\nabla \times \boldsymbol{B} = \mu_o \boldsymbol{J}$ gives the following equation governing the penetration of an applied magnetic flux density into a superconductor,

$$\nabla^2 B = \frac{B}{\lambda_L^2} \tag{2.5}$$

which has an exponentially decaying solution $B = B_o e^{-x/\lambda_L}$. An applied magnetic flux density will therefore penetrate only a short distance into the superconductor before it is screened completely, resulting in the Meissner effect.

2.2.3 GL Theory

One of the main triumphs of Ginzburg-Landau (GL) theory is its applicability to circumstances in which n_s varies, beyond the scope of London theory. GL theory [9]

introduced a complex pseudo-wavefunction, the order parameter $\Psi = |\Psi| e^{i\phi}$, having both magnitude and phase, where the local density of superelectrons is given by $n_s = |\Psi|^2$. By expanding the condensation energy of the superconductor in powers of Ψ and $\nabla\Psi$ about T_c - a framework previously proposed by Landau's theory of second order transitions - they found a functional form of the free energy. The resulting GL equations reveal that the properties of the superconductor depend on just two parameters $\alpha(T)$ and β, where $n_s = \alpha/\beta$. They are closely linked to two characteristic length scales associated with the theory, the GL penetration depth,

$$\lambda = \sqrt{\frac{m\beta}{4\mu_o e^2 |\alpha|}} \tag{2.6}$$

and the GL coherence length,

$$\xi = \sqrt{\frac{\hbar^2}{2m|\alpha|}} \tag{2.7}$$

In a similar result to that found in section 2.2.2, GL theory predicts that an applied magnetic field will be screened from the interior of the superconductor over a characteristic length scale, λ. The GL coherence length can be interpreted as the characteristic length over which spatial changes in the superconducting order parameter occur.

Both ξ and λ are temperature dependent and found to diverge as $(1-T/T_c)^{-1/2}$ near T_c. The ratio of the two characteristic length scales defines the dimensionless Ginzburg-Landau parameter,

$$\kappa = \frac{\lambda}{\xi} \tag{2.8}$$

Its value is approximately independent of temperature and as will be discussed in the next section, separates superconductors of type I and type II.

2.2.4 Type I and Type II Superconductivity

Abrikosov [10] (1957) calculated general solutions of GL theory and showed that they fall into one of two groups depending upon the sign of the superconducting-normal interfacial surface energy. Type I materials satisfy the inequality $\kappa < 1/2^{0.5}$ and have positive surface energy. The length of the interface separating superconducting and normal regions is minimised when in equilibrium. Type II materials satisfy the inequality $\kappa > 1/2^{0.5}$ and have negative surface energy. This results in the subdivision of any normal regions until a quantum limit is reached, and the relative interface length is maximised. Instead of a discontinuous breakdown of superconductivity at B_c, there is a continuous increase in flux penetration for applied fields larger than B_{c1}. Total penetration occurs at B_{c2} in a second order phase transition

to the normal state. The form of flux penetration between B_{c1} and B_{c2}, called the mixed state, is that of a regular array of quantised flux tubes* called Abrikosov vortices, each containing one flux quantum, Φ_o, given by equation 2.9.

$$\Phi_o = \frac{h}{2e} = 2.067 \times 10^{-15}\ \text{Wb} \tag{2.9}$$

This mixed state of partial diamagnetism means that the upper critical field, B_{c2}, can be very much larger than the thermodynamic critical field, B_c.

For a typical classic type I superconductor [7], such as pure elementary superconductors, $\lambda \approx 50$ nm and $\xi \approx 300$ nm giving $\kappa < 1/2^{0.5}$. For YBCO, $\kappa \sim 100$ resulting extreme type II behaviour.

2.3 The Flux Vortex

The Abrikosov vortex possesses a normal core with a radius approximately equal to one coherence length. Circulating supercurrents give rise to the term *vortex*, and they decay over a distance equal to the penetration depth. Figure 2.3(a) shows schematically the variation of order parameter, Ψ, and local magnetic flux density, b_L, over a cross section of an isolated vortex.

As the macroscopic magnetic flux density, B, is increased there is an associated increase in the density n (in m^{-2}) of vortices within the superconductor through the simple relation, $B = n\Phi_o$. Qualitatively, B_{c2} and B_{c1} correspond to the fields at which the distance between vortices is equal to the normal core radius, ξ and penetration depth, λ, respectively.

As initially predicted by Abrikosov, the flux vortices form an array named the flux line lattice (FLL). The lowest free energy is associated with a triangular arrangement with spacing a_o

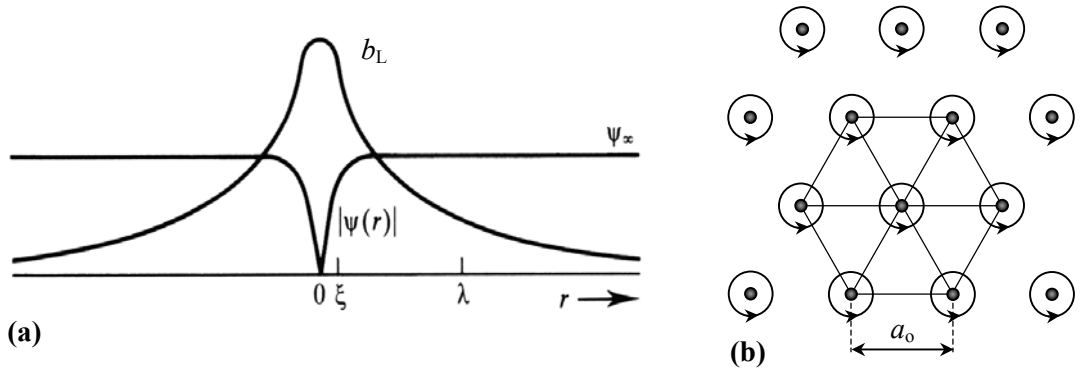

Figure 2.3.(a) Variation of Ψ and local flux density, b_L, over a cross section of an isolated Abrikosov flux vortex. (b) Triangular FLL formed by flux vortices (directed out of the page) penetrating a type II superconductor [7]. Arrows indicate circulating supercurrents.

* More accurately it is a quantity called the *fluxoid* that must always take on quantised values.

between flux lines. The FLL is sketched in figure 2.3(b) and was first experimentally observed by Essmann and Träuble [11]

The average induction associated with the FLL is given by equation 2.10.

$$B = n\Phi_o = \frac{2\Phi_o}{\sqrt{3}a_o^2} \quad \text{where rearranging gives,} \quad a_o = 1.075\sqrt{\frac{\Phi_o}{B}} \tag{2.10}$$

A full theoretical description of the FLL only exists for homogeneous materials and in general the FLL is distorted, curved in three dimensions and can be extremely defective [12].

2.4 Flux Flow and Flux Pinning

2.4.1 Flux Lines and Transport Currents

Superconductors only carry current with infinite conductivity under certain conditions: (1) for suitably low magnetic fields and temperatures, and (2) for transport currents below a certain critical value called the critical current, I_c, which itself depends on magnetic field and temperature. The dissipation that ensues for currents above I_c can be directly characterised in terms of the dependence of voltage, V, on current, I; termed the V-I transition or characteristic. Variations on this form of characterisation include the plotting of E-J and V-J curves.

When in the mixed state, the effect of passing a current through the superconductor is to apply a transverse Lorentz force to each of vortex. The force per unit length [N/m] experienced by an isolated vortex exposed to a laminar current flow, $\boldsymbol{J}$, is given by,

$$\boldsymbol{f}_L = \Phi_o \boldsymbol{J} \times \boldsymbol{m} \tag{2.11}$$

where $\boldsymbol{m}$ is a unit vector along the flux line, in the direction of the magnetic field. By summing over a number of vortices we get the Lorentz force density [N/m^3],

$$\boldsymbol{F}_L = \boldsymbol{J} \times \boldsymbol{B} \tag{2.12}$$

This force will tend to move flux lines in a direction transverse to the current, and in doing so will dissipate energy by generating an E-field (see next section). If they are allowed to move freely, then above B_{c1}, current flow will necessarily lead to dissipation.

2.4.2 Viscous Flux Flow Theory

The properties of a moving flux lattice have been successfully described by a phenomenological theory in which the driving Lorentz forces are balanced by a viscous damping term, which is dependent on the velocity of the vortices, $\boldsymbol{v}_f$ (see, for example [7]).

We introduce a viscous drag coefficient, η [Ns/m^2], such that the viscous force per unit length on a flux vortex is given by $-\eta \boldsymbol{v}_f$. Neglecting pinning forces and cross effects, the force balance equation for a single vortex becomes,

$$\boldsymbol{J}\Phi_o = \eta \boldsymbol{v}_f \tag{2.13}$$

The uniform motion of flux lines induces an electric field [13],

$$\boldsymbol{E} = \boldsymbol{B} \times \boldsymbol{v}_f \tag{2.14}$$

This can be thought of as a rate of change of flux linkage inducing an electric field as described by Faraday's law. The resulting dissipation per unit volume is simply $\boldsymbol{J}\cdot\boldsymbol{E}=n\eta v_f^2$ where n is the vortex density. Using equations (2.13) and (2.14) the flux flow resistivity, ρ_f, defined by the relation $\boldsymbol{E}=\rho_f\boldsymbol{J}$, can be deduced as,

$$\rho_f = \frac{E}{J} = \frac{B\Phi_o}{\eta} \tag{2.15}$$

Assuming η is independent of v_f means that equation (2.15) results in a linear E-J characteristic, the gradient of which (ρ_f) is linear in B. Both experimentation [14] and microscopic theory (Bardeen and Stephen [15]) reveal that the flux flow resistivity is approximately linked to the normal state resistivity, ρ_n, and the upper critical field through the relation,

$$\rho_f \approx \rho_n \frac{B}{B_{c2}} \tag{2.16}$$

The flux flow resistivity increases linearly with magnetic flux density below B_{c2}, connecting smoothly to the normal state resistivity when $B = B_{c2}$. Firstly, it should be noted that equation 2.16 is obeyed to greater degree at lower temperatures. Secondly, in the presence of pinning and thermal activation, this simple flow picture is somewhat altered, as will be discussed in the next sections.

2.4.3 J_c and Flux Pinning

In order to prevent vortex motion and achieve a finite critical current, driving Lorentz forces must be balanced. Balancing forces are provided by vortex pinning sites, which are caused by interactions of the flux lines with defects and inhomogeneities in the superconducting material. Local variations in λ, ξ, H_c and T_c will cause local variations in the free energy of a flux line and, as a result, certain locations of the line will be favoured over others. The elementary core and magnetic pinning interactions are associated with defects with dimensions on the order of the core radius and the penetration depth respectively.

The presence of an average pinning force, F_p, modifies the flux flow picture obtained in section 2.4.2. For $F_L(J) < F_p$ the FLL will be static and current will flow with zero resistance. For $F_L(J) > F_p$ the FLL will be de-pinned and move, resulting in the dissipative current flow described above. Ideally, therefore, the presence of flux pinning will lead to an abrupt onset of resistivity at J_c and a linear flux flow regime for increasing current, giving

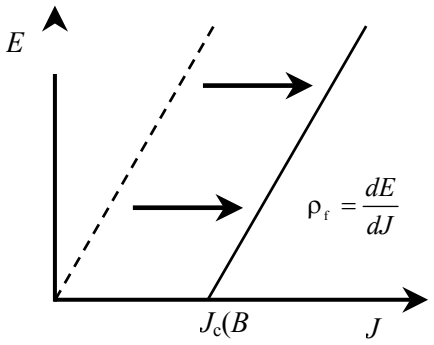

Figure 2.4. Schematic *E-J* transition of a superconductor with ideal flux flow and pinning. The dotted curve represents the case of no pinning.

$$E = \rho_f (J - J_c) \tag{2.17}$$

The extra dissipation due to the pinning will also ideally be J_cE. As indicated in figure 2.4 this corresponds to a shifting of the linear flux flow *V-I* curve, while maintaining the same gradient ρ_f. A study of critical currents is therefore practically equivalent to a study of flux pinning through the relation $F_p = J_cB$. More generally it can be said that,

$$F_p = \left| \boldsymbol{J}_c \times \boldsymbol{B} \right| \tag{2.18}$$

One special case arising from equations 2.12 and 2.18 is called the *force free configuration*. If the applied field is parallel (or anti-parallel) to the transport current, equation 2.12 implies zero Lorentz force on flux vortices. Within the flux flow model this also implies an infinite J_c. This is not experimentally observed (see chapters 8 and 9), and the finite J_c found in this regime is often attributed to helical instabilities in the FLL [16].

2.4.4 Pinning Sites in $YBa_2Cu_3O_7$

YBCO samples possess a number of defects that can act as pinning sites, influencing vortex dynamics and the electronic properties of the material. Some of the most common defects are summarised below:

Point Defects: Departure from stoichiometry at even a single atomic site in YBCO is sufficient to locally depress superconductivity. This is because of the short HTS coherence length. Common point defects are oxygen vacancies due to the sensitivity of YBCO to oxygen content (see figure 2.2).

Dislocations and Stacking Faults: Dislocations are the most common of type of defect, particularly in thin film samples [17]. As will be discussed in Chapter 3, the core of a dislocation is insulating and can provide a correlated disorder for effective flux pinning.

Grain Boundaries: Although high angle GBs act as 'weak links' that severely limit J_c, low angle GBs consist of an array of separated dislocations that can exhibit an anisotropic pinning behaviour. The investigation of their pinning and channelling properties is central to this work and is discussed in detail in chapter 3 onwards.

Twins: Prominent planar defects in YBCO, samples are frequently 'microtwinned' on small scales, often spaced by 100 nm [18]. The *a* and *b* axes are interchanged across a twin boundary, resulting in a 1.8° plane rotation. Unlike grain boundaries, no dislocations form along the twin interface. The analogous electronic behaviour of twins and low angle grain boundaries will be discussed in depth chapter 8.

2.4.5 Flux Flow in HTS

For currents below the critical current it is still possible to observe dissipation. Even when Lorentz forces are less than pinning forces, diffuse motion of flux lines can occur in the direction of the Lorentz force due to thermal fluctuations. This effect is known as flux creep and was described by Anderson and Kim [19] in terms of the thermal activation of flux lines pinned in a periodic potential. They took a jump rate of the form,

$$R = \omega_o e^{-U/kT} \tag{2.19}$$

where ω_o is a characteristic frequency of flux vortex vibration, and U is the activation energy a flux line, or flux bundle, must overcome to move to an adjacent potential minimum. Introducing a transport current tilts this pinning potential distribution spatially, making it easier for flux to jump in the direction in which the driving Lorentz force acts. This effect is illustrated schematically in figure 2.5.

The *net* jump rate will be zero for zero transport current. However, for currents near the critical current the net jump rate increases significantly. This is manifest as a rounding of the *E-J* characteristic near J_c, as shown in figure 2.6. Just how significant this curvature is depends on the temperature. Thermal activation effects play a much more prominent role in HTS materials and can be evident even for $J << J_c$. The activation energy barrier, U, is

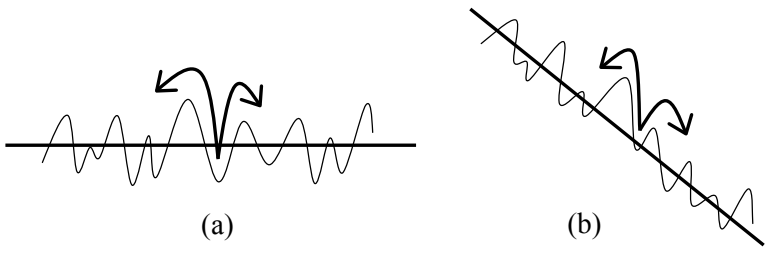

Figure 2.5. Schematic of flux lines jumping over a pinning potential distribution, with (a) no transport current, and (b) transport current; the Lorentz force tilts the potential in its driving direction and flux jumps are favoured in the 'downhill' direction [7].

smaller and the value of kT is almost an order of magnitude larger than at low T_c temperatures. The result is that the flux jump equation for creep (equation 2.19) becomes exponentially larger. The *V-I* rounding effect becomes much more pronounced, smearing out a clear measure of J_c and dominating to such an extent that the linear flux flow regime is difficult to observe. As a result, most HTS exhibit power law-like *V-I* transitions, and are often characterised by an 'n' value where $E = \rho J^n$.

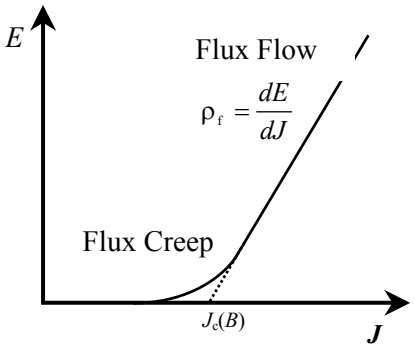

Figure 2.6. Flux creep distorts the *E-J* transition from that expected for ideal pinning, causing a rounding of the curve at J_c.

It is because of flux creep rounding that the critical current of a superconductor, at least for transport measurements, is often defined experimentally using a voltage or electric field criterion. It is, however, possible to observe the flux flow regime in YBCO if large enough *E*-fields can be generated [20] - by moving further up the *E-J* characteristic we would expect to observe the curvature decrease until at some point linearity is reached. It is the conclusion of this work that the linear viscous regime is accessed in low angle GB transport (chapter 6).

2.5 The Critical State

One of the main macroscopic manifestations of pinning in a superconductor is the hysteretic behaviour of its magnetisation curve. The Bean model [21] explains this effect by considering a zero field cooled (ZFC) type II superconductor in an increasing magnetic field. At B_{c1} flux lines will start to nucleate within the sample, initially at the edges, then move to the centre. Pinning forces oppose this flow, however, preventing the vortices from forming a thermodynamically stable array of equal density throughout the material. The result is a flux gradient set up by a force balance between pinning and Lorentz forces (the critical state) with a magnitude determined by the J_c of the material [22]. This is shown in figure 2.7(a). If the external applied field is then decreased back to zero, a substantial amount of flux can be left trapped corresponding to a large region within the material with a nonzero, positive magnetisation (figure 2.7(b)). Thus as the external field is cycled the magnetisation *M-H* curve becomes a hysteretic loop.

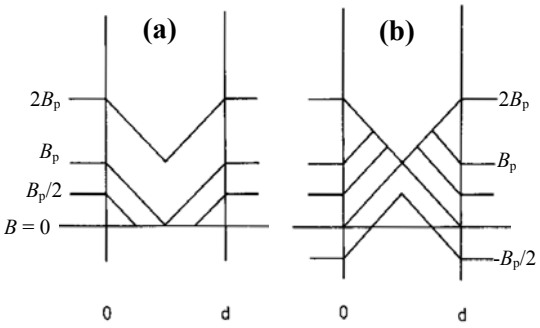

Figure 2.7. Flux profiles in the interior of a superconductor of size *d* for (a) increasing field, and (b) decreasing field, with a penetration field of B_p [22].

2.6 The Effect of Anisotropy

2.6.1 Anisotropic GL Theory

The effect of the cuprate anisotropy leads to anisotropy in all the key GL parameters. The penetration depths and coherence lengths in the *c* and *ab* directions are λ_c, ξ_c and λ_{ab}, ξ_{ab} respectively. A measure of the degree of anisotropy of a material is given by the GL anisotropy parameter, Γ, defined as,

$$\Gamma = \left(\frac{m_c}{m_{ab}} \right)^{1/2} = \frac{\lambda_c}{\lambda_{ab}} = \frac{\xi_{ab}}{\xi_c} \tag{2.20}$$

where $\Gamma \approx 5\text{-}7$ for YBCO and $\Gamma \approx 150$ for the highly anisotropic $Bi_2Sr_2CaCu_2O_8$. As both the upper and lower critical fields are strongly dependent on these lengths, they also show pronounced anisotropy, the expressions for B_{c2} becoming,

$$B_{c2} = \frac{B_{c2}^c}{\varepsilon_\theta} \quad \text{where} \quad \varepsilon_\theta = \sqrt{\cos^2\theta + \varepsilon^2 \sin^2\theta} \tag{2.21}$$

where $\varepsilon = 1/\Gamma$ and θ is the angle measured from the *c*-axis. Approximate values of the anisotropic ξ and λ for YBCO ($T = 0$ K) are $\xi_{ab} \approx 1.6$ nm $\lambda_{ab} \approx 135$ nm $\xi_c \approx 0.24$nm $\lambda_c \approx 890$nm [23]. Equation 2.21 is also applicable to other angular dependent quantities and effectively constitutes a scaling law.

2.6.2 Vortex Structure

As the dimensions of an isolated flux vortex are characterised by the parameters ξ and λ, the rotation of a magnetic field in an anisotropic superconductor will be accompanied by variation in vortex structure. The flux line geometry will depend upon the direction it is lying in relative to the crystallographic axes: lying along the *ab*-plane the vortex core will have a

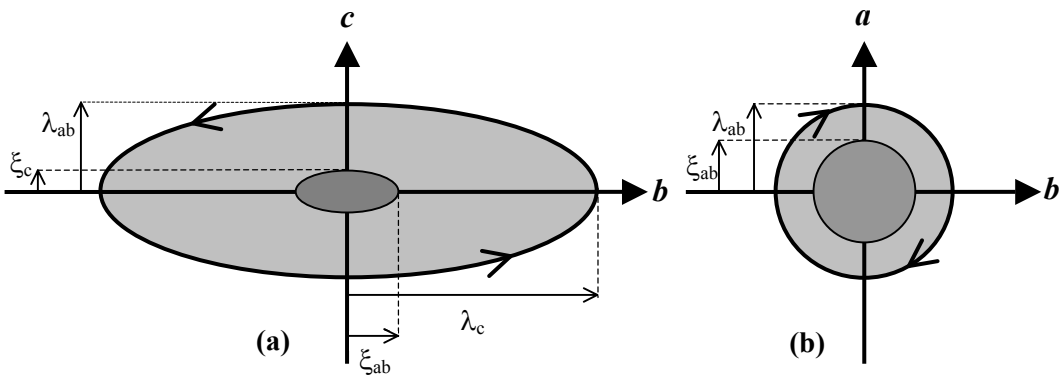

Figure 2.8. Schematic cross sections of vortices lying along (a) the *a*-axis, and (b) the *c*-axis in an anisotropic type II superconductor.

radius of ξ_{ab}; lying along the *c* axis it will have a radius of ξ_c, where $\xi_c << \xi_{ab}$. This is illustrated schematically in figure 2.8. Note that the penetration depths λ_{ab} and λ_c refer to the screening by supercurrents flowing in the *ab*-plane and *c* direction respectively, where $\lambda_c > \lambda_{ab}$. The overall effect for a vortex lying along the *ab*-plane is the distortion of the core and screening currents into an ellipse with larger dimensions in the *ab*-plane.

2.7 J_c with angle of Applied Field

This study makes extensive use of angular scans, in which J_c is measured as a function of the rotation in angle of applied field with respect to a sample. Roas *et al* [24] were the first to perform such a measurement on thin film *c*-axis YBCO. They found strong peaks in $J_c(\theta)$ for field aligned with the *ab*-planes of the material as field was rotated in a plane perpendicular to the transport current. An example is shown in figure 2.9 at 4.2 K, 3 T. This scan geometry corresponds to rotating in θ, at $\phi = 0°$ in figure 4.6, and is explained and investigated in detail in chapter 9.

The peak for field along the *ab*-plane is commonly referred to as the intrinsic pinning peak, after a model proposed by Tachiki and Takahashi [30,31]. They argued that the intrinsically layered structure of YBCO creates a periodic pinning potential along the *c*-direction due to a modulation of the order parameter. Vortices lying in the *ab*-plane are preferentially confined to the less conductive regions between CuO_2 planes. The mechanism becomes increasingly effective as flux aligns with the *ab*-plane, resulting in a peak in $J_c(\theta)$.

Blatter *et al* [25] also pointed out that a peak in $J_c(\theta)$ is expected for field aligned with *ab* by simply considering variation in the key GL parameters with angle (section 2.6.1). This model considers an anisotropic but homogeneous material. Other models by Solovjov *et al* [26] and Kes *et al* [27] have also been used to explain the existence of the intrinsic J_c peaks.

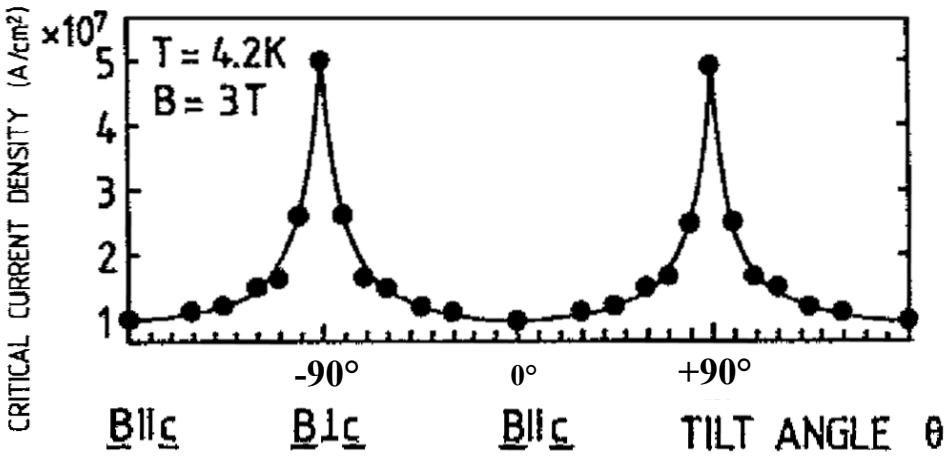

Figure 2.9. The variation of J_c with angle, θ, between the applied magnetic field and the *c*-axis of a thin film YBCO sample [24].

2.8 The Irreversibility Line

In addition to B_{c1} and B_{c2} there is another critical field of importance called the irreversibility field, $B_{irr}(T)$. This appears to be an intrinsic property of the cuprate superconductors. $B_{irr}(T)$ falls between B_{c1} and B_{c2} and in the B-T phase diagram is referred to as the irreversibility line (see figure 2.10). In the region below the irreversibility line flux is pinned effectively, the resistance of the sample will be zero and the corresponding magnetisation curves will be hysteretic. In the region above the irreversibility line the material shows a substantial electrical resistance even though it is superconducting in the sense that it has a finite order parameter. The dissipation observed in this region corresponds to easy flux flow, and magnetisation curves correspondingly show a reversible nature associated with a lack of effective pinning. The position of the line has been found to depend on the strength of pinning present but is also strongly related to the degree of coupling between CuO_2 planes [23]. There is some debate as to whether the irreversibility line represents a melting of the flux line lattice, a phenomenon that occurs in conventional superconductors but is obscured as it is very close to B_{c2}. The most widely supported theory is that the decoupling of vortices into almost independent pancakes in adjacent CuO_2 layers (as predicted by Clem [28]) renders localised point pinning centres ineffective. B_{irr} is expected to vary with angle of applied field [29], but for YBCO $B_{irr} \approx 4$ T at 77 K and $B_{irr} \approx 25$ T plus at 60 K for field in the c-direction.

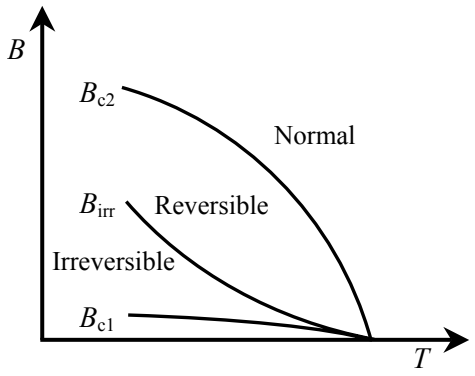

Figure 2.10. The irreversibility line in the B-T plane. The concave shape of B_{irr} compared to the upper and lower critical field [23].

2.9 Demagnetising Effects

The expulsion of flux in the simple form of the Meissner effect only occurs for samples with 'small' dimensions normal to the external magnetic field. The expulsion will in general lead to an increase in flux density at the edges of the sample. For an applied field H, the enhanced field H_e at the edge is given by $H_e = H/(1\text{-}D_m)$, where D_m is the demagnetising factor. D_m ranges from 1, for an infinite flat slab perpendicular to the field, to zero, for a long rod parallel to the magnetic field. For type II superconductors with finite demagnetising factors the result is that the mixed state is established for $H_{c1}(1\text{-}D_m) < H < H_{c2}$. the magnitude of field enhancement for thin film samples (width W, thickness t_f) has been calculated by Huebener *et al* [30] as (W/t_f) and Zeldov *et al* [31] as $(W/2t_f)^{1/2}$. They both estimated the thin film track to be an ellipse with semimajor axis $W/2$, and semiminor axis $t_f/2$.

2.10 References

[1] G. Bednorz and K. A. Müller, *Z. Phys*. **B64**, 189 (1986)

[2] C. P. Poole Jr., T. Datta, and H. A. Farach, *Copper Oxide Superconductors*, John Wiley & Sons, New York, (1988)

[3] J. Rossat-Mignod, L. P. Regnault, C. Vettier, P. Burlet, J. Y. Henry, and G. Lapertot, *Physica B*. **169,** 58-65 (1991)

[4] T. Datta, "Oxide Superconductors: Physical Properties", *Concise Encyclopedia of Magnetic and Superconducting Materials*, Ed. J. E. Evetts, Pergamon, Oxford (1992)

[5] S. W. Tozer, A. W. Kleinsasser, T. Penney, D. Kaiser, and F. Holtzberg, *Phys. Rev. Lett.* **59,** 1768-1771 (1987)

[6] W. Meissner and R. Ochsenfeld, *Naturwissenschaften* **21**, 787 (1933)

[7] M. Tinkham, *Introduction to Superconductivity*, 2nd Edition, McGraw-Hill, New York (1996)

[8] F. and H. London, *Proc. Roy. Soc.* (London) **A149**, 71 (1935)

[9] V. L. Ginzburg and L. D. Landau, *Zh. Eksp. Teor. Fiz*. **20**, 1064 (1950)

[10] A. A. Abrikosov, *Zh. Eksp. Teor. Fiz*. **32**, 1442 (1957)

[11] U. Essmann and H. Träuble, *Phys. Lett.* **24A**, 526 (1967)

[12] H. Brandt and J. E. Evetts, "Flux Line Lattice", *Concise Encyclopedia of Magnetic and Superconducting Materials*, Ed. J. E. Evetts, Pergamon, Oxford (1992)

[13] B. D. Josephson, Phys. Lett. **16** 242 (1965)

[14] Y. B. Kim, C. F. Hempstead, and A. R. Strnad, *Phys. Rev. Lett*. **12**, 145 (1964); *Phys. Rev.* **139**, A1163 (1965)

[15] J. Bardeen and M. J. Stephen, Phys. Rev. **140**, A1197 (1965)

[16] E. H. Brandt, *Rep. Prog. Phys*, **58**, 1465 (1995)

[17] B. Dam, J. M. Huijbregtse, F. C. Klaassen, R. C. F. van der Geest, G. Doornbos, J. H. Rector, A. M. Testa, S. Freisem, J. C. Martinez, B. Stauble-Pumpin and R. Griessen, Nature **399**, 439 (1999)

[18] T.E. Mithchell, "Oxide Superconductors: Electron Microscopy", *Concise Encyclopedia of Magnetic and Superconducting Materials*, Ed. J. E. Evetts, Pergamon, Oxford (1992)

[19] P. W. Anderson and Y. B. Kim, *Rev. Mod. Phys*. **36**, 39 (1964)

[20] M. Kuncher, D.K. Christen and J.M. Philips, *Phys. Rev. Lett*. **70**, 998 (1993)

[21] C. P. Bean, *Phys. Rev. Lett*. **8**, 250 (1962)

[22] M. Cyrot and D. Pavuna, *Introduction to Superconductivity and High T_c Materials*, World Scientific, London, (1995)

[23] J. R. Waldram, *Superconductivity of Metals and Cuprates*, IoP Publishing, London, (1996)

[24] V. Roas, L. Schultz and G. Saemann-Ischenko, *Phys. Rev. Lett*. **64**, 479 (1990)

[25] G. Blatter, V. B. Geshkenbein, and A. I. Larkin, Phys. Rev. Lett. **68**, 875

[26] V.F. Solovjov, V.M. Pan, H.C. Freyhardt, *Phys. Rev. B* **50**, 13724 (1994)

[27] P. H. Kes, J. Aarts, V. M. Vinokur and C. J. van der Beek, *Phys. Rev. Lett*. **64**, 1063 (1990)

[28] J.R. Clem, *Phys. Rev. B* **43**, 7837

[29] S.K. Gupta, Shashwati Sen, J.C. Vyas, S.P. Pai, R. Pinto, V.C. Sahni, *Physica C* **324**, 137 (1999)

[30] R. P. Heubener, R. T. Kampwirth and J. R. Clem, *J. Low Temp. Phys*. **6**, 275 (1972)

[31] E. Zeldov, J. R. Clem, M. McElfresh and M. Darwin, Phys. Rev. B, **49**, 9802 (1994)

3 Low Angle Grain Boundaries in $YBa_2Cu_3O_7$

This chapter reviews the properties of low angle grain boundaries (LAGBs) in the high temperature superconductor YBCO. Initially introduced are the problems associated with the presence of grain boundaries in HTS materials. This is followed by a description of LAGB microstructure and the various mechanisms - both electronic and structural - that are thought to influence their behaviour. The remaining sections discuss the transport properties of LAGBs and their interaction with flux vortices in an applied field. Remarkably, both flux channelling *and* flux pinning behaviour are observed, phenomena that will be further elucidated in chapters 6-9.

3.1 Critical Current with Misorientation Angle – The Grain Boundary 'Problem'

Early work by Chaudhari *et al* [1] first identified grain boundaries in HTS as responsible for low critical currents and increased sensitivity of J_c to magnetic fields. In the ground breaking studies of Dimos *et al* [2,3] that followed, it was shown that the critical current across an YBCO grain boundary is exponentially reduced as a function of its misorientation angle. Dimos *et al* [2] initially studied the behaviour of [001]-tilt boundaries, fabricated by the epitaxial deposition of YBCO onto bicrystalline $SrTi0_3$ substrates (bicrystals) with pre-determined misorientation angles. The geometry of the [001]-tilt boundary, illustrated in figure 3.1, involves a tilt of one substrate around the *c*-axis (the [001] direction) with respect to the other. The misorientation of the bicrystal is defined as the angle, θ_m, between the shaded (100) planes. Although the [001]-tilt geometry is only one of three general misorientation types (as listed in appendix A) it is of particular interest for research as it constitutes the predominant boundary type present in biaxially aligned 'coated conductors' [53]. As such, it also forms the basis of this study into LAGB behaviour.

The thin films of YBCO studied by Dimos *et al* were deposited by electron beam evaporation and misorientation information gathered using back Laue X-ray diffraction. By patterning tracks both across the grain boundary, and within the grains, they were able to measure the ratio of *grain boundary* critical current density, J_c^{GB}, to the *intragrain* critical current density, J_c^{IG}. The now famous Dimos *et al* result [2] is shown in figure 3.2. They found that as θ_m increases, J_c^{GB} decreases, marking a transition in intergranular coupling from strong and

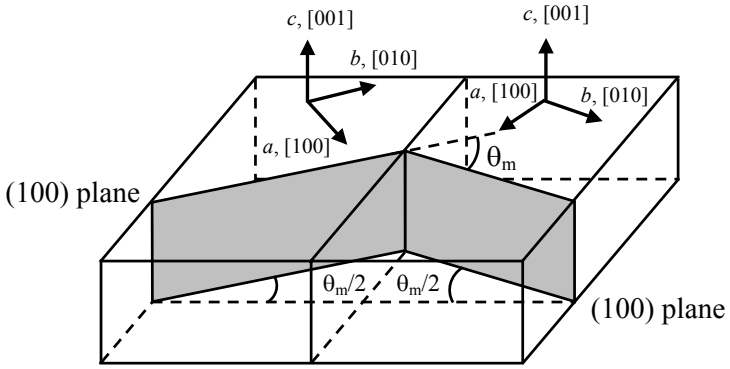

Figure 3.1. Schematic geometry of a symmetrical [001] tilt $SrTiO_3$ bicrystal substrate of misorientation, θ_m. Deposition of an epitaxial YBCO thin film results in an artificial YBCO grain boundary with the pre-determined misorientation of the substrate bicrystal. The (100) planes are shaded (after [2]).

single crystal-like, to weak and Josephson junction-like. The decrease was also found to be extremely rapid, the ratio $\delta = J_c^{GB}/J_c^{IG}$ falling off by almost two orders of magnitude with increasing [001]-tilt misorientation (also found for *other* types of tilt – see appendix A).

Low angles were found to display larger J_c^{GB} values on the order of J_c^{IG}. Higher angles displayed a drastically reduced and extremely field sensitive J_c^{GB} that could be suppressed almost completely by just a few millitesla of applied field (chapter 7). In addition, the *V-I* characteristic is often RSJ-like for HAGBs [4,5] and flux flow dominated for LAGBs (chapter 6). The key transition, from low angle strong-coupling to high angle weak-link behaviour, was found to occur over an angular range of $\theta_m \approx 5°\text{-}10°$. Further increase of misorientation resulted in the saturation of J_c^{GB}/J_c^{IG} to 10^{-2} at 20°.

The ratio of $\delta = J_c^{GB}/J_c^{IG}$ is a very useful one, in that it provides, for a given material a clear indication of the degree of impediment to current flow the presence of the boundary creates.

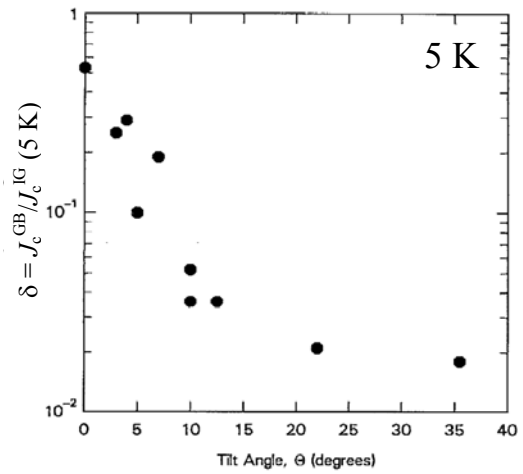

Figure 3.2. Original dependence of the ratio of grain boundary (GB) to intra-grain (IG) critical current densities, $\delta = J_c^{GB}/J_c^{IG}$, with [001]-tilt misorientation angle as found by Dimos *et al* [2].

While a ratio of $J_c^{GB}/J_c^{IG} \sim 1$ implies the boundary is effectively 'transparent', a ratio of $J_c^{GB}/J_c^{IG} \sim 10^{-2}$ indicates a severe limitation compared to the IG norm. For LAGBs the ratio is especially informative, and as will be shown in chapters 7-9, this work has found that δ is both strongly dependent on field magnitude, field angle and temperature.

There are, however, problems associated with a normalisation to IG properties such as seen in figure 3.2, particularly for *higher* misorientations [6]. The foremost of these is the

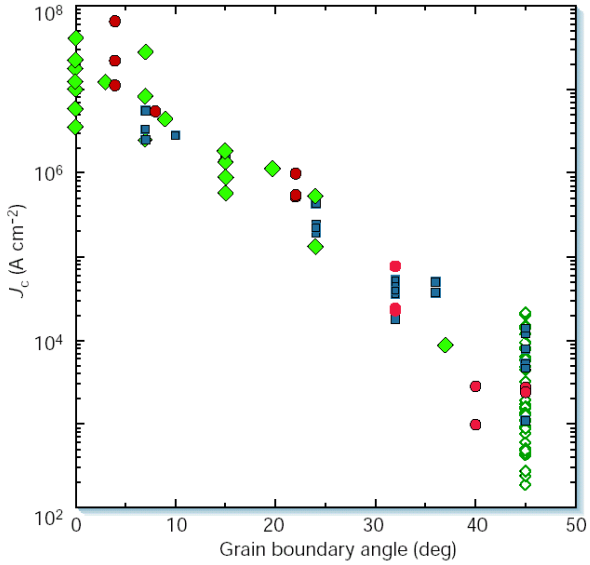

Figure 3.3. Compilation of J_c^{GB} data with [001]-tilt misorientation angle at 4.2 K, 0 T, for thin film YBCO samples. Substrates include bicrystal $SrTiO_3$ [squares and filled diamonds] YSZ [circles] and 'bi-epitaxial' junctions [open diamonds]. Compiled by [12].

fact that variations in J_c^{IG}, from sample to sample, or material type to material type, could effectively mask the intrinsic dependence of J_c^{GB} with θ_m. Whereas J_c^{IG} is determined by the flux pinning strength of the IG material in question, J_c^{GB} is determined by a number of factors over the misorientation range: at high angles J_c^{GB} is dominated by Josephson coupling between the grains, at lower angles J_c^{GB} is influenced by flux pinning and flux channelling. The ratio δ therefore contains information on both GB and IG transport behaviour; for example, artificially increased values of J_c^{GB}/J_c^{IG} can simply result from poor IG properties.

The Dimos *et al* rapid decrease in J_c^{GB}/J_c^{IG} was soon confirmed and improved upon by other groups. Separate but consistent results obtained by Ivanov *et al* [7], Gross *et al* [6], Amrein *et al* [8], Heinig *et al* [9,10,11] and Hilgenkamp *et al* [5], revealed a clear *exponential* dependence of absolute J_c^{GB} with θ_m. Figure 3.3 presents a compilation of absolute J_c data taken at zero field and 4.2 K [12]. The indicated relationship between J_c^{GB} and θ_m is of the form given by equation 3.1.

$$J_c^{GB}(\theta_m) = J_{co} e^{-\left(\frac{\theta}{\alpha}\right)} \tag{3.1}$$

The angle α marks the misorientation at which J_c^{GB} falls to 1/e of its value at $\theta_m = 0°$, J_{co}. Nominally*, the value of J_{co} should be simply that of the intragranular material, J_c^{IG}. The magnitude of α gives us *one* indication of the position of the transition from low angle to high angle behaviour (another is the channel model overlap angle, θ_c, introduced in section 3.5).

* Experiments on 0° bicrystal films produced in the same manner as those for $\theta_m > 0°$ have yielded $J_c^{GB}(0) < J_c^{IG}$. This has been attributed to the inaccuracy in fabricating truly 0° interfaces [46] and extrinsic effects associated with the artificial GB fabrication method (section 3.4).

Table 3.1 provides a summary of some of the values obtained in the literature. The spread in α can be linked in most cases to the noise on the $J_c^{GB}(\theta_m)$ curve, although measurement at lower temperature yields larger α.

Table 3.1. Measured values of α and J_{co} for thin film and bulk [001]-tilt grain boundaries at zero applied field and 77 K. Thin film YBCO samples yield a spread in α of approximately 3 - 6°.

Group	Temperature	Type	J_{co} (MA/cm^2)	α
Hilgenkamp *et al* [5]	4.2 K	Thin film YBCO	~ 20	5.6°
Verebelyi *et al* [13]	77 K	Thin film YBCO	3	3.2°
Heinig *et al* [9-11]	77 K	Thin film YBCO	5	4.0°
Gross *et al* [6]	77 K 4.2 K	Thin film YBCO	3 7	4.1° 4.9°
Ivanov *et al* [7]	77 K	Thin film YBCO	3	4.4°
Todt *et al* [14]	77 K	Bulk YBCO	0.04	8.7°

The three most common types of YBCO bicrystal studied are epitaxial thin film, melt processed and flux grown [15]. The latter two are termed 'bulk' grain boundaries, and although generally they exhibit the same exponential decrease of $J_c^{GB}(\theta_m)$, they tend to fall off more slowly with increasing misorientation (see figure 3.4 [16]). Values of $\alpha \approx 7$ - 9° have been observed by Field *et al* [17] and Todt *et al* [14], and other measurements suggest this figure could be pushed even higher [18,19]. The striking aspect of bulk GB data is that J_c^{GB} is some thirty times lower in magnitude than the thin film data. In this respect, the increased strong to weak coupled transition in these materials is misleading: J_c^{GB} for a given misorientation below the 'transition' is still drastically reduced compared to equivalent thin film misorientations.

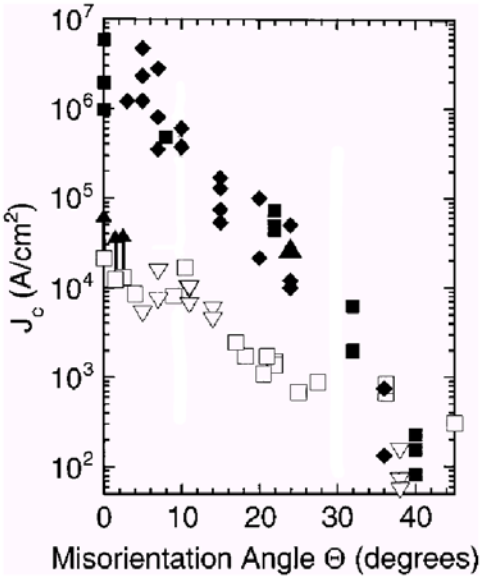

Figure 3.4. J_c^{GB} with misorientation [16]. Filled symbols are taken from thin film samples, open symbols are from bulk samples.

It is worth noting that high angle grain boundaries in conventional, low T_c superconductors do not behave as weak links. This illustrates a remarkable difference in properties associated with the cuprates. As mentioned in section 2.4.4, one major influencing factor is the short superconducting coherence length of HTS materials, $\xi(0\ K) = 1.6$ nm (YBCO) [6] and sensitivity to hole concentration. The result is that

interfaces, defects and impurities as small as just a few nanometers may cause a drastic reduction of the order parameter [4]. Such obstructions to the flow of current can result in blockages with effective cross sections that are considerably larger than the physical size of the defect [20]. Interestingly however, although the presence of high angle boundaries plagues attempts to develop high current and field applications of HTS materials, they also form the foundation of thin film technologies based on the Josephson effect.

3.2 The Dislocation Array

Put simply, grain boundaries are structural defects that interrupt the lattices of adjacent misoriented crystals. They can vary in structure depending on the type and degree of misorientation between the two crystals. Low angle YBCO [001]-tilt boundaries consist of an array of edge dislocations that accommodate the lattice mismatch between the two crystals. The YBCO lattice *between* the dislocations in a LAGB has been found to be relatively undisturbed [2,21,22]. The dislocations cores, however, have been found to be insulating (section 3.3). Higher angle boundaries consist of a much more complex atomic arrangement, and structure can vary substantially with angle of misorientation [23].

The basic geometry of an edge dislocation in a simple cubic structure is illustrated in figure 3.5(a) as the line DC. It is obtained by the insertion of an extra half plane of atoms, ABCD, into the lattice. The accommodation of grain misalignments by the formation of an array of such edge dislocations can be seen schematically in figure 3.5(b); it is this array that constitutes a low angle grain boundary. The direction of the Burgers vectors, ***b***, is also indicated in the diagram. This is the vector required to complete the Burgers circuit around the dislocation in a perfect crystal (see, for example, Hull and Bacon [23]).

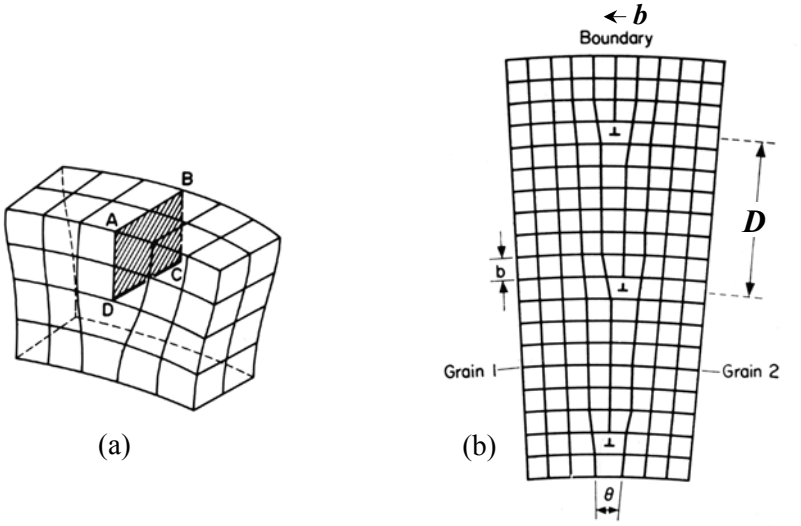

Figure 3.5. Schematic illustrations of (a) an edge dislocation (the line DC) in a simple cubic lattice, formed by the insertion of an extra half plane of atoms, ABCD, and (b) the arrangement of dislocations in a symmetrical LAGB [23]. The Burgers vector, ***b***, is normal to the grain boundary plane.

For an ideal [001]-tilt boundary the array dislocations will be normal to the *ab*-plane of both crystals, and extend linearly in the *c* direction. The distance between dislocations, *D*, is given by the Read-Shockley (or Frank's) formula,

$$D = \frac{|\boldsymbol{b}|}{2\sin(\theta_m/2)} \tag{3.2}$$

where $b \approx 0.39$nm for YBCO [2,21]. For a 4° YBCO grain boundary, $D \approx 5.6$ nm.

As YBCO possesses a non-simple cubic structure (see figure 2.1) the dislocation structure is slightly more complicated. The distinction may be drawn between two separate types of dislocation that form in YBCO LAGBs; those that centre on a copper column and those that centre on an yttrium/barium column [24]. Figure 3.6(a) illustrates schematically both of these scenarios. Figure 3.6(b) shows a Z-contrast scanning tunnelling electron microscopy (STEM) image of a LAGB, displaying dislocations of both types. The brighter columns consist of Y and Ba atoms, the weaker columns consist of Cu(1), Cu(2) and O(4) atoms. Columns consisting solely of oxygen atoms scatter too little to show up on the image.

It can be seen from equation 3.2 that the greater the misorientation angle, the closer the inter-dislocation distance, *D*. This effect is nicely illustrated in the high-resolution TEM (or HREM) measurements performed by Wen *et al* [25] shown in figure 3.7. They imaged YBCO [001]-tilt grain boundaries formed by liquid phase epitaxy on MgO bicrystal substrates of 4°, 8°, 16° and 45° misorientations. As misorientation is increased, the edge dislocations - which are seen as white regions - move closer together, decreasing the width of the undisturbed

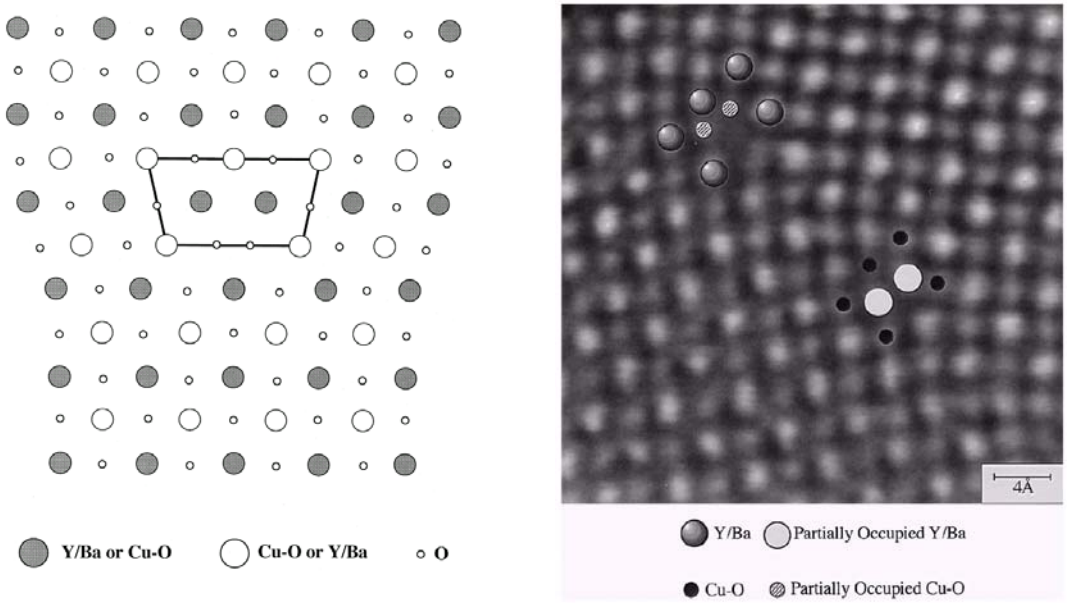

(a) **(b)**

Figure 3.6. (a) Schematic of a perfect edge dislocation core in YBCO with a burgers vector of [100] or [010], and (b) Z-contrast STEM image of a [001]-tilt LAGB in YBCO. Dislocations cores are identified forming on both Cu and Y/Ba columns [24].

channel areas. By 45° it can be seen that the dislocations overlap, forming a continuous interface. When this occurs, current transport across the boundary is governed entirely by the electronic properties of the dislocation structure.

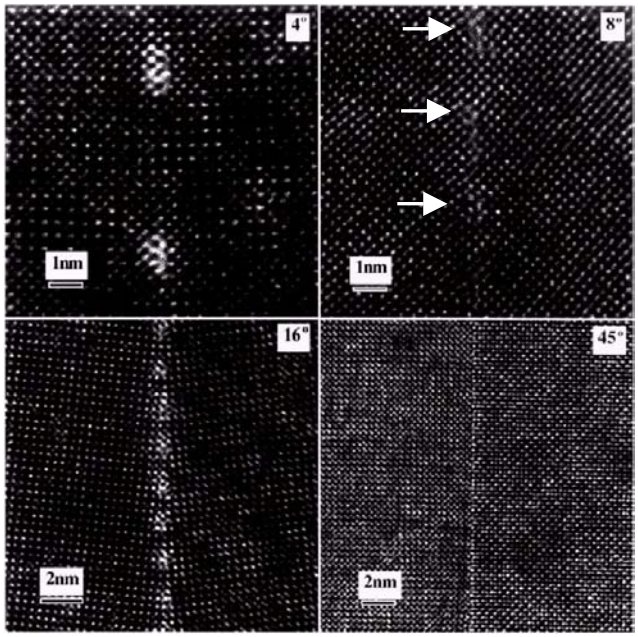

Figure 3.7. HREM images of 4°, 8°, 16° and 45° YBCO grain boundaries (LPE deposition on bicrystal MgO) [25].

The nature of the overlapping dislocation cores that occur at HAGBs has been investigated by Browning *et al* [24] and interpreted in terms of the *structural units* model. The boundary is comprised of a series of adjacent structural arrangements, or units. In fact, the units are formally equivalent to the dislocation core model, and can be the same structures as observed at isolated LAGB dislocation cores (figure 3.6(a)).

3.3 Dislocation Properties

The decrease in $J_c^{GB}(\theta_m)$ can naturally be accounted for by assuming that there are regions of suppressed order parameter near the dislocation cores. Such cores would block supercurrent through the GB. Non-superconducting dislocation cores can result from a mixture of local hole concentration and stoichiometric variations, additional quasi-particle scattering and significant strain fields. The structural and electronic properties of YBCO dislocation cores are discussed below.

3.3.1 Structure and Strain

In their influential study, Dimos *et al* [2] first postulated that the dislocations observed in YBCO grain boundaries created localised regions of suppressed order parameter. To further investigate, Gao *et al* [22] studied the dislocation cores of a [001]-tilt LAGB in

polycrystalline YBCO thin films using HREM and image simulations. In addition to confirming the LAGB dislocation array structure, they found the dislocation cores to be Cu rich and to possess a structural radius of about r_d = 1 nm. The radius previously assumed was that of the much smaller burgers vector, *b,* usually observed in non-superconducting ceramics. Figure 3.8(a) shows an enlarged image taken of a dislocation found in a 3.5° LAGB. The open circles represent a superimposed rigid 3.5° boundary. The large relaxation (indicated by arrows) and amorphous nature of the core region led to the conclusion the core material was indeed non-superconducting. They attributed this to the structural composition and complexity of the material.

In their landmark publication, Chisholm and Pennycook [26] proposed that elastic strain fields associated with the dislocation cores would lead to an extended region of reduced order parameter. The strain contours they calculated using linear elasticity theory are shown in figure 3.8(b) as a function of the reduced distance, $X = x/D$ and $Y = y/D$, from the dislocations. The criterion they used to define core size was 1 % strain. This magnitude has been found to result in the formation of tetragonal non-superconducting phase of YBCO in place of the superconducting orthorhombic [24]. The calculations show that in addition to being narrow, the channels are also relatively long. For example, a 5° boundary results in an effective core size ($2r_d$) of 2.9 nm along the boundary, and 8.9 nm perpendicular to it.

The strain fields have been found to decay exponentially over the length $\lambda_{st} = D/2\pi$, which decreases with D as θ_m increases [27]. Compared to the 5° core size along the GB mentioned above, Chisholm and Pennycook calculated a core size of 1.8 nm for a 10° misorientation. Within the calculations, strain fields will not touch for any angle. Gurevich *et al* [27] also

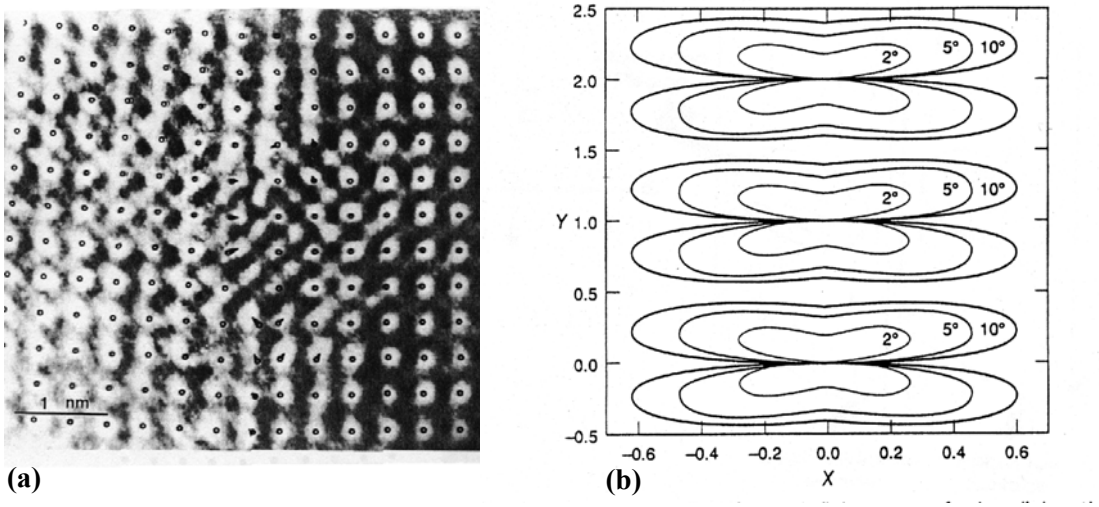

Figure 3.8.(a) HREM image of a dislocation core in a 3.5° YBCO thin film boundary with a superimposed rigid lattice (open circles). Arrows indicate lattice relaxation about the dislocation, which is particularly large at the core [22]. (b) Strain fields calculated by Chisholm and Pennycook [26] for an infinite array of dislocations comprising 2°, 5° and 10° tilt boundaries, showing 1% strain contours as a function of reduced distances, $Y=y/D$ and $X=x/D$.

found the strain to be strongly affected by the in-plane *a-b* anisotropy, and that additional diagonal components of strain may reduce channel widths.

3.3.2 Carrier Depletion

The suppression of the order parameter at dislocation cores is amplified by the proximity of HTS to the metal-insulator transition, creating a localised insulating antiferromagnetic phase [27]. The precise nature of the suppression has been investigated both directly, through the use electron energy loss spectroscopy (EELS) [28,29], and via a bond valence analysis by Browning *et al* [24]. By measuring bond lengths extracted using STEM they were able to estimate the valence of the Cu atoms in and around the boundary. Crucially, the valence of Cu is found to vary with YBCO oxygenation, being ~2.3 in fully oxygenated YBCO and ~1.2 in fully oxygen deficient YBCO. In this manner they were able to use Cu valence as an indicator of carrier concentration. Cross sections taken across the dislocations on figure 3.6(b) are given in figure 3.9, showing a clear reduction in valence at the core. They argued that there exists an *intrinsic* under-coordination of copper sites within the boundary, as there is physically not enough space to accommodate an additional oxygen atom. They also found that the depletion was dependent upon the particular sub-lattice of the dislocation core, the Cu-O site having more of a deleterious effect than the Y-Ba site.

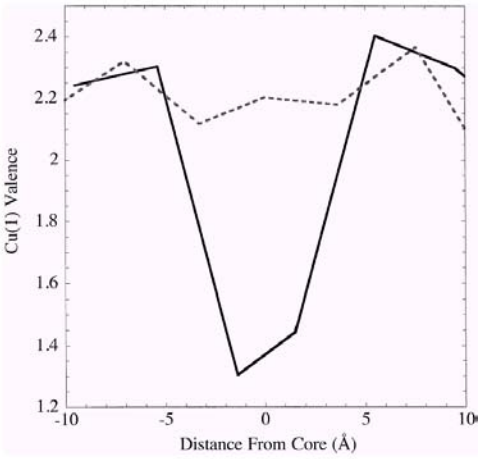

Figure 3.9. Copper (1) valence as a function of distance from the dislocation cores of figure 3.8 centred on the Cu-O (solid line) and Y-Ba (dashed line) columns [24].

3.3.3 Band Bending

It was first postulated by Mannhart and Hilgenkamp [30] that the electronic band structure in the vicinity of cuprate grain boundaries is distorted. This is because the characteristic bending length scale, the Debye length (λ_d = 0.5 - 1.0 nm), is comparable to the small HTS coherence length, ξ(0 K) ~ 1.6 nm [31].

In 1998, Gurevich *et al* [27] calculated the misorientation dependence of J_c^{GB} using such a model. They postulated that excess ion charge on GB dislocations results in a shift of the chemical potential in a layer of the order of the screening length λ_d near the dislocations. The result of such a distortion of the band structure is a depletion of order parameter next to the interface due to a transition to the antiferromagnetic, insulating state [27]. Figure 3.10(a) illustrates the band bending scenario predicted to occur at HAGBs, with an insulating layer of

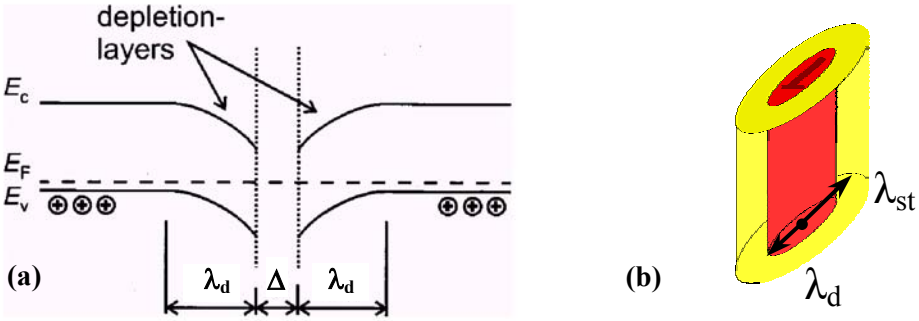

Figure 3.10.(a) Sketch of possible band bending scenario, forming depletion layers. Adapted from [5]. (b) Low angle dislocation core surrounded by strain and charge distortions [32].

thickness Δ at the interface [5]. Two regimes may be identified depending upon the relative sizes of λ_{st} and λ_d :

Lower Angle Dislocations: $\lambda_{st} > \lambda_d$**.** For small angles $\theta_m < 4° - 7°$ the dislocation strain fields become larger than the Debye screening length [32,27]. Strain induced modifications determine the effective dislocation size, and electrical charging effects can be neglected. The regime is sketched in figure 3.10(b).

Higher Angle Dislocations: $\lambda_{st} < \lambda_d$**.** For misorientations $\theta_m > 4° - 7°$ the electro-neutrality observed at low angles becomes invalid. The effective dislocation size is strongly influenced by the electronic band distortions due to localised charge screening.

The boundaries investigated in this work range in angle from $\theta_m \approx 4° - 5°$, and so would appear to fall within the uncertainty separating these two regimes.

3.4 GB Heterogeneity

Although the LAGB boundary is well described as an array of dislocations punctuated by undisturbed channels, the grain boundary structure *can*, as described in the following sections, be more complicated.

3.4.1 GB Meandering

This effect is common to grain boundaries formed by thin film deposition onto bicrystal substrates. While the misorientation relationship and macroscopic boundary plane in a bicrystal *substrate* can be predetermined with precision, the same cannot be said of the YBCO thin film boundary formed on top. Although TEM measurements reveal the substrate GB to be planar even on a near-atomic scale [33,34,35], the film GB can meander significantly from the pre-determined substrate boundary [34,36,37,38]. The magnitude of deviation has been measured to generally range from 50 to 250 nm. Alarco *et al* [33] first interpreted the

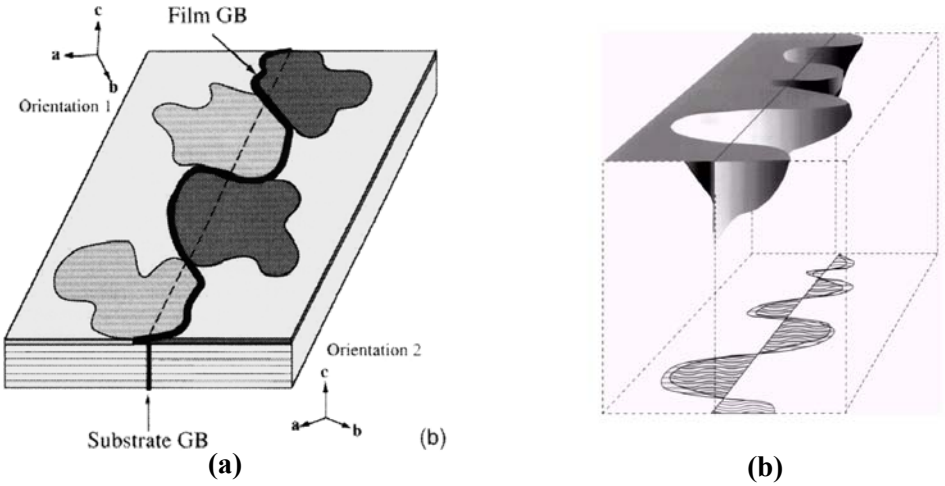

Figure 3.11.(a) Schematic of island growth inducing GB meander [39], and (b) its effect on the 3-dimensional GB topography [37]. The interface is inclined to the substrate normal (see chapter 5).

presence of grain boundary 'waviness' in terms of the island-like growth mechanism of YBCO films. YBCO islands that form near the substrate GB, overgrow the boundary despite the different substrate orientation on the other side of the bicrystal line. The film GB is thus formed between overgrown YBCO grains and will meander across the underlying $SrTiO_3$ boundary. This is schematically illustrated in figure 3.11(a), where grains of the same orientation are appropriately shaded [39]. The magnitude of meander (wavelength and amplitude) has been found by to depend sensitively upon the deposition rate.

Additionally, cross sectional TEM performed by Træholt *et al* [34] revealed that the GB plane can deviate from the substrate normal in the film growth direction. This feature has been termed 'multiple meander', and is illustrated in figure 3.11(b). Further evidence of such an inclined boundary plane to the *c*-axis is found in moiré interference fringes. The first cross sectional TEM measurements on a thin film LAGB are presented in chapter 5, and the importance of the effect on transport in the presence of flux vortices is discussed in chapters 8 and 9.

3.4.2 GB Faceting

Meandering thin film boundaries are actually composed of an irregular arrangement of facets with lengths of tens of nanometers upwards and a range of (*hkl*) values. It is this faceting that causes the interface to appear 'wavy' on the mesoscopic scale of figure 3.11 [20]. Thin film boundaries have been reported to contain sections of both symmetric and asymmetric boundary facets [34], each described by different structural units, and possessing slightly different GB width. Carrier depletion is therefore expected to be modulated along such a faceted boundary [24]. Additionally TEM measurements have revealed that LAGB dislocations can be inhomogeneously distributed [40] and even paired [41] along GB facet

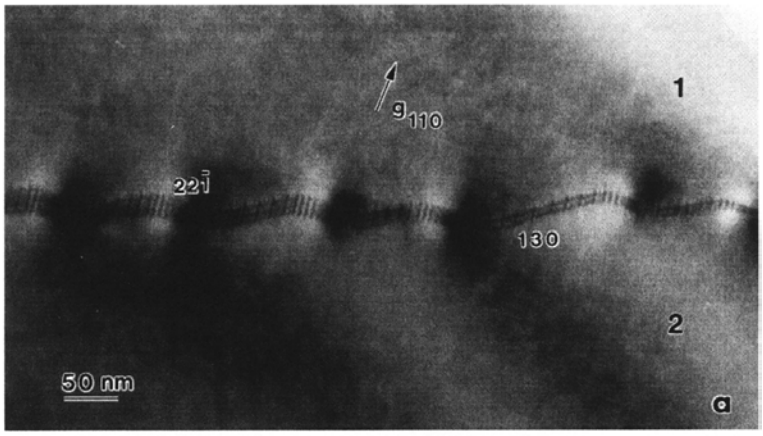

Figure 3.12. Diffraction contrast image of the dislocation network in a 6° [001]-tilt flux grown bulk bicrystal sample. Large strain fields indicated by increase contrast can be seen at facet junctions between (130) and (221) planes [40].

planes. On average, however, they are found to obey the Read-Shockley equation (equation 3.2).

TEM measurements performed by Tsu *et al* [40] on a flux grown 6° LAGB revealed the presence of extensive strain fields associated with facet *junctions* (figure 3.12). These extended up to 30 nm away from the GB, and were significantly larger than the strain due to the individual dislocations (approximately 9 nm out of the GB plane for $\theta_m = 5°$ [26]). Such strain fields will inevitably modify the superconducting properties of the surrounding material, increasing the width of disorder and dissipation during current transport (see chapter 6). Although calculated to be of only minor importance by Gurevich *et al* [27], it has also been suggested that dissipation at HAGBs may be mediated by the interaction of facet planes and the *d*-wave order parameter [30].

3.4.3 Substrate Defects

The nature of the substrate bicrystal GB may directly influence the behaviour of the GB formed in the thin film YBCO grown on top. Although, as already mentioned, the $SrTiO_3$ boundary is found to be more planar than that in the film, it is still found to display inhomogeneities. Two defect types are reported:

(a) **Facet Voids**: Facetted grooves are formed at the $SrTiO_3$ GB [34,42,43] for annealed HAGB bicrystals. They are triangular in nature and form along the [100] and [010] axes of the substrate. As such, their aspect ratio is dependent upon GB misorientation.

(b) **Hole defects**: Circular hole defects, very different in structure to the facetted voids are also formed along the substrate GB. These were first detected by McDaniel *et al* [44,45] using used near-field scanning optical microscopy (NSOM) and AFM as shown in figure 3.13.

Intriguingly, they were also observed (with the same density) in a specially fabricated $\theta_m = 0°$ bicrystal substrate [46]. This indicates that they form as a result of the bicrystal fusion process.

The presence of hole defects under YBCO thin film GB tracks were found by McDaniel at al to be linked to lower critical currents and local deviations of the YBCO GB by up to a micron. These features were all attributed to the effect of strain fields associated with the defects influencing YBCO growth and superconducting properties. Details of defect density and dimensions are given in chapter 5, which reveals the nature of the LAGB substrate line discovered in this study.

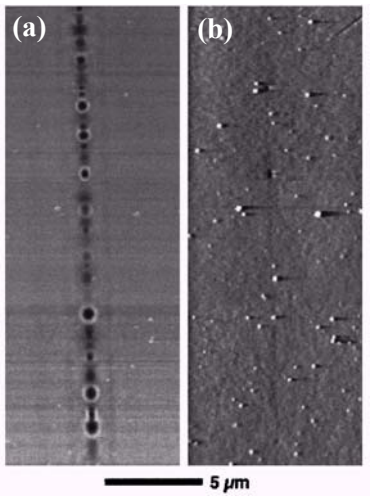

Figure 3.13 Transmission NSOM and (b) topographic AFM images of the same section of a 24° $SrTiO_3$ bicrystal boundary [44].

3.5 The Channel Model of Transport

The channel model provides an attractively simple description of the strong to weak transition with increasing misorientation angle. The basic principle is that the insulating LAGB dislocation cores act to locally reduce the track cross sectional area available for current flow. This restricts transport to those regions of good lattice that exist *between* the dislocations – the 'channels'. This is illustrated schematically in figure 3.14. Hence, as the angle of misorientation is increased, progressively more of the grain boundary becomes non-superconducting as dislocations move closer together according to equation 3.2. This result is that current transport becomes pinched off as the area of track available for transport vanishes.

At some critical angle the cores will overlap, resulting in a drastic drop in critical current and a change in the nature of transport. We can estimate the critical angle, θ_c, at which overlap occurs by setting $D = 2r_d$ in equation 3.2 and rearranging for θ:

$$\theta_c = 2\sin^{-1}\left(\frac{|\boldsymbol{b}|}{4r_d}\right) \qquad 3.3$$

If we assume that dislocation cores have a 'conventional' radius of $r_d \approx b$, this critical angle is found to be $\theta_c \approx 29°$. This may be consistent with the observed low plateau behaviour of J_c initially observed by Dimos *et al*, but does not explain the strong to weak coupling transition observed in YBCO over the range $\theta_m \approx 5°\text{-}10°$.

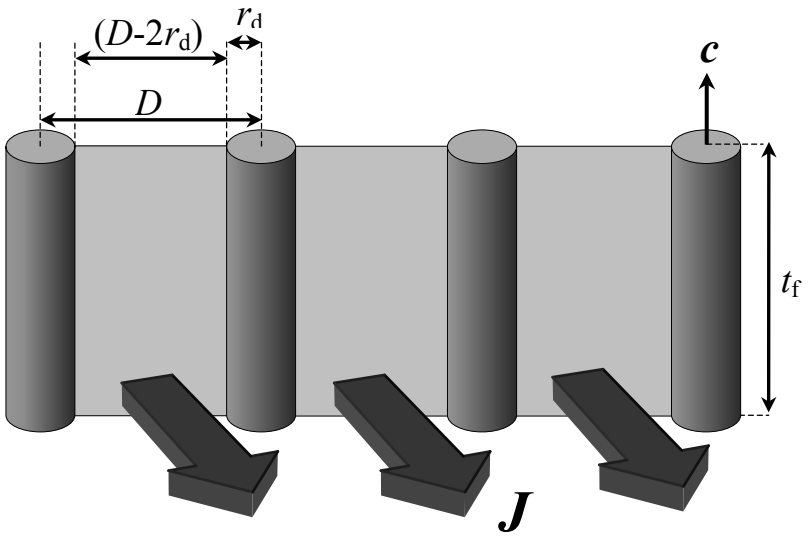

Figure 3.14. Suppression of the order parameter around dislocation cores (shaded cylinders) reduces the effective cross sectional area of the interface across which superconductivity is strongly coupled, and through which current may flow (arrows).

The first modification to such a channel model must be to include the increased radius predicted - and observed - to exist (section 3.3). This acts to reduce the critical overlap angle. In an initial calculation, Chisholm and Pennycook [26] assumed the transparency ratio of J_c^{GB} to J_c^{IG} to be $\delta_c = (D\text{-}2r_d)/D$, which to a first approximation for small tilt angles becomes,

$$\delta_c = \frac{J_c^{GB}}{J_c^{IG}} = 1 - \frac{2r_d}{|\boldsymbol{b}|}\theta_m \tag{3.4}$$

predicting a linear decrease of δ_c (and J_c) with increasing angle (in radians) for LAGBs. By fitting equation 3.4 to the slope of Dimos *et al* [2] between $\theta_m = 0°$ and 10° Chisholm and Pennycook found that $r_d \approx 2.9b$. Much larger than b, this figure is consistent with the ~ 1 nm value found by Gao *et al* [22] (figure 3.8(a)). This increased dislocation radius leads to an overlap angle of $\theta_c \approx 10°$ from equation 3.3, more consistent with the thin film results. The results of a more detailed calculation of the dislocation strain fields using linear elasticity theory (figure 3.8(b)) confirmed this figure; that for misorientations beyond 10° the conducting gaps between dislocations become less than the dimensions of the unit cell, destroying the structural order required for superconductivity everywhere along the boundary.

Although the linear dependence of equation 3.4 is much weaker than the exponential dependence observed experimentally, (see figure 3.3), for low enough angles they are practically the same. Taking the gradient of equation 3.1 at $\theta_m = 0°$ yields the *same* linear dependence,

$$\frac{J_c^{GB}}{J_{co}} = 1 - \frac{\theta}{\alpha} \tag{3.5}$$

Where the critical angle, α, can by comparison with equation 3.4 be equated with the core size as $\alpha = b/2r_d$. Interestingly, this result implies that the increased magnitude of α found at lower temperatures implies a decreased r_d – this temperature dependent radius is evidence for the modulation of T_c across a dislocation core as will be discussed in section 7.2.3.

Further refinement to the model included the suggestion by others that weak link behaviour should be expected when the width between dislocations becomes less than the superconducting coherence length, $\xi(T)$ [47]. Such models treat the current channels as a parallel array of point contacts [27,48,49]. The critical angle is thus expected to be encountered at even lower values of misorientation, and weak link behaviour becomes apparent not when strain fields overlap, but when the dislocations are spaced by $D = 2r_d + \xi(T)$. From equation 3.2 we find:

$$\theta_c = 2\sin^{-1}\left(\frac{b}{2\left[2r_d + \xi(T)\right]}\right) \tag{3.6}$$

In this case, if we take $r_d \approx b$ at 77 K ($\xi(77\text{ K}) \approx 3.5$ nm), then $\theta_c \approx 5.2°$. But using the larger core observed by Gao *et al* of $r_d \approx 1$ nm yields an even smaller value of $\theta_c \approx 4°$. Further disparity is introduced by using the strain field width calculated by Chisholm and Pennycook result: for low angle misorientations, $r_d \approx 1.7$ nm and equation 3.4 gives $\theta_c \approx 3.3°$.

As can be seen, the predicted 'critical angles' at which the onset of weak link behaviour is *expected* to be observed span the wide angular range ~ 3° - 29°. Table 3.2 summarises the predicted coupling strength of 2°, 5° and 10° misorientation boundaries for two overlap models that regard the transition to occur for channels smaller than the lattice spacing (Model A), and the coherence length (Model B).

Table 3.2. Values of the dislocation spacing (D), channel width (D-$2r_d$), calculated transparency ratio (δ_c) and coupling strength for GBs of a given misorientation as calculated by Chisholm and Pennycook [26].

θ_m	2°	5°	10°
***D* (nm)**	11.20	4.50	2.20
r_d (nm)	2.15	1.45	0.90
D-$2r_d$ (nm)	6.9	1.6	0.4
$\delta_c = (D\text{-}2r_d)/D$	0.61	0.36	0.18
Model A	Strong	Strong	Strong/Weak
Model B	Strong	Weak	Weak

The transport measurement results of this work on 4° and 5° boundaries (chapters 6-9) would tend to suggest that they do not behave as weak links at 77 K as predicted by Model B. This conclusion however, is subject to inconsistencies that exist in the definition of what *experimentally* constitutes weak link behaviour in mid to low misorientation boundaries; Small J_c^{GB} values, sensitivity to applied field, re-entrant $J_c^{GB}(B)$ curves, RSJ-like *V-I* characteristics, and *V-I* (and impedance) resonances are all used as evidence of weak link character, but are not all observed in LAGBs.

An interesting dichotomy in behaviour is observed in the mid-misorientation range boundaries. Redwing *et al* [50] have observed both strong coupling *and* weak coupling behaviour as temperature is varied for the same mid-misorientation (10°) boundary (see section 6.3.3). This coupling temperature dependence is attributed the fact that the coherence length is a function of temperature, varying with T as $\xi(T) \approx (1-T/T_c)^{-1/2}$.

The $J_c^{GB}(\theta_m)$ data of figures 3.2 and 3.3 display a large degree of scatter, of up to an order of magnitude. This also acts to prevent an accurate determination of the critical transition to weak coupling. This $J_c^{GB}(\theta_m)$ noise is attributed by numerous authors to the heterogeneity discussed in section 3.4. Paired and inhomogeneously distributed dislocations will result in multiple channel widths for a given misorientation [24,41]. Growth conditions will influence factors such as facet strain fields [24,38] and the diffusion of Sr and Ti along the dislocations from the substrate [9]. This heterogeneity introduces both sample-to-sample variation and point-to-point variation along the same GB. As such, for a given sample and given misorientation, there will be areas of boundary across which coupling is stronger and dislocations, or insulating barriers, are wider. The measured J_c^{GB} of a boundary will thus represent an averaged, macroscopic response and be less indicative of the fundamental J_c^{GB}.

3.6 High Angle $J_c(\theta_m)$ Dependence

For angles of misorientation $\theta > \sim 10°$ the GB dislocations cores form a continuous insulating barrier, and current flow occurs via a tunnelling process. Halbritter [51] showed that in this regime J_c^{GB} can be expressed as,

$$J_c^{GB} = J_{co} e^{-2\tau\Delta} \tag{3.7}$$

where J_{co} is the bulk critical current, Δ the interface width and τ the decay constant (7.7/nm) [29,51]. It is expected that the linear increase of Δ with θ_m at high angles, as observed by Browning *et al* [29], will naturally lead to an exponential dependence of the form of equation 3.1.

3.7 Low Angle $J_c(\theta_m)$ Dependence

There is widespread consensus regarding the existence of the exponential - or very close to exponential - dependence of $J_c^{GB}(\theta_m)$. This is particularly true at higher angles of misorientation, where equation 3.7 results in the observation of $e^{-\theta/\alpha}$ over a wide range of θ_m. There is less consensus however over the exact form of the $J_c^{GB}(\theta_m)$ dependence at lower angles, particularly for $\theta_m < \sim 7°$. It was postulated in 1999 by Heinig *et al* [9-11] that there existed two distinct regimes: one at low angles ($\theta < 7°$) where there is *no depression* of J_c^{GB} from J_c^{IG}, and one at higher angles, where the exponential dependence is recovered. Figure 3.15 shows the data from which they drew this conclusion. The dashed and dot-dashed lines represent equation 3.4 with $r_d = b$ and $2.9b$ respectively. They argued that it is the more perfect, or 'best' examples of LAGB J_c^{GB} that should be considered for a given misorientation rather than the 'worst'. The existence of the 'low angle plateau' is controversial, but backed to an extent by Magneto Optic measurements made on both thin film [52] and coated conductor samples [53]. They show a lack of flux penetration at low fields for angles $\theta_m < \sim 3°$. Others, however, *have* reported field penetration and lower J_c at 2° and 3° LAGBs [54].

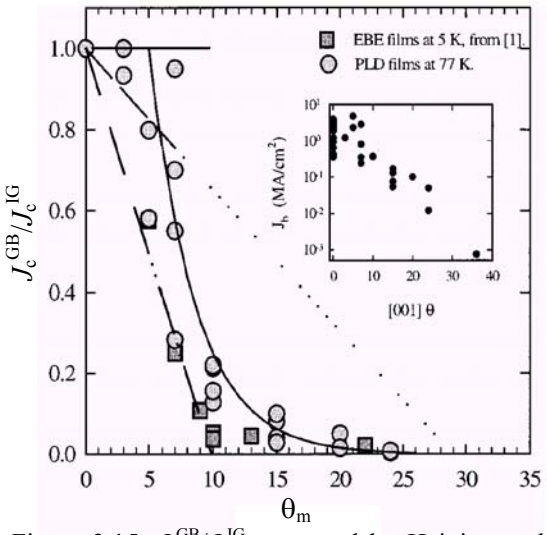

Figure 3.15. J_c^{GB}/J_c^{IG} measured by Heinig *et al* [10] at 77 K, 0 T. Data is compared with [2] at 5 K. Inset shows the same data on semi-logarithmic axes. Two distinct regions are claimed: low angle, with constant J_c, and high angle with an exponentially decreasing J_c, as marked with solid lines. The dashed lines are fits to equation 3.4 (see text)

The true situation is concealed by both the large degree of sample-to-sample scatter and the variation in IG film quality, which affects J_c^{GB} and the ratio of J_c^{GB}/J_c^{IG} (see section 3.1). Due to the crossover in transport mechanism from cross sectional limitation to tunnelling, it is certainly possible for LAGBs to possess a different θ_m dependence than the exponential clearly seen for HAGBs. However, it is unlikely that LAGB J_c^{GB} is truly independent of θ_m, and the samples measured in this study certainly possessed $J_c^{GB} < J_c^{IG}$ at 77 K, 0 T.

3.8 The Vortex-GB Interaction - Flux Channelling and Pinning

Elucidating the transport properties of LAGBs in an applied magnetic field requires a development of the channel model, and a more detailed understanding of the nature of the

vortex-GB interaction. J_c^{GB} in the presence of a magnetic field depends not only on the effective cross sectional area available for transport across the boundary (determined by δ_c), but also on the flux pinning properties of the interface and surrounding material. Grain boundaries can display both flux pinning [55] and flux channelling [56,57] properties, depending upon temperature, applied field and the angle of field with respect to the GB. The sections below contain a review of the current understanding of the vortex-GB interaction, forming a basis for the developments presented in the results chapters to follow.

3.8.1 Vortices At Grain Boundaries

It is now widely accepted that the structure of vortices at grain boundaries can be very different to those that reside within the IG regions, and will vary significantly with angle of misorientation [57,58]. The transformation of vortex structure occurs due to the localised reduction in depairing current at the boundary, J_b, with respect to that in the bulk material, J_d. As a result, it is expected that the vortex core length will become extended to a value $l \approx \xi J_d/J_b(\theta_m)$ which is a function of misorientation [59,60]. With increasing θ_m, Gurevich *et al* [57,58] describe the transition from an Abrikosov (A) type vortex at low angles to an Abrikosov-Josephson (AJ) vortex at intermediate angles. At higher angles, l becomes greater than the penetration depth and the vortex finally transforms into a Josephson (J) type vortex of size $\lambda_J = \phi_o/16\pi^2\lambda J_b$. In addition, the normal core of the A vortex is proposed to vanish for both AJ and J cores, which simply become 2π phase kinks. Figure 3.16 shows the calculated current streamlines of AJ vortices at an interface, for $l = 0.2a_o$. The precise range of misorientations for which A, AJ and J vortex behaviour exists is unclear, although the AJ state is expected to exist for $J_d/\kappa < J_b(\theta_m) < J_d$, where $\kappa = \lambda/\xi \approx 100$ for YBCO. In a recent letter, Gurevich *et al* claim to have observed evidence that 7° LAGBs possess no normal cores [57]. Whether this is truly the case is uncertain (chapter 9 presents a core pinning model that fits 5° data well), but it is likely that the transition from A to AJ is a smooth one dependent on local GB microstructure.

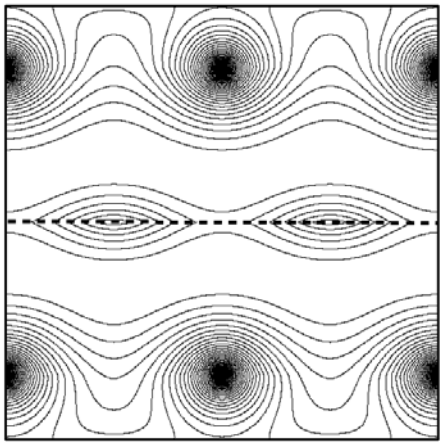

Fig 3.16. Current streamlines around AJ vortices on a GB (dashed line) and bulk A vortices in the grains [57]. Weaker pinning of AJ vortices results in vortices channelling past pinned A vortices.

3.8.2 LAGB Flux channelling

On the microscopic scale, LAGBs are thought of in terms of the channel-dislocation array. On the meso-scopic and macro-scopic scale however, LAGBs can be thought of as planar defects.

The vortex pinning force of such a planar defect will be extremely anisotropic, depending critically upon the direction of the Lorentz force, and as such, the direction of current flow. For *Lorentz forces* parallel to the LAGB[#], localised channelling of vortices along the defect occurs, reducing J_c^{GB} from that of J_c^{IG} [56]. For *Lorentz forces* perpendicular to the LAGB pinning forces are expected to be much greater, and may increase J_c^{GB} with respect to J_c^{IG} [60].

Channelling effects can occur for two main reasons. Firstly, pinning of GB vortices is lower than that in the bulk material. As discussed in section 2.4.3, pinning occurs through the creation of potential minima by defects, producing variation of the vortex energy as a function of position [16]. For a J vortex, the energy is contained solely in its circulating supercurrents, and the pinning force is due to the gradient of the Josephson energy density [60]. For an A vortex, an additional contribution is made from its normal core of radius ~ ξ. As normal core pinning density may be estimated as $F_p \approx E_c(T)/\xi_{ab}(T)$, where E_c is the condensation energy (section 9.3.4), the elongated core size predicted to exist by Gurevich *et al* will naturally result in a decrease of pinning.

Secondly, although the current limiting nature of the LAGB ($J_c^{GB}/J_c^{IG} < 1$) is to blame for the elongation of vortices, the cross sectional reduction (section 3.5) is also a mechanism for channelling in itself. The localised increase in current density at the LAGB due to the reduction in current carrying cross section will result in initial vortex de-pinning at the interface during a transport measurement. This effect is independent of the particular vortex structure or pinning force.

During transport measurements of tracks containing LAGBs, channelling can be manifest in both measurement of the *V-I* characteristic and of $J_c^{GB}(\theta,\phi)^*$ as a function of the *angle* of applied field:

- **Channelling and the *V-I* Characteristic**

The *V-I* characteristics of thin film LAGB samples are often found to display an offset linear characteristic, in marked contrast to both intragranular and HAGB characteristics. Measurements of a 4° LAGB taken by Díaz *et al* [56] are shown in figure 3.17, where the IG *V-I* is plotted for comparison. The underlying cause of this disparity in characteristic is the dissipative mechanism, believed to be viscous vortex channelling along the LAGB [56,61]. Motion of a single row, or even several rows, of vortices creates extremely localised dissipation at the LAGB. This can result in extremely high electric fields (e.g. up to 300 V/m

[#] In transport measurements where ***J*** is perpendicular to the LAGB plane (as is always the case in this work), this situation corresponds to flux aligned perpendicularly to ***J***.
[*] θ and ϕ define the direction of the field with respect to the GB, as given in figure 4.6

for a 10 μV voltage drop [56]). It is likely that such high electric fields effectively move the *V-I* characteristic out of the creep dominated regime, and into the linear, viscous flux flow regime discussed in section 2.4.2. Detailed measurements of *V-I* are presented in chapter 6, 8 and 9, which map out the range of parameters (T, B, θ, ϕ) over which this effect is observed.

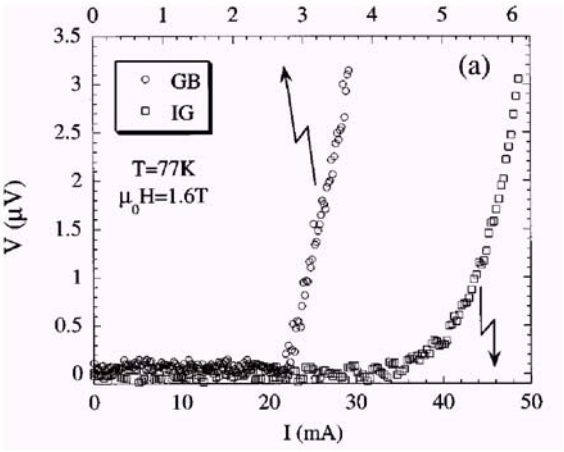

Figure 3.17. *V-I* characteristics for a 4° [001]-tilt LAGB and comparative IG measurement [56] for 1.6 T parallel to the *c*-axis.

- **Channelling and $J_c(\theta,\phi)$ Measurement**

The pinning or channelling properties of a system of defects can be evaluated in a straightforward manner by measuring the dependence of J_c on the angle between an external field $\boldsymbol{H}_{app}$ and the system of defects. The effect of channelling along a planar defect is seen in magnetisation measurements and transport measurements where there is a component of the vortex Lorentz force along the defect plane. It is manifest as a sharp decrease in $J_c(\theta,\phi)$ as the applied field, and hence internal vortices[#], become aligned with the defect. The dip is a direct consequence of rotating the vortices from the relatively high pinning IG material, into the planar defect where pinning is low for longitudinal motion. This work presents details of a pronounced LAGB channelling dip for field rotations in the *ab*-plane in chapter 8. This is the first observation of its kind, and the LAGB channelling behaviour is found to be closely analogous to that which is often observed along twin boundaries [62,63].

3.8.3 Flux Pinning

As introduced in the section above, J_c^{GB} is reduced from that of the IG material due to cross sectional and vortex elongation effects. The fact that J_c^{GB} is finite and not zero, however, implies that pinning of vortices at LAGBs *does* occur.

Pinning to a particular defect type is most effective when the defect size matches the vortex size in question, ξ or λ. The coherence length of YBCO in the *ab*-plane, $\xi_{ab}(0\ K) \approx 1.6$ nm, is of a similar size to the dislocation cores within LAGBs (~ 1 nm, see section 3.3). Vortex line energy may also be saved along the whole extent of the correlated defect as opposed to just a single point. This led to the early suggestion by some [2,21] that grain boundary dislocations may play an active role in the pinning of flux. The effect has been quantified by Gurevich and

[#] As will be seen in chapters 8 and 9, however, the external field and the internal vortices are not always aligned.

Cooley [60]. They calculated that the longitudinal pinning force on a vortex with core length l by a defect of length L_d increases linearly with L_d for $l >> L_d$, and decreases as $1/L_d$ for $l << L_d$. The longitudinal pining force is thus maximum for defects of the order of the core size $l \approx L_d$.

Evidence of pinning at LAGBs has, to date, been found in the following measurements:

- **Angular Measurements of $J_c^{GB}(\theta,\phi)$**

Indisputable evidence of pinning at YBCO LAGBs was provided by Díaz *et al* [55] in transport measurements on a thin film 4° [001]-tilt bicrystal. They found that for rotation of the field in the plane of the boundary (and perpendicularly to $\boldsymbol{J}$), J_c displayed a maximum for $\boldsymbol{B}$ almost aligned with the c axis. This peak, absent in measurements on IG material, was interpreted as being due to pinning of vortices to the dislocation array. The occurrence of the 'LAGB pinning peak' is investigated in depth in chapter 9.

- **Measurements of $J_c(B,T)$**

Transport measurements of $J_c(B,T)$ and the V-I characteristic can be used to probe the value of the irreversibility field [10]. Dislocation pinning at the LAGB could be expected to increase the boundary B_{irr}^{GB} over B_{irr}^{IG}, as in experiments on irradiated samples. However, this work has found that any enhancement of B_{irr}^{IG} is in fact limited to B_{irr}^{IG}, as transport measurements on the GB are performed in series with a two IG regions. Evidence for the pinning of vortices at the interface in $J_c^{GB}(B,T)$ will be discussed further in Chapter 7.

- **Magneto-Optic Measurements**

MO measurements (see next section) can be used to extract B and J_c at the grain boundary, and have also provided evidence for pinning at LAGBs. As will be presented in chapter 7, Polyanskii *et al* [52] found an increasing ratio of J_c^{GB}/J_c^{IG} for 5° and 7° boundaries with increasing temperature. This was ascribed to reduction in dimensionality of thermal fluctuations experienced for vortices pinned to either LAGB dislocations or within the a planar defect [64]. More evidence of pinning was produced by MO performed by Albrecht *et al* on 2° and 3° LAGBs. They found an increase of *local* j_c^{GB} with *local* field for low fields (< 0.1 T), due to the pinning of vortices at the LAGB by the static vortex array in the IG banks.

Although dislocations are thought to be primarily responsible for high field pinning peaks in thin film LAGBs, there is evidence of pinning at GBs to the 'extrinsic' defect structure – such as the facet structure [65] and meandering morphology [16]. The latter effect, due to the similarity in size between meander wavelength and vortex penetration depth

[$\lambda(0\ K) \sim 800$ nm] is thought to be at least partly responsible for the higher J_c^{GB} values obtained for thin film over bulk scale GBs.

3.8.4 Magneto-Optic Investigations

The current carrying capability of grain boundaries can be effectively investigated through use of a technique called magneto-optic (MO) imaging. The normal component of the magnetic flux density distribution $B_z(x,y)$ can be determined using a garnet indicator as a field sensing element [66]. Due to saturation of the garnet at high fields, the maximum measurable field is relatively low, usually being up to 200 mT.

Polyanskii *et al* [52] performed the first thorough investigation of the effect of grain boundary misorientation on flux density distribution in thin film [001]-tilt GBs. Flux is found to penetrate the samples preferentially along the grain boundary. Figure 3.18 shows MO images taken on 3°, 5° and 10° thin film YBCO boundaries at 7 K in an external applied field of ~ 40 mT. The bright regions correspond to high values of the normal flux component $B_z(x,y)$ and the dark central stripes to vortex free regions, where only Meissner currents flow. Although the 3° boundary only weakly disturbs the magnetic flux distribution, a dramatic increase in flux penetration can be seen with increasing misorientation. For the 10° boundary, $J_c^{GB} \approx 0.1 J_c^{IG}$ and the magnetisation currents in the IG regions become practically independent, and simply behave as decoupled, adjacent superconductors. In this regime, the magnetisation currents change direction sharply at the discontinuity (d) lines, indicated in figure 3.18(b) and (c) as local diagonal minima in $B_z(x,y)$ running away from the GB.

For a given applied field an enhancement of B_z at the boundary plane is also observed, an effect termed 'flux focussing'. This is very similar to the demagnetisation enhancement of B_z observed at the edges of a flat thin superconductor in perpendicular field (section 2.9). For

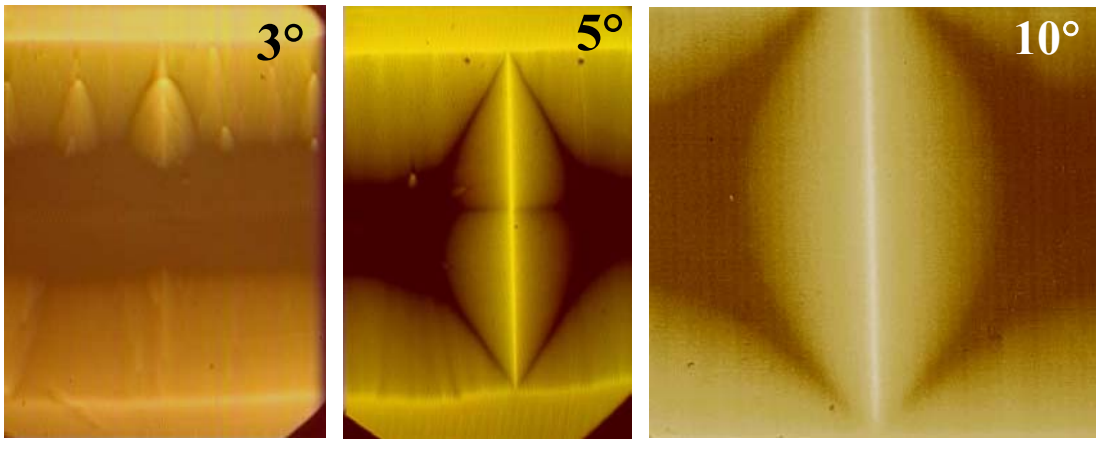

Figure 3.18. Magneto-optic images of flux penetration into (a) 3°, (b) 5° and (c) 10° [001]-tilt thin film YBCO grain boundaries at 7 K and approximately 40 mT applied field [52].

high angle GBs at low applied field it is predicted that $B_z(\text{GB}) \approx 2B_z(\text{edge})$, as the HAGB represent simply two neighbouring superconductor edges [66]. The enhancement found for a LAGB is presented in section 5.3.

3.9 GB Resistance Measurements

R-T measurements taken on HAGB junctions exhibit a pronounced foot that is not present in the IG resistive transition. This foot has been explained in terms of a thermally activated phase slip process (TAPS) proposed by Gross *et al* [67]. The treatment assumes the barrier is a current driven Josephson junction and predicts a decreasing R_{TAPS} component with increasing junction critical current.

The *R-T* curves of samples containing GBs can be interpreted as representing a double T_c transition: the main transition at ~ 90 K represents T_c^{IG} of the grains, and the foot represents the reduced T_c^{GB} of the GB. Above T_c^{IG} the normal state resistivity is therefore expected to be increased above the IG value by an amount equal to the additional GB contribution. Measurements by Heinig *et al* [68] would tend to suggest this contribution is significant, but the foot region is often found to be absent in lower angle boundaries, and indeed was not observed in the measurements on ~4° bicrystals in this dissertation (section 5.4). Other authors *have* charted an increase in the foot region with misorientation angle [69], as shown in figure 3.19. The development of the foot is normally associated with the transition from strong to weak coupling with angle of misorientation.

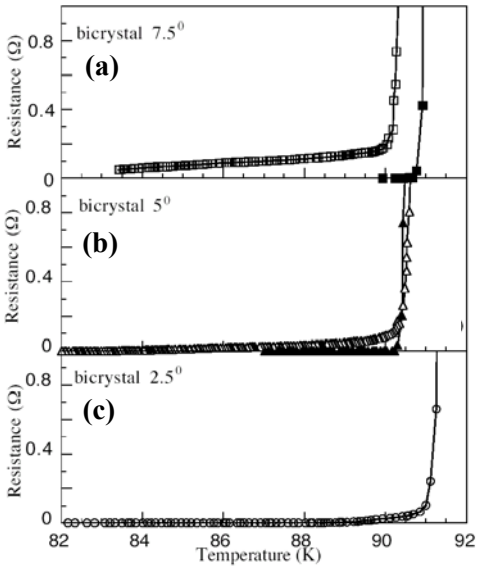

Figure 3.19. LAGB *R-T* measurements for 2.5°, 5° and 7.5° [001]-tilt thin film boundaries [69].

The R_n of a HAGB is more normally extracted from the *V-I* characteristic at high driving currents where the Ohmic, normal response of the GB is obtained. The LAGB *V-I* gradient however, is thought not to represent R_n, but be linked to the flux flow resistivity, ρ_f, as shall be seen in chapter 6. Typical measured values of HAGB R_nA range from 0.1 - 0.5 Ω μm^2 (15°) to 2 - 6 Ω μm^2 (36°) [17,5].

3.10 References

[1] P. Chaudhari J. Mannhart, D. Dimos, C.C. Tsuei, J. Chi, M.M. Oprysko and M. Scheuermann, *Phys. Rev. Lett*. **60**, 1653 (1988)

[2] D. Dimos, P. Chaudhari, J. Mannhart, and F. K. LeGoues, *Phys. Rev. Lett*. **61**, 219 (1988)

[3] D. Dimos, P.Chaudhari, and J. Mannhart, *Phys. Rev. B* **41**, 4038 (1990)

[4] H. Hilgenkamp and J. Mannhart, *Rev. Mod. Phys*. (in press)

[5] H. Hilgenkamp and J. Mannhart, *Appl. Phys. Lett.* **73**, 265 (1998)

[6] R. Gross, *Interfaces in High-T_c Superconducting Systems*, Ed. S.L. Shinde and D.A. Rudman, Springer-Verlag, New York (1993)

[7] Z.G. Ivanov, P.A. Nilsson, D.Winkler, J.A. Alarco, T. Claeson, E.A. Stepanstov and A. Ya. Tzalenchuk, *Appl. Phys. Lett.* **59** 3030 (1991)

[8] R. Amrein, L. Schultz, B. Kabius and K. Urban, *Phys. Rev. B* **51**, 6792 (1995)

[9] N.F. Heinig, R.D. Redwing, I-Fei Tsu, A. Gurevich, J.E.Nordman, S.E. Babcock and D.C. Larbalestier, *Appl. Phys. Lett* **69**, 577 (1996)

[10] N.F. Heinig, R.D. Redwing, J.E.Nordman and D.C. Larbalestier, *Phys. Rev. B* **60,** 1409 (1999)

[11] N.F. Heinig, PhD Dissertation, University of Wisconsin-Madison (1999)

[12] D. Larbalestier, A. Gurevich, D. M. Feldmann and A. Polyanskii, *Nature* **414**, 368 (2001)

[13] D.T. Verebelyi, D.K. Christen, R. Feenstra, C. Cantoni, A. Goyal, D.F. Lee, M. Paranthaman, P.N. Arendt, R.F. DePaula, J.R. Groves and C.Prouteau, *Appl. Phys. Lett*. **76**, 1755 (2000)

[14] V.R. Todt, X.F. Zhang, D.J. Miller, M. St.Louis-Weber and V.P. Dravid, *Appl. Phys. Lett*. **69**, 3746 (1996)

[15] S. E. Babcock and J. L. Vargas, *Annu. Rev. Mater. Sci*. **25**, 193 (1995)

[16] K.E. Gray, M.B. Field and D.J. Miller, *Phys. Rev. B* **58** 9543 (1998)

[17] M.B. Field, D.C. Larbalestier, A. Parikh and K. Salama, *Physica C* **280**, 221 (1997)

[18] A. Parikh, B. Meyer, K. Salama, *Supercond. Sci. Tech* **7**, 455 (1994)

[19] D.W.A. Willen and K. Salama, *Physica C* **201,** 311 (1992)

[20] S.E. Babcock, *Micron* **30**, 449 (1999)

[21] M. F. Chisholm and D. A. smith, *Phil. Mag*. **59**, 181 (1989)

[22] Y. Gao, K. L. Merkle, G. Bai, H. L. M. Chang, and D. J. Lam, *Ultramicroscopy* **37**, 326 (1991)

[23] D. Hull and D. J. Bacon, *Introduction to Dislocations*, Butterworth Heinemann, Oxford (1984)

[24] N.D. Browning, J.P. Buban, P.D. Nellist, D.P. Norton, M.F. Chisholm, S.J. Pennycook, *Physica C* **294**, 183 (1998)

[25] J.G. Wen, T. Takagi and N. Koshizuka, *Supercond. Sci. Technol*.**13**, 820 (2000)

[26] M.F. Chisholm and S.J. Pennycook, *Nature* **351**, 47 (1991)

[27] A. Gurevich and E.A. Pashitskii, *Phys. Rev. B* **57**, 13 873 (1998)

[28] N.D. Browning, M.F. Chisholm, S.J. Pennycook, D.P. Norton and D.H. Lowndes, *Physica C* **212**,185 (1993)

[29] N.D. Browning, J.P. Buban, C. Prouteau, G. Duscher and S.J. Pennycook, Micron **30**, 425 (1999)

[30] J.Mannhart and H. Hilgenkamp, *Supercond. Sci. Technol*. **10**, 880 (1997)

[31] J.Mannhart and H. Hilgenkamp, *Mater. Sci. Eng. B* **56**, 77 (1998)

[32] K. Guth, H.U. Krebs, H.C. Freyhardt and Ch. Jooss, *Phys. Rev. B* **64**, 140508R (2001)

[33] J.A. Alarco, E. Olsson, Z.G. Ivanov, P.A. Nilsson, D. Winkler, E.A. Stepantsov and A. Y. Tzalenchuk, Ultramicroscopy **51**, 239 (1993)

[34] C. Traeholt, J. G. Wen, H. W. Zandbergen, Y. Shen, and J. W. M. Hilgenkamp, Physica C **230**, 425 (1994)

[35] B. Kabius, J.W. Seo, T. Amrein, M. Siegel, K. Urban and L. Shultz, *Physica C* **231**, 123 (1994)

[36] D. J. Miller, T.A. Roberts, J.H. Kang, J. Talvacchio, D.B. Buchholz and R.P.H Chang, *Appl. Phys. Lett*. **66**, 2561 (1995)

[37] J. Ayache, A. Thorel, J. Lesueur, and U. Dahmen, *J. Appl. Phys*. **84**, 4921 (1998)

[38] X.F. Zhang, D.J. Miller and J. Talvacchio, *J. Mater. Res.* **11**, 2440 (1996)

[39] X.F. Zhang, V.R. Todt and D.J. Miller, *J. Mater. Res.* **12**, 3029 (1997)

[40] I-Fei Tsu, S. E. Babcock, and D. L. Kaiser, *J. Matter. Res*. **11**, 1383 (1996)

[41] H. Kung, J.P Hirth, S.R. Foltyn, P.N. Arendt, Q.X. Jia, M.P. Maley, *Physica C* **357**, 959 (2001)

[42] Q. D. Jiang, X. Q. Pan, and J. Zegenhagen, *Phys. Rev. B* **56**, 557 (1997)

[43] Q. D. Jiang, Z.J. Huang, A. Brazdeikis, M. Dezaneti, C.L. Chen, P. Jin and C.W. Chu, *Appl. Phys. Lett*. **72**, 3365 (1998)

[44] E. B. McDaniel, S.C. Gausepohl, C.T. Li, M. Lee, J.W.P. Hsu, R.A. Rao and C.B. Eom, *Appl. Phys. Lett*. **70**, 1882 (1997)

[45] E. B. McDaniel, J.W.P. Hsu, *J. App. Phys.* **84**, 189 (1998)

[46] J. W. P. Hsu, E.B. McDaniel, A.L. Campillo, S.C. Gausepohl, M. Lee, R.A. Rao and C.B. Eom, *IEEE Trans. Appl. Supercon*. **9**, 3413 (1999)

[47] K.K. Likharev, *Rev. Mod. Phys.* **51**, 101 (1979)

[48] E. Sarnelli, P. Caudhari, and J. Lacey, *Appl. Phys. Lett*.**62**, 777 (1993)

[49] B.H. Moeckly, D.K. Lathrop and R.A.Buhrman, *Phys. Rev. B* **47**, 400 (1993)

[50] R.D. Redwing, B.M. Hinaus, M.S. Rzchowski, N.F. Heinig, B.A. Davidson and J.E. Nordman, *Appl. Phys. Lett*. **75**, 3171 (1999)

[51] J. Halbritter, *Phys. Rev. B* **46**, 14861 (1992)

[52] A.A. Polyanskii, A. Gurevich, A. E. Pashitskii, N.F. Heinig, R.D. Redwing, J.E. Nordman and D.C. Larbalestier, Phys. Rev. B **53**, 8687 (1996)

[53] D. M. Feldmann, J. L. Reeves, A. A. Polyanskii, G. Kozlowski, R. R. Biggers, R. M. Nekkanti, I. Maartense, M. Tomsic, P. Barnes, C. E. Oberly, T. L. Peterson, S. E. Babcock, and D. C. Larbalestier, *Appl. Phys. Lett*. **77**, 2906 (2000)

[54] J. Albrecht, S. Leonhardt and H. Kronmuller, *Phys. Rev. B* **63**, 014507 (2001)

[55] A. Díaz, L. Méchin, P. Berghuis, and J. E. Evetts, *Phys. Rev. Lett.* **80**, 3855 (1998)

[56] A. Díaz, L. Méchin, P. Berghuis, and J. E. Evetts, *Phys. Rev. B* **58**, R2960 (1998)

[57] A. Gurevich, M.S. Rzchowski, G. Daniels, S. Patnaik, B.M. Hinaus, F. Carllo, F. Tafuri and D.C. Larbalestier, *Phys. Rev. Lett.* **88**, 97001 (2002)

[58] A. Gurevich, *10th International Workshop on Critical Currents*, University of Wisconsin, USA (1998)

[59] A. Gurevich, *Phys. Rev. B* **46**, 3187 (1992)

[60] A. Gurevich and L.D. Cooley, *Phys. Rev. B* **50**, 13 563 (1994)

[61] M. J. Hogg, F. Kahlmann, E.J. Tarte, Z.H. Barber and J.E. Evetts, Appl. Phys. Lett. **78**, 1433 (2001)

[62] M. Oussena, P.A.J de Groot, K. Deligiannis, A.V. Volkozub, R. Gagnon and L. Taillefer, *Phys. Rev. Lett.* **76**, 2559 (1996)

[63] M. Oussena, P.A.J de Groot, R. Gagnon and L. Taillefer, *Phys. Rev B* **51**, 1389 (1995)

[64] G. Blatter, M.V. Feigel'man, V.B. Geshenkbein, A.I. Larkin and V.M. Vinokur, *Rev. Mod. Phys.* **66**, 1125 (1994)

[65] X.Y. Cai, A. Gurevich, I.F. Tsu, D.L. Kaiser, S.E. Babcock and D.C. Larbalestier, *Phys. Rev. B* **57**, 10951 (1998)

[66] Ch. Jooss, L.O. Kautschor, M.P. Delamare, B. Bringmann, K. Guth, V. Born, S. Sievers, H. Walter, J. Dzick, J. Hoffmann, H.C. Freyhardt, B. de Boer, B. Holzapfel and F. Sandiumenge, Matt. Res. Soc. Symp. Proc. 659, 117 (2001)

[67] R. Gross, P. Chaudhari, D. Dimos, A. Gupta and G. Koren, Phys. Rev. Lett. **64**, 229 (1990)

[68] N.F. Heinig, G.A. Daniels, M. Feldmann, A. Polyanskii, D.C. Larbalestier, P. Arendt and S. Foltyn, *IEEE Trans. Appl. Supercond.* **9**, 1614 (1999)

[69] G. Grimaldi, V. Boffa, G. Celentano, F. Fabbri, U. Gambardella, S. Pace and T. Petrisor, *IEEE Trans. Appl. Supercond.* **11**, 3776 (2001)

4 Experimental Method

This chapter details the experimental methods, including sample preparation and characterisation techniques that were used in this work. Preparation involved the patterning of current tracks aligned across the bicrystal boundary and within the epitaxial grain. The principal measurement technique involved the use of a precision two-axis goniometer to perform angular transport measurements as a function of field and temperature.

4.1 Sample Preparation

The following sections detail the process by which samples were prepared for electronic measurement.

4.1.1 Sample Sources and Deposition

Appendix B contains a list of the thin film samples investigated in this work. Films were deposited upon (100) $SrTiO_3$ [001]-tilt bicrystal substrates. These were purchased as nominally 4° ± 0.5° [001]-tilt misorientation from the companies Shinkosha Ltd, Pi-Kem Ltd and Crystal GmbH. Some measurements were also made on films deposited on single crystal (100) $SrTiO_3$ substrates.

The films studied were all '*c*-axis', in which the *c*-axis of the unit cell (see figure 2.1) grows normally to the substrate surface. The two primary deposition techniques employed to grow the films were (1) pulsed off-axis laser deposition (PLD), performed by Dr. F. Kahlmann, and (2) high pressure on-axis DC sputtering, performed by Dr. V. Tsaneva. Of the bicrystal samples studied, most quantitative electrical measurements were obtained from samples pk2 and s2, both of which were deposited using PLD.

Deposition requires high temperatures, and is extremely sensitive to oxygen concentration. The PLD system involves the pulsed firing of a laser at a stoichiometric target, creating a plume of ablated material. In the off-axis technique, the substrate is positioned with its surface parallel to the plume direction. Deposition occurred at approximately 780°C for 30 minutes, followed by an annealing stage in oxygen at 500°C for 30 minutes to oxygenate the sample.

The sputtering system relies on the acceleration of ionised argon towards a biased target to create a plume. Deposition occurred at 800°C for approximately 300 minutes (including a reverse side pre-sputtering step) then annealed at 500°C for 20 minutes.

The laser ablated and sputtered samples were deposited upon substrates of size $10 \times 10 \times 0.5$ mm^3, and $5 \times 10 \times 0.5$ mm^3 respectively. Sample pk2 was diced in to 3 parts in order to send sections away for MO imaging (see section 4.3.5) and TEM (see section 4.3.4). Dicing was performed after initial coating with a photoresist layer (see section 4.1.4) to protect the film surface.

4.1.2 Sample Cleaning

Cleaning of substrates prior to YBCO deposition, and YBCO films prior to patterning, took place in the research group clean room. This was particularly necessary after AFM imaging (occurring in a non-vacuum environment) or dicing. The full cleaning process started by placing the sample in chloroform (or acetone) in an ultrasound bath for a set time period (depending on how dirty the surface was). The sample was then airbrushed, first with acetone, then with iso-propanol, and dried using compressed air. Care was taken not to leave 'dry' marks, created when the solvent dries too slowly, on the surface of the sample.

Ideally YBCO films should not come into contact with water or water vapour, as YBCO reacts to form non-superconducting $Ba(OH)_2$ degrading film quality. However, this was unavoidable in some of the steps involved in the patterning procedure (sections 4.14 – 4.16).

4.1.3 Deposition of Contacts

In order to allow measurement of the large critical currents obtained at low temperatures and fields it was essential to make good quality, low resistance, electrical contacts. Good contact is also associated with low extrinsic noise measurements. Contacts were deposited onto the YBCO films immediately after growth in order to minimise any surface deterioration effects. The aim of the contact is to allow the transfer of currents of up to 1 A through the sample with as little heating as possible. Contact heating leads to the setting up of a thermal gradient across the sample, and a corresponding thermal offset voltage. Large enough contact resistance can result in the variation of the offset voltage over the course of a *V-I* measurement, distorting the characteristic, and leading to problems in maintaining temperature stability of the sample.

The contact pads consisted of an initial layer of silver, then a secondary layer of gold, both evaporated onto the film using an (Edwards) electron beam evaporator. The sample was placed behind a metal mask and exposed to the plume for 30 seconds (Ag) and 40 seconds

(Au). The resulting two rows of 8 pads terminate the patterned YBCO tracks in section 4.1.6. In order to further reduce contact resistance, the samples were annealed by heating in an oxygen environment. It was found that annealing in 1 atmosphere of oxygen at 400°C for 60 minutes followed by a slow cool to room temperature yielded the best results. The effect of annealing is to allow the silver to diffuse into the YBCO, and the gold layer to form an Ag-Au alloy. This prevents the break up of the silver layer into droplets by 'dewetting'.

It should be noted that although all efforts were made to produce low resistance contacts, it was often the case that measurements had to be truncated to an extent. This in effect confined the measurement of certain tracks to higher temperatures and fields. Somewhat disappointingly, this sometimes restricted the degree of *direct* comparison achievable between high J_c intragranular and lower J_c grain boundary measurements.

4.1.4 Removal of the Underside Layer of YBCO

Both the PLD and sputtering deposition methods leave a thin layer of YBCO on the reverse side of the STO substrate that needs to be removed. The sample is placed in a photoresist spinner and a few drops of positive photoresist (Hoechst AZ1529) placed on the surface, enough to cover the sample. After spinning at 6000 rpm for 30 seconds the sample is baked for 1 minute, at 100°C. Without exposing, the sample is stirred in YBCO etch (2.5% phosphoric acid) for 30 seconds, or until the YBCO layer is gone. The resist is then removed by ultrasounding and airbrushing with acetone.

4.1.5 Revealing the Grain Boundary

The artificial boundary that forms in the YBCO thin film is not easily visible, except when viewed at an oblique angle or under strong backlighting (transmission mode). In order to align the mask in section 4.1.6 to the GB line during the patterning procedure, the boundary needs to be exposed properly. This is achieved by removing the edges of the YBCO film and stirring in hydrofluoric (HF) acid, which preferentially etches the $SrTiO_3$ boundary line.

The revealing process starts by spinning and baking photoresist onto the sample as described in the previous section. Using a projection mask aligner (Cannon projection system) the appropriate mask pattern is positioned centrally on the sample and focussed onto its surface. Any areas of the sample allowed by the mask to be exposed to ultraviolet light will later dissolve in developer solution. Thus, the 'edging' mask allows only the edges of the sample to be exposed (see figure 4.1(a)). As the edges of the sample are covered by a thicker layer of photoresist (due to an edge bead effect) the sample is over exposed for 2 minutes to ultraviolet light. The sample is then stirred in a diluted developer solution (1 part to 4 parts

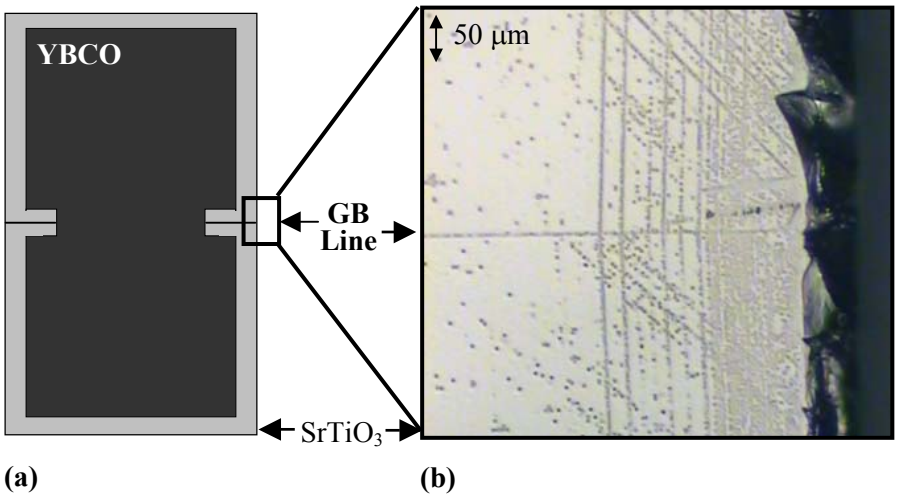

Figure 4.1.(a) Schematic of a bicrystal sample after the removal of YBCO at the sample edge followed by HF etching to make visible the GB interface. (b) Optical image of the etched grain boundary.

water) for 40 seconds, after which time it is stirred in water to stop the developing process. It is then stirred in YBCO etch for approximately 30 seconds, depending upon the YBCO film thickness. After stirring in 7% HF solution the GB is revealed as a straight line in the STO at the edges of the sample, as shown in figure 4.1(b). Interestingly, additional etching lines are often found running across the boundary. The marks provide a useful correlation of the [001]-tilt misorientation as measured by x-ray diffraction (sections 4.3.2 and 5.1).

4.1.6 Patterning of Tracks

Precision transport measurements can only be made on films that have been patterned with current tracks and current and voltage tabs. A number of tracks were patterned onto each sample to enable novel effects to be checked for consistency and allow a direct *in situ* comparison of the critical current within the grain with that across the grain boundary.

Mask patterns were refined during the course of this work in order to optimise to number of measurable tracks per sample. An example mask is shown in figure 4.2(a). The pattern, shown enlarged in figure 4.2(b), consists of four GB tracks (across the GB) and three measurable IG tracks (parallel to the GB). In general, GB tracks range in width from 2.5 to 24 μm, and were 70 μm long. IG tracks were all 10 μm wide, and were longer than GB tracks with lengths ranging from 100 to 170 μm. In addition to the square contact pads, figure 4.2(a) possesses 500 μm^2 squares of YBCO placed at the GB and within the IG regions. These were to enable both MO imaging and (post transport measurement) TEM analysis of the LAGB and film (section 4.3 and chapter 5).

Tracks were patterned by using the following procedure: After revealing the GB in section 4.1.5, and once again spinning and baking a photoresist layer, the track mask was focussed onto the sample surface. It was then carefully aligned to the contact pads and to the GB line

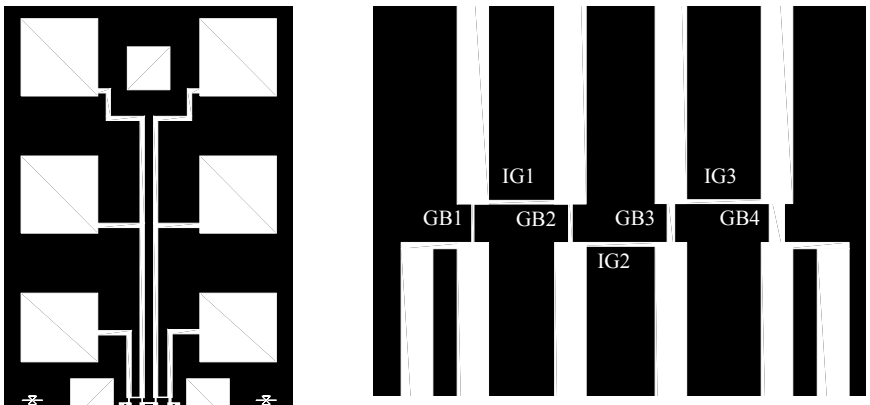

Figure 4.2.(a) Example mask pattern used to pattern GB and IG tracks. The revealed GB is lined along the alignment marks. (b) Current tracks shown in more detail. In this pattern 4 GB tracks and 3 IG tracks are measurable.

using the alignment marks on the mask (see figure 4.2(a)). The sample was then exposed for 45 seconds and developed for 30 seconds. Provided vibration was kept to a minimum, even the smallest track (about 2.5 μm in width) was possible to pattern using projection lithography. The sample was then etched using an ion milling system. The process involves accelerating Ar^+ ions toward the sample, which ablate both the exposed YBCO and the covering of resist. The thickness difference results in the YBCO (few hundred nm) being milled away before the resist (few μm) that covers the desired pattern. Ion milling at normal incidence combined with periodic rotation of the sample can, unlike wet etching, result in very sharp etching steps and a well defined current track.

4.1.7 Artificial FIB Channel

In order to emulate the channelling behaviour of a LAGB (see chapters 6, 8 and 9), an artificial vortex channel was created using a Focussed Ion Beam (FIB) FEI 200 XP®. The FIB method uses an accelerated beam of gallium ions to ablate material over an extremely small region. The FIB was used[#] to cut a channel, or trench, across the width of a patterned IG track of YBCO, providing a localised reduction in film thickness. It was hoped that the resulting localised reduction in track cross sectional area could be compared to the reduction due to the

[#] All FIB milling was kindly performed by Dr. D.J. Kang, based at the Department of Materials, University of Cambridge.

dislocation cores (channel model) at a LAGB. The aim of the experiment was to induce flux flow at the channel but, as for the LAGB, maintain a significant critical current across the channel.

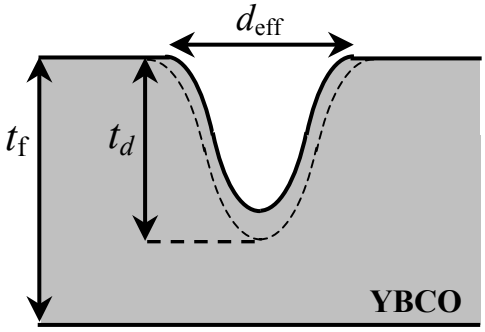

Figure 4.3. Schematic profile of the FIB milled artificial vortex channel (AC) in an IG track. d_{eff}(surface) ~ 50-70 nm. Gallium implantation regions are indicated by dashed lines, producing a total 'damaged' depth t_{d}.

Although ideally meant to be rectangular, the trench possessed a tapered profile due to the large aspect ratio caused by the film thickness $t_{\mathrm{f}} = 230$ nm (sample 1237b). This is sketched in figure 4.3. The trench width at the surface is estimated as $d_{\mathrm{eff}} \sim$ 50-70 nm. This includes the effects of gallium implantation, which reduces T_{c} and increases the width by an estimated 10 nm [1] as indicated in figure 4.3 by the dashed line. The depth of the trench was intended to be approximately $t_{\mathrm{d}} \sim 150$ nm, giving a 60 to 70 % region of 'damage' (30 - 40% *reduction* in track area). In reality, the true magnitude of t_{d} is unknown to a precise extent due to beam defocusing effects during FIB milling.

As the process of imaging tracks during the FIB technique also leads to gallium contamination, the milling process involved initially imaging and cutting a test track (of width 10 μm) in order to calibrate. Then beam was then moved by a set amount to the track to be electrically measured (of width 6 μm) and the channel was cut 'blind'. Figure 4.4 shows an FIB image of the initial test channel created on sample 1237b.

The results of measurement on the artificial channel (AC) will be presented in section 8.7.

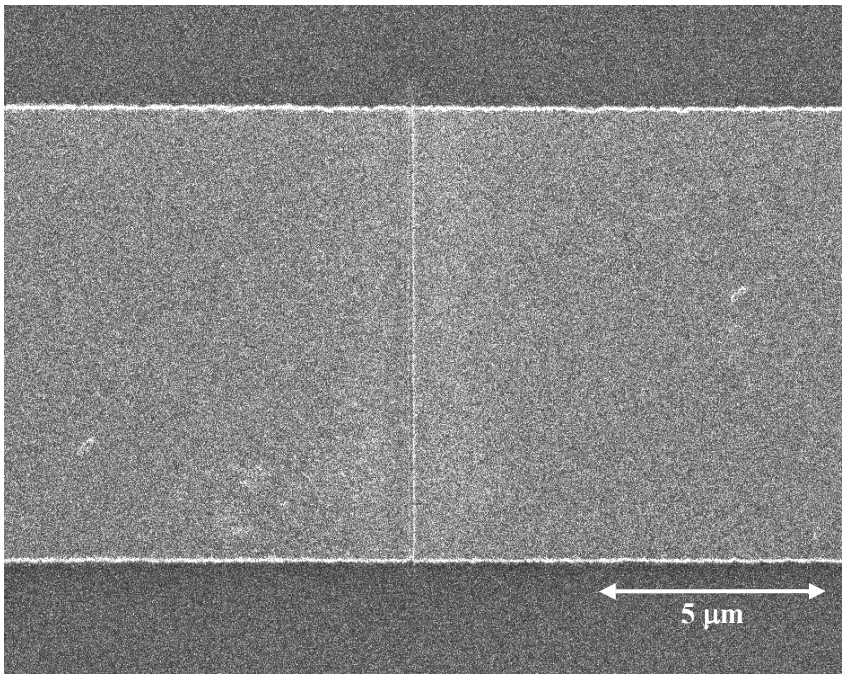

Figure 4.4. Test FIB channel cut into an IG track of width 10 μm patterned on sample 1237b.

4.2 Electrical Measurement System

4.2.1 Two-Axis Goniometer

The transport current measurements central this work were made using a two-axis cryogenic goniometer stage with unique precision and versatility. The ability to rotate the sample in two axes relative to a magnetic field proved pivotal to the successful angular investigations presented in chapters 7 to 9.

The probe was designed and constructed by R. Herzog [2,3] and forms part of a computer controlled, automatic measurement system. The bottom section (sample stage) of the probe is pictured in figure 4.5(a), which in operation is lowered into the Variable Temperature Insert (VTI) of an Oxford Instruments long hold cryostat. The sample to be measured is mounted on a copper block, the orientation of which may be controlled by a system of gears connected to two drive shafts. The shafts are rotated by two stepper motors, which are driven by a microstepping controller. The controller allows positioning to a high degree of resolution; one degree of rotation requires 2166 ⅔ motor steps [4].

The shafts also drive two mechanical counters positioned at the top of the probe (figure 4.5(b)) positioned outside the VTI to provide a manual verification of the sample orientation. The values of these counters are checked constantly to ensure consistency between the actual orientation and the recorded orientation displayed by the computer.

Rotation of the two drive shafts controls the value of two angles, θ_e and ϕ_e which correspond

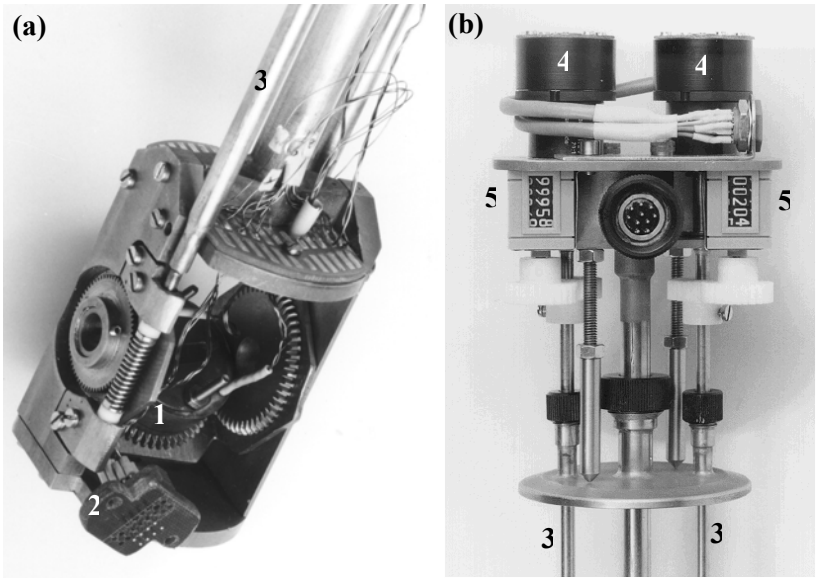

Figure 4.5. (a) The rotation stage in which the sample is mounted, and (b) the top section of the two-axis goniometer [4,3]. The copper mounting block (1), Pogo pin array (2), drive shafts (3), motors (4) and mechanical counters (5) are all indicated. More details of the goniomter construction may be found in [2]. The probe rotates the sample through two angles θ_e and ϕ_e that are related to the angles θ and ϕ as defined for a current track 'frame of reference' in figure 4.6.

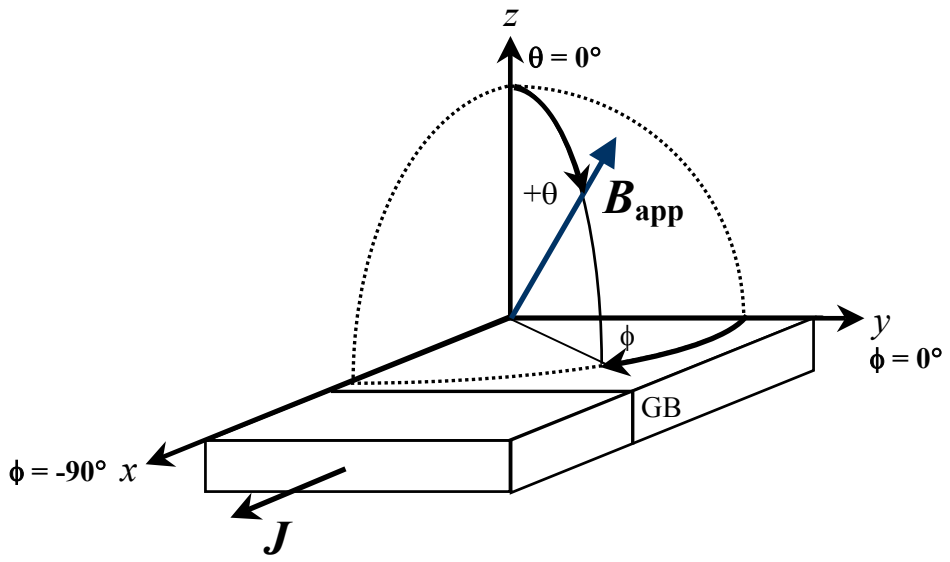

Figure 4.6. Definition of the orientation of an applied flux density in θ and ϕ, relative to the current track. Although the example shown is a GB track, θ and ϕ are also defined as shown for IG tracks.

to rotation about an axis lying in the sample surface (rotation in θ_e) and about an axis normal to the film surface (rotation in ϕ_e). These angles must be transformed into θ and ϕ which define the relative orientation of an applied magnetic field with respect to the current track as shown in figure 4.6. For a GB track, the transformation is simply $\theta = \theta_e$ and $\phi = \phi_e$. Applied field is always parallel to the *c*-axis (*z* direction) for θ = 0°, and always parallel to the *ab*-plane for θ = ± 90°. As shown, the GB always runs perpendicularly to the transport current and applied field is aligned with the GB plane for (a) all θ at ϕ = 0° *and* for (b) ϕ = 0° with θ = ± 90°.

In general, IG tracks were perpendicular to GB tracks (see figure 4.2) and the transformation to the track 'frame of reference' becomes $\theta = \theta_e$ and $\phi = \phi_e - 90°$. In this manner, the angles θ and ϕ define the field orientation with respect to the track as is shown in figure 4.6 for *both* GB and IG tracks. The particular field scan geometries used in this work are discussed in more depth in chapters 8 and 9.

The precision of the angular alignment of the sample is estimated [3] as 0.02°, but imperfections in mounting the sample can lead to larger offsets on the order of 1°. This offset can become evident when the field is almost aligned with the *ab*-planes of the YBCO film, and J_c is varying rapidly with angle due to the intrinsic pinning peak effect. Systematic shifting of the intrinsic position as a function of temperature and field, however, can be attributed to a flux trapping effect as discussed in section 9.3.5.

4.2.2 Sample Mounting

An array of eight spring-loaded 'Pogo' pins mounted within the probe were used to make quick and reliable electrical contact to the contact pads on the patterned sample. A small slice

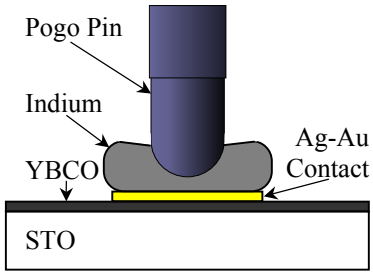

Figure 4.7. Cross section of the Pogo pin contact arrangement used in the J_c probe. After [3].

of malleable indium was placed between contact pad and Pogo pin in order to (a) enlarge the current transfer cross section, and (b) to help prevent opening of the contact upon cooling. This is illustrated in figure 4.7. Care was taken to only use small sections of indium in order to prevent shorting between pads due to deformation when mounting.

4.2.3 Temperature Control and the Cryostat

The 8 T Oxford Instruments cryostat consists of central sample space, or VTI, surrounded by toroidal layers designed to provide an applied field, cool and insulate. The cryostat and mounted goniometer are illustrated schematically in figure 4.8. The cooling layers consist of baths of helium and nitrogen, separated by vacuum spaces and a radiation shield.

The helium bath is linked to the bottom of the VTI by a capillary tube controlled by needle valve A. By externally pumping at the top of the VTI, the rate of which is controlled by needle valve B, helium is sucked through the capillary and into the VTI. This then boils and cools the suspended probe and sample. At the bottom of the VTI there is a carbon-glass temperature sensor connected to an Oxford Instruments ITC 4 controller. This normally reads approximately 4.2 - 4.7 K when cooled and in stable operation.

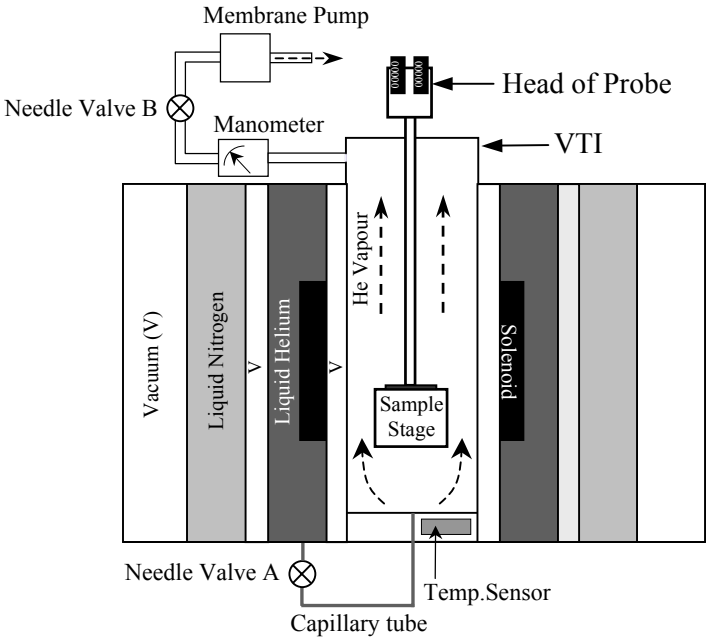

Figure 4.8. Basic schematic of the cryostat with probe. Two needle valves vary the flow of He vapour through the VTI. The sample temperature is controlled by a temperature sensor and heater within the mounting block (see next section)

The copper block on which the sample is mounted also contains a heater and temperature sensor (see figure 4.9). Temperature is measured using a Lakeshore Cryotronics Cernox resistance sensor, having a range of 3 K to 305 K. The conductance of the sensor is measured under an applied constant voltage by another temperature controller (ITC4). This converts conductance into temperature using a calibration table. Calibrations were made for two temperature ranges; (1) from 4.2 K to 101 K, and (2) from 75 K to 305 K. The temperature reading is estimated as accurate to ± 50 mK [4]

Noise can also be introduced by thermal fluctuations of the sample. The thermal stability depends very much on the temperature and field, larger J_c values resulting in more heating and instability. At its worst, the temperature controller can start to 'hunt', oscillating about the equilibrium value by up to 2 K. This is manifest as a similar oscillation of the *V-I* characteristic.

When in use, the manometer attached to the VTI should read atmospheric pressure, failure to do so indicating that either needle valve A is not open sufficiently or is blocked. Needle valve A was very prone to blockage by ice, and came equipped with a fairly inadequate needle valve heater. Prolonged use of the heater *while not pumping* on the VTI was sometimes successful in partially unblocking the capillary, but only at extremely low helium levels. The only certain remedy found was to warm the cryostat up to room temperature and flush with dry helium gas.

4.2.4 Measurement Rig

Figure 4.9 shows a block diagram of the measurement system. Four point measurements were performed using an HP 3245A current source to pass current through the sample. For currents greater than 100 mA, a purpose built voltage-controlled current source was used. The particular current track was selected via a matrix board connected to the Pogo pins mentioned in section 4.2.2. The track length, *L*, was defined as the distance between the points at which the voltage difference was taken. The current flowing *through the track* was independently measured using a Keithley 199 multimeter. Voltage developed *across the track* was measured by a Keithley 182 nanovoltmeter.

The measurement system is nearly fully automatic, and is addressed from a Labview program predominantly written by Dr. John Durrell [4] that allows measurement of *V-I* and J_c as a function of angle, temperature and field. It can be controlled remotely to perform transport measurements over any chosen trajectory in θ, ϕ, *B* and *T*. *V-I* characteristics were recorded as current was stepped up in incremental amounts to a maximum voltage, usually 10 μV. The critical current was extracted at a voltage criterion by fitting a smoothed polynomial to the *V-I*

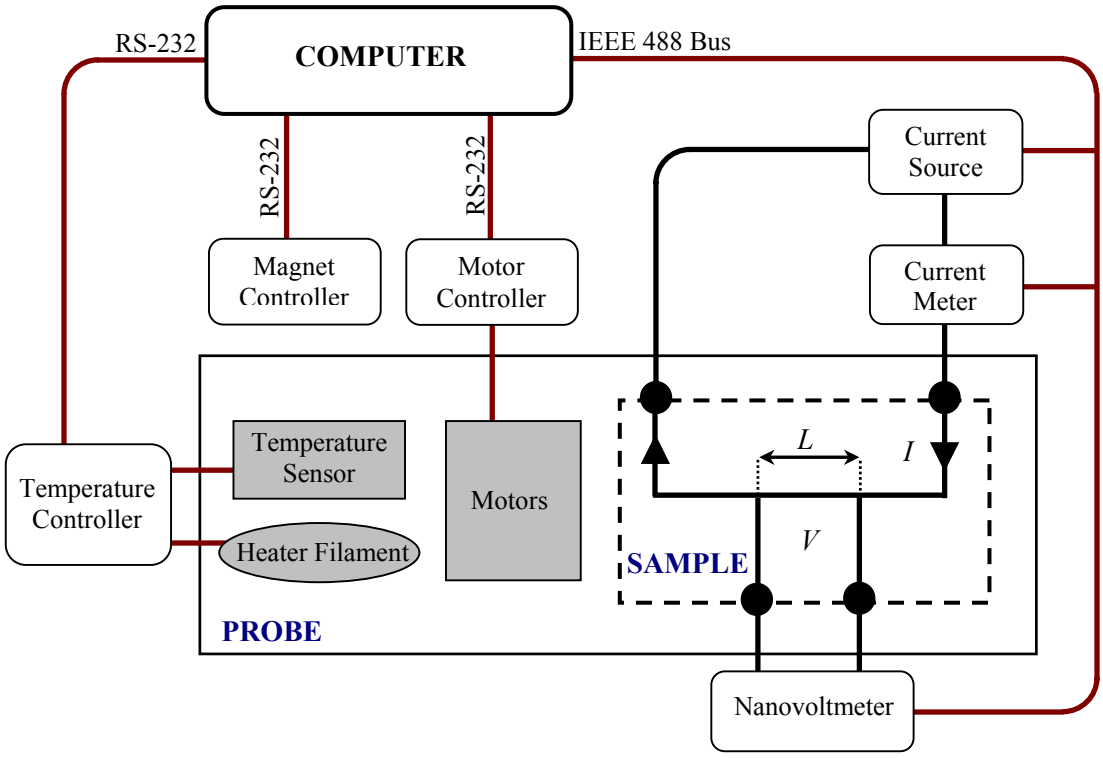

Figure 4.9. Block diagram of the 4-point measurement and computer control. The probe and sample are indicated as sold and dashed rectangles respectively. After [3] and [4].

data points. In a similar manner, the gradient of the *V-I* characteristic could also be deduced at a given voltage criterion or over the whole *V-I* characteristic. The consequences of using a voltage criterion for both IG and GB tracks will be discussed in more detail in the next section.

Extrinsic noise levels were reduced through the use of a built in analogue filter with an integration time of 250 ms – this was necessary at particularly high fields or for particularly noisy contacts. Noise levels below J_c were usually measured to be less than 0.2 μV, although for a poor measurement they could exceed 1 μV. The effect of such filtering on the 'intrinsic' noise measured in chapter 6 was found to be at least *qualitatively* negligible.

4.2.5 Voltage criteria and Track Comparison

For the GB tracks, a 1 μV criterion was taken in order to extract J_c^{GB}. Due to the track length difference between LAGB and IG tracks, a *larger* voltage criterion was used in order to extract J_c^{IG}. The IG voltage criterion was scaled up by a factor equal to the ratio of the two tracks, $Q = (L_{IG}/L_{GB})$, giving $V_c^{IG} = QV_c^{GB}$. This was in order to obtain the *same* *E*-field criterion as would be obtained in an IG track of equivalent length to the GB track; a 1 μV level of dissipation would produce an *E*-field a factor *Q* smaller for the longer IG track over

one equal to the length of the GB track. As a result of this increased V_c^{IG} criterion, the IG value of dV/dJ taken at the criterion also needed scaling, by a factor 1/Q.

For example, as just mentioned, the GB criterion was taken as $V_c^{GB} = 1$ μV. For track IG3 in figure 4.2(b) however, the criterion taken was $V_c^{IG} = QV_c^{GB} = 2.4$ μV, and the gradient extracted scaled down by multiplication by 1/2.4.

The scaling described here is *only* to effectively transform measurements taken on a long IG track to one of length equal to the GB track. The effect the presence of the GB has on transport must be compared to an equivalent measurement on a track with no GB. Although this argument does not take into account the inhomogeneous E-field distribution at the LAGB, it is *essential* for comparison of tracks above the irreversibility line – in which case dissipation occurs across the whole track length for both GB and IG tracks. The appropriateness of this scaling method is found in the merging of GB and IG properties in this regime, seen in the measurements of chapter 6 – 9.

It should be noted that below the irreversibility line, the unknown width over which dissipation occurs at the GB will still result in an *inconsistent* E-field criterion between J_c^{GB} and J_c^{IG}. This problem is one that has not received attention in the literature, and is discussed further in chapter 7.

4.3 Additional Sample Characterisation Techniques

In addition to the transport measurements that provided most of the results in this thesis, other techniques were employed to characterise samples. These are listed in the following sections.

4.3.1 Optical and Atomic Force Microscopy

Bicrystal GB and IG regions were imaged both before and after deposition of the YBCO film using optical and atomic force microscopy (AFM). The optical microscope had an approximate resolution of 1 μm and allowed digital image capture. A Digital Instruments Nanoscope III AFM was used in tapping mode for finer scale imaging. The technique deduces the surface height of the sample by measuring changes in the oscillation amplitude of a micro-fabricated cantilever. The acquired AFM images are presented in two forms (a) tip amplitude data, which highlights sharp changes in surface height, and (b) height data, which can be easily used for quantitative analysis - such as measuring patterned track widths or obtaining a statistical measure of film thickness. The z-axis AFM resolution after calibration was ± 2 nm.

4.3.2 X-ray Diffraction

X-ray diffraction (XRD) measurements were performed in order to confirm bicrystal misorientations and the epitaxial nature of the samples. All XRD measurements were performed using an automated Philips X'Pert diffractometer using Cu K_α radiation (λ = 1.542 Å). The scans used will be discussed in section 5.1.

4.3.3 SQUID Measurements

Chapter 9 contains measurements of magnetisation loops, taken using a Quantum Design superconducting quantum interference device (SQUID) magnetometer. The SQUID, based on the Jospehson effect, measures sample magnetisation as a function of applied magnetic field H_{app}. The system allowed measurement with fields of up to 7 T, over a temperature range 4.2 to 300 K.

4.3.4 Transmission Electron Microscopy

Transmission electron microscopy (TEM) was performed on sample pk2 in order to investigate the grain boundary microstructure. The technique required the production of a number of suitably thin sections (or 'lamellae') of the sample to be imaged. All measurements were performed by Sibe Mennema [5], while at the Faculty of Applied Sciences, Delft University of Technology in the Netherlands.

4.3.5 Magneto-Optical Flux Imaging

In order to probe the LAGB flux penetration behaviour, sample pk2 was imaged magneto-optically by Dr. Christian Jooss at the University of Göttingen, Germany. The technique, as introduced in chapter 3, involves the use of an active garnet indicator layer to sense local flux density to a sensitivity of 0.1 mT. Because the *x-y* resolution is limited to approximately 1 μm, measurements were performed upon the patterned square of 500 μm^2 discussed in section 4.1.6.

4.4 References

[1] D.J. Kang, Department of Materials Science, University of Cambridge, *Private Communication*, (2001)

[2] R. Herzog and J.E. Evetts, *Rev. Sci. Instrum*. **65**, 3574 (1994)

[3] R. Herzog, PhD Dissertation, University of Cambridge (1997)

[4] J. Durrell, PhD Dissertation, University of Cambridge (2001)

[5] S. Mennema, MSc Dissertation, Delft University of Technology, Delft (2001)

5 Initial Characterisation

This chapter presents the results of initial LAGB characterisation prior to transport measurement. XRD, AFM and TEM were used to probe the precise LAGB misorientation and morphology. MO imaging was used to investigate the flux focussing enhancement at the GB, and *R-T* measurements were used to determine T_c and normal state resistivity.

5.1 Misorientation Measurement

The bicrystal substrates were supplied as nominally 4° [001]-tilt misoriented, with a quoted error of ± 0.5°. XRD measurements were performed in order to check the precise misorientation, as for lower angle misorientations such errors become proportionally more significant. This proved to be a judicious precaution, as it was found for sample pk2, the measured misorientation exceeded the stated misorientation by almost 1°.

The in-plane misalignment of the bicrystal (the [001]-tilt component) was determined using a Philips X'Pert automated texture goniometer unit. 'ϕ-scans' were performed on the {110} and {111} substrate planes and the {225} YBCO planes. The geometry of the ϕ-scan is sketched in figure 5.1, and involves rotation in the plane of the thin film at a fixed tilt angle ψ[#]. For such scans on IG material, four poles spaced by 90° rotations would be found. The effect of an ideal [001]-tilt misorientation is to split each of the poles by an amount equal to the tilt in

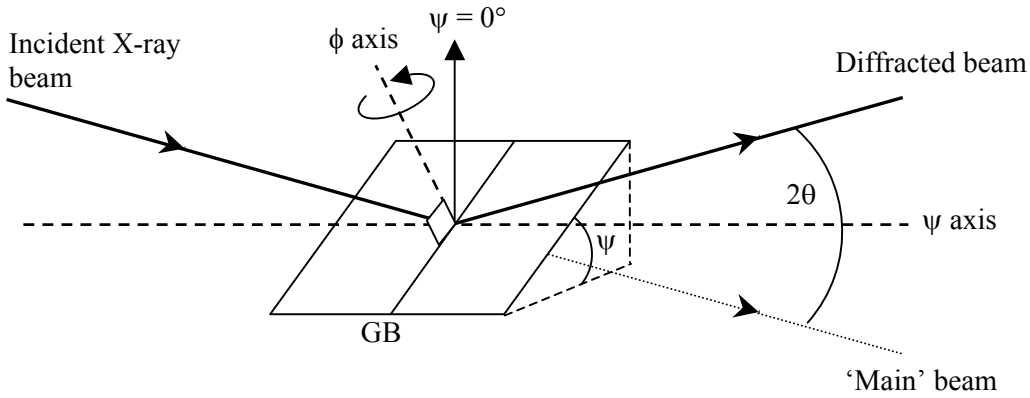

Figure 5.1. XRD ϕ-scan geometry using the texture goniometer unit, at ϕ = 0°. For the {110} $SrTi0_3$ planes ψ = 45°, 2θ = 32.1°.

[#] The angles referred to here should not be confused with those that define the sample position during a transport measurement (see section 4.2.1).

the *ab*-plane. Figure 5.2 sketches an example pole figure for the {110} planes (ψ = 45°), found at ϕ = 0°, 90°, 180° and 270° with the sample as aligned in figure 5.1.

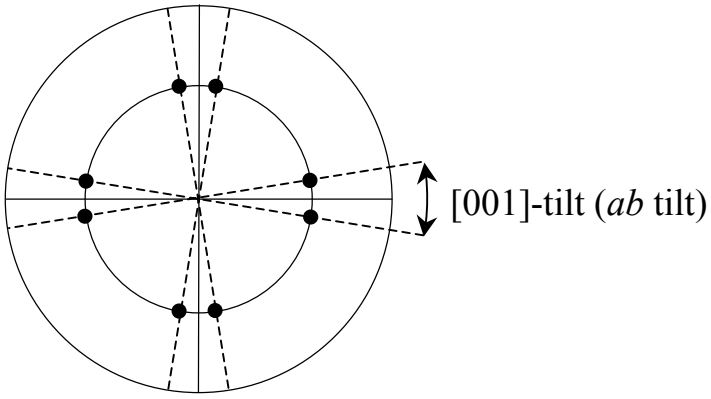

Figure 5.2. Schematic {110} pole figure showing splitting due to the θ_m = [001]-tilt misorientation.

5.1.1 Substrate

Characterisation of sample misorientation was initially performed upon the bicrystalline substrate peaks, as they are both powerful and well defined, allowing an accurate assessment. Figure 5.3(a) shows an example ϕ-scan performed on the {110} peaks of sample pk2. Splitting occurs around each pole during the rotation, as figure 5.3(b) shows in more detail at ϕ = 360° (0°).

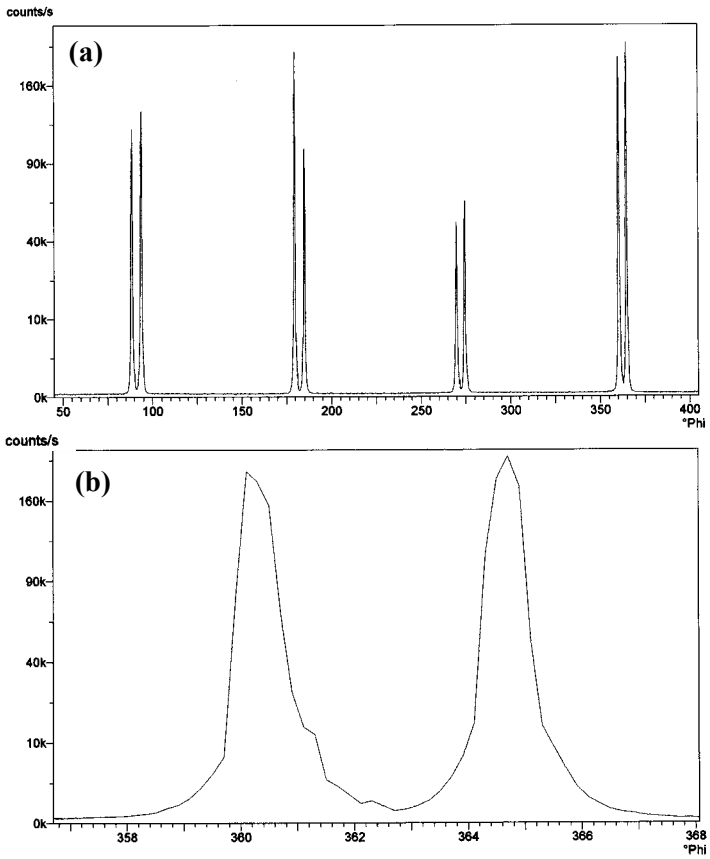

Figure 5.3.(a) ϕ-scan on {110} poles of pk2 $SrTiO_3$ bicrystal to determine *ab*-tilt misorientation and (b) the peak splitting that occurs at the 360° (0°) pole in detail.

Table 5.1. Sample misorientations (to 0.1°) as measured by XRD on bicrystals purchased as nominally 4° [001]-tilt misaligned.

Sample	[001]-tilt	[100]-tilt	[100]-twist
pk2	4.9°	0.1°	0.4°
s2	3.8°	0.2°	0.2°
773c	4.0°	0.2°	0.3°

The measured splitting angle, however, varies slightly from pole-pair to pole-pair in figure 5.3(a). This is due to the presence of additional small components of [100]-tilt and [100]-twist, as defined in appendix B. An additional [100]-tilt shifts the $\phi = 90°$ poles away, but also shifts the $\phi = 270°$ poles together by an equal and opposite amount [1]. The same is true of [100]-twist and the 0° and 180° poles. The actual [001]-tilt may be easily found as the average of the four measurements of split angle per ϕ-scan. Table 5.1 gives the misorientations measured for samples s2, pk2 and 773c in such a manner. Very good correlation was made between [001]-tilt XRD measurements and the HF etch lines formed during processing (see chapter 4).

Direct measurements were made of [100]-tilt and [100]-twist by performing 'ω-scans' on the (002) $SrTiO_3$ poles. The scans involve fixing the incident beam and detector at a given 2θ and

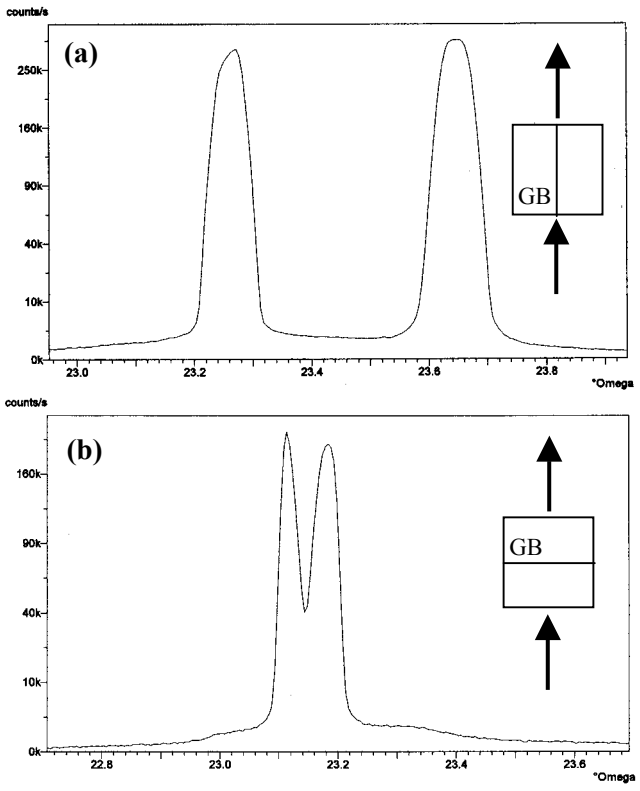

Figure 5.4. XRD ω-scans to determine (a) [100]-twist (0.4°) and (b) [100]-tilt (0.1°) misorientation components. Insets show the alignment of the GB to the incident and diffracted beam.

rocking the sample in angle ω along the beam path direction. The particular misorientation component measured depends upon the ω-scan geometry with respect to the sample GB. The [100]-twist and [100]-tilt components are measured for ω-scans parallel and perpendicular to the GB respectively. Example measurements are shown in figure 5.4 for sample pk2. The extracted twist and tilt components were all found to be small, and are given in table 5.1.

5.1.2 Film

Measurements were also performed on the YBCO film to confirm epitaxial growth and the adoption of the substrate [001]-tilt misorientation. Figure 5.5(a) shows an example ϕ-scan in detail, performed on the {225} YBCO planes (ψ = 59.7°) of sample pk2. The peaks are broader and less intense than those in figure 5.3, but reveal the same [001]-tilt misorientation of ~ 5°.

In addition to instrumental effects, the broadening is caused by the slightly misoriented granular nature of the 'epitaxial' IG regions of YBCO. The increased breadth implies that in the YBCO film the GB is manifest as an average misorientation with an associated range. Another source of increased breadth could be the twinned nature of thin film YBCO. Recent high resolution XRD measurements on a 2° thin film LAGB performed by Verebelyi *et al* [2] show that splitting of the {225} peaks occurs due to the IG twin domain structure, which was found to vary along the GB. The twin boundaries each represent a 1.8° rotation, and although they introduce no dislocations themselves, the GB interface was modulated by θ ± 0.9° which *does* vary the interface dislocation count. Although not seen in the measurements of section 5.2.2, such a twin structure (often unidirectional) has been found in thin film YBCO with a spacing of 30 - 100 nm [3]. The {225} peaks are in fact predicted to split into three; one dominant central spike flanked by two lesser peaks. The shoulders in figure 5.5(a) may be indicative of this effect, only smeared due to the resolution limits of the texture goniometer.

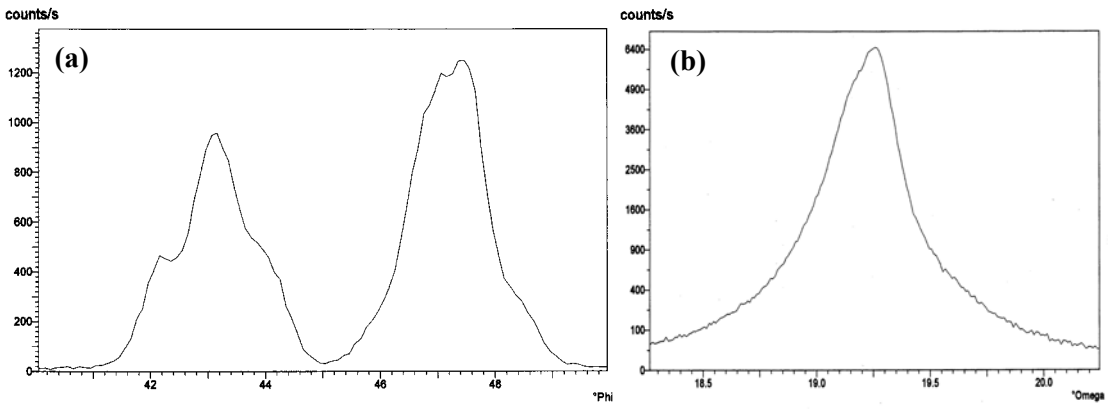

Figure 5.5.(a) ϕ-scan on {225} YBCO planes of sample pk2. Average [001]-tilt misorientation is found to be approximately equal to that of the substrate bicrystal.(b) rocking curve (ω-scan) on the (005) YBCO plane in the [100]-tilt measurement geometry.

Rocking curves were also performed upon the (005) YBCO peak to check the out of plane spread. An example is shown in figure 5.5(b) for sample pk2. The [100]-tilt component of the substrate (0.1°) is absorbed and results in an increase in breadth, giving a FWHM of approximately 0.4 - 0.5°. The same measurement performed away from the GB yielded a FWHM of ~0.3°, indicating a reasonably good *c*-axis alignment [4], given that instrumental effects were not removed.

5.2 LAGB Morphology

5.2.1 AFM Imaging

5.2.1.1 Substrates

As discussed in section 3.4.3, the $SrTi0_3$ grain boundary can possess defects that affect the quality of the boundary formed in the YBCO film. Such 'extrinsic' defects could complicate interpretation of J_c^{GB}, and locally increase the width over which dissipation occurs at the YBCO boundary. The substrate bicrystals were therefore imaged in order to ascertain both the surface quality and the nature of the fusion line.

All bicrystals investigated were found to contain hole defects at the GB, as previously reported for HAGB samples (section 3.4.3). Figure 5.6 shows an example AFM image taken from sample 773c (4°). They were commonly distributed on the micron scale (on average ~1/μm), with diameters ranging from 100 - 300 nm. Depths ranged from 10 – 15 nm (in figure 5.6) to 2 nm, found for samples s2 and pk2.

As discussed in chapter 3, in HAGB samples such holes have been directly linked to YBCO meander and a reduced I_cR_n. A 10 μm track across the GB, for example, will span 10 defects. In order to check the possible impact they may have on LAGB tracks, an annealing experiment was performed. This involved cycling a bicrystal substrate through the thermal stages of the deposition process up to the point at which deposition would take place. In this way the nature of the hole defects, and hence their impact on film growth, could be assessed just prior to YBCO deposition.

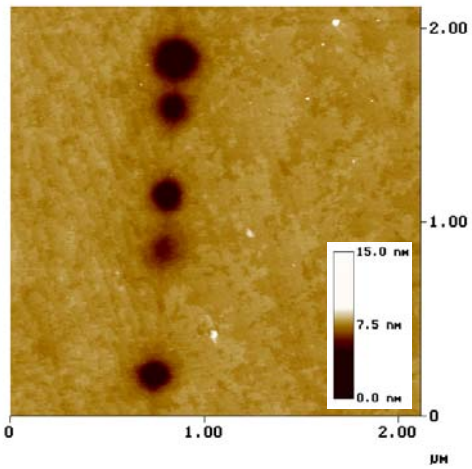

Figure 5.6. AFM height plot of hole defects at the$SrTiO_3$ LAGB (sample 773c)

AFM images of the same scan size and z-range were taken before and after annealing 4° substrate sample 773d at 780° for 25 minutes. The results, shown in

figures 5.7(a) and (b) respectively, seem to show that the annealing step has a 'healing' effect, reducing the hole depth significantly. This is highlighted quantitatively by the corresponding cross sections taken along the boundary given in figure 5.7(c) and (d). Although the scans are not at exactly the same position (they are not the same holes), the reduced depth *was* found at a number of locations along the interface. For samples pk2 and s2, which possessed smaller defect depths, the deposition process may actually have healed them completely. As LAGBs possess larger critical currents than HAGBs, any detrimental influence the defects may have on GB current transport is likely to be of lesser importance.

It should also be noted that, as opposed to post-annealed HAGB samples, no faceting of the GB was found to occur, probably due simply to the reduced misorientation (see section 3.4.3).

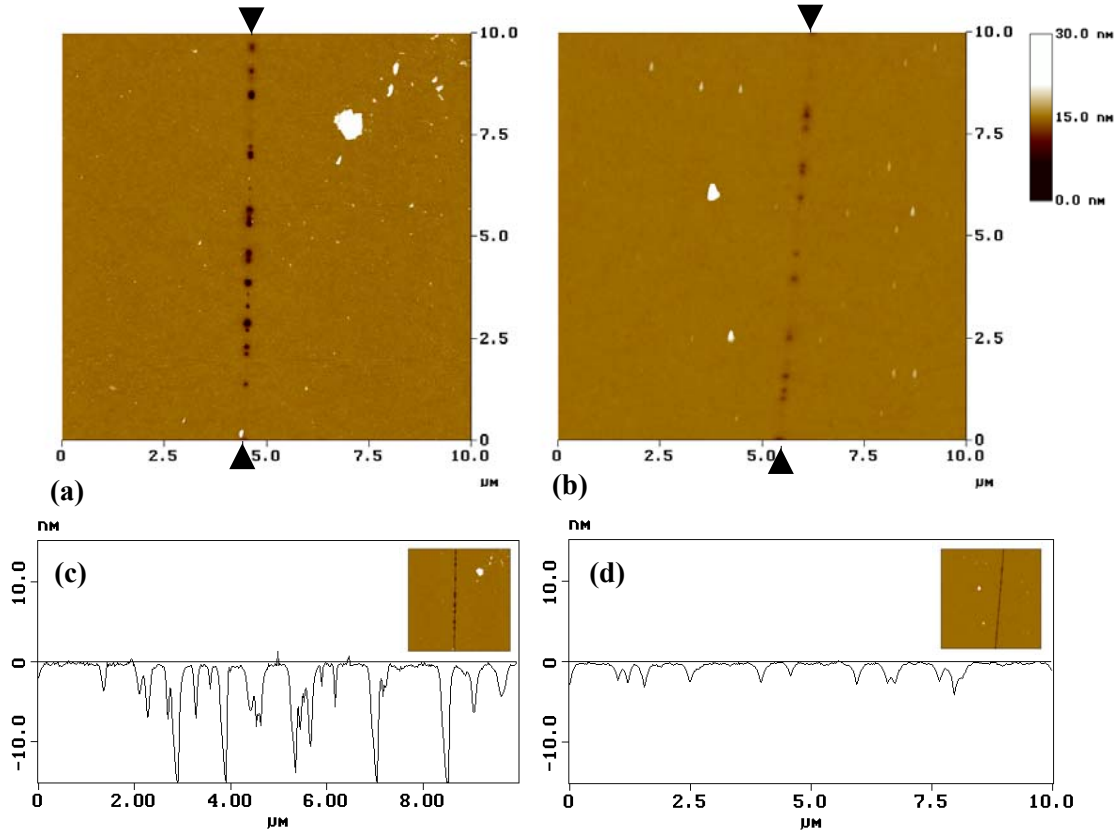

Figure 5.7. AFM height images of the (773d) $SrTiO_3$ bicrystal GB (a) before, and (b) after annealing at 780°C for 25 minutes. Heating took place at 20°/min. The heat treatment appears to significantly 'heal' the defects as can be seen in the cross sections along the GB (c) before, and (d) after annealing.

5.2.1.2 Films

The surface morphology of the YBCO boundaries were AFM imaged in a process requiring strong oblique lighting to expose the GB location under an optical alignment microscope. They generally reveal the YBCO boundary as a meandering, but linearly correlated depression in thickness. Examples are shown in figure 5.8 for samples pk2 and s2 (both of

thickness t_f ~145 nm) prior to patterning. Although grown in the same PLD system (with a few months between depositions), both films possessed slightly different morphologies.

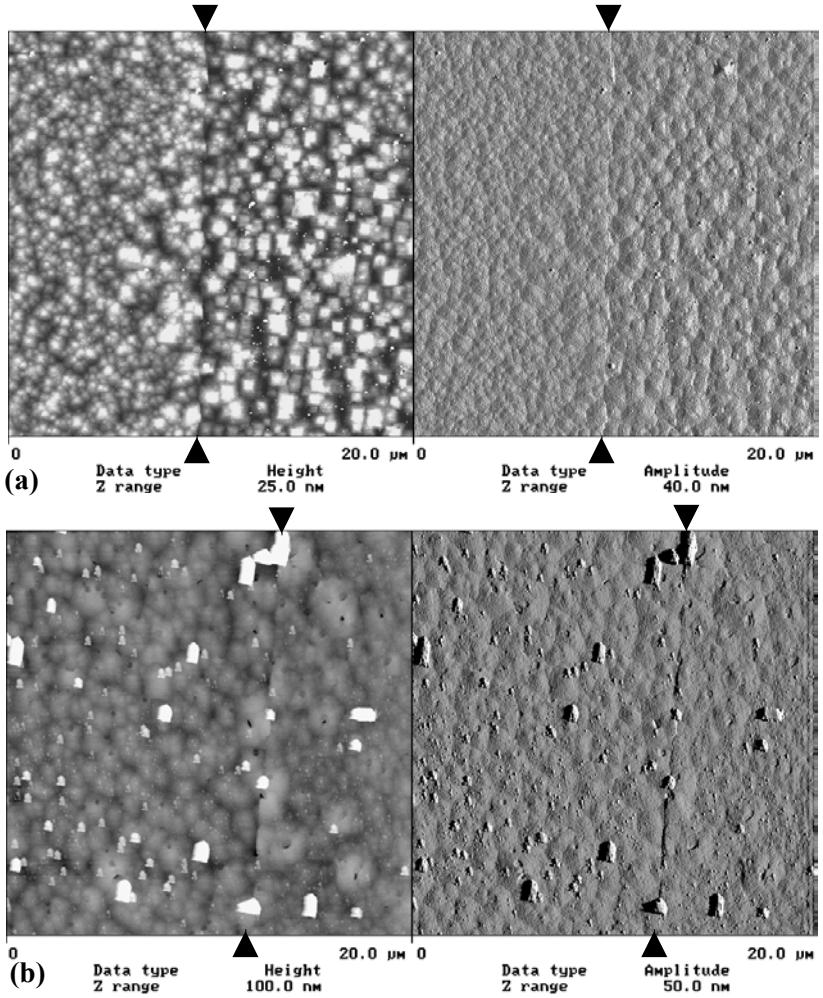

Figure 5.8. Height (left) and amplitude (right) AFM images of samples (a) pk2 (4.9°) and (b) s2 (3.8°) taken prior to patterning. Images are plotted on the same *x*-*y* scale, and the GB line is indicated by arrows.

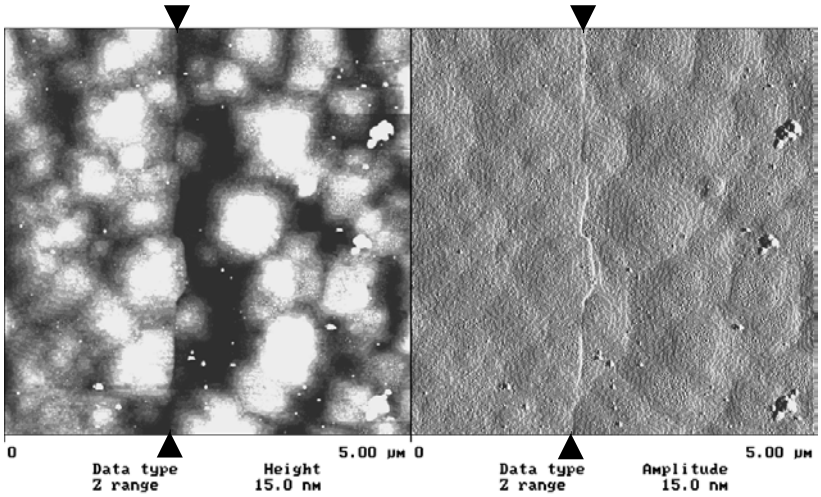

Figure 5.9. Higher magnification height (left) and amplitude (right) AFM images of sample pk2 (4.9°). The GB displays meander due to island-like film growth.

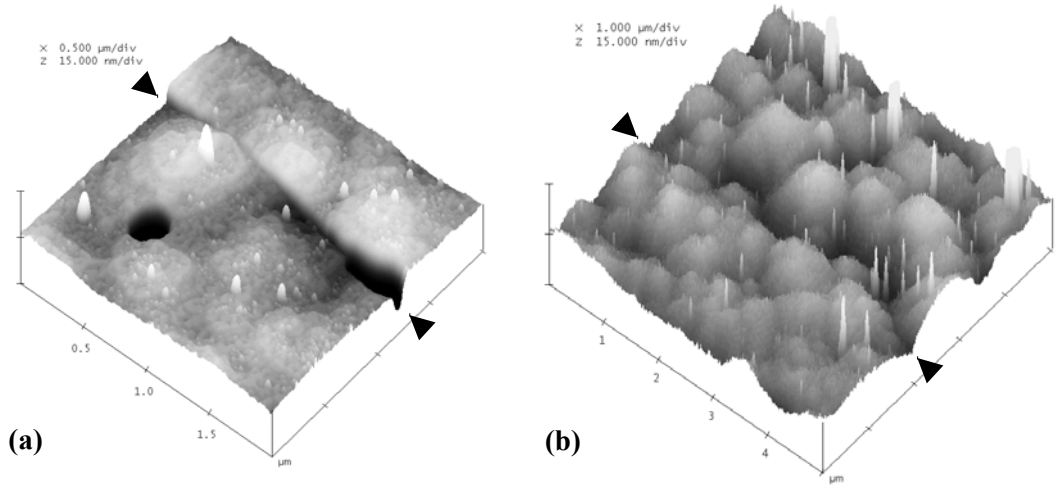

Figure 5.10. 3D AFM plots of (a) s2 (2 μm^2) and (b) pk2 (5 μm^2) grain boundaries (indicated by arrows). Sample s2 displays less meander, as the grains do not overgrow the GB to the same extent.

Sample pk2 has relatively few outgrowths, and a square-like IG grain structure of height of ~ 10 nm. Sample s2 possesses a rounded grain structure of height ~ 4 nm, but more out growths and scattered pinholes. Most samples had grain diameters of up to 1 – 1.5 µm.

Figure 5.9 shows the pk2 boundary line in more detail. The meander can be seen as a direct consequence of the impingement of island-like grains of one misorientation across the interface. As the GB is defined by the edges of grains, it is associated with a meandering depression. For some samples this depression was found to be enhanced, ranging from 4 % (pk2) to 10 % (773b) of the film thickness. The degree of meander was generally found to be up to 250 nm (sample pk2, 773c), although only 100 nm for s2, which demonstrated much less depression and impingement across the GB. This difference is highlighted in the detailed 3D plots of figure 5.10 for s2 and pk2.

The morphology of the IG film is also found to be slightly different on each side of the GB line. This can be seen in figure 5.8(a), where grain size is smaller on the left hand side. This is important for comparison of GB and IG transport behaviour, and may account for some of the variation in IG properties recorded in the next chapters. A particularly clear example of this behaviour is seen in figure 5.11, which shows an AFM taken on a 2° LAGB. Holes are clearly visible on the right side of the sample, but almost totally absent on the left. Such behaviour may be linked to the out of plane components of misorientation; [100]-tilt and [100]-twist. As one

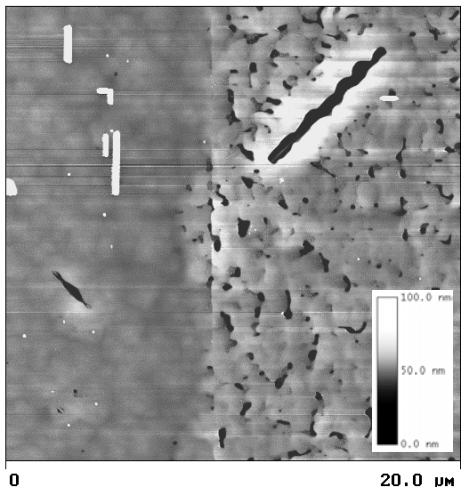

Figure 5.11. AFM height plot of a 2° LAGB sample 640a2, showing morphology change across the GB.

substrate will be more vicinal than the other, its surface will not be ideal (100). Both sides will therefore require slightly different optimal deposition parameters. Additionally, pinhole defects have been found to be characteristic of YBCO films grown on vicinal substrates [5].

5.2.2 TEM Imaging

TEM images were taken on sample pk2 in order to assess the YBCO boundary structure *within* the film. Figure 5.12 shows a low resolution TEM of the GB taken in plan view – looking along the *c*-axis of the film. In agreement with the AFM results in the previous section, the boundary plane is seen to facet on a scale of several tens of nm, resulting in the meandering behaviour seen on the surface. It should also be noted that the GB region is not completely sharp. The dark band and smearing could indicate either a tilting of the GB plane in the *c*-axis, as will be presented later, or a generally increased region of YBCO distortion. The latter would tend to increase the width of dissipation of the GB interface as the strain at the GB extends further into the grains. As introduced in chapter 6, this may create a $J_c^{GB}(x)$ profile across the GB with which vortices may interact.

Cross sections of the GB were also taken to directly assess the structure of the interface in the growth direction. Figures 5.13(a) and (b) show cross section images taken on the same lamella (see section 4.3.4) along the [100] direction of the film on the right and left side of the LAGB respectively. The LAGB follows a nearly straight line from substrate to film surface, parallel to the *c*-direction ($\theta = 0°$ in figure 4.6). Slight deviation only occurs near the surface of the film and near the film-substrate interface. However, cross section images taken on another lamella at another position along the LAGB revealed different behaviour. This is seen in figures 5.13(c) and (d), also taken along the [100] direction on the right and left sides of the GB respectively. Large deviation from the $\theta = 0°$ direction is seen, of up to approximately 45°. Indeed, the magnitude of lateral displacement at the film surface (~ 100 nm) is on the order of the film thickness $t_f = 145$ nm. These results show 'multiple meander' (section 3.4.1) for the first time in a LAGB thin film sample. This spread in angle has implications for vortex alignment in the angular measurements of $J_c^{GB}(\phi)$ and $J_c^{GB}(\theta)$, as field is scanned out of the

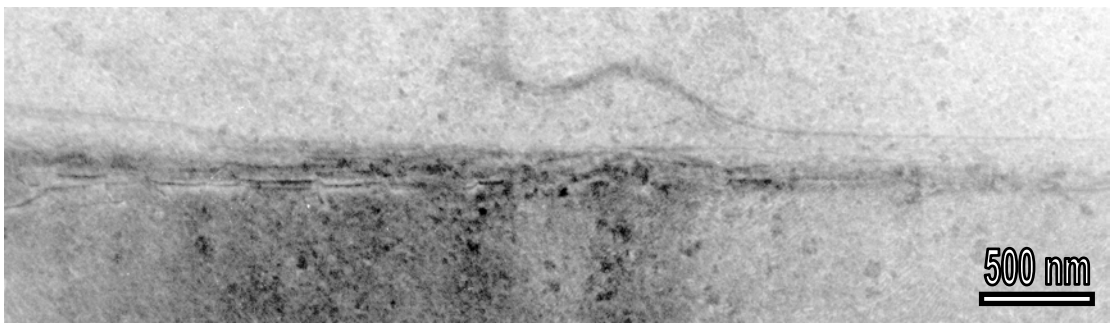

Figure 5.12. Low-resolution TEM image of the LAGB in sample pk2 in plan view (looking along the *c*-axis).

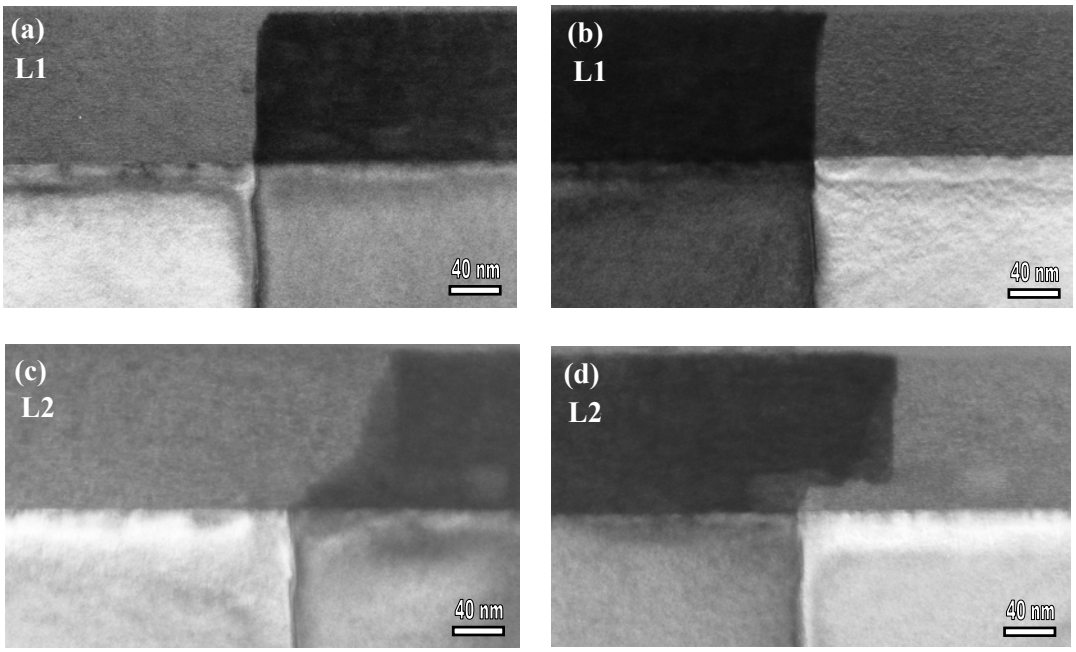

Figure 5.13. Cross section TEM images of two lamellae (L1 and L2) containing the pk2 LAGB, taken along the [100] direction of the film on the right hand side [figures (a) and (c)] and the left hand side [figures (b) and (d)] of the GB. The top and bottom sections of each image are YBCO thin film and $SrTiO_3$ substrate respectively.

GB plane. This will be discussed in more depth in sections 8.6 and 9.4 respectively.

5.3 Magneto-Optic Imaging

MO images of the LAGB region of sample pk2 were taken at 4.2 K after zero field cooling (ZFC). Flux density maps were measured for the 500 μm^2 patterned square (section 4.1.6) as the applied field was first ramped up (denoted B^+) and then ramped down (denoted B^-). Figure 5.14 presents the results for increasing [(a) to (c)] and decreasing [(d) to (f)] field, applied along the *c*-axis ($\theta = 0°$). Each image is accompanied by cross sections showing the flux density both across and along the GB line. Even for a small applied field of 16 mT (figure 5.14(a)) the GB is fully penetrated with flux before any significant penetration into the IG regions has occurred. This can be seen as a sharp spike in the profile running across the GB, the magnitude of which (~38 mT) exceeds the applied flux density by over a factor of two. The fact that flux penetration occurs so readily indicates that for this 4.9° sample, $J_c^{GB} << J_c^{IG}$ at 4.2 K and low field.

The enhancement of flux density at the GB noted above is due to the demagnetising enhancement of field that occur near the edges of thin film samples (see section 2.9 and 3.8.4). Termed the 'flux focussing' effect, the degree of enhancement at the GB is related to the coupling strength across it, and hence θ_m (see figure 3.18). As discussed below, these measurements show the sign and magnitude of the enhancement component is also sensitively related to the direction (B^+ or B^-) in which the field is ramped.

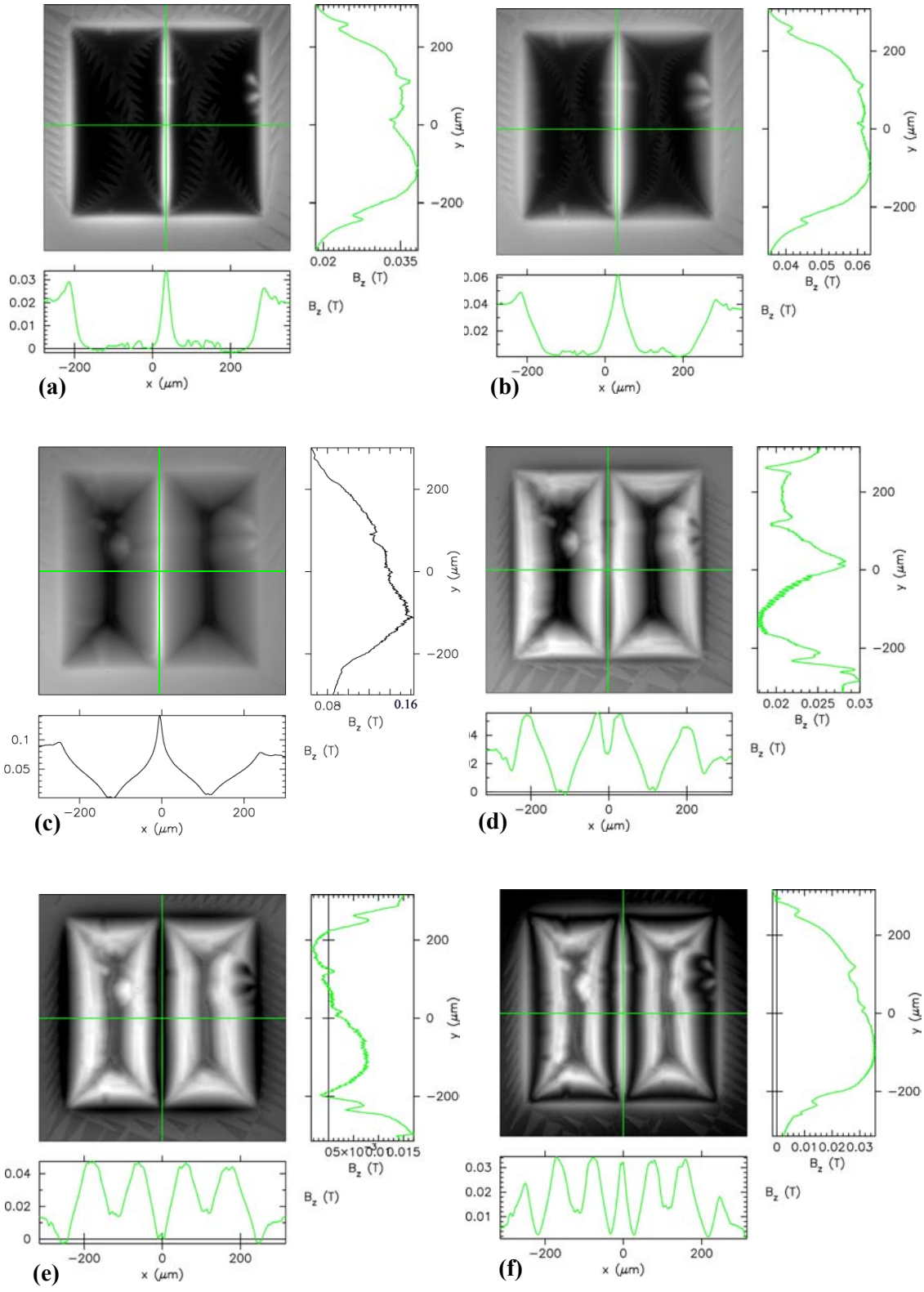

Figure 5.14. Magneto-optic flux images of $B_z(x,y)$ taken on a 500 μm^2 square patterned at the GB of sample pk2. Images were taken after zero field cooling. Applied flux density was then ramped up to (a) 16 mT, (b) 32 mT, and (c) 93 mT, then ramped down to (d) 48 mT, (e) 22.4 mT, and (f) 0 mT. Field was applied along the *c*-axis (θ = 0°), and cross sections are shown of B_z both along and across the GB line.

Table 5.2 lists the applied flux density, B_{app}, the flux density at the GB, B_{GB}, and the calculated *additional* component, B_{rev}, due to the flux focussing effect, where $B_{rev} = B_{GB} - B_{app}$. The table, and figures 5.14(a) to (c), show that with increasing field, the additional component is seen to be both positive and increasing in magnitude. This enhancement is seen to persist up to the maximum measured field of 93 mT, at which level the recorded flux density at the GB (~ 184 mT) is expected to saturate the imaging active layer. Although much less than that predicted by Huebener *et al* $(W/t_f) \sim 3400$, or Zeldov *et al* $(W/2t_f)^{1/2} \sim 40$ [6,7], the enhancements of up to a factor of 2 are significant.

Table 5.2. Applied flux density, B_{app}, and extracted values of flux density at the GB, B_{GB}, and *additional* LAGB flux component, B_{rev}, from figure 5.14.

B_{app} (mT)	B_{GB} (mT)	B_{rev} (mT)
16.0 (B^+)	38	+ 23
32.0 (B^+)	62	+ 30
63.0 (B^+)	102	+ 39
93.0 (B^+)	165 to 184	+ 72 to + 91
48.0 (B^-)	28	- 21
23.0 (B^-)	0	- 23
0.0 (B^-)	-32	- 32

As field is reduced, it can be seen that B_{GB} sharply decreases, leading to a localised dip in the flux profile across the GB in figure 5.14(d). B_{rev} also switches sign to become negative in table 5.2, and by $B_{app} = 0$ T the flux at the GB is approximately $B_{GB} = -32$ mT[#].

This effect is directly related to the magnetisation of the IG regions of the square of YBCO - the flux profile in the IG regions is expected to sensitively control the sign and magnitude of the additional GB flux component. As seen in figure 5.14, a bean model-like flux penetration in the grains of the material occurs as the applied field is ramped up. This is illustrated schematically in figure 5.15(a). The diamagnetic response forces an additional flux around the edges of the sample and through the GB due to the large demagnetising factor, giving B_{rev} = +ve. Subsequent applied field reduction leaves a remanant paramagnetic moment in the grains (dashed line in figure 5.15(a)) that drives a reverse flux component through the GB, giving B_{rev} = -ve. This effect can be envisaged as a closure of the trapped flux lines in the IG material that are no longer supported by the external field. The flux at the LAGB for

[#] The MO images and cross sections only display the flux density *magnitude*, so this appears as a positive peak in figure 5.14(f).

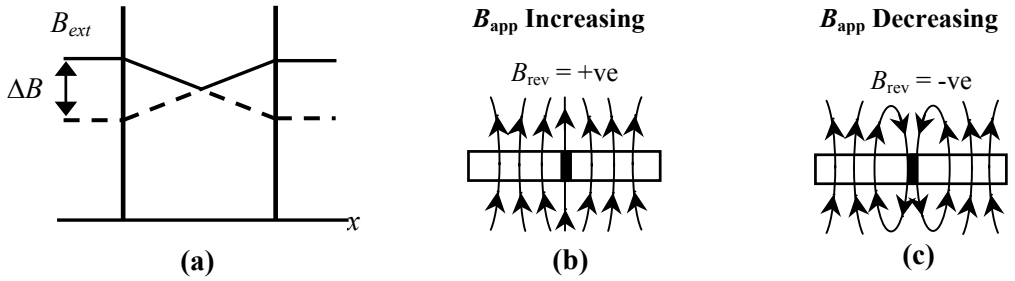

Figure 5.15. (a) Schematic of the flux profile in the intragranular regions of the square (*x* parallel to GB) and the resulting additional flux component at the LAGB for (b) increasing and (c) decreasing applied field.

increasing and decreasing scenarios is sketched in figure 5.15(b) and (c) respectively. As the penetration field for the IG regions appears to be approximately 0.1 T (figure 5.14(c)) a full switch in IG flux penetration profile is only expected for field ramped down to $B_{app} = -0.1$ T.

This effect is almost certainly the prime cause of both static and angular hysteresis in $J_c^{GB}(\theta)$ discussed in sections 7.1.6 and 9.3.5 respectively.

5.4 *R-T* Measurement

Four point resistance measurements were performed as a function of temperature (termed *R-T*) in order to determine the critical transition temperature, T_c. Measurements of T_c were made on both GB and IG tracks in order to contrast behaviour. As discussed in section 3.9, the nature of the *R-T* for a GB track is expected to vary as a function of the misorientation - the development of a 'foot' at higher angles is believed indicative of weak link behaviour.

Figure 5.16 shows example logarithmic plots of *R-T* measured for a selection of GB tracks and one IG track patterned on sample pk2 at 0 T. As can be seen, the precise T_c^{GB} was found to vary to a degree from track to track, and as such T_c^{GB} *can* be measured to exceed T_c^{IG}. This is likely to be due to inhomogeneities along the GB across the IG film. It was generally found for samples s2 and pk2 that T_c^{GB} ranged from 89.5 to 90.3 K.

The foot region was not observed in any of the bicrystal samples measured in this study (from $\theta_m = 3.8°$ to 4.9°) apart from on the smallest track measured (of width 2.5 μm) on pk2. For this track, T_c^{GB} was depressed to approximately 87 K, as shown in figure 5.16. However, this is most likely to be due to track damage during the patterning procedure as opposed to being indicative of the LAGB coupling strength. Any reduction in T_c at the edges of a track due to the patterning process will become increasingly important as track width decreases.

As the foot was absent in other track *R-T*s it may be concluded that the boundary is sufficiently strongly coupled to mitigate the effect. This means that although T_c is modulated at the LAGB interface, particularly across the dislocation cores (see sections 3.3 and 7.2.3), the GB region is not behaving as a slab of reduced T_c material dividing the track in two.

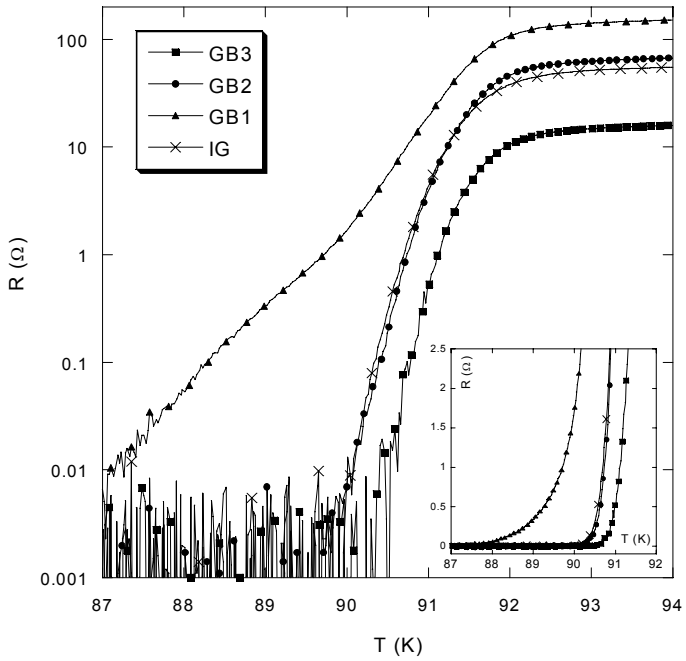

Figure 5.16. *R-T* measurements taken on three GB tracks, and one IG track patterned on sample pk2. The tracks were of width 2.5 μm (GB1), 6 μm (GB2), 24 μm (GB3) and 10 μm (IG). The inset shows the same data plotted on a linear *R* axis.

An example of the LAGB normal state behaviour, for $T >> T_c$, is shown in figure 5.17 for sample s2. The figure plots the normal state resistivity for two GB tracks and an IG track. The resistivity was calculated simply by using the track length and cross-section. The GB and IG curves are seen to be very similar, and fall within an estimated 10 % track dimension error plotted on the IG trace. This similarity indicates that the contribution to normal state

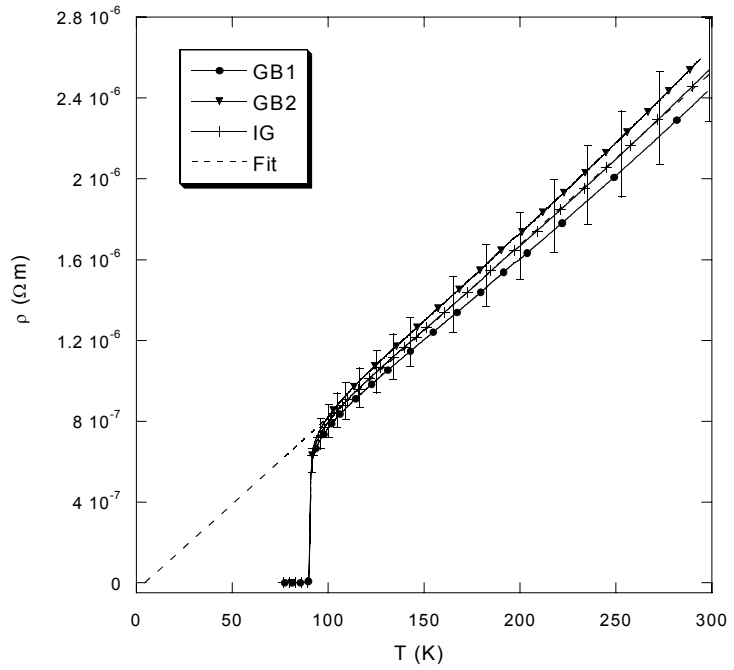

Figure 5.17. LAGB and IG track normal state resistivity at high temperatures. Resistivity was calculated using the track dimensions of GB1, GB2 and IG tracks. The dashed line shows a fit to the IG data of $\rho = -3.7 \times 10^{-8} + 8.55 \times 10^{-9} T$.

resistivity made by the LAGB is relatively small, and within noise limits. This result correlates with the absence of the *R-T* foot, which if present would indicate a significant additional resistive component due to the LAGB.

All curves at high temperature displayed a linear dependence with temperature and possessed small zero temperature offsets, a feature indicative of good quality YBCO [8]. For s2 and pk2 values of $d\rho_n/dT = 1.08 \times 10^{-8}$ $\Omega m\, K^{-1}$, and $d\rho_n/dT = 8.55 \times 10^{-9}$ $\Omega m\, K^{-1}$ were found respectively.

5.5 Summary

The misorientations of the nominally [001]-tilt LAGB samples have been confirmed through XRD analysis, which show only small additional components of out of plane tilt and twist. AFM and TEM measurements show a meandering LAGB line formed in the thin film YBCO layer. In particular, the TEM cross section images reveal the GB can deviate from the *c*-axis in the direction of growth. The deviation is most likely to be due to the growth mode of the thin film. The effect of hole defects in the underlying substrate GB is also found to be mitigated at the high temperatures used for deposition.

Magneto-optic imaging has confirmed for the first time that the sign of the additional enhancement of flux at a LAGB is critically dependent upon the applied field history. Finally, the fact that no significant additional normal state resistivity was found for the LAGB samples is indicative of a strong coupling behaviour.

5.6 References

[1] J. Leake, Department of Materials Science, University of Cambridge, *Private Communication* (2001)

[2] D.T. Verebelyi, C. Cantoni, J.D. Budai, D.K. Christen, H.J. Kim and J.R. Thompson, *Appl. Phys. Lett*. **78**, 2031 (2001)

[3] J.D. Budai, M.F. Chisholm, R. Feenstra, D.H. Lowndes, D.P. Norton, L.A. Boatner and D.K. Christen, *Appl. Phys. Lett*. **58**, 2174 (1991)

[4] L. Mechin, P. Berghuis and J.E. Evetts, *Physica C* **302**, 102 (1998)

[5] J.H. Durrell, PhD Dissertation, University of Cambridge (2001)

[6] R.P. Heubner, R.T. Kampwirth and J. R. Clem, *J. Low Temp. Phys*. **6**, 275 (1972)

[7] E. Zeldov, J.R. Clem, M. McElfresh and M. Darwin, *Phys. Rev. B*, **49**, 9802 (1994)

[8] C.P. Poole, H.A. Farach and R.J. Creswick, *Superconductivity*, Academic Press, London (1995)

6 The *V-I* Characteristic

This chapter presents measurements of the LAGB *V-I* characteristic with magnetic field applied along the *c*-axis. The characteristic is a valuable probe of the dominant dissipative mechanism, which for the LAGB is found to differ from both HAGB and IG material. The LAGB characteristic displays an offset linear nature that is observed to develop into a kinked structure at lower temperature. Although other models and influencing factors are discussed, this behaviour can be well interpreted in terms of dissipation dominated by the *viscous flux flow* of vortices along the GB.

6.1 Previous Measurements

Although variations exist with temperature and applied field, figure 6.1 illustrates the general *V-J* characteristics[#] reported for HAGB, LAGB and IG tracks. It has been found that HAGBs typically display a *V-J* characteristic well described by the Resistively Shunted Junction (RSJ) model [1,2], resulting in a negative curvature as sketched in figure 6.1(a). For LAGBs however, there has been a lack of consensus on the shape of the *V-J* characteristic above J_c and the dissipation mechanism that determines it. Although smaller angle LAGBs ($\theta_m < \sim 3°$) have been reported to possess a curved characteristic [3] referred to as 'flux flow', higher angle LAGBs ($3° < \theta_m < 10°$) are generally found to display *V-I*s with an offset linear nature (figure 6.1(b)) [4,5]. Both high *and* low angle grain boundaries display behaviour that is markedly different to that measured in the IG material, which is dominated by flux creep and is often power-law in nature (figure 6.1(c)).

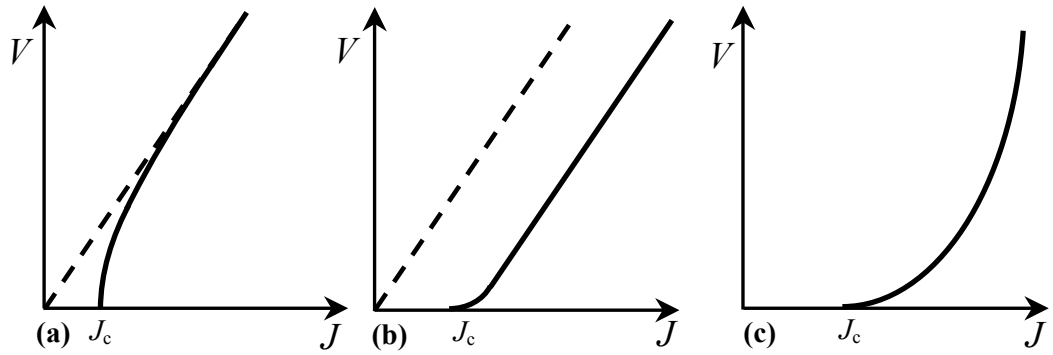

Figure 6.1. Sketch of the typical *V-I* characteristics displayed by (a) HAGB (b) LAGB and (c) intragranular (IG) YBCO material.

[#] Variants of the *V-I* characteristic include plots of voltage with current density, *V-J*, and electric field with current density, *E-J*.

One of the first *detailed* examinations of the LAGB *V-I* characteristic was performed by Díaz *et al* [4] on a 4° thin film YBCO boundary. In contrast to a creep rounded IG transition, they observed the linear characteristic previously shown in figure 3.17. Confirmation of this offset linear nature was provided by Verebelyi *et al* [5] who measured the extended *V-J* characteristics of a 4.5° LAGB. Figure 6.2 shows the *V-J* data they found for both grain and GB at various fields. Linear regions may be clearly seen in the GB transitions, before becoming increasingly curved at higher current density. The introduction of this curvature is due to ensuing dissipation in the intragranular regions of the GB track, which dominates the *V-I* response (see section 6.6).

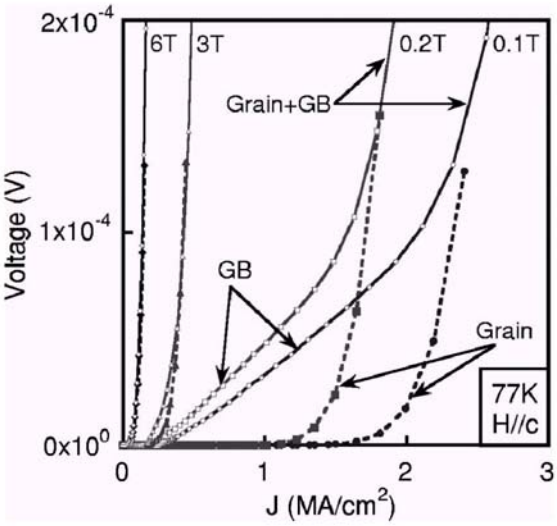

Figure 6.2. *V-J* characteristics measured for a 4.5° LAGB and comparative grain at 77 K for several applied fields parallel to *c* [5].

In another study, Verebelyi *et al* [3] investigated the *V-J* characteristics of GBs of several misorientations at 77 K. Figure 6.3 gives the characteristics they found for 10° and 7° boundaries compared to IG material and a coated conductor ('RABiTS') at 3 T. As θ_m decreases, increased rounding of *V-I* characteristics is observed. As θ_m increases beyond 10° (not shown in figure 6.3), an RSJ-like curvature develops. Similar results were observed by Heinig *et al* [6], although the double logarithmic axes they used to plot data tended to obscure the linear regime. It is clear that between the very high and very low angle limits, there exists a low angle regime of θ_m over which *V-I* characteristics are non-RSJ *and* linear for certain fields. Although field dependent, this range can be identified as $2\text{-}3° < \theta_m < 10°$ at 77 K. There is, however, a lack of detailed measurement in the literature of the LAGB *V-I* at low temperatures.

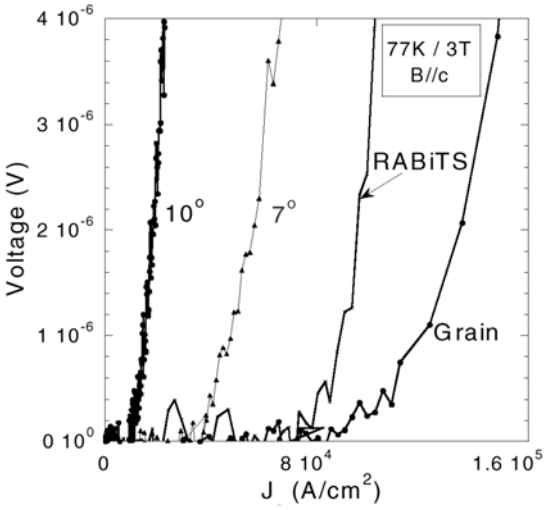

Figure 6.3. *V-J* characteristics measured for 7° and 10° GBs compared to those measured in the grain and across a coated conductor 'RABiTs' for 3 T parallel to *c* [3].

Daniels *et al* [7] also observed LAGB linearity in a study into the effects of Ca doping of 5° LAGBs. The *V-I* characteristics of the *undoped* GB demonstrated clear linearity at 77 K ($t = T/T_c = 0.85$) but those of the doped

sample (30% Ca) displayed *V-I* curvature indicative of creep rounding. This is consistent with a reduction in *E*-field as discussed in the section 6.3.1.

6.2 LAGB Vortex Channelling

Although the dislocations forming GBs have been found to enhance the pinning of vortices (section 9.3) J_c is still depressed significantly by the reduced effective cross sectional area of the boundary and core elongation effects (chapter 3.8.2). Because $J_c^{GB} < J_c^{IG}$, the dissipation observed during a transport measurement is necessarily very localised to the GB. Only at sufficiently high driving currents is the intragranular J_c^{IG} exceeded, resulting in an IG contribution to voltage and a delocalisation of dissipation away from the LAGB.

Díaz *et al* [4] proposed that when J_c^{GB} is exceeded, a single line of vortices along the LAGB become depinned and respond to the transverse Lorentz force. This line is then channelled along the boundary, between banks of pinned vortices in the grains, as illustrated in figure 6.4. In reality, this work finds that the number of rows channelling may be more than one, and will depend on the structural and electronic width of the GB.

The proposed small distance over which this dissipation occurs, on the order of one vortex lattice spacing, leads to the presence of electric fields up to ~10^4 times that expected in an intragranular YBCO track – as mentioned in section 3.8.2, there are reported fields of up to 300 V/m for voltages of a few μV [4]. The measured voltage difference appears not across the whole track, as in an IG measurement, but across a small effective distance termed the dissipative width, d_{eff}. The transformation of voltage to *E*-field can be calculated by analysing the generation of the voltage induced by flux flow with the Josephson relation,

$$\frac{\partial \varphi_{AB}}{\partial t} = \frac{2eV_{AB}}{\hbar} \tag{6.1}$$

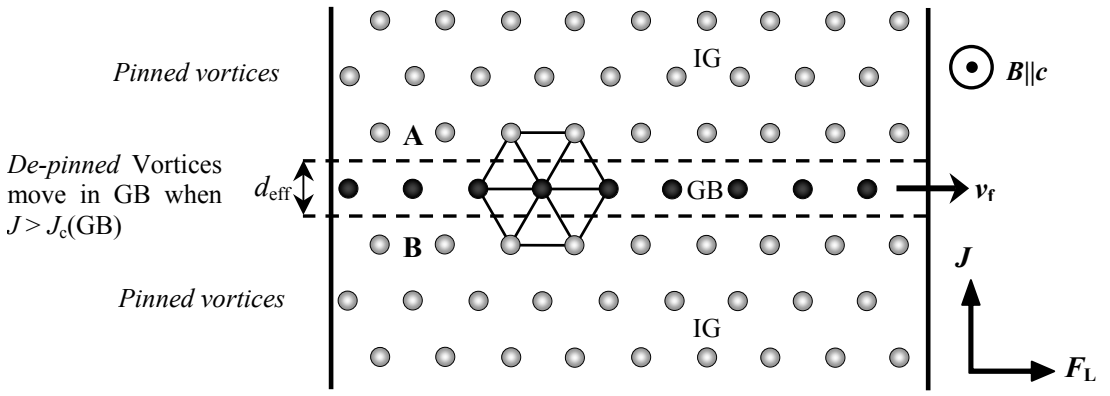

Figure 6.4. Schematic of the hexagonal vortex FLL in a track containing a [001]-tilt GB. The line of vortices pinned by dislocations in the GB (dark) will move with velocity $\boldsymbol{v}_f$ under the Lorentz force, $\boldsymbol{F}_L$, when the current density exceeds $J_c(GB) < J_c(IG)$. For $J < J_c(IG)$ vortices in neighbouring grains (light) will remain pinned, and hence static.

linking the instantaneous voltage V_{AB} generated by the rate of change of phase difference φ_{AB} of the order parameter between two points A and B on either side of the boundary (figure 6.4). The passage of a vortex across the line connecting A and B will induce a phase change of 2π. By assuming that s rows of vortices flow in the GB with a velocity $\boldsymbol{v}_f$, and that the vortex spacing in the GB is a_o, then the average rate of change of phase is,

$$\overline{\frac{\partial \varphi_{AB}}{\partial t}} = \frac{2s\pi}{a_o} v_f \tag{6.2}$$

Inserting this into the left hand side of equation 6.1, and using the result that $E = v_f B$ (equation 2.14) we find that the averaged E-field is,

$$\overline{E}_{AB} = \frac{1}{s}\left(\frac{V_{AB} a_o B}{\Phi_o}\right) = \frac{1}{s}\left(\frac{2V_{AB}}{\sqrt{3}a_o}\right) = \frac{V_{AB}}{d_{eff}} \qquad \text{where} \quad d_{eff} = s\left(\frac{\sqrt{3}a_o}{2}\right) \tag{6.3}$$

and equations 2.10 and 2.9 for B and Φ_o have been used. By choosing $s = 1$, the Díaz *et al* [4] result of single row flow is recovered. Interestingly, the single row assumption leads to a d_{eff} equal to the lattice spacing perpendicularly to the LAGB in the lattice geometry seen in figure 6.4. This is only one of two possible orientations, the effects of which have been studied by Pruymboom *et al* at low T_c artificial easy flow channels [8].

6.3 Mechanisms Predicting *V-I* Linearity

There are a number of possible mechanisms that *could* account for the offset linear nature of LAGB *V-I* characteristics. Three possible interpretations are discussed below.

6.3.1 Viscous Flux Flow

It was first argued by Díaz *et al* [4] that the *V-I* linearity observed in LAGB characteristics was indicative of dissipation in the viscous flux flow (VFF) regime. As discussed in chapter 2, in this limit the Lorentz driving forces are balanced by both viscous drag and pinning forces. It is the presence of such high E-fields that shift the E-J curve out of the creep dominated region and into the regime of linear viscous flux flow. The gradient in this case will be related to ρ_f, the flux flow resistivity.

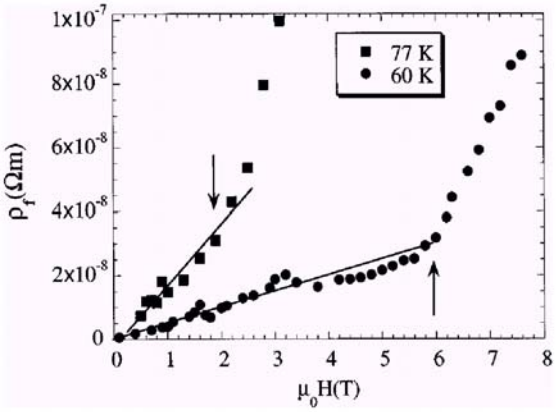

Figure 6.5. ρ_f with field extracted from the E-J characteristics of a 4° thin film LAGB, for B parallel to c [4]. Linear fits are shown.

Accordingly, Díaz *et al* transformed their measured voltage data into electric field data by

using equation 6.3 derived for $s = 1$. By taking the gradient of the *E-J* curve as *equal* to ρ_f, they obtained the results shown in figure 6.5. The curves show a linear dependence of ρ_f on B as predicted by the Bardeen-Stephen relation of equation 2.16. In theory it is therefore possible to estimate a value for the upper critical field B_{c2} from a linear fit. However, such an extraction of ρ_f and B_{c2} will depend critically on the number of rows flowing along the GB. By assuming s rows to flow instead of one, the calculated flux flow resistivities and critical fields are altered by a factor s relative to the $s = 1$ values as,

$$\rho_f(s) = \frac{\rho_f^{s=1}}{s} \quad \text{and} \quad B_{c2}(s) = sB_{c2}^{s=1} \tag{6.4}$$

VFF also explains the transition to curved characteristics as GB misorientation tends to zero (or to the average grain misalignment in the intragranular regions): for lower θ_m dissipation no longer remains localised to the GB and d_{eff} tends to the track length. The result is a reduced *E*-field for a given voltage difference and an introduction of flux creep. Strong evidence for the VFF interpretation will be presented in sections 6.4 and 6.7.

6.3.2 Non Viscous Channelling

Gurevich *et al* [9] have also developed a channelling model that predicts *V-I* linearity at GBs due to the presence of the AJ vortex structure. Their model applies to the range of misorientations in which AJ vortices with no normal cores exist at the GB - they assumed applicability to be $\theta_m < 24°$.

They derived and solved nonlocal Josephson electrodynamic equations in the case of zero pinning. By assuming a particular core length and structure, they were able to calculate *V-J* curves at various fields shown in figure 6.6(a) for J normalised to the depairing current density J_b. Linear regions below J_b may be identified. They also found an equation for the flux flow resistance, R_G, due to the motion of AJ vortices along the contact,

$$R_G = \frac{R\sqrt{H}}{\sqrt{H + H_o}} \quad \text{where} \quad H_o = \frac{\Phi_o}{(2\pi l)^2} \tag{6.5}$$

where l is the core length and R is the quasiparticle resistance of the GB per unit area. Fits of equation 6.5 to data from a 7° GB are shown in figure 6.6(b) for various temperatures.

The upturn in the 77 K curve at ~ 4 T was proposed to mark an increase in dissipative width as $s = 1$ becomes $s = 2$ at the LAGB. A similar upturn was observed by Díaz *et al* in figure 6.5 Although changes in the number of vortex rows flowing at the GB do occur and are visible in the *V-I* characteristic (see section 6.4), this is not the dominant mechanism at play in the

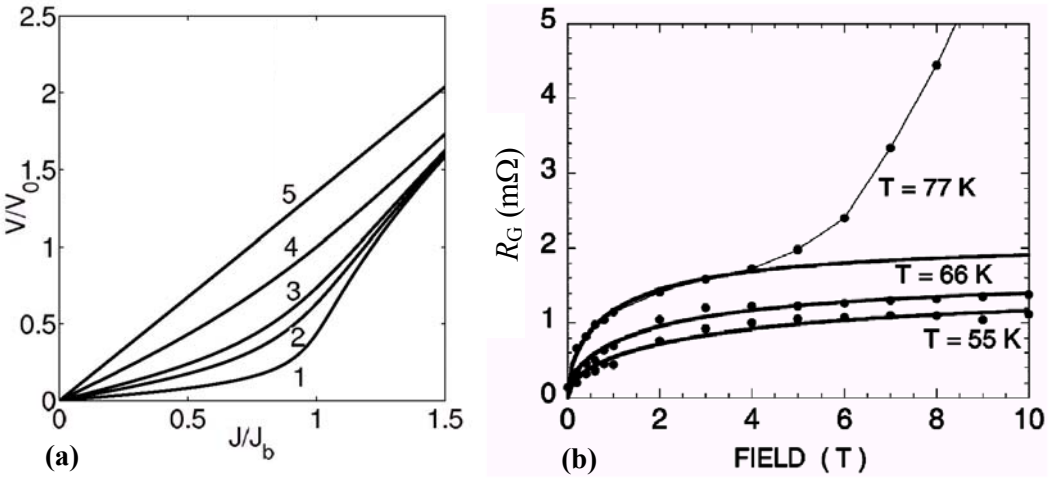

Figure 6.6. (a) Normalised *V-J* curves calculated by Gurevich *et al* for an AJ vortex structure as a function of applied field, where H/H_o = 0.01(**1**), 0.05(**2**), 0.1(**3**), 0.5(**4**) and 10(**5**). (b) *V-I* gradient (R_G) with field measured for a 7° GB. Fits to equation 6.5 are shown [9].

upturn. As detailed in sections 6.6 and 6.7, the real cause is due to crossing the grain irreversibility field.

6.3.3 Long Josephson Junction Behaviour

Another possible source of LAGB *V-I* linearity is long Josephson junction (LJJ) behaviour, a characteristic of some high angle grain boundaries. Long junction *V-I* curves are also characterised by a similar offset linear behaviour. The junction normal resistance defines the linear gradient (as seen in the simple RSJ model at high currents), and an excess supercurrent offsets the curve by an amount I_c.

Evidence against the long junction interpretation for LAGBs has been provided by Redwing *et al* [2]. They observed a change in *V-I* nature with temperature, from flux flow to long junction-like, above 75 K in zero field for a 10° GB. The crossover was explained in terms of both an increasing Josephson penetration depth $\lambda_J(T)$ and a decreasing normalised junction width w/λ_J with increasing T (w is track width). Above 75 K, it was postulated that the channels between dislocations act as weak linked dayem bridges as $\xi(T)$ exceeds the channel *length* (perpendicular to the boundary). This observation would tend to support the applicability of the VFF model for misorientations less than 10° (giving wider and longer channels) at comparable or lower temperatures (giving smaller $\xi(T)$).

It has also been shown that *V-I* resonances that occur in HAGB characteristics under r.f. excitation are indicative of a normal boundary [1]. Recently, Xin *et al* [10] investigated the presence of resonances, or steps, in the microwave impedance of GBs of various θ_m. Such steps - expected within a long junction model - were conspicuously absent in low angle GBs of $\theta_m < 7.5°$ at 75 K. This lead to the conclusion that the long junction mechanism is not

applicable for LAGBs and the dominant dissipative mechanism is not that of Josephson coupling across a normal or insulating barrier.

6.4 LAGB *V-I* Kinking

6.4.1 Experimental Observation

V-I measurements have been performed on thin film YBCO bicrystal LAGBs over a range of temperature (10 K to 85 K) and field (to 8 T). Linearity is observed in various forms in most of the *V-I* transitions, but the precise structure is found to be strongly field and temperature dependent. Figure 6.7 shows a typical transition observed at higher temperatures, measured at 75 K and for 1 T parallel to the *c*-axis of sample s2 (θ_m = 3.8°). As *E-J* requires a precise knowledge of d_{eff}, we plot *V-J* where $J = I/A$ (*A* being track cross section, $A = 8 \times 10^{-13}$ m^2 for the GB in this case). Consistent with the current limiting behaviour of grain boundaries, the figure shows that J_c^{GB} is reduced from J_c^{IG}. Significantly, the curves also display a qualitatively different nature; the GB transition is much more offset linear than the curved, creep dominated IG trace.

In addition to the occurrence of the simple linear *V-I*, this work reveals for the first time a kinking, or faceting, of the curve into several, and in some cases numerous linear segments. The classic single-line, linear trace of figure 6.7 is found to occur only at higher fields and temperatures. In general, for lower field and temperature, the piecewise linear nature is seen to develop as shown in figure 6.8 for sample s2 at 2.5 T and 60 K. Over the 10 μV range the boundary *V-J* can be seen to consist of three separate linear segments, in stark contrast to the smoothly curved intragranular trace also plotted (on the upper scale) for comparison. The inset of figure 6.8 depicts a particularly clear example of kinking in detail, for the same track

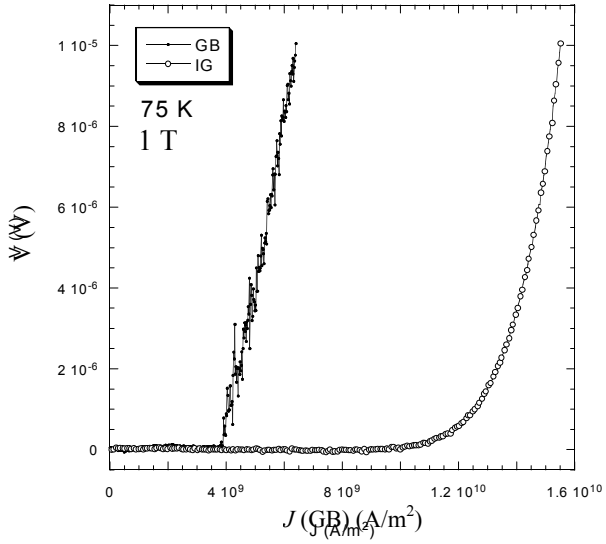

Figure 6.7. *V-J* curves for LAGB and IG material at 75 K and 1 T applied field parallel to the *c*-axis for a 3.8° boundary. Track width *w* = 5.5 μm (GB) and 9.8 μm (IG) (sample s2).

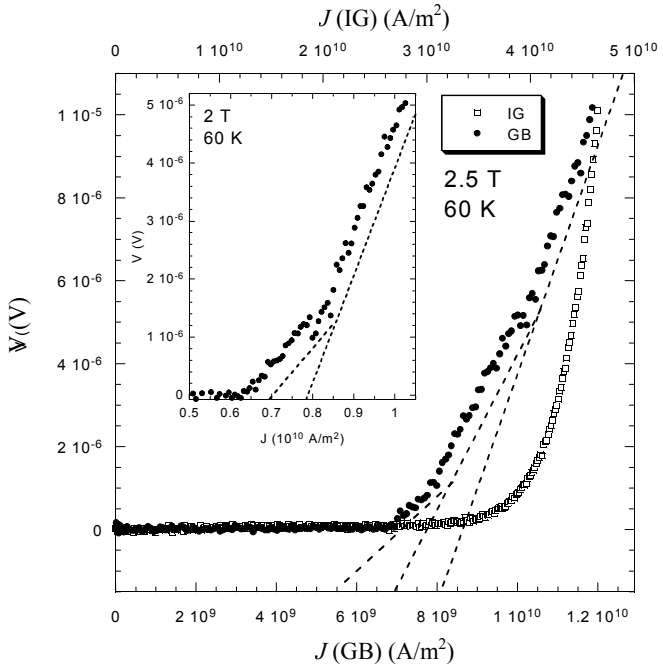

Figure 6.8. *V-J* curves for LAGB (bottom axis) and IG material (upper axis) at 60 K and 2.5 T applied field parallel to the *c*-axis for sample s2 (3.8° boundary). In comparison to the smooth IG transition, faceting of the grain boundary *V-J* into three linear segments may be seen. The inset shows a kink in more detail on a trace taken at 2 T, 60 K. Track widths are 9.1 μm (GB) and 9.8 μm (IG).

at 2 T. The transition above J_c can clearly be seen to comprise two linear sections of differing gradient, where d*V*/d*J* becomes discontinuous at the kink between segments.

Examples of the *V-J* temperature dependence are shown in figure 6.9. At 70 K, *V-J*s show clear linearity up to a dissipation level of 10 μV. As *T* is reduced, both an increase in J_c and a decrease in d*V*/d*J* are observed. Within the VFF model, this d*V*/d*J* decrease may be understood in terms of a corresponding reduction in ρ_f with *T*, as $\rho_f \propto 1/B_{c2}(T)$ (equation 2.16). Further reduction in *T* results in the appearance of the multiply kinked *V-J* transition shown in figure 6.9 at 35 K. Linear segments are identified by eye and marked as (1) to (4) with increasing gradient. The IG traces were found to be smoothly curved at both 70 K and 35 K, the latter being plotted for comparison. *Smoothly* curved LAGB *V-J*s (for measured $\theta_m = 3.8 - 4.9°$) were only ever observed at large applied fields when the granular irreversibility field was exceeded (section 6.6).

The difference in behaviour between IG and GB characteristics in figure 6.9 can be explored by differentiating both curves in order to extract the gradient, d*V*/d*J*. This was performed by first smoothing the data - using a standard averaging window and polynomial fit technique - then taking a first order differentiation. The results for the 35 K grain boundary *V-J* of figure 6.9 are shown in figure 6.10, where an averaging window of 30 data points has been used (each point is smoothed by considering the 15 points on each side). An *independent* comparison was made by performing simple linear fits to the identifiably linear segments (1) to (4) of the GB data in figure 6.9. These fits are plotted as solid lines in figure 6.10.

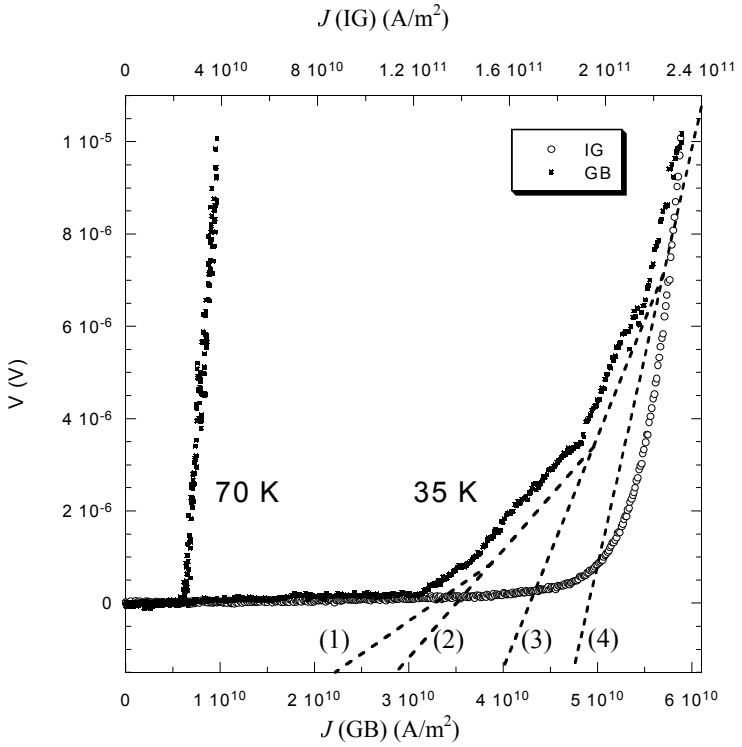

igure 6.9. Temperature dependence of LAGB *V-J* curves at 70 K and 35 K for 1 T applied field arallel to the *c*-axis for a 3.8° boundary (w = 5.5 μm). An intragranular curve at 35 K, 1 T is plotted on the upper scale for comparison (w = 9.8 μm). Linear segments (1) to (4) are identified. Sample s2.

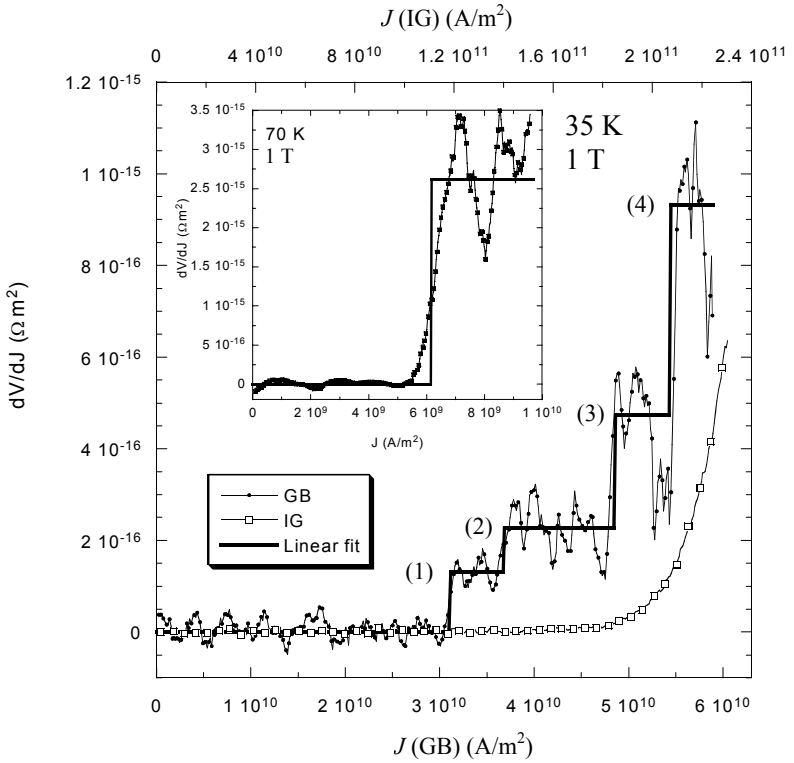

Figure 6.10. d*V*/d*J* extracted from the *V-J* plots of figure 6.9 at 35 K for the grain boundary (lower ale) and intragranular track (upper scale) using an averaging window technique. The straight lines, umbered (1) to (4), are *independent* linear fits to the segments identified as linear in the GB trace in figure 6.9. The inset shows the same analysis on a GB *V-J* at 70 K (sample s2).

Direct contrast can also be drawn to the intragranular d*V*/d*J*, also extracted using an averaging window of 30 points and plotted in figure 6.10 on the top axis. While the IG gradient is as smoothly curved as the IG *V-I* characteristic, the GB gradient displays noisy plateaus for *J* ranges corresponding to linear segments. The oscillation reflects both increased noise in the LAGB *V-J* traces and the effect of smoothing over segments of varying size with a fixed averaging window. The inset of figure 6.10 shows the same analysis performed at 70 K, 1 T, showing a single plateau that again corresponds to d*V*/d*J* of the single segment linear trace observed in figure 6.9.

V-I faceting effects were observed in three different samples (with nominally $\theta_m \sim 4°$) and numerous tracks, indicating that this is a processing independent result and indicative of an intrinsic dissipation mechanism. We interpret these findings in terms of a variation in the dissipative width (d_{eff}) defined by vortex flow at the interface.

6.4.2 Flux Flow Model

In order to explain the occurrence of kinking we use a modification of a simple coated conductor flux-channelling model [11]. The *V-I* characteristic of a coated conductor is modelled assuming a 2-D network of LAGBs and the formation of percolative vortex channels along GB segments. Assuming a constant d_{eff} (one vortex row), the constraint that ΔV across each vortex path be constant along the entire path length will necessitate a constant

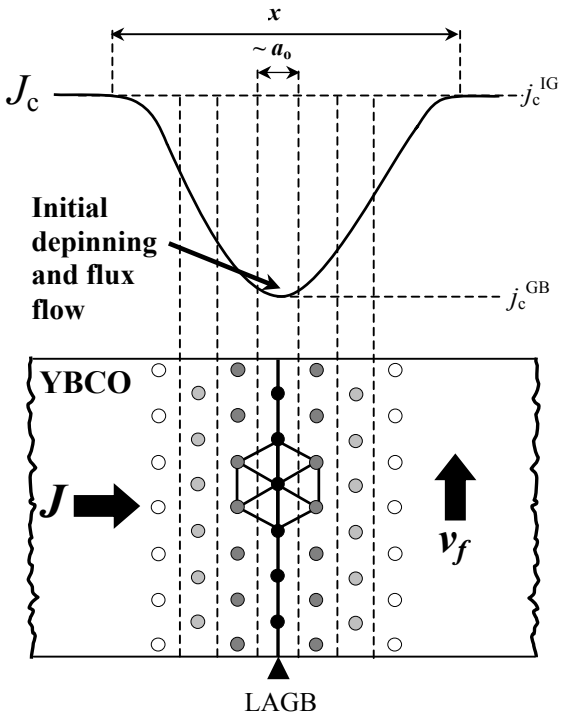

Figure 6.11. Proposed effective J_c profile across an LAGB. The number of rows channelled along the LAGB, $s(J)$, is a function of the transport current, where $d_{eff} = s(J)[3^{1/2}a_o/2]$.Vortices will be initially depinned at the LAGB (dark), with surrounding rows progressively depinning as *J* is increased (shaded lighter as row j_c increases).

LAGB *E*-field and vortex flow velocity, v_f, through the relation $\boldsymbol{E} = -\boldsymbol{v_f} \times \boldsymbol{B}$. Whereas for a granular coated conductor, a kink in the sample *V-I* is predicted to occur due to the formation of an additional vortex percolation channel, in the case of a single LAGB we can attribute kinking to a change in the number of vortex *rows* flowing at the LAGB. It is proposed that this variation in dissipative width reflects the presence of an effective J_c profile *across* the boundary (in the direction of current flow), as illustrated in figure 6.11. Such a profile will caused by the cross sectional reduction at the LAGB (section 3.5) and may be enhanced in magnitude by the GB meander and facet strain fields associated with the heterogeneous boundary (sections 5.2 and 3.4). Moving away from the LAGB, local j_c gradually increases from a minimum value ($J_c = j_c^{GB}$) within the interface to a maximum given by the IG critical current density ($J_c = j_c^{IG}$). The effects the profile will depend upon its relative width with respect to the local vortex spacing (function of *B*) and vortex size (function of *T*). Vortex dragging effects may also act to extend its influence [9].

If we assume that each vortex row flows with a linear *V-I* given by a constant flux flow resistivity, ρ_f, then the k^{th} row will become depinned at $j_c(k)$ and create an electric field $E_k = \rho_f [J - j_c(k)]$. If the width of one row is $\sqrt{3}a_o/2$, then the voltage drop across the track will be a summation of $\Delta V_k = (\sqrt{3}a_o/2)E_k$ over the total number of rows flowing, *s,* giving

$$V = \sum_{k=1}^{s} \Delta V_k = \sum_{k=1}^{s} \frac{\sqrt{3}}{2} a_o E_k = \sum_{k=1}^{s} \frac{\sqrt{3}}{2} a_o \rho_f [J - j_c(k)] \tag{6.6}$$

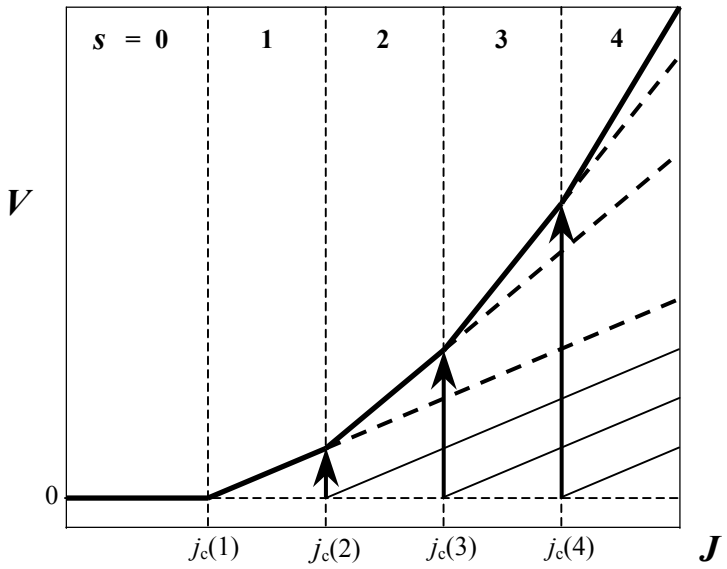

Figure 6.12. Kinked LAGB *V-J* expected for an assumed *s*(*J*). In this case *s* increases by one in regular intervals of *J*. The k^{th} vortex row starts to flow when $J = j_c(k)$, where $j_c(k) < j_c(k+1)$ and $J_c^{GB} = j_c(1)$. The track *V-J* (thick solid line) is simply a summation of individual vortex row *V-Js* (thin solid lines), a step increment in d*V*/d*J* (marked by arrows) being associated with a change in the number of rows flowing.

whence the slope of the *V-J* characteristic will become,

$$\frac{\mathrm{d}V}{\mathrm{d}J} = \gamma_{\mathrm{f}} s(J) \qquad \text{where} \qquad \gamma_{\mathrm{f}} = \frac{\sqrt{3}}{2} a_{\mathrm{o}} \rho_{\mathrm{f}} \tag{6.7}$$

This simple result predicts that the number of active vortex rows, $s = s(J)$ a function of the overall current density, will determine the gradient of the *V-J* transition as an integer multiple of γ_{f} (assumed constant for a given B and T). Thus, as illustrated in figure 6.12, a change in the number of rows flowing will result in a step increment in the track $\mathrm{d}V/\mathrm{d}J$.

This result is similar to the work of Jones *et al* [12], who showed that an inhomogeneous distribution of J_{c} along a low-T_{c} track can lead to *V-I* rounding despite a locally linear characteristic.

6.5 *V-I* Heterogeneity

Although the characteristics observed do point to a VFF mechanism it is clear that the full description is somewhat more complex. The following sections discuss the 'heterogeneous' nature of the LAGB *V-I*, and propose the possible underlying mechanisms. A full description of observed *V-I* curvature will be left until section 6.6.

6.5.1 Experimental Observation

It is found that the incremental stepping that occurs in the gradient $\mathrm{d}V/\mathrm{d}J$ is not always in *integer* steps of γ_f (see figure 6.10) - which is expected to be defined by the gradient of the first linear *V-J* section above J_{c}. In addition, steps do not always result in sequentially increasing *V-J* gradient, which *can* produce an RSJ-like shape in some transitions. The position of kinks and sections of linearity are frequently irreproducible from scan to scan and are often absent in some *V-J*s at lower temperatures, which exhibit instead a noisy erratic curvature. Such noise can be extremely pronounced and is both field and temperature dependent.

Examples of the field dependence of such transitions are shown in figure 6.13(a) for sample s2. They contain segments of linearity, but are also characterized by noise on various J scales. IG transitions are plotted in figure 6.13(b) for comparison. Note that noise only appears *above* J_c and does not appear in the IG transitions, suggesting that it is intrinsic to the LAGB and not indicative of instrumental effects. An example of the temperature dependence of *V-I* noise is shown in figure 6.14(a) for sample s2 at 1 T; as temperature increases, from 67.5 K to 82.5 K, *V-I* noise is found to decrease.

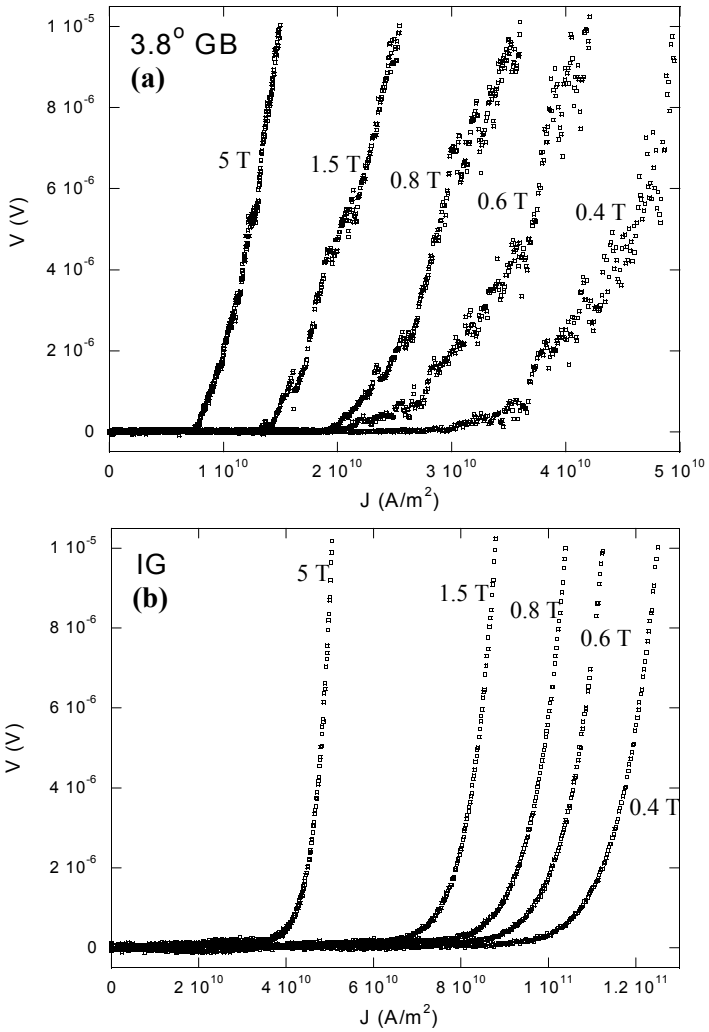

Figure 6.13. *V-J* characteristics measured for s2 (a) LAGB and (b) IG tracks at 50 K in fields of 0.4 T to 5 T. The LAGB transitions show segments of linearity and kinking, but are also characterized to various extents by degrees of noise. In contrast, the IG measurements display smoothly curved transitions at the same dissipation (voltage) levels. w = 5.5 μm (GB), 9.8μm (IG).

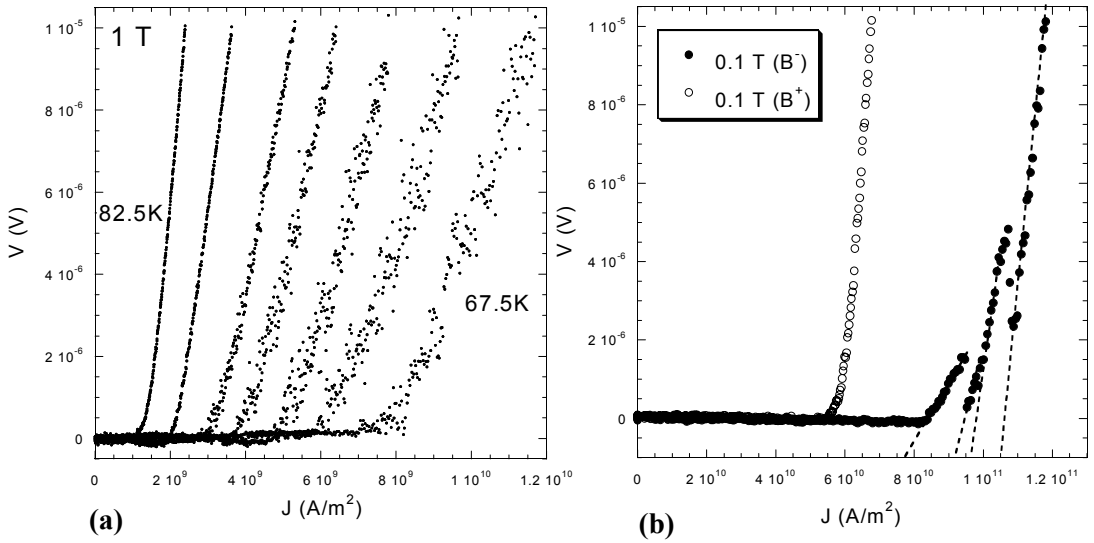

Figure 6.14. (a) *V-J* characteristics at 1 T with increasing temperature from 62.5 K to 82.5 K, in steps of 2.5 K for sample s2 (3.8°). Pronounced noise can be seen. (b) *V-J* taken at 10 K and 0.1 T for sample pk2 (4.9°) after ramping from zero field (B^+) and ramping down from 2 T (B^-). J_c hysteresis may be seen and *V-J* discontinuities at gradient kink positions for the B^- curve. Both GB tracks are w = 5.5 μm.

It can be seen in figure 6.13(a) that the *V-J* curve itself (not just d*V*/d*J*) is commonly observed to become discontinuous at kink positions. A clear example of this behaviour is shown in figure 6.14(b) for sample pk2 (4.9°) at 10 K, where linear segments have been highlighted with dashed lines. Such effects were present in all studied LAGBs, but were more noticeable in the 4.9° sample. The smooth curve in figure 6.14(b) was recorded after ZFC and ramping field up to 0.1 T (marked B^+), while the kinked curve was observed after ramping the field *down* from 2 T to 0.1 T (marked B^-). Two effects are occurring: (a) a marked hysteresis in $J_c(B)$, and (b) a marked change in *V-I* structure. Both are related to the hysteretic flux focussing that enhances or decreases the net flux at the LAGB (as measured by MO in chapter 5) depending on field ramp direction. Hysteresis in $J_c(B)$ is discussed further in section 7.1.6.

6.5.2 The Flow of Partial Vortex Rows

Faceting of the *V-I* gradient in non-integer steps of γ_f can be explained within the VFF model by relaxing the simplifying assumptions made in our treatment. In practice the LAGB is inhomogeneous on several length scales and there will be deviations in size and shape of the J_c profile along the length of the interface. Such deviations may give rise to the channelling of *partial* rows of vortices, and indeed, a simple modification to the model of section 6.4 shows that non-integer steps of γ_f would be expected for such behaviour. Appendix C contains the derivation of the expected kink in d*V*/d*J* if a second row started flowing only over a length of GB equal to w_{II} (see figure 6.15) The result is a modification of equation 6.7 to give,

$$\frac{\mathrm{d}V}{\mathrm{d}J^{\mathrm{A}}} = \gamma_f \, s'(J) \quad \text{where} \quad s'(J) = \frac{2w}{(w_I + w)} \tag{6.8}$$

where w_I is the region of single row flow and w is the track width. Whereas in equation 6.7 the gradient was an integer multiple $s(J)$ of γ_f, now the gradient may step in a non-integer multiple $s'(J)$ dependent upon the relative lengths of regions I and II. For example, for $w_I = w_{II} = w/2$, $s'(J) = 4/3$.

Another important effect that may produce irregular steps in d*V*/d*J* gradient is the expected variation in the viscous drag coefficient due to the variation in vortex core size at the LAGB [13]. At high *J*, the outer rows of vortices that flow along the GB will experience an increased viscosity and a reduced ρ_f through equation 2.15. Such an effect is likely to become increasingly pronounced as θ_m increases and the full AJ structure - lacking the normal core – develops at the GB.

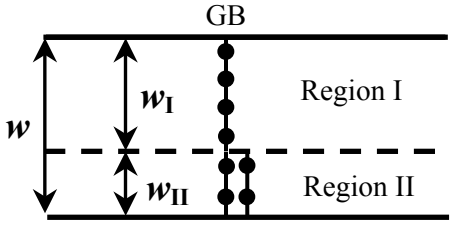

Figure 6.15. Schematic of the possible flow of a 'partial' vortex row (black dots), where $s = 2$ for region II.

6.5.3 *V-I* Noise

Possible sources of the noise presented in section 6.5.1 are summarised below. The most likely mechanism is based on flux flow, in agreement with VFF, but the contribution of heating effects and HAGB noise are also discussed for completeness.

- ***Vortex Flow***

V-I structure has also found in the characteristics of type II superconductors and interpreted in terms of the reorientations of the flowing flux lattice at certain values of driving current density [14]. It is expected that in the presence of pinning the lattice will tend to flow along its high symmetry directions, reorienting to the Fourier components of the pinning potential. Such reorientations would be expected to produce a kink or change of slope of the *V-I* characteristic, as the flux lattice will experience a slightly different pinning for each orientation. For LAGB transport, such effects may be manifest as noise; finer scale structure from processes on a local scale, and more pronounced features from larger realignments or redistributions. If the *V-I* of the LAGB is determined predominantly by flux flow, such effects would be expected to be much more obvious than the small scale effects seen by Lumley *et al* in bulk material [14]. Noise stemming from this process will depend on the rigidity of the lattice – which will be temperature dependent - and the periodicity of the pinning potential.

Within the VFF model, *V-J* discontinuities would be expected if the additional rows of vortices that started to flow affected the properties, in particular J_c and γ_f, of rows already flowing. Interaction between flowing vortex rows and the static IG vortex configuration may lead to a modified flow pattern; vortices will arrange themselves and adopt positions such as to minimise deformation energy and maintain the uniformity of B [15]. This will be a function of J due to the effective J_c profile of figure 6.11. Indeed, experiments performed by Pruymboom *et al* [15] on easy flow channels also discovered significant noise levels, attributed to the instability of the flux line lattice configuration at the channel. For instance, as shown schematically in figure 6.16, upon commencement of the flow of a second row, it is feasible that redistribution occurs, altering the J_c of both rows.

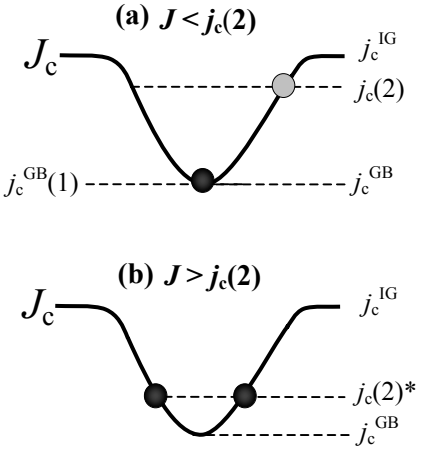

Figure 6.16. Schematic of $J_c(x)$ profiles and vortex row positions (dark = depinned) at the LAGB for (a) $J < j_c(2)$ and (b) $J > j_c(2)$. Redistribution of vortex rows occurs for $J > j_c(2)$, resulting in a reduced critical current density for both rows, $j_c(2)^*$.

Another effect that may contribute to the noise in LAGB

V-I characteristics is a characteristic instability of the vortex dynamics predicted by Larkin and Ovchinnikov [16,17]. The assumption that the vortex viscosity is independent of vortex velocity is found to break down in YBCO thin films at very high velocities. The result is a reduction of the viscosity coefficient above a certain critical vortex velocity, which in turn leads to a higher velocity. The onset of this critical velocity, v^*, produces a noticeable jump in the *V-J* characteristic. Table 6.1 gives values of v^* extracted by Xiao *et al* [17] for thin film YBCO. The vortex velocity in a LAGB can be calculated using $v_f = E/B = V/(d_{eff}B)$, where d_{eff} is the dissipative width. For an IG track, d_{eff} is equal to the track length, L. For a LAGB track we assume a width $d_{eff} \sim a_o = 50\text{nm}/B^{1/2}$. Table 6.1 shows comparative values of flux velocity for a voltage difference of 10 μV across GB and IG tracks.

Table 6.1. Values of v^* measured by Xiao *et al* [17] on thin film IG YBCO at 60 K compared to calculated flux flow velocities in a LAGB track with width of dissipation ~ a_o, and an IG track of length 170 μm.

B (T)	v^* (m/s)	v_f, LAGB (m/s)	v_f, IG (m/s)
0.1	3000	632	0.6
0.5	1500	283	0.12
1	750	200	0.06
2	300	141	0.03
4	200	100	0.15
8	-	71	0.07

Although v_f in the LAGB is some 10^3 larger than that in an IG track (as is the E-field), it is smaller than the critical velocity over all applied fields in this range. For higher fields, it appears to be about half of v^*. According to Larkin-Ovchinnikov theory however, v^* is a function of quasiparticle mean free path. As it is suggested that there exists increased quasiparticle scattering at grain boundaries [18,19] it is a possibility that some reduction in this value may occur, enabling access of the instability in LAGB transport. Caution must be taken however, as this argument depends heavily upon the number of rows flowing at the LAGB. The results of sections 6.4 and 6.7.1 suggest multiple rows flowing at the GB at lower temperatures. As such, this mechanism could only contribute to noise at higher temperature $T > \sim 60$ K

- ***Heating effects***

The effects of local joule heating due to the presence of a planar defect, such as a low angle grain boundary have been calculated by Gurevich [20]. Thermal instabilities may be triggered by flux jumping at the LAGB, creating local hot spots amplified by the high E-fields present at the interface. Heating is manifest in an upturn of the *V-J* characteristic, which was

calculated to become significant at an estimated 1-1.5 MA/cm^2 for a 7° GB. However in this work, curvature was observed in *both* the GB and IG *V-I* characteristics (samples pk2, s2, 773c) at low temperatures where J_c becomes large. This was undoubtedly due to *contact* heating mentioned in section 4.1.3.

The large *E*-fields at the LAGB and large current densities do indeed result in extremely large power densities $jE \sim 1.5 \times 10^{12}$ Wm^{-3} [4]. Calculations by Díaz *et al* [4] however suggest that due to the small dissipation volume, to a first approximation[#] the local increase in temperature at a 4° LAGB is at 60 K is only $\Delta T(60\text{ K}) \sim 8$ mK. Although small at high *T*, the effects of heating – both at the current contacts and the LAGB – will become more important at lower temperatures.

- ***HAGB noise***

Noise in the *V-I* measurements of high angle boundaries has been extensively investigated (see e.g. Hao *et al* [21]). The presence of excess noise is found to have a maximum near I_c that is usually attributed to critical current fluctuations $\delta I_c/I_c$. Another maximum is found at high bias currents and attributed to resistance fluctuations $\delta R_n/R_n$. It has been shown that the absolute magnitude of δI_c is independent of applied field [21], implying an increasing $\delta I_c/I_c$ with field. Also, $\delta I_c/I_c$ is also found to be almost independent of temperature.

For the LAGBs measured in this study, the noise levels seen in figure 6.13 show decreasing noise with increasing field, and noise is found to peak in temperature over the range 55 K to 65 K before decreasing (see figure 6.14(a)). This would appear not to match the predictions based on RSJ models assuming weak coupling reviewed by Hao *et al*. The LAGB strong coupling combined with flux flow kinks seen in the *V-I* structure suggest that such treatments are not appropriate. Focussed measurements of noise power spectral density would be needed to fully investigate noise *T* and *B* dependence.

6.6 LAGB *V-I* Curvature

As discussed in section 6.4, the LAGB characteristic is found to be a perfectly linear single segment up to voltages of 10 μV only for a field dependent range of temperature. At high temperatures, one source of LAGB *V-I* curving is due to dissipation occurring in the intragranular regions of the track. This effect can be seen in figure 6.17, showing the boundary and intragranular *V-J* characteristics for sample s2 at 80 K as field is increased from 2.5 T to 5.8 T. Due to the larger IG track length, the IG *V-J* characteristics have been scaled to

[#] Assuming heat transfer limited by the thermal conductivity of the $SrTiO_3$ substrate, $\kappa(\text{STO}) \sim 10$ Wm^{-1}K^{-1}

the length of the GB track, by multiplying V by a factor $1/Q = L_{GB}/L_{IG}$. This is as described in section 4.2.5, but instead of scaling up the voltage criterion, we simply scale down the *V-J*.

For low fields, $J_c^{GB} < J_c^{IG}$ and the LAGB *V-J* is linear. As field is increased, the intragranular J_c^{IG} decreases more strongly with field, resulting in a degree of dissipation in the grains of the GB track and causing curvature of the GB *V-J*. By 5.8 T, both grain boundary and intragranular *V-J*s overlap; dissipation is now dominated by the response of the grains of the GB track. This effect can be clearly seen in a plot of *V-J* gradient with increasing field, plotted on the right hand scale of figure 6.18 for 80 K. Also plotted is J_c of the LAGB and IG tracks. Again, comparative values of GB and IG J_c and dV/dJ were obtained by simple scaling to the GB track length, where in this case $V_c^{IG} = QV_c^{GB} = 5.4V_c^{GB} = 5.4$ μV (section 4.2.5).

Above a certain field named *B**, or the merging field, both $J_c(B)$ and dV/dJ merge as *V-J* characteristics map onto each other and $J_c^{GB} = J_c^{IG}$. The nature of the field *B** (which is linked but not equal to B_{irr}^{IG}) and $J_c(B)$ will be investigated in more depth in chapter 7. The fact that measurement of J_c^{GB} is limited by J_c^{IG} at *B** is evidence that the mechanism behind this *V-I* curvature may be distinguished from the increasing dissipative width predicted by additional rows flowing in the VFF model. The latter are observed at low temperature, well below *B**

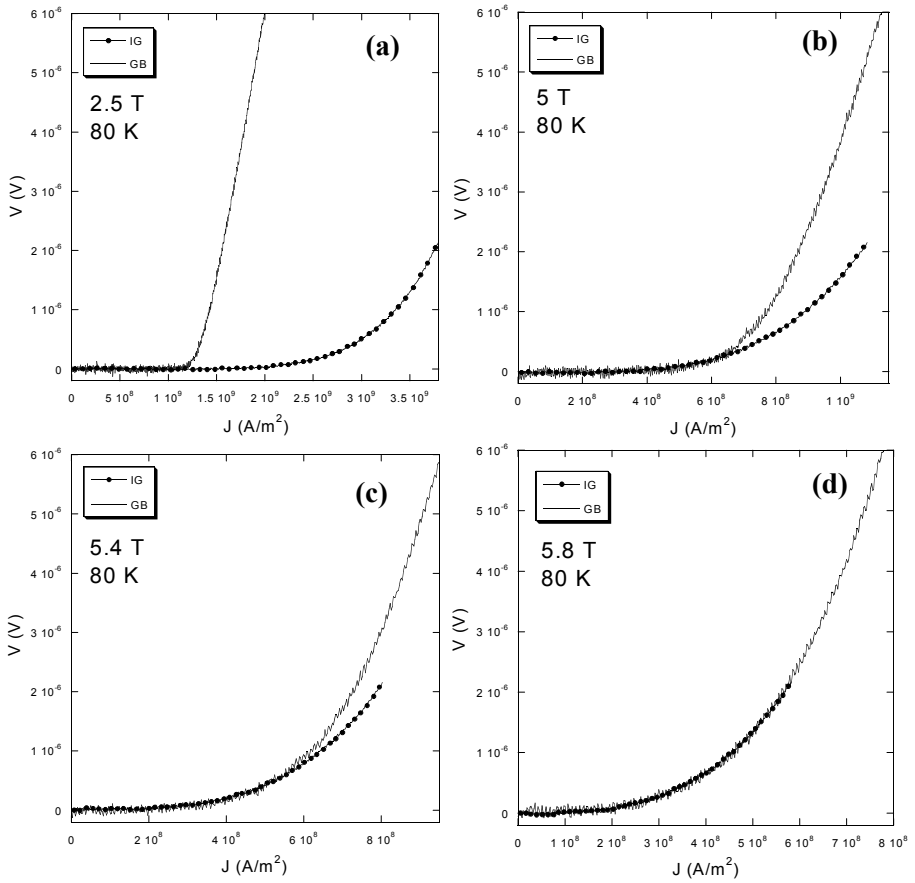

Figure 6.17. GB and IG track *V-J* characteristics for sample s2 (3.8°) at 80 K for increasing fields from 2.5 T to 5.8 T. As B_{irr}^{IG} is approached and crossed in the grains, J_c^{IG} is reduced more rapidly with field than J_c^{GB}. The result is a merging of *V-J*s as the IG sections of the GB track dominate dissipation. (IG track has been scaled to GB track size – see text).

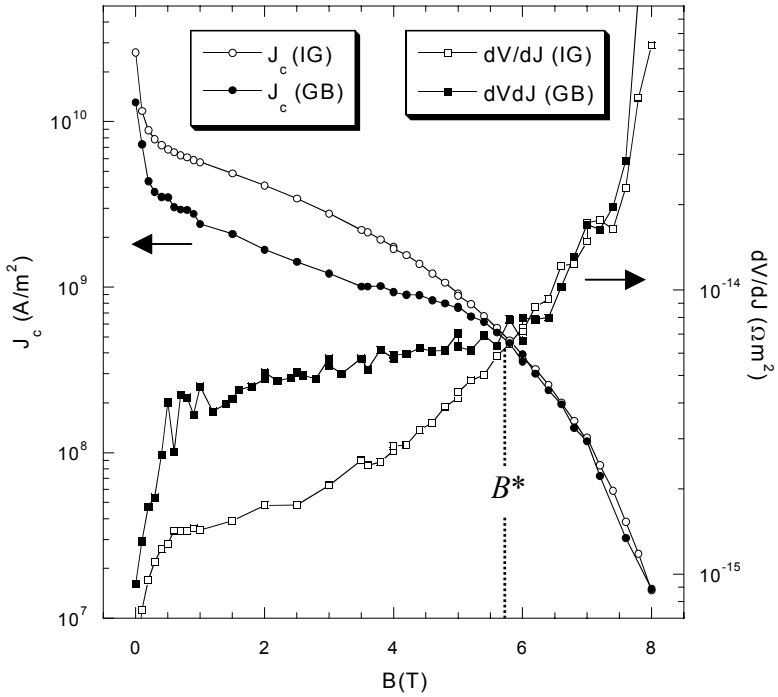

Figure 6.18. Left hand scale shows J_c^{GB} and J_c^{IG} with field measured on a 3.8° LAGB sample s2. Plotted on the right hand scale is *V-J* gradient ($V_c^{IG} = QV_c^{GB} = 5.4V_c^{GB} = 5.4$ μV).

and B_{irr}^{IG}. This high field, high temperature curvature is clearly due to the effect of exceeding the irreversibility line in the grains. The IG dissipation that ensues appears across the whole track length, not vortex row by row at the GB. This is an important finding, as previously the upturn of d*V*/d*J* observed at *B** for the LAGB characteristics had been associated with an increase from one to two rows flowing along the interface (section 6.3.2) [9].

Curvature can also occur to an extent at lower temperature. For example, at 1 T the single linear curve is observed over the range 60 – 80 K in 3.8° sample s2. For lower temperatures kinked *V-I*s such as presented in section 6.4.1 and figure 6.9 can develop. Some *V-I*s however

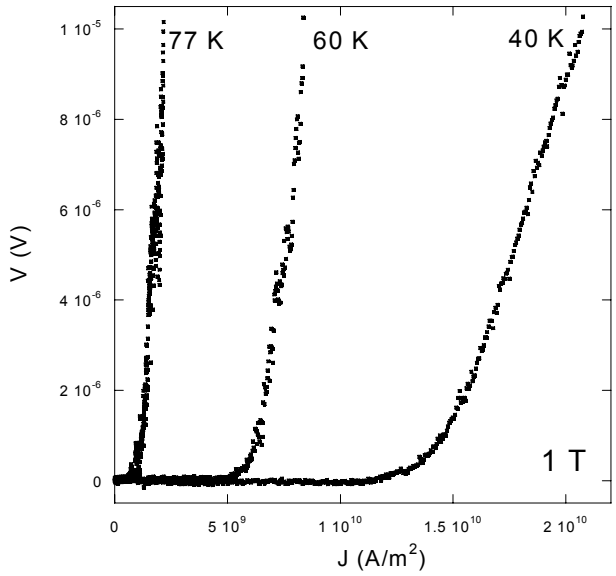

Figure 6.19. *V-J* curves at 1 T for sample pk2 (4.9°) at various indicated temperatures. Characteristics display a degree of low voltage curvature.

display a low voltage curvature prior to linearity that is reminiscent of the transition from flux creep to VFF (figure 2.6). An example is shown in figure 6.19, showing *V-J* curves for 4.9° pk2 at 1 T for 77, 60 and 40 K. As temperature decreases, the low voltage curvature increases in magnitude. Such curvature could be due to a delocalisation of dissipation with decreasing temperature more rows flowing (see section 6.7) resulting in a decreased *E*-field and hence an increased level of flux creep. Figure 6.20 shows the 40 K LAGB transition and comparative IG transition. Despite the low voltage curvature of the LAGB characteristic, at higher voltages the linearity is regained, in contrast to the curved IG transition. Also shown on figure 6.20 are the results of a fit to the Anderson-Kim flux creep model, $V = J\rho_o L\exp[-U/k_B T]$, where k_B is the Boltzman constant, ρ_o an effective flux flow resistivity, L the width of dissipation, and $U(J,B,T) = U_{AK}(1-J/J_c)^n$ the pinning energy barrier [22]. A good fit was made initially to the IG curve, obtaining $\rho_o L$ = 1.848 × 10-16 Ω m^2, n = 1.5, $J_c = 1.55 \times 10^{11}$ A/m^2 and $U/K_B T$ = 35. The same values of $\rho_o L$ and n were obtained when fitting to the curved region of the GB *V-J* but different values of $U/K_B T$ = 24 and $J_c = 1.65 \times 10^{10}$ A/m^2. No fit to the higher voltage (above the dashed line) linear region of the LAGB characteristic was possible. By increasing $U/K_B T$ (to 30) and decreasing J_c (to 1.4×10^{10}) fits to progressively lower *J* regions of the curve were possible. Within this analysis, the reduced value of the pinning potential found for the GB fit could simply be indicative of the channelling nature of the nature of the GB for field aligned with the defect plane (see chapters 8 and 9).

Another source of the curvature in figure 6.20 could be the flow of partial rows along the GB

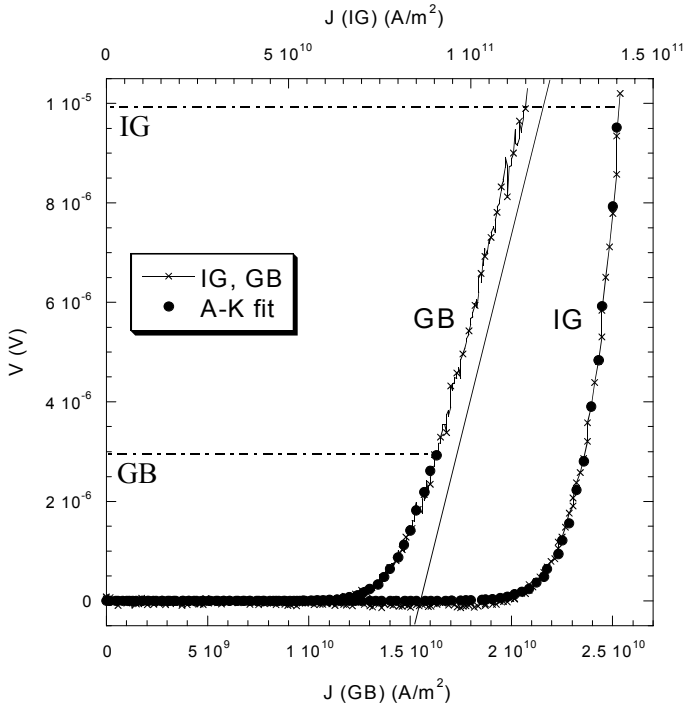

Figure 6.20. *V-J* curves for 4.9° GB (bottom scale) and IG (top scale) at 40 K, 1 T for sample pk2 (marked as crosses). Fits were possible to the Anderson-Kim flux creep model (filled circles) up to the indicated dashed lines (see text).

due to an inhomogeneous LAGB J_c profile. As investigated in section 6.5.2, non-integer steps of γ_f are to be expected from such an effect. Multiple, fine scale kinking could therefore produce curvature. For example, the region of curvature in figure 6.20 at 40 K spans $\sim 5 \times 10^9$ A/m^2 before linearity is obtained. At 1 T, the track width contains $w/a_o \sim 100$ vortices for a track width of $w = 5.5$ μm and vortex spacing $a_o(1\text{ T}) = 50$ nm. If one partial row of vortices were to grow in length, w_{II}, by a single vortex per 5×10^8 A/m^2, this represents 100 possible kinks in the *V-I* transition over the 5×10^9 A/m^2 current range, which would be visible as curvature. In the scope of the VFF model, the additional flow of a whole single row of vortices may only double the gradient, so the curvature at 40 K would need many more rows to flow – which will increase the figure from 100.

To conclude, the LAGB *V-I* curvature *can* be linked to an increase in the dissipative width at the LAGB. This is either directly due to the increase in the number of rows flowing at the GB through the VFF model (section 6.4.2 and 6.5.2) or through a reintroduction of creep as *E*-fields correspondingly decrease. As *V-I* linearity *is* visible at low temperature (figure 6.9), the dominant cause is likely to be the former.

6.7 Flux Flow with Applied Magnetic Field

As shown previously in figure 6.18, above the merging field *B**, d*V*/d*J* of the LAGB simply becomes that measured to exist in the intragranular regions of the track. For fields *below B**, d*V*/d*J* for the LAGB is found to (a) be much larger than the IG material, and (b) to display a

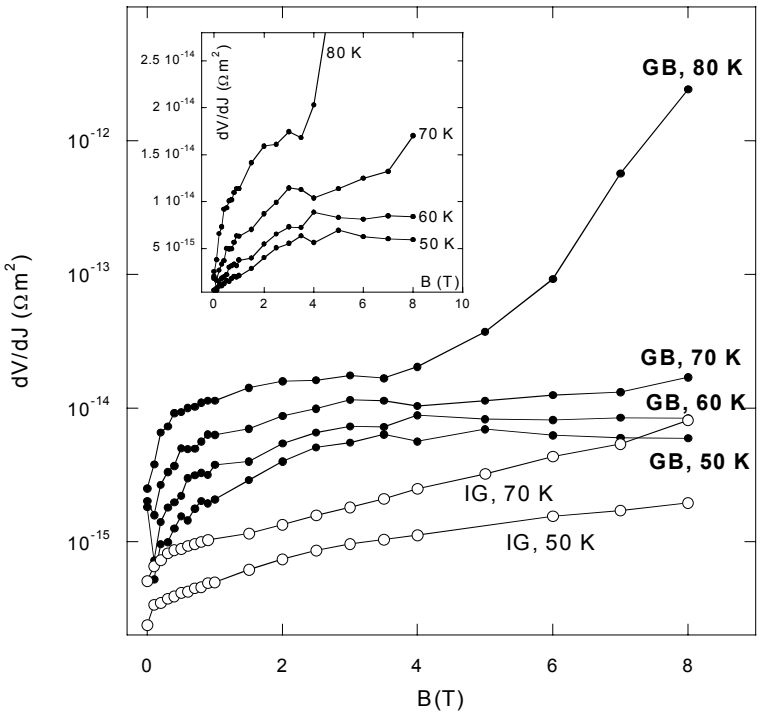

Figure 6.21. d*V*/d*J*(*B*) for GB and IG tacks of sample pk2 as a function of applied field for 50 – 80 K (extracted at 5μV (GB) and 12μV (IG) – see text). Inset shows the GB d*V*/d*J* on linear plot.

different field dependence – this is consistent with one being determined by ρ_f and the other by flux creep. The temperature dependence of this result is shown in figure 6.21. The figure gives plots of $dV/dJ(B)$ for the GB and IG extracted for sample pk2 at temperatures of 50 K to 80 K. Comparative voltage criteria were used (here $V_c^{IG} = 2.4V_c^{GB} = 12$ μV and $V_c^{GB} = 5$ μV) with an averaging window of 150 points. The relatively large window size and high criterion voltage were necessary to smooth over the large degree of featuring and *V-I* noise.

The difference in behaviour between GB and IG becomes more apparent at lower temperatures, where the GB curve can be seen to level off at higher fields when compared to the IG. The following sections examine the expected GB dV/dJ field dependence in more detail, in terms of both VFF and the non-viscous model of Gurevich *et al* [9].

6.7.1 Flux Flow Resistivity

In order to extract a value of ρ_f from dV/dJ data, it is necessary to transform voltage to electric field by assuming a dissipative width at the LAGB over which the potential difference occurs. There are two approaches one may take in order to calculate a value of ρ_f from the measured LAGB *V-J* characteristics. The first is to identify linear segments in the *V-J* curves and assume they represent the viscous flow of a certain number of rows. In the VFF model, the lowest possible *V-J* gradient will be defined by ρ_f, provided flux creep can be neglected.

The main problem with this approach is that the precise number of rows flowing at the LAGB is *unknown*, and the lowest gradient linear segment need not represent dissipation due to the motion of a single line of vortices, $s = 1$. It is likely that s will vary with field and temperature as the effective J_c profile is defined by j_c^{GB} and j_c^{IG}, both of which possess different temperature dependences. In addition, the effects of vortex interaction resulting in the dragging of additional rows of vortices along the GB will also be B and T dependent [9]. The fact that LAGB *V-I* characteristics frequently display noisy erratic featuring also renders routine identification of linear segments problematic.

An easier, and much more illuminating method is to extract an average gradient at a certain fixed voltage criterion and assume a single vortex row, $s = 1$. In this manner, $dV/dJ(B)$ is transformed to $dE/dJ(B)$ by dividing by a *field dependent* width $d_{eff} \sim a_o$. Figure 6.22 shows dE/dJ extracted in such a manner from the data of figure 6.21. Errors associated with the extraction of the gradient from the *V-I* are estimated as up to 15 %. As can be seen, for fields up to 3 T a reasonably *linear* dependence of dE/dJ on field is seen. This is consistent with dE/dJ equalling the flux flow resistivity and obeying the linear dependence predicted by the Bardeen Stephen equation, where $\rho_f(T)/\rho_n(T) = B/B_{c2}(T)$. At higher fields, however, this linearity does break down, as is shown in the inset. It should be noted that the values of ρ_f

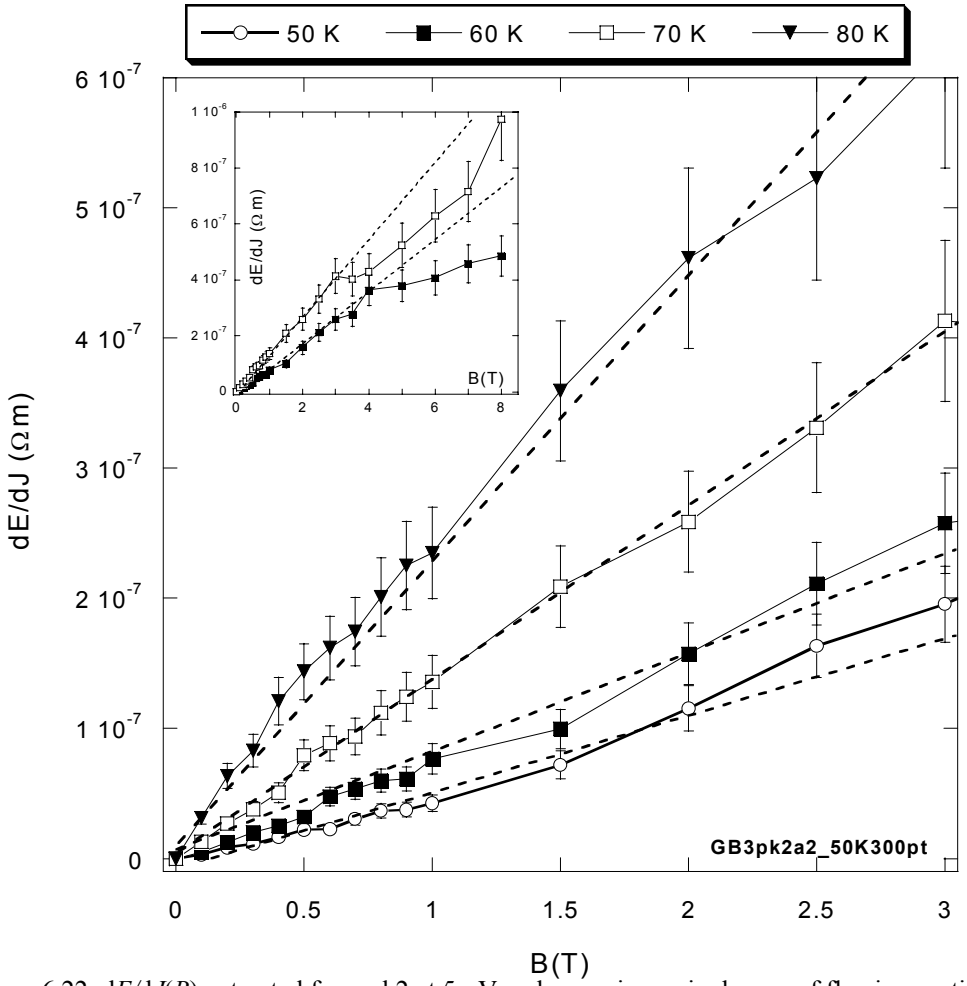

Figure 6.22. d*E*/d*J*(*B*) extracted from pk2 at 5 μV and assuming a single row of flowing vortices, $s = 1$, with a width $d_{eff} = a_o$. Dashed lines show linear fits to the data, predicted by the Bardeen Stephen equation (equation 2.16). Inset shows 60 and 70 K data up to 8 T, where the linear fit breaks down.

extracted here for this 4.9° LAGB (pk2) are approximately an order of magnitude larger than those calculated by Díaz *et al* [4] for a 4° LAGB. One reason is that Díaz *et al* scaled *J* to the reduced cross section at the LAGB, not to the track width as here. This increased their calculated ρ_f by a factor of $1/\delta_c = 4.3$. If this step *is* required, the measurements of chapter 8 suggest that it should actually only result in a factor of $1/\delta_c \sim 1/(0.8) = 1.3$ (section 8.4).

From figure 6.22, we can extract a value of $d\rho_f / dB$, which may be used in the Bardeen Stephen equation as,

$$\frac{d\rho_f}{dB} = \frac{\rho_n(T)}{B_{c2}(T)} \tag{6.9}$$

Although Díaz *et al* used this form to calculate a value of B_{c2} in order to validate the use of $s = 1$[#], it is perhaps more useful to use values of B_{c2} to estimate the expected value of $d\rho_f/dB$

[#] They did get a good estimate of B_{c2}, but the use of an incorrect value of δ_c (out by a factor of 3) suggests this may have been coincidental.

from Bardeen Stephen. This is informative as the observation of *V-J* kinking suggest that $s \neq 1$, at least for a certain range of T and B. The following method was used to estimate the true number of vortex rows flowing. From the slope of the normal state resistivity, measured for sample pk2 to be $d\rho_n/dT = 1.08 \times 10^{-8}$ ΩmK^{-1}, a value of $\rho_n(T)$ may be calculated for $T = 50$ to 80 K. $B_{c2}(T)$ can be estimated by using the experimentally measured result that B_{c2} varies as $(dB_{c2}/dT)(T_c - T)$ where $dB_{c2}/dT = -2$ T/K [23] and $T_c = 89.5$ K. By inputting the values of $B_{c2}(T)$ and $\rho_n(T)$ into equation 6.9 an *expected value* of $d\rho_f/dB$ may be calculated. In accordance with equation 6.4, the ratio of measured over expected $d\rho_f/dB$ will result in a value for the number of rows flowing at the GB*. The results are given in table 6.2, and show that the number of rows flowing at the 5 μV criterion is (a) *more* than one (for 50 K – 80 K), and (b) increases as temperature decreases. This is consistent with the fact that for lower temperature characteristics the multiply kinked structure (see section 6.4) implies the flow of numerous vortex rows, not one. Furthermore, the development of the kinked structure and shorter segment lengths as temperature decreases is consistent with the *increase* in *s* at a given voltage criterion.

Table 6.2. Extraction of the number of rows, *s*, flowing at the LAGB (sample pk2, 4.9°) through application of the Bardeen Stephen equation 6.9. See text for method of calculation of upper critical field, B_{c2}, normal state resisitivity ρ_n and $d\rho_f/dB$ (expected). $d\rho_f/dB$ (measured) was taken from figure 6.22.

T (K)	B_{c2} (T)	ρ_n (μΩm)	$d\rho_f/dB$ (ΩmT^{-1}) (Expected)	$d\rho_f/dB$ (ΩmT^{-1}) (Measured)	*s* Vortex rows
80	19	0.864	4.5×10^{-8}	6.6×10^{-8}	1.4
70	39	0.756	1.9×10^{-8}	8.5×10^{-8}	4.4
60	59	0.648	1.1×10^{-8}	1.3×10^{-7}	12.2
50	79	0.540	6.8×10^{-9}	2.0×10^{-7}	30.0

It should be noted that the linearity, $dE/dJ \propto B$, observed in figure 6.22 is due to the fact that a field dependent dissipative width has been used, $d_{eff} \sim a_o(B) = (50nm)B^{-1/2}$, to transform, dV/dJ to dE/dJ. This results in a decrease of the width with increasing field and suggests that $dV/dJ \propto (dE/dJ)a_o \propto B^{1/2}$. This can be seen in the GB data of figure 6.21. If a fixed, field independent width were to be used, a $dE/dJ \propto B^{1/2}$ dependence would be found instead. However, the fact that the linear $dE/dJ \propto B$ *is* observed in figure 6.22 can be taken as evidence for the appropriateness of taking a field dependent d_{eff}.

* The expected ρ_f (and $d\rho_f/dB$) corresponds to a single row of vortices, $s = 1$. More rows flowing will increase our calculated value of ρ_f (and $d\rho_f/dB$) from the actual value by a factor *s*.

6.7.2 Non-Viscous Channelling

In order to investigate the applicability of the model proposed by Gurevich *et al* [9] (see section 6.3.2), fits were made of the data in figure 6.21 to equation 6.5. The results can be seen in figure 6.23 which plots d*V*/d*I* with field at 70 K with the fitted curve, $R_G(B)$. Also plotted is a simple $B^{1/2}$ fit, which as just discussed is consistent with the VFF Bardeen Stephen model for d*V*/d*I*.

The model predicts that AJ vortices, which lack normal cores, overlap at a field H_o, resulting in a flattening out of the d*V*/d*I*(*B*) curve. Qualitatively, this flattening can be seen in figure 6.23 at higher fields $B \sim> 3$ T, as the $B^{1/2}$ fit becomes less appropriate. At 70 K, R_G appears to fit well at both high and low field. At lower temperatures however the errors in the extracted values of *R* and H_o increased as the fit became less appropriate. The extracted values of *R* and H_o are given in figure 6.24. In disagreement with the result that HAGB boundary normal resistance varies only weakly with temperature [24] the results here suggest a strong decrease with decreasing *T*.

The fact that J_c^{GB} is finite above the core overlap field H_o was taken by Gurevich *et al* as proof that the AJ vortices possesses no normal core. The values H_o extracted from sample pk2 are significantly larger than those extracted by Gurevich for a 7° GB, who found only $H_o(70\text{ K}) = 2$ T and $H_o(80\text{ K}) = 0.2$ T compared to 4.7 T and 3.8 T for this sample

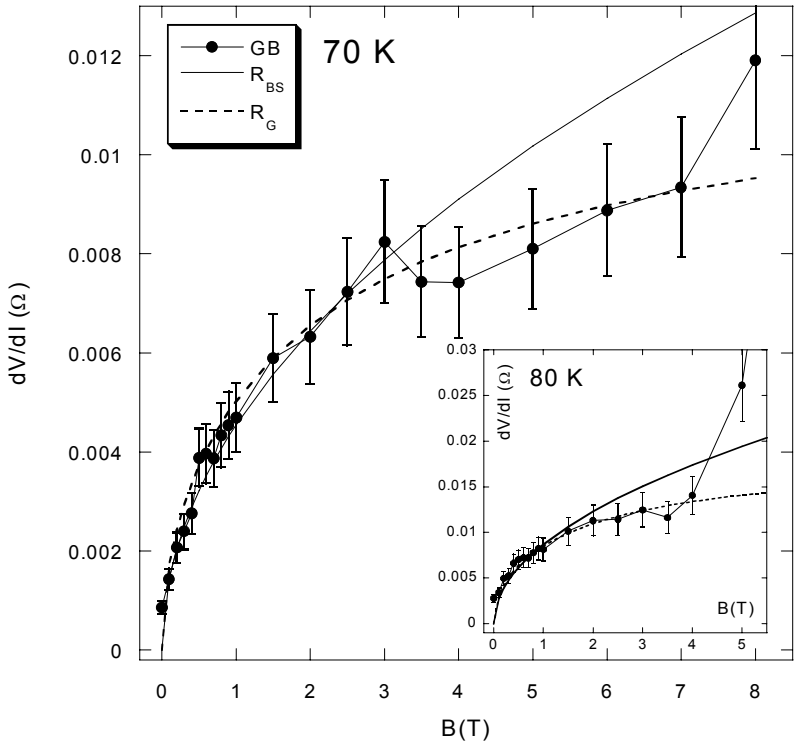

Figure 6.23. d*V*/d*I*(*B*) for sample pk2 as a function of applied field at 70 K. Fits to equation 6.5 and to a $B^{1/2}$ dependence are shown as dashed and full lines respectively. Inset shows the same fits performed at 80 K.

respectively. This is consistent with the fact that H_o is inversely dependent upon core length (equation 6.5) – a larger H_o could therefore be indicative of the smaller angle of the 4.9° sample pk2 compared to a 7° GB.

The main failing of the Gurevich *et al* model is that it incorrectly predicts the increase in the GB *V-J* gradient seen at *B** (figure 6.18) with the transition from s = 1 to s = 2. In fact, as discussed in section 6.6, the upturn is due to the irreversibility line and the kinked characteristics found in this work are only seen at lower temperatures.

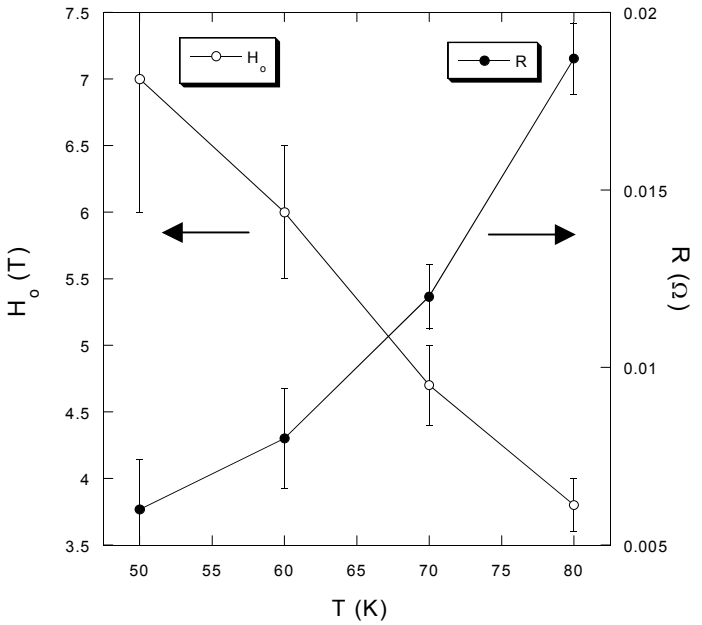

Figure 6.24. Fit parameters, H_o and R extracted from the dV/dJ curves in figure 6.21 using equation 6.5.

6.8 Summary

This chapter has investigated the *V-I* characteristics of low angle grain boundaries, which are found to be influenced by flux flow along the interface for fields applied parallel to the *c*-axis (and GB defect plane). Although fits to the Gurevich *et al* [9] model were possible, stronger evidence is found for a presented *viscous* flux flow mechanism whereby changes in the numbers of rows flowing at the GB are manifest as kinks in the *V-J*. The development of this kinked structure at lower *T* has been correlated well with a calculated increase in the average number of rows flowing within the VFF model. At high fields and temperatures, curvature is introduced through the irreversibility line in the grains. This is incorrectly identified in the Gurevich *et al* [9] analysis as the switch to *s* = 2. At lower fields and temperatures, curvature may be introduced by multiple kinking within the VFF model, or through a reintroduction of creep effects due to a reduction in the electric field with each new row flowing.

As will be seen in chapters 8 and 9, the linearity of the *V-I* characteristic also correlate well with evidence of a channelling minimum in the angular $J_c^{GB}(\theta,\phi)$ data.

6.9 References

[1] H. Hilgenkamp and J. Mannhart, *Rev. Mod. Phys*. (in press)

[2] R.D. Redwing, B.M. Hinaus, M.S. Rzchowski, N.F. Heinig, B.A. Davidson and J.E. Nordman, *Appl. Phys. Lett*. **75**, 3171 (1999)

[3] D. Verebelyi, C. Prouteau, R. Feenstra and D. Christen, *IEEE Trans. Appl. Super*. **9**, 2655 (1999)

[4] A. Díaz, L. Méchin, P. Berghuis, and J. E. Evetts, *Phys. Rev. B* **58**, R2960 (1998)

[5] D.T. Verebelyi, D.K. Christen, R. Feenstra, C. Cantoni, A. Goyal, D.F. Lee, M. Paranthaman, P.N. Arendt, R.F. DePaula, J.R. Groves and C.Prouteau, *Appl. Phys. Lett*. **76**, 1755 (2000)

[6] N.F. Heinig, PhD Dissertation, University of Wisconsin-Madison (1999)

[7] G.A. Daniels, A. Gurevich and D.C. Larbalestier, *Appl. Phys. Lett.* **77**, 3251 (2000)

[8] A. Pruymboom, P.H. Kes, E. van der Drift and S. Radelaar, *Phys. Rev. Lett* **60**, 1430 (1988)

[9] A. Gurevich, M.S. Rzchowski, G. Daniels, S. Patnaik, B.M. Hinaus, F. Carllo, F. Tafuri and D.C. Larbalestier, *Phys. Rev. Lett.* **88**, 97001 (2002)

[10] H. Xin, D.E. Oates, G. Dresselhaus and M.S. Dresselhaus, *J. Supercond*. **14**, 637 (2001)

[11] J. E. Evetts, M. J. Hogg, B. A. Glowacki, N. A. Rutter, and V. N. Tsaneva, Supercond. Sci. Technol. **12**, 1050 (1999).

[12] R.G. Jones, E.H. Rhoderick and A.C. Rose-Innes, *Phys. Lett. A* **24,** 318 (1967)

[13] A. Gurevich, *Phys. Rev. B* **46**, 3187 (1992)

[14] J.M. Lumley, J.E. Evetts and C.H. Chao, *Le Journal De Physique Letters* **39**, L-393 (1978)

[15] A. Pruymboom, P.H. Kes, E. van der Drift and S. Radelaar, *Phys. Rev. Lett.* **60**, 1430 (1988)

[16] A.I. Larkin and Yu.N. Ovchinnikov, *Sov. Phys. JETP* **41**, 960 (1976)

[17] Z.L. Xiao and P. Ziemann, *Phys. Rev. B* **53**, 15265 (1996)

[18] D. Dimos, P.Chaudhari, and J. Mannhart, *Phys. Rev. B* **41**, 4038 (1990)

[19] A. Gurevich and E.A. Pashitskii, *Phys. Rev. B* **57**, 13 873 (1998)

[20] A. Gurevich, *Appl. Phys. Lett.* **78**, 1891 (2001)

[21] L. Hao, J.C. Macfarlane and C.M. Pegrum, *Supercond. Sci. Technol.* **9**, 678 (1996)

[22] P. Berghuis, R. Herzog, R.E. Somekh, J.E. Evetts, R.A. Doyle, F. Baudenbacher and A.M. Campbell, *Physica C* **256**, 13 (1996)

[23] M. Kuncher, D.K. Christen and J.M. Philips, *Phys. Rev. Lett*. **70**, 998 (1993)

[24] R. Gross, P. Chaudhari, M. Kawasaki and A. Gupta, *Phys. Rev. B* **42**, 10735

7 LAGB $J_c(B,T)$ Measurements

This chapter examines the dependence of $J_c^{GB}(B,T)$ and $J_c^{IG}(B,T)$ for field applied at a fixed angle θ to the sample *c*-axis ('static' scans). In particular, measurement of the transparency $\delta(B,T) = J_c^{GB}/J_c^{IG}$ is used to reveal the relative behaviour of the LAGB with respect to the intragranular material. It is found that the LAGB is effectively transparent to current transport above a temperature, sample and angle dependent merging field, B^*. Above B^*, transport is dominated by dissipation in the grains of the LAGB track as the grain irreversibility line is crossed. In addition, a pronounced hysteresis in $J_c^{GB}(B)$ is measured on a LAGB for the first time. This is linked to the hysteretic flux focussing discussed in chapter 5 and the angular hysteresis to be presented in chapter 9.

7.1 $J_c(B)$: Field Dependence

7.1.1 Previous Measurements

There is now a large body of work focussing on the zero-field impediment to current flow, the ratio $\delta = J_c^{GB}/J_c^{IG}$, with misorientation angle θ_m. There have been relatively few reports however, of $J_c^{GB}(B)$, $J_c^{GB}(T)$ and $\delta(T,B)$ for low angle grain boundaries. The main findings have been published by Heinig *et al* [1] and Verebelyi *et al* [2]. Figure 7.1 shows the $J_c(B)$ measurements of GBs of [001]-tilt angle varying from 2° to 24° at 77 K for applied field parallel to ***c***. As can be seen, the key characteristics of HAGB $J_c(B)$ are low J_c^{GB} values and a sharp drop off of J_c^{GB} with small applied field. Lower angle boundaries display a similar decrease with field, but much higher values of J_c^{GB} (three orders of magnitude). At higher fields, both LAGB and HAGB display a relatively field insensitive plateau in J_c^{GB} when compared to J_c^{IG}. For HAGBs this 'residual supercurrent' has been attributed to structural disorder at the boundary creating a pinhole effect [3] - areas of

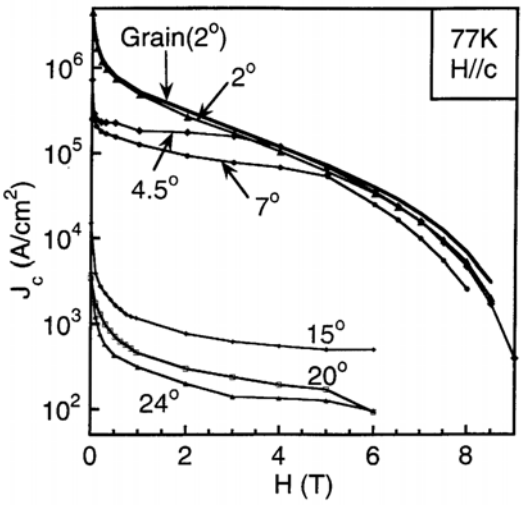

Figure 7.1. Field dependence observed by Verebelyi *et al* of [001]-tilt thin film GBs with θ_m = 2° to 24° [2].

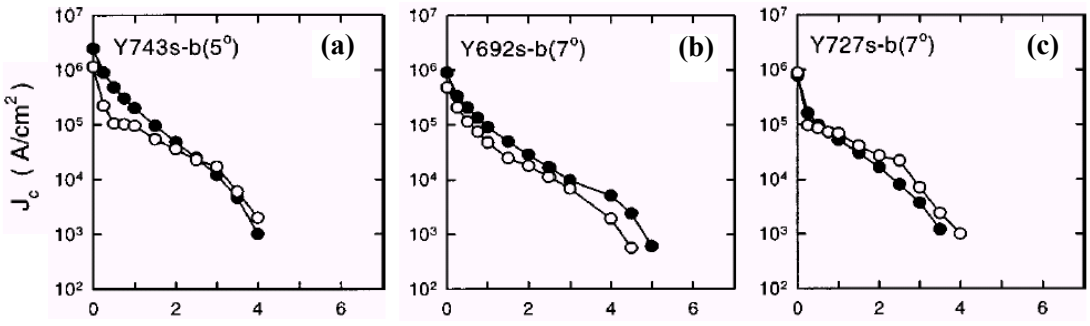

Figure 7.2. $J_c^{GB}(B)$ (open circles) and $J_c^{IG}(B)$ (filled circles) as measured by Heinig *et al* on (a) 5°, (b) 7° and a second (c) 7° thin film [001]-tilt YBCO GBs [1].

strongly coupled GB *remain* strongly coupled at higher fields, yielding a small yet finite J_c^{GB}.

Direct comparison of J_c^{GB} to the response of the film it resides in is an important procedure - a grain boundary can only be as good as the film within which it is located, and its properties must be compared to the properties of the neighbouring IG film. For the 2° sample in figure 7.1, both J_c^{GB} and its field dependence can be seen to be equivalent to that observed in the IG region, implying that it constitutes no impediment to current flow at all. For the 4° and 7.5° samples, $J_c^{GB}(B)$ can be seen to converge with, and follow $J_c^{IG}(B)$ at a field that appears to be misorientation dependent. This effect is investigated more thoroughly in section 7.1.2, and is also seen for the first time in the angular measurements presented in chapter 9.

Heinig *et al* [1] also performed measurements of $J_c^{GB}(B)$, and compared directly to the IG response of the film (figure 7.2). They found a similar dependence to that observed by Verebelyi *et al* for 5° and other higher angle GBs, but also found variability in behaviour. Two 7° GBs were measured (figure 7.2(b) and (c)), one showing a similar behaviour to the IG material, the other an apparent cross over of J_c^{GB} and J_c^{IG} at higher fields - J_c^{GB} becomes *greater* than J_c^{IG}. This behaviour could be explained by experimental errors in the determination track size, which influences the calculation of J_c from I_c. It is perhaps more likely to be indicative of variability, both along the GB and across the film, introduced by the heterogeneity discussed in sections 3.4 and 5.2.

Although J_c^{GB} is usually observed to decrease monotonically with increasing field, Cai *et al* [3] have observed a pronounced increase for certain fields when measuring 15° [001]-tilt bulk scale boundaries (figure 7.3). The peaks are attributed to a vortex

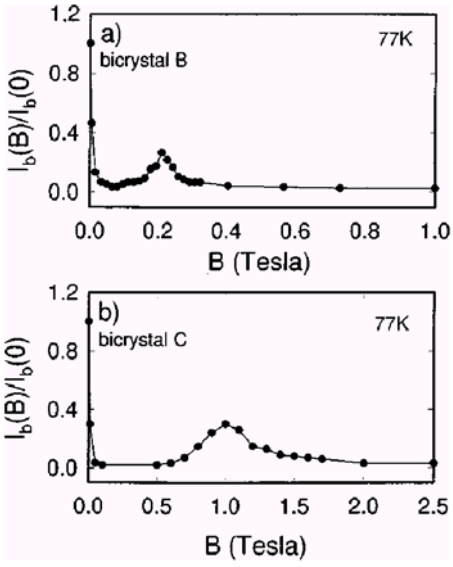

Figure 7.3. Normalised I_c^{GB} with field for a bulk scale 15° GBs [3].

matching effect, and correspond to fields for which a_o is commensurate with the wavelength of a periodic facet structure they observed by TEM. The facet strain fields possessed wavelengths of 80 nm and 35 nm, corresponding approximately to the matching fields of 0.2 T and 1 T respectively. The enhancement is direct evidence that faceting, and GB heterogeneity in general, can strongly modulate J_c^{GB}.

The initial sharp drop-off in J_c^{GB} with field has been attributed to the destruction of weakly linked regions of GB for high angle boundaries. A similar mechanism may operate in the LAGB dependence. The $J_c^{GB}(B)$ dependence has been described alternately as exponential [1] and power-law [2]. The power law dependence $J_c^{GB}(B) \propto B^{-1/2}$, has been predicted by several models. For HAGBs, Fistul and Giuliani [4] predict the $B^{-1/2}$ for a Josephson junction in a model whereby the flux lattice in the grains dephases the order parameter near the GB. This has been applied by Verebelyi *et al* [2], although they found exponents of 0.15 and 0.63 for 4.5° and 24° GBs respectively.

Díaz *et al* [5] also discovered an approximate $J_c^{GB} \propto B^{-1/2}$ dependence for a 4° LAGB - they found that the pinning force density, $F_p = J_c B$, possessed a $F_p \propto B^{1/2}$ dependence. This was attributed to pinning of a single line of vortices to the dislocation array at the LAGB. For fields below the matching field for the dislocations (~ 70 T for a 4° LAGB [5]) the approximation can be made that the pinning force per unit length of each vortex, $f_p(B) \approx f_p$, where $F_p = J_c B = n(B) f_p$ and $n(B)$ is the vortex density. They argued that for a single line of vortices it is the linear vortex density, $n_l(B) \propto B^{0.5}$ that determines the pinning force, giving the observed $F_p = n_l(B) f_p \propto B^{0.5}$.

Both power law J_c^{GB} predictions are undermined to an extent by the observation of the *same* dependence in IG films, $J_c^{IG}(B) \propto B^{-1/2}$ [6,7]. This has been predicted for strong pinning to extended pinning centres present in the IG film parallel to the flux lines [6]. This underlines the importance of sample variability and the need to directly compare GB and IG behaviour in the *same* sample.

Lower field ($B < 0.1$ T) investigations [8,15] have also revealed an interesting range of behaviour for LAGBs. Using the MO technique (chapters 4 and 5), Albrecht *et al* [15] found through an inversion of the Biot-Savart law that *local* j_c^{GB} increases with *local* flux density B_z. Similar behaviour has also been observed at antiphase boundaries by Jooss *et al* [9]. This effect was predicted by Gurevich and Cooley [10] to occur at planar defects, and is due to the pinning of AJ vortices in the GB by the strongly pinned A vortices in the IG regions. The A vortices in the banks provide an effective quasiperiodic pinning potential, the effectiveness of which increases J_c with field as $J_c \propto B^{1/2}$ (up to 0.1 T). Kim *et al* [8] also observed a correlated effect at fields less than 0.1 T (77 K) in an 11° coated conductor GB. By field

cooling the sample they observe an increase in J_c^{GB} by a factor of 2 over zero field cooling. This feature was ascribed to an increased flux density in the IG regions arising from field cooling, producing increased AJ pinning and J_c^{GB}.

7.1.2 $J_c^{GB}(B)$ Limitation by $J_c^{IG}(B)$

Figure 7.4 shows typical J_c(B) measurements taken at 80 K for both GB and IG tracks patterned on the 3.8° LAGB, sample s2. Qualitatively, the curves can be seen to agree well with those reported by Verebelyi *et al* and two distinct regions of behaviour can be observed. At low fields the LAGB displays a reduced $J_c^{GB} < J_c^{IG}$, implying that dissipation occurs only locally to the GB (chapter 6). For fields of 0.5 T – 5.5 T a reduction in field sensitivity of $J_c^{GB}(B)$ compared to $J_c^{IG}(B)$ is also found. The sharp drop off seen for J_c^{GB} with field is indicated in the decrease of the ratio $\delta = J_c^{GB}/J_c^{IG}$, also plotted on the right hand scale for comparison. At higher fields, above a field value B^*, termed the merging field, the IG and GB curves are seen to converge to within 10 % and display the same field dependence[#]. Accordingly, above $B^* \sim 5.5$ T, the ratio δ can also be seen to tend to a value of unity, resulting in the LAGB becoming totally transparent to current flow.

The field B^* is determined by both the irreversibility field in the grains, B_{irr}^{IG}, *and* the magnitude of $J_c^{GB}(B)$ – which is related to the GB misorientation θ_m. The effect of the

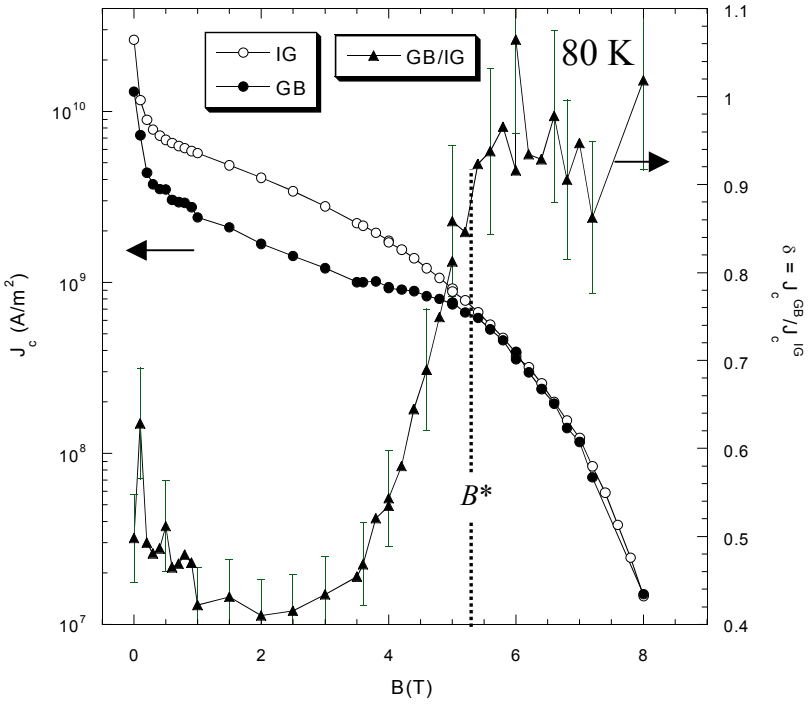

Figure 7.4. $J_c(B)$ measured for GB and IG tracks on a 3.8° LAGB sample s2 ($B||c$). $\delta = J_c^{GB}/J_c^{IG}$ is plotted on the right hand scale, and shows that GB and IG curves meet (to within a 10% error) at a merging field B^* ($V_c^{IG} = QV_c^{GB} = 5.4V_c^{GB} = 5.4$ μV, see section 4.2.5). Width $w = 9.1$ μm (GB and IG).

[#] The 10% error plotted on $\delta(B)$ is estimated from the uncertainty in track dimension (see section 8.3.3)

irreversibility field is seen in the measurement of intragranular $J_c^{IG}(B)$ as a gradual tapering off at high fields, as seen in figure 7.4. The merging of $J_c^{GB}(B)$ and $J_c^{IG}(B)$ at B^* arises because the GB is effectively being measured in *series* with two IG sections of track. As $J_c^{IG}(B)$ tapers off, it therefore necessarily limits any measurement of J_c^{GB} (as shown in the *V-I* measurements of figure 6.17). The effect is illustrated schematically in figure 7.5, which shows J_c^{IG}(B) and J_c^{GB}(B) for boundaries of several misorientations. The exact position of B^* is dependent on misorientation; as θ_m increases, $J_c^{GB}(\theta_m)$ decreases which shifts B^* to larger values. Two regimes may be identified:

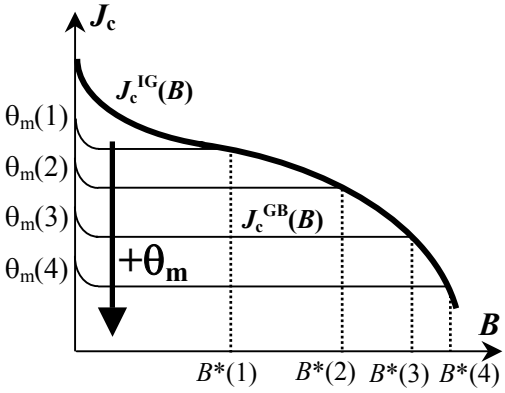

Figure 7.5. Schematic of $J_c^{IG}(B)$ and $J_c^{GB}(B)$ and the effect of misorientation on the merging field B^* for $\theta_m(1) < \theta_m(2) < \theta_m(3) < \theta_m(4)$, assuming a constant $J_c^{IG}(B)$.

- For $B < B^*$, measurement of the LAGB track reflects measurement of dissipation localised to the LAGB. $J_c^{GB}(B,T)$ and *V-I*(B,T) will represent the electronic response of the boundary.
- For $B > B^*$, measurement of the LAGB track reflects measurement of dissipation across the whole track length, both LAGB and IG regions. Dissipation is no longer localised to the GB and $J_c^{GB}(B,T)$ and *V-I*(B,T) will be dominated by the electronic response of the IG material; $J_c^{IG}(B,T)$ and the intragranular *V-I*(B,T).

This behaviour can be contrasted to that observed in samples containing irradiated columnar defects – they can show an enhanced B_{irr} at 77 K by up to a factor of 1.5 - 2 [11]. Pinning to the dislocation array (or facet structure) of a LAGB may well be expected therefore to produce a similar enhancement of B_{irr}, from B_{irr}^{IG} to B_{irr}^{GB}. It is not possible, however, to *directly* measure an enhanced B_{irr}^{GB} due to the *series* transport measurement of the LAGB dislocation array with the IG regions of track. This leads to the disappearance of GB pinning at the irreversibility field of the grains. This is not to say however, that B_{irr}^{GB} in not enhanced – below B^* evidence of increased GB vortex pinning may well lead to such an effect (see section 7.1.4) – it just cannot be measured.

In reality, the simple picture presented in figure 7.5 is more complicated, as $J_c^{IG}(B)$ properties can vary significantly from sample to sample - and as found in this study from location to location in the same film. Figure 7.6 compares the $J_c(B)$ measurements taken at 80 K on sample s2 and sample pk2 with misorientations of 3.8° and 4.9° respectively. Below B^* it can be seen that J_c^{GB} is smaller for pk2 than s2, as predicted by the channel model of section 3.5. Contrary to the prediction of figure 7.5 however, the *magnitude* of B^* is seen to be smaller,

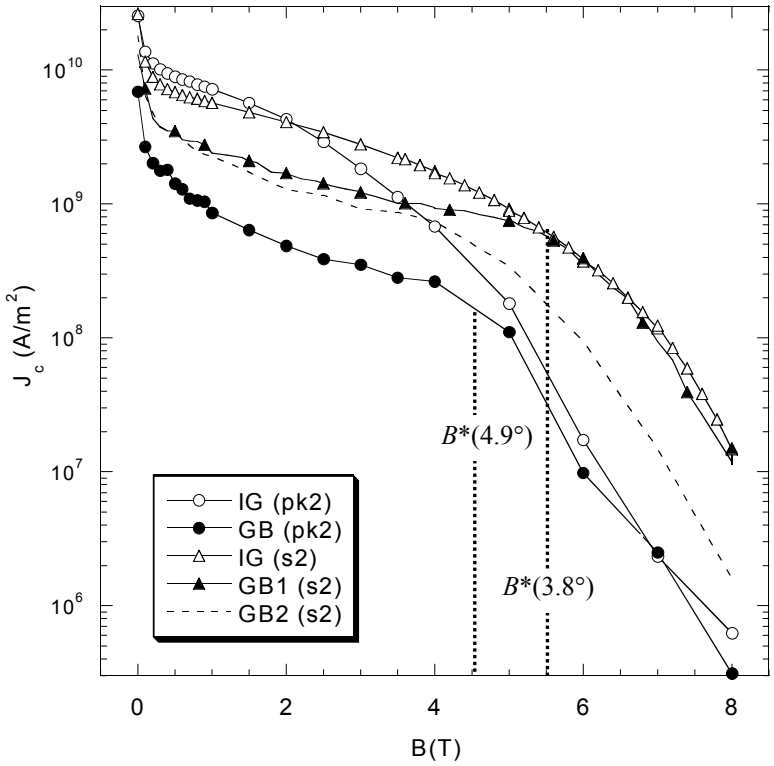

Figure 7.6. Measurements of $J_c^{GB}(B)$ (filled symbols) and $J_c^{IG}(B)$ (open symbols) for 3.8° LAGB s2 (triangles) and 4.9° LAGB pk2 (circles) at 80 K for $B \parallel c$. All tracks were approximately 10 μm wide, apart from GB2 on sample s2 (dashed line), where w = 5.5 μm. Q = 2.4 (pk2) and 5.4 (s2).

not larger, for pk2 than for s2. The cause is the reduced B_{irr}^{IG} of sample pk2, resulting in the greater reduction in $J_c^{IG}(B)$ seen at high fields.

Variation in J_c^{IG} is also seen between tracks patterned in the same sample. Figure 7.6 includes a $J_c^{GB}(B)$ measurement taken from a different track (GB2) on sample s2, marked as a dashed line. The track possesses both a lower value of B*, and lower J_c^{GB} values below B*. It is most likely that the reduction of B* is due to a *local* reduction (in the GB contact material) of B_{irr}^{IG} and hence J_c^{IG} at high fields. This variation is probably responsible for high-field measurements of Heinig *et al* [1] in figure 7.2, in which J_c^{GB} is observed to be greater than J_c^{IG}. The reduced values of J_c^{GB} below B* (~24% at 2 T) can be ascribed to the heterogeneity along the length of the GB.

7.1.3 $J_c^{GB}(B)$ with Temperature

The results of the previous section show that B* is dependent on both misorientation *and* the local (to the LAGB track) value of J_c^{IG}. As $B_{irr}^{IG}(T)$ is a function of temperature (see section 2.8) it is also expected that B* should be a strong function of temperature. At lower temperatures B_{irr}^{IG} is increased, resulting in a corresponding increase in the value of B*. On lowering temperatures below 77 K, such that B_{irr} and B* are above our experimentally attainable field of 8 T, we should therefore see no merging of $J_c^{IG}(B)$ and $J_c^{GB}(B)$. This effect

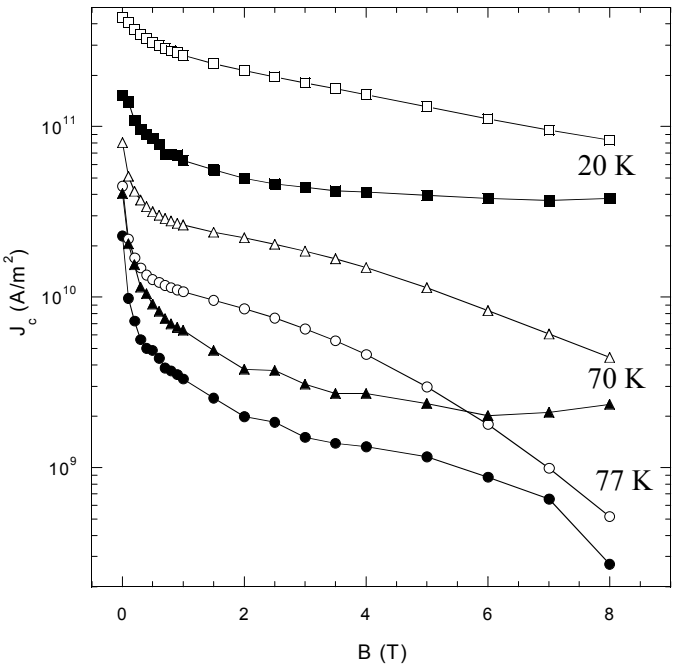

Figure 7.7. Measurements of $J_c^{GB}(B)$ (filled symbols) and $J_c^{IG}(B)$ (open symbols) for 3.8° LAGB s2, for $B \parallel c$ at 77 K (circles), 70 K (triangles) and 20 K (squares). w = 5.5 μm (GB), 9.1 μm (IG), Q = 5.4.

is indeed observed and is shown in figure 7.7, presenting J_c^{GB} and J_c^{IG} data for a 3.8° LAGB sample s2 at 77 K, 70 K and 20 K for $\boldsymbol{B} \parallel \boldsymbol{c}$. At 77 K B^* can be seen at approximately 6 T, but at 70 K and lower, no limitation by the grains is observed and $J_c^{GB}(B)$ reflects dissipation localised to the GB over the whole field range 0 - 8 T.

Figures 7.8(a) and 7.8(b) show in detail how the curves of $J_c^{GB}(B)$ and $J_c^{IG}(B)$ evolve as temperature is varied from 20 K to 83 K. The sharp downturn of $J_c^{GB}(B)$ due to B^* is only observed in the curves of 7.8(a) at 83 K, 80 K and 77 K. Below 77 K, the $J_c^{GB}(B)$ curves all show a reduced dependence with field when compared to the IG measurements in figure 7.8(b). In fact, at high fields and low temperatures it can be seen that there is actually a slight *increase* in the magnitude of $J_c^{GB}(B)$ with field. This is reminiscent of the enhancement in $J_c^{GB}(B)$ observed by Cai *et al* [3] due to the matching of field to the facet structure at a bulk-scale boundary (figure 7.3).

Enhancement of J_c^{GB} due to matching effects is expected to occur if the condition $na_o(B) = mD_f$ is satisfied, where n and m are integers and D_f is the defect spacing [3]. For increasing field a maximum enhancement is expected at $a_o(B) = D_f$. In our case, the enhancement cannot be seen to peak at a given field due to the limitation in measurement to fields of up to 8 T. As such, the enhancement could be consistent with the large matching fields expected from the LAGB dislocation array - from equation 3.2, for a 3.8° boundary the dislocation spacing is expected to be 5.9 nm, giving a matching field of 72 T using equation 2.10 ($a_0 \sim 50\text{nm}/B^{1/5}$). Another possibility is matching to the facet structure ($D_f \sim$ 10's of nm)

that forms the thin film meander discussed in section 3.4.2. A matching field of 8 T or more would imply a defect spacing of 17.7 nm or less, which corresponds roughly to the facet size. However, the fact that no similar increase in $J_c^{GB}(B)$ was observed for the 4.9° sample (pk2) - even though the pk2 GB displayed a *greater* degree of meander (chapter 5) - would suggest this is not the dominant mechanism.

To investigate the power law predictions of $J_c^{GB}(B)$ on field, figure 7.9 shows log-log plots of the data in figure 7.8. In figure 7.9(a), power law fits to the GB data can be seen to become increasingly appropriate at low temperatures; at 20 K, $J_c^{GB}(B) \propto B^{-0.3}$. The exponent of 0.3,

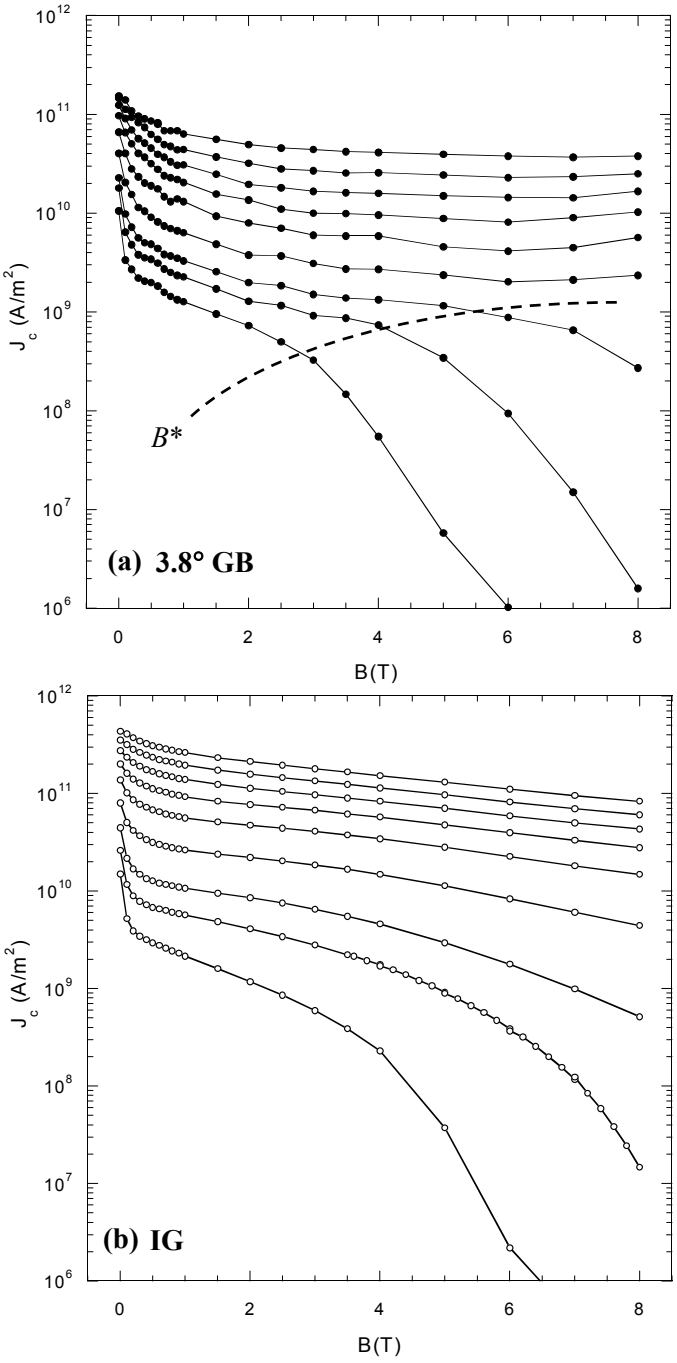

Figure 7.8.(a) $J_c^{GB}(B)$ and (b) $J_c^{IG}(B)$ curves as a function of temperature for field along the *c*-axis of 3.8° LAGB (sample s2, same tracks as figure 7.7). Curves are from top to bottom: 20, 30, 40, 50, 60, 70, 77, 80 and 83 K. The *B** field is indicated in (a).

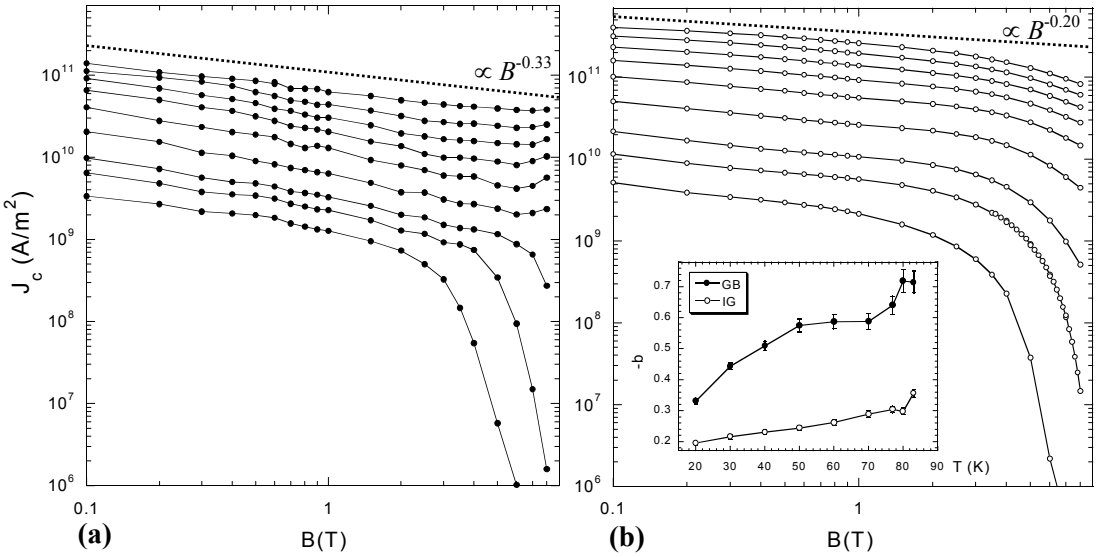

Figure 7.9. Double logarithmic plot of the data in figure 7.8, showing (a) $J_c^{GB}(B)$ and (b) $J_c^{IG}(B)$ curves as a function of temperature. Curves are from top to bottom: 20, 30, 40, 50, 60, 70, 77, 80 and 83 K.

however, is somewhat smaller than the predicted $B^{-0.5}$ dependence [4,5]. With increasing temperature the power law dependence becomes less appropriate, particularly high fields - both above B^* and where J_c^{GB} is enhanced. For comparison, the IG data in figure 7.9(b) only displays power law dependence at low field, $B < 1$ T. The inset of figure 7.9(b) shows the results of power fits of $J_c \propto B^b$ to both IG and GB data where appropriate. The relative field sensitivity of $J_c^{GB}(B)$ at low fields (the sharp drop off compared to $J_c^{IG}(B)$) is manifest as a larger exponent value b for the GB fits. Very approximately, a $J_c^{GB}(B) \propto B^{-0.5}$ dependence may be identified over the temperature range 40 - 70 K.

7.1.4 $\delta(B) = J_c^{GB}/J_c^{IG}$: Comparison of GB to IG Properties

As previously discussed, the degree of transparency of a LAGB may be investigated through the ratio $\delta = J_c^{GB}/J_c^{IG}$. Figure 7.10 shows the dependence of $\delta(B)$ at various temperatures, 20 K to 77 K for sample s2 (3.8°). Common to all curves is a drop off of $\delta(B)$ with field for $B < 2 - 3$ T and an increase with field for $B > 2$ - 3 T. As discussed in section 7.1.1, the low field drop off may be linked qualitatively to the destruction of weak linked, proximity coupled regions of the LAGB. The modulation of coupling strength and channel width along a LAGB is certainly to be expected from the heterogeneity revealed by TEM (Chapters 3 and 5), and the LAGB *V-I* structure discussed in chapter 6.

The increase of $\delta(B,T)$ at high fields may be attributed to two factors. At high temperatures, the increase is due to approaching the IG irreversibility line which pushes J_c^{IG} down to J_c^{GB} levels and increases δ - ideally to unity above the merging field B^* (figure 7.4). However, as shown in the previous section, at suitably low temperatures B_{irr} becomes exceedingly high,

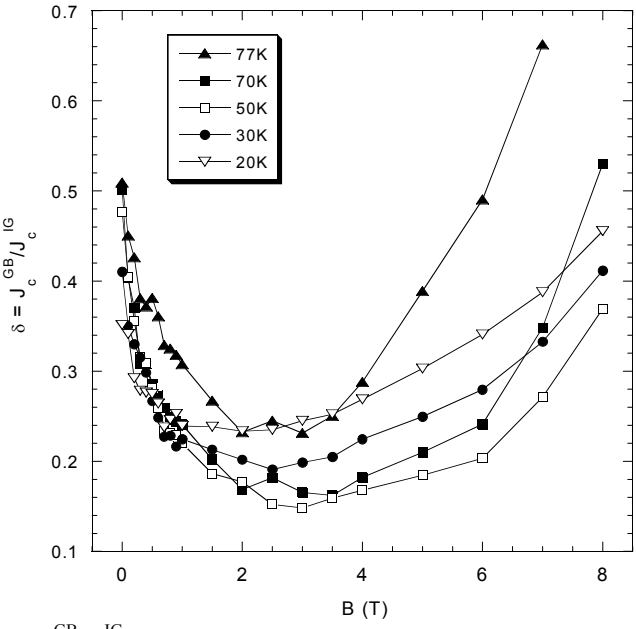

Figure 7.10. $\delta(B,T) = J_c^{GB}/J_c^{IG}$ as a function of temperature for s2 (3.8° LAGB). Field is parallel to the *c*-axis.

and well above our maximum field of 8 T. Therefore, the increase in $\delta(B)$ with field at low temperatures cannot be directly ascribed to the irreversibility line effect. Instead, it may be linked to an increase in vortex pinning at the LAGB with increasing field, which increases $\delta(B)$ through an increase in $J_c^{GB}(B)$. This is consistent with the angular measurements of section 9.3, which find a pinning peak for applied field aligned with the LAGB dislocation array for field rotation within the LAGB plane. Below the irreversibility line, this peak is also found to increase with field (figure 9.9), implying a corresponding increase in the effectiveness of LAGB flux pinning. For the static measurements of figure 7.10, not only is the result an increase in the ratio J_c^{GB}/J_c^{IG}, but at sufficiently high fields an increase in J_c^{GB} itself for sample s2.

Comparison of s2 (3.8°) and pk2 (4.9°) data reveal the effect of misorientation on LAGB transparency. Figure 7.11 shows $\delta(B)$ for both s2 and pk2 at 50 K and 70 K. At 50 K, similar

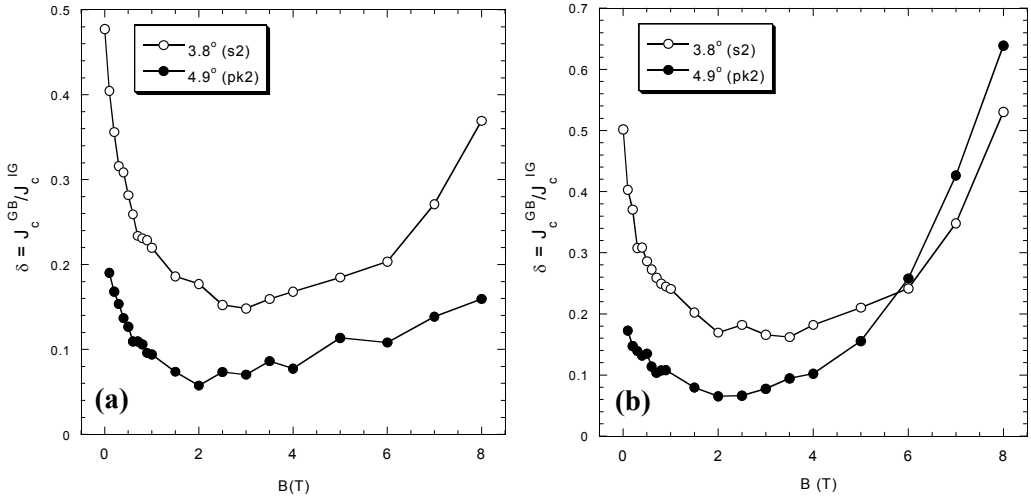

Figure 7.11. Comparison of $\delta(B,T)$ for sample pk2 (4.9°, filled symbols) and s2 (3.8°, open symbols) at (a) 50 K and (b) 70 K. Field is directed along the *c*-axis. GB tracks are w = 5.5 μm (s2), 9.8 μm (pk2).

behaviour is exhibited for both samples, but in keeping with the larger channel width of the 3.8° boundary, s2 displays an increased transparency that shifts its curve upwards. At 70 K, the curves approximately merge for $B > 6$ T, a value below B^*(70 K) but indicative of the dominating effect of B_{irr}^{IG}(70 K).

7.1.5 $J_c^{GB}(B)$ with Angle of Applied Field

The dependence of J_c^{GB} on field has also been investigated for fields applied at an angle θ to *c*-axis. Scans involving rotation of the applied field at a given field magnitude are dealt with in depth in chapters 8 and 9. This section looks at the 'static' measurement of $J_c^{GB}(B)$ as a function of field at a given angle θ. Figure 7.12 shows $J_c^{GB}(B,0°)$ (filled symbols) and $J_c^{GB}(B, 90°)$ (open symbols) at 80 K and 60 K for sample pk2. The inset shows the experimental geometry, where the θ = 90° position corresponds to field perpendicular to ***J*** and parallel to *ab* (ϕ = 0 in figure 4.6). For fields parallel to the *ab*-plane $J_c^{GB}(B)$ is seen to be larger than for fields parallel to the *c*-axis at both 80 and 60 K. This can be ascribed to the intrinsic pinning mechanism that operates for fields aligned with *ab*-plane (see section 2.7).

Another striking feature is that for fields lying along the *ab*-direction the B^* transition is not observed. This is true even at temperatures up to 80 K, for which B^* can be clearly seen for θ = 0° at ~ 4.5 T. This is indicative of the increased irreversibility line for fields lying in the *ab*-direction and is associated with the material anisotropy. This may be understood through the GL scaling law (see section 2.6) predicting an increase in B_{c2}, B_{c1} and B_{irr} with angle due to anisotropy in coherence and penetration depths [12].

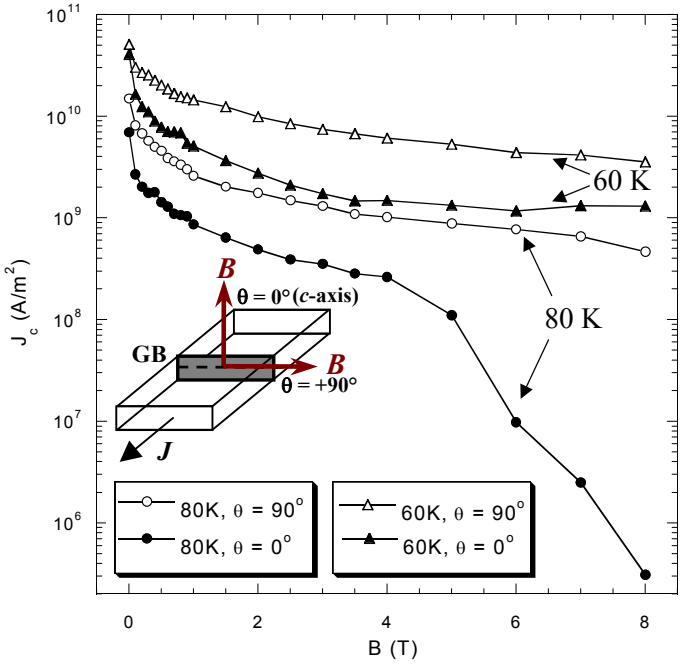

Figure 7.12. $J_c^{GB}(B,0°)$ (filled symbols) and $J_c^{GB}(B, 90°)$ (open symbols) at 80 K and 60 K for sample pk2 (4.9°). The inset shows experimental geometry, θ = 90° corresponding to the intrinsic position.

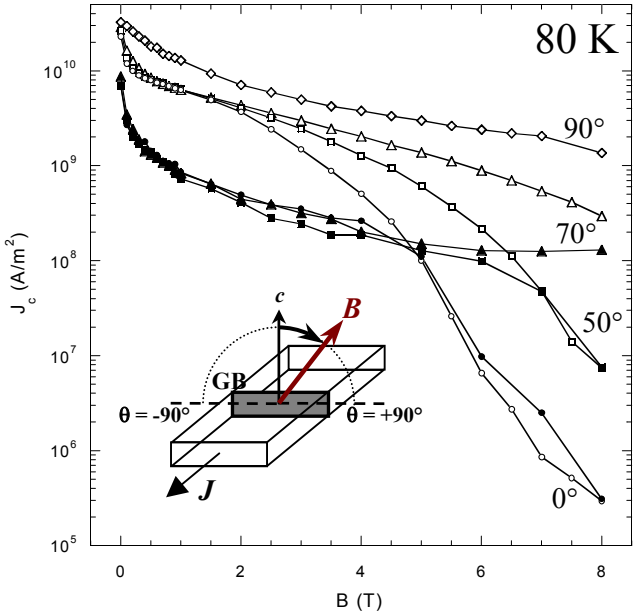

Figure 7.13. $J_c(B,\theta)$ for GB (filled symbols) and IG (open symbols) tracks of sample pk2 (4.9°) for angles θ = 0° (circles), 50° (squares), 70° (triangles). $J_c^{IG}(B,\theta = 90°)$ is also plotted (diamonds). Inset shows the experimental geometry.

This effect is nicely depicted in figure 7.13, which shows $J_c^{IG}(B)$ at 80 K for pk2 for θ = 0°, 50°, 70° and 90°. The corresponding measured traces of $J_c^{GB}(B)$ are also shown for θ = 0°, 50° and 70°. They clearly chart an increase of B^* as θ is increased, until $B^* > 8$ T at 70°. This correlates well with the observation of $B^*(\theta)$ seen in the angular measurement of $J_c^{GB}(\theta)$ in figure 9.11.

For a range of fields $B < B^*$ it can also be seen that $J_c^{GB}(50°) < J_c^{GB}(0°)$ in figure 7.13. This implies the presence of the previously mentioned LAGB pinning peak in $J_c^{GB}(\theta)$, which is maximum for field aligned with the dislocation array. In agreement with the findings of section 9.3 and figure 9.11, the peak is only found to occur below B^*.

7.1.6 Static $J_c(B)$ Hysteresis

This work has found that measurements of individual LAGB $J_c^{GB}(B,\theta = 0°)$ can display a pronounced hysteresis; different curves are traced out for increasing (B^+) and decreasing (B^-) applied fields, B_{app}. This hysteresis becomes increasingly apparent at low temperatures, and can be linked to the flux focussing effect directly measured by MO in chapter 5. An example is shown in figure 7.14 at 10 K for sample pk2. As shown in the inset, no hysteretic behaviour is found for the same sample at 70 K. For the purposes of this work, the effect is termed *static* hysteresis, to distinguish it from the *angular* hysteresis presented in section 9.3.5.

As found in section 5.3, the *net* field local to the LAGB is $B_{GB} = B_{app} + B_{rev}$, where B_{rev} *switches sign* upon a reversal of the ramp direction. As a higher flux density is experienced at

the GB upon ramping field *up*, a correspondingly lower $J_c^{GB}(B)$ magnitude is obtained. Additionally, as a lower flux density is experienced at the GB upon ramping field *down*, a larger J_c^{GB} is expected. A similar model was used to explain static hysteresis in $J_c(B,\theta = 0°)$ observed in polycrystalline samples containing HAGBs by Evetts and Glowacki [13], shown in figure 7.15(a). The process is illustrated nicely in figure 7.15(b) which links the change in $J_c(B)$ with the flux profile in the grains as field is increased (numbers 1-2) and subsequently

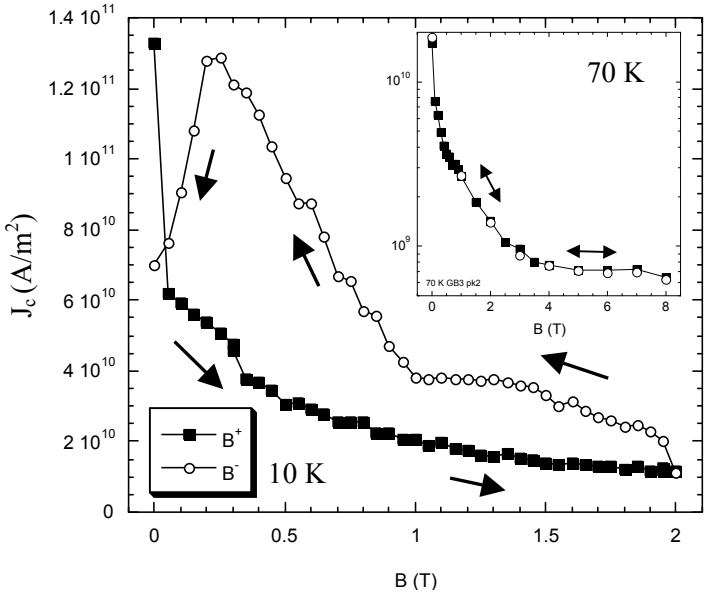

Figure 7.14. $J_c^{GB}(B,\theta = 0°)$ measurement on sample pk2 at 10 K for increasing (B^+) and decreasing (B^-) field (w = 5.5 μm). Arrows also indicate the sweep direction. The inset shows a measurement made at 70 K, displaying no hysteresis.

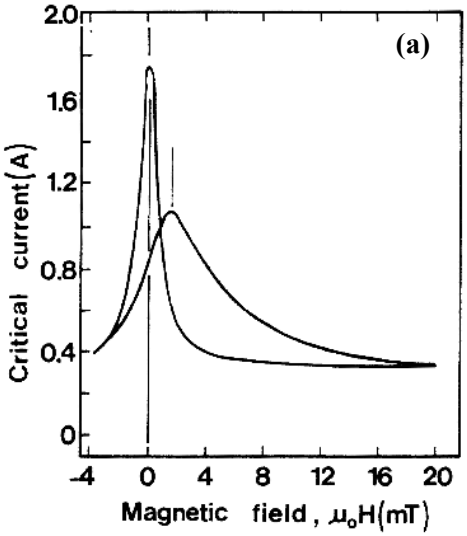

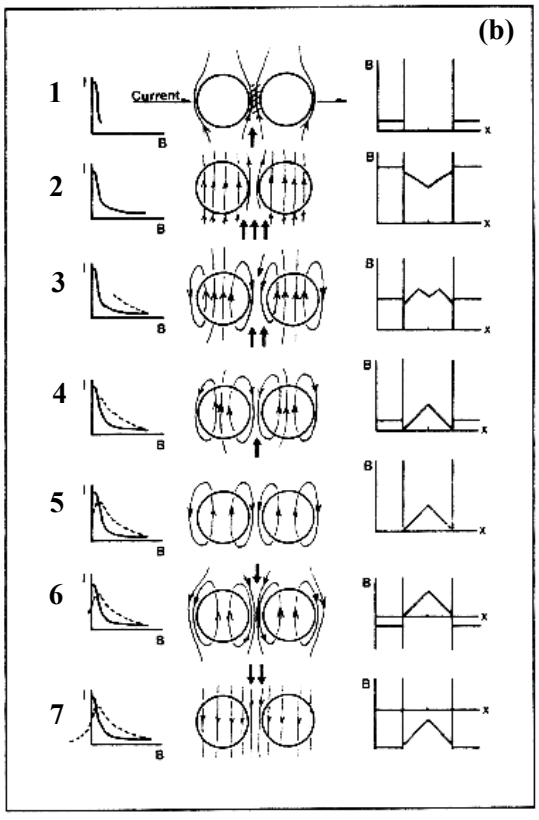

Figure 7.15. (a) Static $J_c(B)$ hysteresis for field ramping up, then down in polycrystalline YBCO (B perpendicular to surface). (b) Schematic of grain flux profile as field is ramped up (1-2) and down (3-7). The corresponding effect on field lines at a grain boundary and $J_c(B)$ are shown. A similar effect is seen at individual LAGBs, indicative of their current limitation [13].

decreased (numbers 3-7).

We can now understand the low field peak in $J_c^{GB}(B)$ that occurs at ~ 0.2 to 0.3 T in figure 7.14 as field is ramped down. It signifies a maximum cancellation of applied flux with the negative B_{rev} component, indicating that B_{rev} ~ - 0.2 to - 0.3 T.

Experiments that rotate the applied field with respect to the *c*-axis also alter the magnitude of field parallel to the *c*-direction in a manner similar to the static measurement. Static hysteresis can therefore lead to the presence of hysteresis in angular measurements, as will be shown in depth in section 9.3.5.

7.2 $J_c(T)$: Temperature Dependence

7.2.1 Previous Measurements

There are fewer reports of $J_c(T)$ measurements performed on LAGBs than of $J_c(B)$ in the literature. Using the MO technique, Polyanskii *et al* [14] were able to extract the boundary and grain critical currents as a function of temperature over the temperature range 4.2 – 77 K (figure 7.16). The ratio $\delta(T) = J_c^{GB}/J_c^{IG}$ was found directly from the angle of the *d*-line (see section 3.8.4). Unlike the numerical inversion technique employed by Albrecht *et al* [15] and Jooss *et al* [16,17] to extract J_c^{GB}, they used a Bean model to first extract J_c^{IG} values, then multiplied by J_c^{GB}/J_c^{IG}. They found that, contrary to expectation [22], $\delta(T)$ increases with increasing temperature. This can be seen in figure 7.16(a), and is found to be more apparent for $\theta_m = 5°$ than for $\theta_m = 7°$. The increase in $\delta(T)$ is due to the *reduced temperature dependence* observed for $J_c^{GB}(T)$ over $J_c^{IG}(T)$, as can be seen in figure 7.16(b) for the 5° GB, and in the inset for the 7° GB. Polyanskii *et al* assumed no field dependence of J_c, as they were operating in the MO low field range of B < 100 mT. Whether the same dependence would be expected for transport measurements and higher fields provided a motive for the

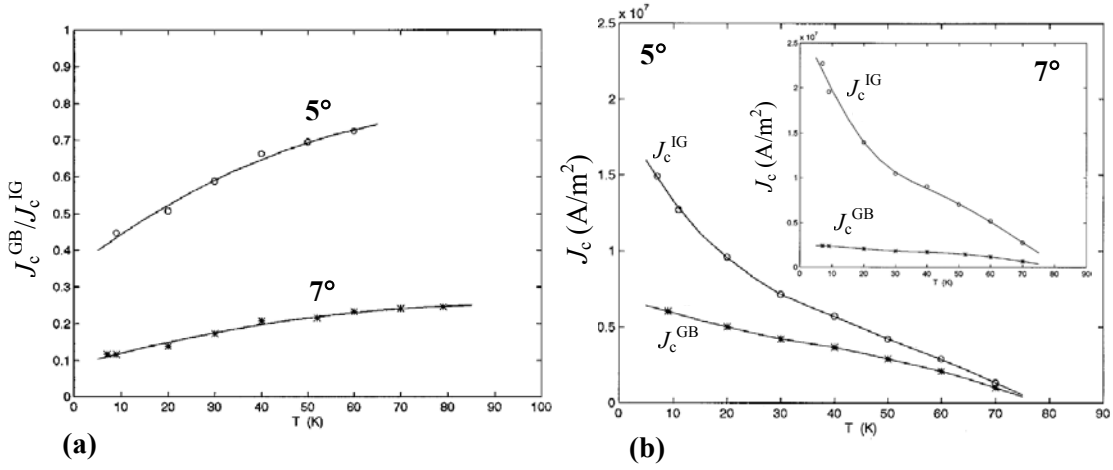

Figure 7.16.(a) Temperature dependence of $\delta(T) = J_c^{GB}/J_c^{IG}$ and (b) $J_c^{GB}(T)$ and $J_c^{IG}(T)$ for 5° and 7° (inset) LAGBs extracted from MO imaging of the GB *d*-lines [14].

investigations in this section.

Mannhart *et al* [18] have published details of fits of $J_c(T)$ models based on a Josephson coupled GB to measured $J_c^{GB}(T)$ curves. They found that for 5°, 10° and 15° boundaries, a good fit could be made to models proposed by Ambegaokar-Baratoff and by Likharev for Josephson junctions. However, the full temperature dependence for $B > 0$ T could not be fully explained by the junction models and showed some consistency with a creep limited behaviour predicted by Tinkham [19].

For critical currents limited by flux creep, such as IG material, one temperature dependence commonly predicted to exist is the approximately linear $J_c(T) \propto \sim(1 - t)^c$ [19], where $c = 1$ and $t = T/T_c$. However, this is not a universal observation for thin film IG tracks and significant variation is found in the literature of the extracted power, c, which ranges from $c = 0.5 – 2$ [18,20]. Pashitskii *et al* [21] have also predicted values of $c = 3/2$ to 2 for a network of LAGBs. Due to the spread in the expected values, drawing any firm conclusions as to the underlying dissipative mechanism from the absolute value of c extracted from LAGB $J_c^{GB}(T)$ is therefore difficult. For this reason, in this work it is the *comparison* of IG and GB $J_c(T)$ measurements that prove most informative.

7.2.2 $J_c^{GB}(T)$ Limitation by $J_c^{IG}(T)$

Figure 7.17(a) presents $J_c(T)$ measured on GB and IG tracks patterned in sample s2, with an applied field of 7 T parallel to the *c*-axis. Both curves display a monotonic increase with decreasing temperature, and $J_c^{GB} < J_c^{IG}$ for $T < 80$ K. Plotted on the right hand scale is $\delta(T) = J_c^{GB}/J_c^{IG}$. At higher temperatures both $J_c(T)$ curves merge, resulting in an increase of the ratio δ approximately to unity. This behaviour is very similar to that observed in section 7.1 for $J_c(B)$ at the merging field B^*. In this case however, it is the merging temperature T^*,

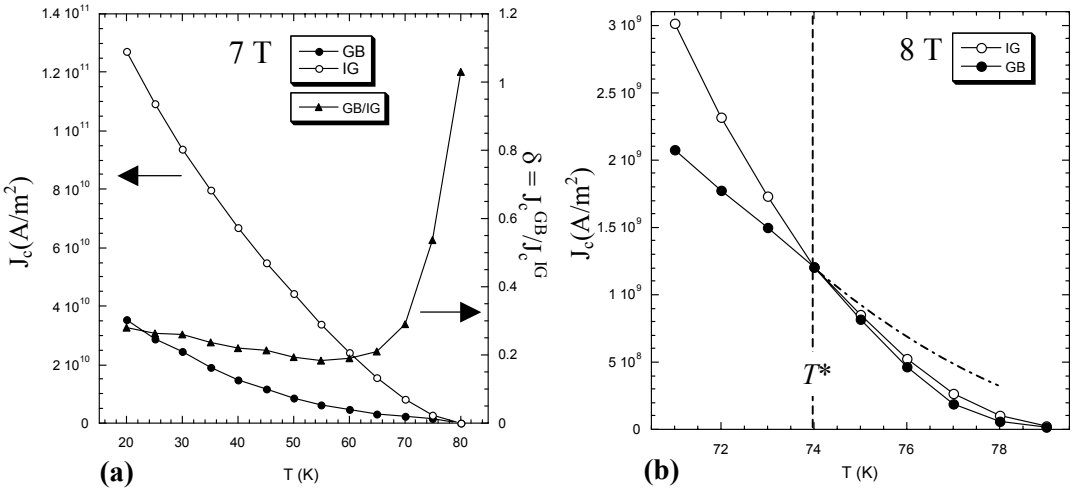

Figure 7.17.(a) $J_c(T)$ for the GB and IG track measured on sample s2 (3.8°) at 7 T applied parallel to *c*. The right hand scale gives the ratio $\delta(T)$. (b) The T^* transition at 8 T in more detail (w = 5.5 μm (GB), 9.8 μm (IG), Q = 2.4).

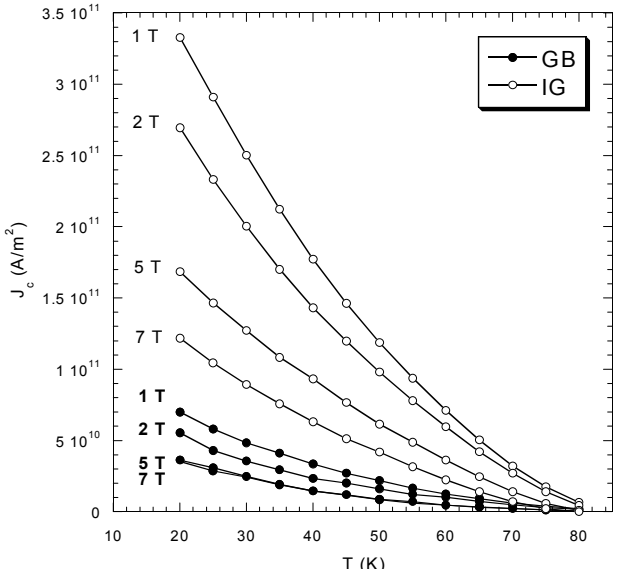

Figure 7.18. $J_c^{GB}(T)$ (filled symbols) and $J_c^{IG}(T)$ (open symbols) measured on sample s2 for various applied fields. From top to bottom the curves correspond to 1, 2, 5 and 7 T.

above which J_c^{GB} reflects the behaviour of J_c^{IG}. Figure 7.17(b) highlights this limiting behaviour in more detail, showing $J_c(T)$ at 8 T for the 3.8° GB and IG tracks. Below T^*, the GB possesses a reduced temperature dependence which results in a noticeable kink in $J_c^{GB}(T)$ at $T^*(8\text{ T}) \sim 74$ K, as highlighted by the dashed line. For the larger misorientation sample pk2, the value of T^* was found to be higher - this is due to the reduced $J_c^{GB}(T)$ values of the higher misorientation which increase T^* through a mechanism similar to that described by figure 7.4.

$J_c(T)$ curves for GB and IG of sample s2 are shown for various applied fields over the range 1 – 7 T in figure 7.18. Although the effect of increasing field is to reduce J_c^{GB} and J_c^{IG} magnitudes, the temperature dependence still remains similar. It should be noted that both the 5 T and 7 T $J_c^{GB}(T)$ curves lie on top of each other for all temperatures below T^*. This is

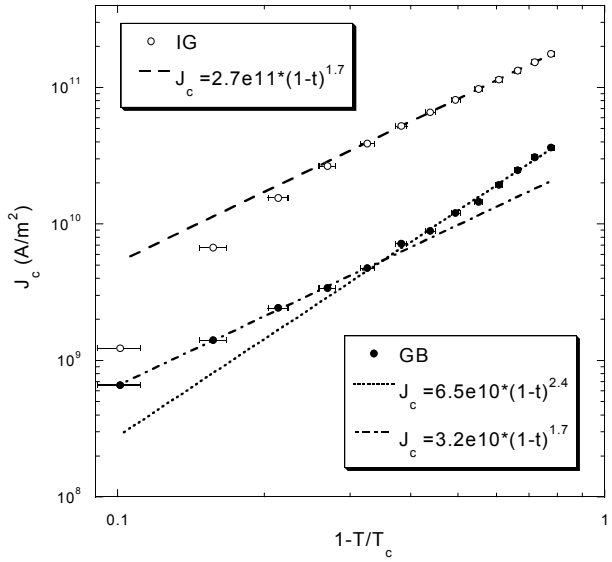

Figure 7.19. Log-log plot of GB and IG $J_c(T)$ with $(1 - t)$ at 5 T for sample s2. Fits of $J_c \propto (1 - t)^c$ to high temperature [low $(1 - t)$] and low temperature [high $(1 - t)$] sections of the GB curve are shown with $c \sim 1.7$ and 2.4. Low temperature fit for the IG curve yields $c \sim 1.7$.

indicative of the reduced field dependence and enhanced GB flux pinning seen at high fields in figures 7.8 and 7.9. This is may be contrasted with the continuing decrease in the magnitude of $J_c^{IG}(T)$ between 5 T and 7 T.

Both $J_c^{GB}(T)$ and $J_c^{IG}(T)$ are *roughly* exponential at low temperatures, as has been found previously for IG material [6]. In order to investigate any possible $J_c(T) \propto (1 - t)^c$ dependence, plots of J_c against $(1 - t)$ were made on double logarithmic axes. An example is shown in figure 7.19 for GB and IG at 5 T. Fits of $(1 - t)^c$ to the GB curve yield larger values of c at lower temperatures ($c \sim 2.4$) than at higher temperatures ($c \sim 1.7$). The IG curve displays a suitable fit only at low temperature, and giving $c \sim 1.7$ for all the fields 1 – 7 T investigated. The change in the dependence of $J_c^{GB}(T)$ relative to $J_c^{IG}(T)$ over the temperature range investigated is manifest in the dependence of $\delta(T)$, as will be discussed in the next section.

7.2.3 $\delta(T) = J_c^{GB}/J_c^{IG}$: Comparison of GB to IG Properties

Figure 7.20 plots the dependence of $\delta(T) = J_c^{GB}/J_c^{IG}$ extracted for various applied fields along the c-axis of sample s2, from 1 – 7 T. All the curves display a similar behaviour - at low T, there is a *decrease* of $\delta(T)$ with increasing temperature, and at high T there is an *increase* of $\delta(T)$ with temperature. The temperature at which the crossover in behaviour is found to occur is an approximately field independent $T_s \sim 55 - 60$ K. The two temperature regions are discussed below:

(A) *High Temperature Region*

The increase in $\delta(T)$ at high temperatures is due to the reduced temperature dependence of $J_c^{GB}(T)$ compared to $J_c^{IG}(T)$, noted in the previous section. This agrees well with the low field

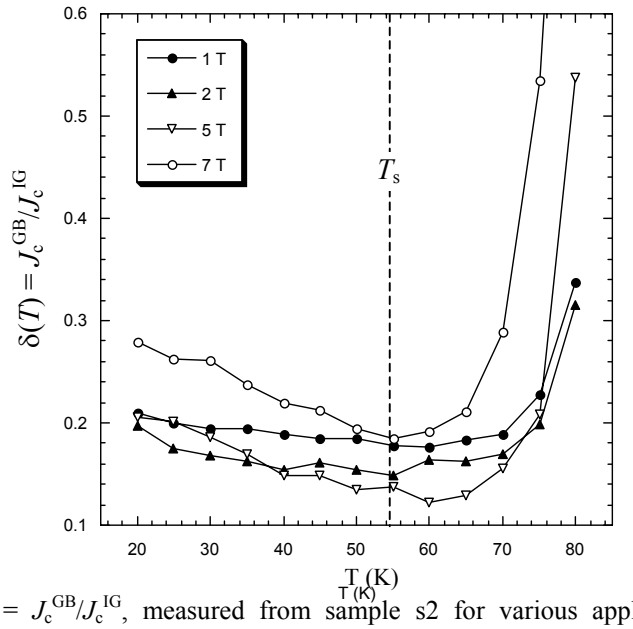

Figure 7.20. $\delta(T) = J_c^{GB}/J_c^{IG}$, measured from sample s2 for various applied fields parallel to c ($w = 5.7$ μm (GB), 8.3 μm (IG), $Q = 2.4$).

results of Polyanskii *et al* [14]. In a similar argument to section 7.1.4 for $\delta(B)$, the increase in $\delta(T)$ can be ascribed to either enhanced pinning at the LAGB (increasing J_c^{GB}) or the approach of the irreversibility line (decreasing J_c^{IG}) with increasing temperature. The latter is certainly the dominant effect at high fields (leading to T^*), but will be of lesser importance at lower fields as T_{irr}^{IG} is increased. The former, increased flux pinning scenario could in this case be due to two effects:

- Firstly, as discussed in section 7.1.3, the dislocation array and heterogeneous strain fields will provide vortex pinning sites. The angular measurements of section 9.3 show that relative to the *ab*-plane pinning peak, the pinning peak seen for field aligned with the dislocation array also *increases* with temperature (up to T^* or B^* - see figure 9.15).
- Secondly, a pinning force enhancement at the LAGB is also expected due to the dimensionally reduced thermal fluctuations for vortices in the GB defect plane [22 (p.1324),14]. The effect of increasing temperature on J_c depends strongly on the dimensionality of the system; models show that vortices trapped in two dimensions result in a $J_c(T)$ that decays only *algebraically*, but that vortices trapped in three dimensions are only marginally pinned, resulting in an *exponential* decay of $J_c(T)$ with T [22]. A strong decrease in the pinning strength due to thermal smoothing is expected to occur above the depinning temperature, $T_{dp} \approx 50$ K for YBCO [22]. As such, the effects of dimensionality are only likely to become important above this temperature. This agrees reasonably well with the increase in $\delta(T)$ observed above $T_s \sim 55 - 60$ K.

(B) *Low Temperature Region*

At lower temperatures, where the dimensionality reduction becomes less important, another mechanism may dominate and lead to the observed *decrease* in $\delta(T)$ with increasing temperature. The main influence is likely to be the variation of $T_c(y)$ *along* the LAGB due to the presence of the LAGB dislocation cores in the boundary [23]. The local suppression of T_c at each dislocation core (due to strain field and band bending effects) will lead to a modulation of $T_c(y)$ of the form illustrated in figure 7.21. This distribution necessarily implies a variation in channel width, and hence transparency, with temperature. As temperature *increases* from

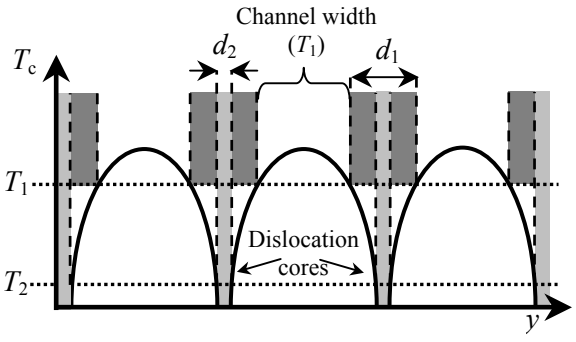

Figure 7.21. Schematic of the possible $T_c(y)$ variation along a LAGB with distance x. The core centres possess $T_c = 0$ K. The diameter of the non-superconducting region around the dislocations are shown as shaded regions for two temperatures $T_1 > T_2$. As T increases, channel width decreases.

T_2 to T_1 in figure 7.21, the non-superconducting core size increases from d_2 to d_1. As such $\delta(T)$ would be expected to decrease with temperature. Evidence for such a change in d is found in the reduced magnitude of the critical angle $\alpha = b/2r_d$ (section 3.5) at 77 K over 4.2 K. Although there is scatter in α, table 3.1 implies a possible decrease in α with temperature from ~5° (4.2 K) to 4° (77 K) giving a possible increase in $d = 2r_d$ of 25 %. The possible implications of a varying dislocation core size on vortex core pinning in the angular measurements of $J_c^{GB}(\theta)$ are discussed in section 9.3.3.

The low temperature reduction in $\delta(T)$ with T was *not* observed in the MO data of Polyanskii *et al* (figure 7.16(a)). It is possible that this is due to the low fields involved in their measurement, $B < 100$ mT. Higher fields may exacerbate the variation of $\delta(T)$ through a suppression of $T_c(y)$.

7.3 Discussion

Static measurements (at a fixed angle) have been made of $J_c^{GB}(B,T)$, $J_c^{IG}(B,T)$ and $\delta(B,T)$. It is found that the LAGB poses *no impediment* to current transport above a merging 'line' defined by B^* and T^*. It is found that B^* depends on both the irreversibility line (which is a function of the angle of applied field) and the GB misorientation. Unfortunately for technological application, the onset of this total transparency only occurs as the critical current in the intragranular regions tends to zero. As will be detailed in chapter 8, another method of dramatically increasing δ without a vanishing critical current is through the simple rotation of field *out* of the GB plane.

Evidence of pinning at the LAGB interface is found below the merging line in both the reduced temperature and field dependence of $J_c^{GB}(B,T)$ at high temperatures and fields respectively. Through a comparison of LAGBs with $\theta_m = 3.8°$ and 4.9° (figure 7.11) it is found that, as expected, transparency is reduced for the larger misorientation. Pinning due to the reduction in dimensionality may be expected to increase with increasing θ_m, as the GB becomes more of a continuous planar defect (see figure 7.16(b)). However, vortex pinning as seen in the angular pinning peak measurements of chapter 9 is found to be enhanced for lower θ_m GBs which possess well separated dislocation cores.

Finally, it should be noted that there are problems associated with J_c^{GB} and its comparison to J_c^{IG}. The E-field criterion could be over 10^3 times larger for the GB (see table 6.1 and associated text), if dissipation is localised to one vortex row. This inconsistency is not solved by the simple normalisation of track lengths described in section 4.2.5. In addition, inconsistency in the measurement of $J_c^{GB}(B,T)$ will also occur over the course of a *given*

measurement. As discussed in chapter 6, the number of vortex rows being channelled along the LAGB at the J_c criterion are likely to vary, particularly with temperature. As such, with decreasing temperature the dissipative width across the interface will *increase*, resulting in a decrease of the E-field criterion used to determine J_c^{GB}.

7.4 References

[1] N.F. Heinig, R.D. Redwing, J.E.Nordman and D.C. Larbalestier, Phys. Rev. B **60**, 1409 (1999)

[2] D.T. Verebelyi, D.K. Christen, R. Feenstra, C. Cantoni, A. Goyal, D.F. Lee, M. Paranthaman, P.N. Arendt, R.F. DePaula, J.R. Groves and C.Prouteau, *Appl. Phys. Lett*. **76**, 1755 (2000)

[3] X.Y. Cai, A. Gurevich, I.F. Tsu, D.L. Kaiser, S.E. Babcock and D.C. Larbalestier, *Phys. Rev. B* **57**, 10951 (1998)

[4] M.V. Fistul and G.F. Giuliani, *Phys. Rev. B* **57**, 10951 (1998)

[5] A. Díaz, L. Méchin, P. Berghuis, and J. E. Evetts, *Phys. Rev. Lett.* **80**, 3855 (1998)

[6] R. Herzog, PhD Dissertation, University of Cambridge (1997)

[7] B. Dam, J.M. Huijbregtse, F.C. Klaassen, R.C.F. van der Geest, G. Doornbos, J.H. Rector, A.M. Testa, S. Freisem, J.C. Martinez, B. Stauble-Pumpin and R. Griessen, Nature (London) **399**, 439 (1999)

[8] D. Kim, P. Berghuis, M.B. Field, D.J. Miller, K.E. Gray, R. Feenstra and D.K. Christen, *Phys. Rev. B* **62**, 12505 (2000)

[9] Ch. Jooss, R. Warthmann and H. Kronmuller, *Phys. Rev. B* **61**,12433 (2000)

[10] A. Gurevich and L.D. Cooley, *Phys. Rev. B* **50**, 13 563 (1994)

[11] L. Civale, A.D. Marwick, T.K. Worthington, M.A. Kirk, J.R. Thompson, L. Krusinelbaum, Y. Sun, J.R. Clem and F. Holtzeberg *Phys. Rev. Lett.* **67**, 648 (1991)

[12] S.K. Gupta, Shashwati Sen, J.C. Vyas, S.P. Pai, R. Pinto, V.C. Sahni, *Physica C* **324**, 137 (1999)

[13] J.E. Evetts and B.A. Glowacki, *Cryogenics* **28**, 641 (1988)

[14] A.A. Polyanskii, A. Gurevich, A. E. Pashitskii, N.F. Heinig, R.D. Redwing, J.E. Nordman and D.C. Larbalestier, *Phys. Rev. B* **53**, 8687 (1996)

[15] J. Albrecht, S. Leonhardt and H. Kronmuller, *Phys. Rev. B* **63**, 014507 (2001)

[16] Ch. Jooss, L.O. Kautschor, M.P. Delamare, B.Bringmann, K. Guth, V. Born, S. Sievers, H. Walter, J. Dzick, J. Hoffmann, H.C. Freyhardt, B. de Boer, B. Holzapfel and F. Sandiumenge, *Mat. Res. Soc. Symp. Proc*. **659**, 11711 (2001)

[17] Ch. Jooss, R. Warthmann and H. Kronmuller, *Phys. Rev. B* **61**,12433 (2000)

[18] J. Mannhart, P. Chaudhari, D. Dimos, C.C. Tsuei and T.R. McGuire, *Phys. Rev. Lett*. **61**, 2476 (1988)

[19] M. Tinkham, *Introduction to Superconductivity*, 2nd Edition, McGraw-Hill, New York (1996)

[20] L.W. Song, E. Narumi, F. Yang, D.T. Shaw, H.M. Shao and Y.H. Kao, *J. Appl. Phys*. **69**, 1538 (1991)

[21] E.A. Pashitskii, V.I. Vakaryuk, S.M. Ryabchenko and Yu. V. Fedotov, *Low Temp. Phys*. **27**, 96 (2001)

[22] G. Blatter, M.V. Feigel'man, V.B. Geshenkbein, A.I. Larkin and V. M. Vinokur, *Rev. Mod. Phys*. **66**, 1125 (1994)

[23] A. Gurevich and E.A. Pashitskii, *Phys. Rev. B* **57**, 13 873 (1998)

8 LAGB $J_c(\phi)$ Measurements

This chapter details the results of $J_c^{GB}(\phi)$ measurements, in which the applied magnetic field is rotated in the *ab*-plane of the LAGB track. For fields aligned with the boundary, a marked vortex channelling minimum is observed in $J_c^{GB}(\phi)$. This provides clear evidence that the electronic response of LAGBs in YBCO is dominated by channelling. In an adaptation of a model previously developed for twin plane channelling, a good description of the LAGB behaviour is found. The presented model describes the $J_c^{GB}(\phi)$ trace in terms of a transition from a kinked to collinear vortex structure and from GB to IG dominated pinning. The channelling effect is investigated through scaling of the critical kinking angle ϕ_K, the dependence of $dV/dJ(\phi)$, and on an artificial channel created by FIB milling.

8.1 Previous Work

The current understanding of the LAGB-vortex interaction almost universally considers a situation in which field is applied along the *c*-axis, being both parallel to the dislocation array and perpendicular to the transport current density (figure 6.4). As such, the existing understanding of *flux pinning* [1] and *flux channelling* [2,3] behaviour that occurs at LAGBs has generally been limited to this geometry. However, rotations of the magnetic field both *away* from the *c*-axis and *out* of the GB plane, can serve to highlight and differentiate pinning [4] and channelling effects - depending critically upon the rotation geometry.

This section details the results of experiments in which the applied field is rotated in the *ab*-plane of the track (termed ϕ-scans), as shown in figure 8.1. This geometry is advantageous for the study of LAGB-vortex interaction, as within the *ab*-plane the superconducting properties of YBCO are almost isotropic. As such, the orientation of the applied field may be varied with respect to the LAGB without encountering the additional complications associated with anisotropic superconductivity. To the author's knowledge, there are no reports of experiments performed in this geometry on grain boundaries – bulk, thin film, high angle or low angle.

This chapter finds that a close analogy in behaviour may be made between the vortex-twin plane and vortex-LAGB interaction. In a similar manner to LAGBs, measurements on twin boundaries reveal that they can display both flux pinning [5,6,7,8] and flux channelling [7,8,9,10] behaviour. The dominant effect is found to be dependent upon the direction of the

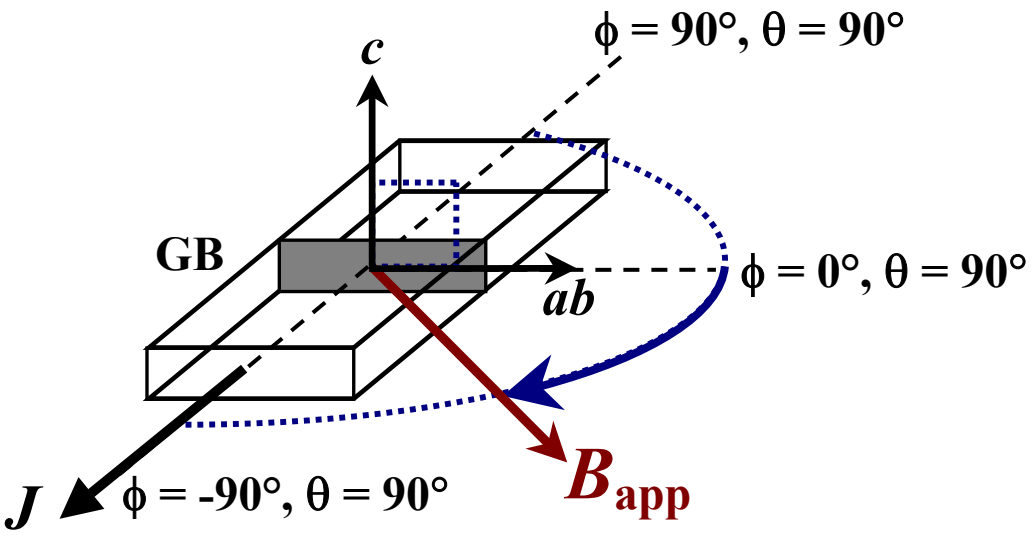

Figure 8.1. Experimental geometry of scan performed in chapter 8. Field is rotated in the *ab*-plane ($\theta = 90°$) where $\phi = 0°$ corresponds to alignment of the field with the LAGB plane and $\phi = -90°$ and $+90°$ correspond to field parallel and anti parallel to the current density, *J*.

Lorentz force [7], the magnitude of applied field and the temperature range [8]. The results found for scans on a LAGB in the geometry of figure 8.1 show a channelling effect that correlates strongly with the behaviour observed for a single domain twinning array [9].

8.1.1 Vortex Accommodation

Although dislocations are not formed intrinsically at twin boundaries, they still represent planar regions of locally reduced superconductivity [9,11]. This is attributed to a localised oxygen deficient zone and a tendency for twins to act as traps for point defects [12,13]. In a similar manner to a LAGB, the twin interface will possess an energy barrier, or pinning potential for vortices, equal to $\varepsilon = \varepsilon_{TP}$. The interaction of vortices with twin boundaries has been considered theoretically by Blatter *et al* [11]. In order for a vortex line to minimise its energy, it is expected to deform and gain energy from the attractive potential well produced by the boundary. The resulting reduction in the vortex line energy due to the trapping of a segment is balanced by an energy cost due to elastic deformation. The degree of deformation, and indeed if trapping occurs, depends critically upon the angle of the applied field with respect to the plane, ϕ. It has been shown that there are two main critical angles, ϕ_L and ϕ_k, the lock-in and kinking angles respectively. For $\phi < \phi_L$, vortices are locked to the attractive potential and will deviate from the external applied field direction. For $\phi_L < \phi < \phi_k$, a kinked vortex structure develops, with segments of flux line lying along the twin plane boundary. In general, the angle of applied flux will still deviate slightly from the net angle of internal flux, ϕ_B. For $\phi > \phi_k$, no accommodation to the twin plane is made, and the angle of the internal flux line reflects that of the external field. Figure 8.2 illustrates the three predicted structures for

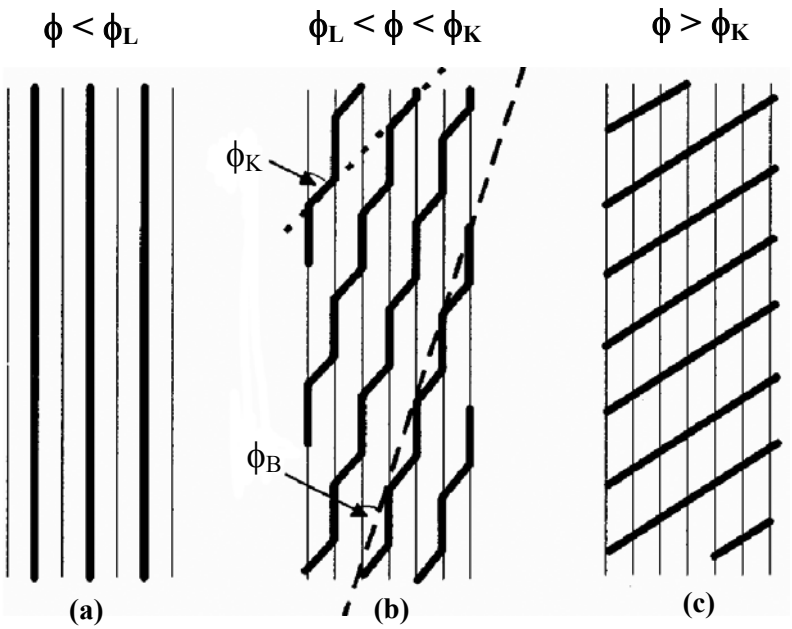

Figure 8.2. Vortex interaction (dark lines) with a twin array (light lines) yeilding (a) locked in [$\phi < \phi_L$], (b) kinked [$\phi_L < \phi < \phi_K$] and (c) collinear [$\phi > \phi_K$] vortex phases. For kinked vortices, the net field lies at an angle ϕ_B (Adapted from [14]).

vortices applied at an angle ϕ [14]. Similar phases may be expected to occur at the defect plane represented by a LAGB, and indeed evidence to this effect is presented in section 8.3.

8.1.2 Twin Plane Channelling and Pinning

The presence of a twinning array in a sample has been found to provide increased pinning at high temperatures [5,6], and easy flow channelling at lower temperatures [8,9,10]. The reason for this lies in the reduced temperature dependence of J_c expected for vortices residing in the 2-dimensional twin plane. This is discussed in chapter 7, and is a result of increased pinning due to a reduction in dimensionality of thermal fluctuations. Only for temperatures below a critical temperature, T_{cross} (directly comparable to T^* for a LAGB in chapter 7) does the pinning strength in the untwinned regions exceed that in the twin [10]. The result is a transition from pinning to channelling with decreasing temperature.

Magnetisation studies by Oussena *et al* [8] first provided definitive proof that the presence of single domain twins[#] can reduce the hysteresis width, and hence J_c, for fields closely aligned with the twin planes. In a follow up study [9], they performed measurements of the hysteresis width ΔM as a function of angle of rotation, θ, away from the *c*-axis and towards the *ab*-plane. Rotating the field out of the twin plane resulted in a marked increase in ΔM, a behaviour they found to be consistent with a transition from a locked in to a collinear vortex structure (figure 8.2).

[#] e.g. only along the [110] direction

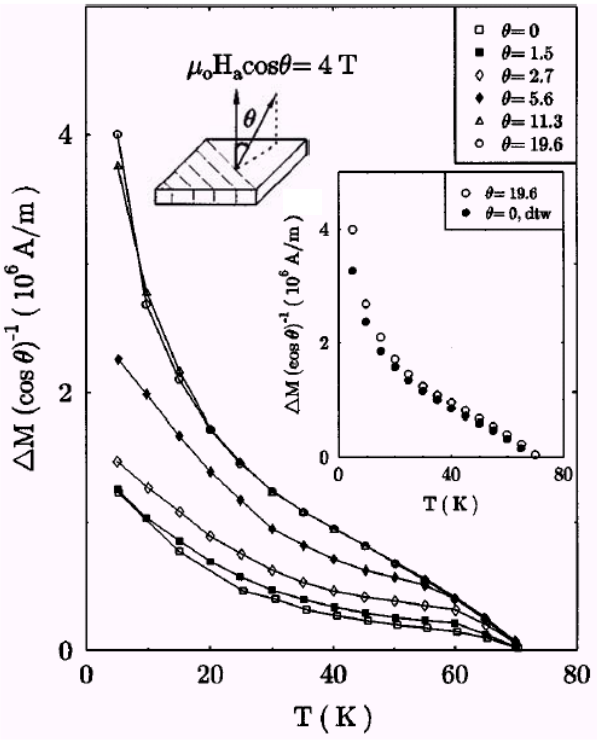

Figure 8.3. Temperature dependence of the magnetisation hysteresis width for field (4 T) rotated away from the twin plane by an amount θ [9]. As θ increases, the temperature dependence becomes stronger due to rotation of vortices from the locked to the kinked, and finally to the collinear state. For $\theta > \theta_K$, the dependence maps onto that of a detwinned sample at θ = 19.6° in the inset.

The transition can be seen in the temperature dependence of the hysteresis width as field is rotated out of the twin planes. This is shown in figure 8.3, where the inset gives the experimental geometry. For fields at an angle less than a value ϕ_K they found a weak temperature dependence reflecting the reduced dimensionality and pinning associated with vortices locked into the twin plane. For fields at an angle greater than a value θ_K they found a stronger temperature dependence that *mapped* onto a response obtained from a detwinned sample. The implication is that for $\theta > \theta_K$, no segments of vortex kink into the twin plane, and the magnetic response is, as such, simply that of the untwined region.

Normalised plots of $\Delta M(\theta)$ with angle away from the twin planes are shown in figure 8.4(a). They reveal the dip in $J_c(\theta)$ found for vortex alignment with the planes (θ = 0°) and show that the angle θ_K is strongly temperature dependent. This increase of θ_K with decreasing T was linked to the increasing magnitude of critical current in the untwined regions. Figure 8.4(b) shows that all channelling dips measured at varying temperature scale onto a single curve by plotting the relative decrease $\Delta_R(\theta)$ against $\theta/[\Delta M(\theta_K)]^{1/2}$ where,

$$\Delta_R = \frac{\Delta M(\theta) - \Delta M(\theta_K)}{\Delta M(\theta_K) - \Delta M(\theta_L)} \tag{8.1}$$

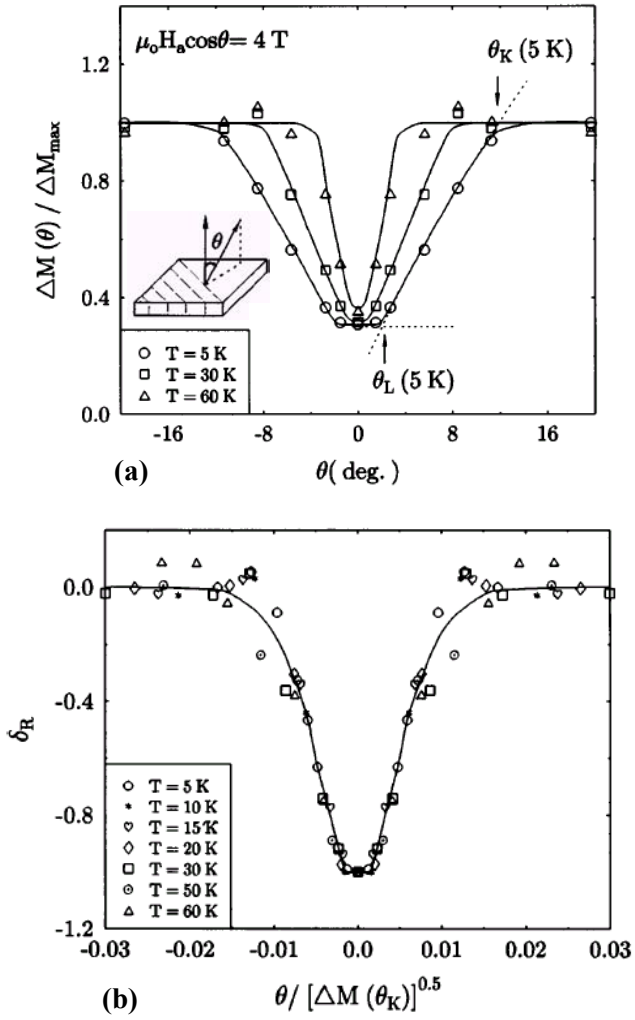

Figure 8.4.(a) Angular dependence of the normalised (to its maximum value) hysteresis width measured on a twinned YBCO sample at 4 T [9]. Curves show a dip at $\theta = 0°$ for fields aligned with the twin planes - see inset for geometry. (b) The curves in (a) scaled onto each other by plotting δ_R against $\theta/[\Delta M(\theta_K)^{1/2}]$ (see text).

where Δ_R equals -1 at the dip minimum ($\theta = 0°$) and 0 for $\theta \geq \theta_K$. The scaling law is therefore $\theta_K \propto [\Delta M(\theta_K)]^{1/2}$, and as the value $\Delta M(\theta_K)$ reflects J_c of the untwined regions, it indicates that θ_K is only determined by the value of pinning in the regions away from the twin. Scaling is therefore expected to be successful by changing J_c in the untwined regions either through temperature *or* field variation.

8.2 Lorentz Force Variation

In order to understand the variation of $J_c^{GB}(\phi)$ measured in the experiments of this chapter it is first important to understand the response expected from a purely intragranular track containing no defect plane, $J_c^{IG}(\phi)$. The effect of the presence of an artificial LAGB within a track will be superimposed upon this background variation.

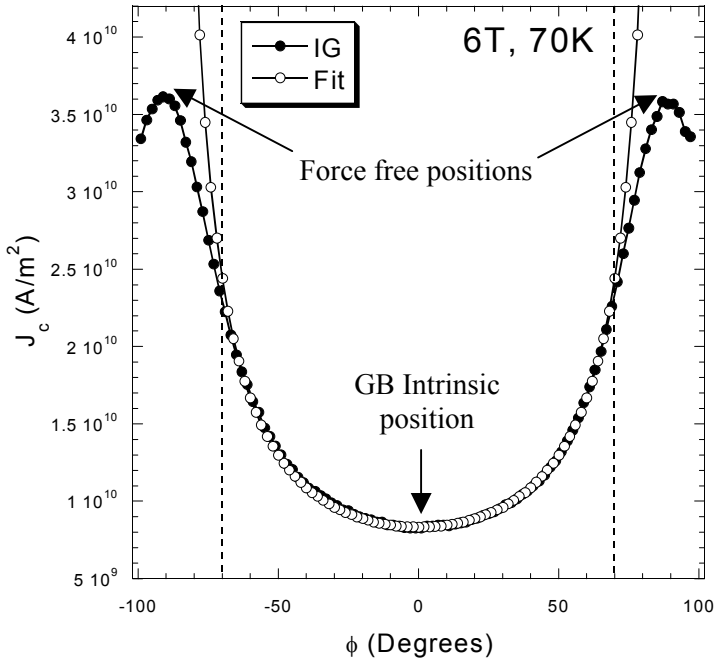

Figure 8.5. $J_c^{IG}(\phi)$ recorded on an IG track (w = 9.8 μm) for field rotation in the *ab*-plane according to figure 8.1 ($\theta = 90°$). The open circles show a fit to equation 8.2 where $J_c(\phi = 0°) = 8.35 \times 10^9$ A/m^2. The fit remains good up to ±70° (dashed lines)

An example measurement of intragranular $J_c^{IG}(\phi)$ is shown in figure 8.5 for 6 T, 70 K. Two mechanisms are at play over the course of such a field scan. The first is the intrinsic pinning mechanism, experienced for flux lines lying along the *ab*-plane. Intrinsic pinning acts to significantly increase $J_c(\theta = 90°)$ over $J_c(\theta = 0°)$, and as such is active over the whole angular range in figure 8.5. As discussed in section 2.7, the intrinsic mechanism is often ascribed to pinning to the layered nature of the YBCO cell structure [15] or the angular variation of the GL parameters [11].

The second mechanism at play is the variation in the Lorentz force on the vortices, $\boldsymbol{F_L} = \boldsymbol{J} \times \boldsymbol{B}$, as the field rotation varies the angle $\chi = \phi + 90°$ between $\boldsymbol{J}$ and $\boldsymbol{B}$. At $\phi = \pm 90°$, F_L is nominally zero, giving the force free position. The measured $J_c(\phi = \pm 90°)$ is actually finite, but significantly larger than $J_c(\phi = 0°)$ - which marks the maximum Lorentz force position $F_L = JB$, as field and current are perpendicular. The result is that rotation in ϕ produces a smooth oscillation of $J_c^{IG}(\phi)$, peaking at the force free configuration, dipping to a minimum at the maximum Lorentz position, which shall henceforth be termed the GB intrinsic position. Vortices are pushed upward and out of the sample surface for $-90° < \phi < 90°$, and downward through the substrate-film interface for $|\phi| > 90°$.

The variation may be fitted quite simply using equation 2.18, which gives $F_p = J_c B \sin(\phi+90°)$. At the GB intrinsic position, $\phi = 0°$, we thus find that $J_c(\phi = 0°) = F_P(0°)/B$. Assuming that F_p remains constant during the scan we can say that,

$$J_c(\phi) = \frac{F_P(0°)}{B\sin(\phi + 90°)} = \frac{J_c(\phi = 0°)}{\sin(\phi + 90°)} \tag{8.2}$$

This very simple model fits very well up to angles $\phi \sim \pm 70°$, as shown in figure 8.5. A development of this model by Nishizaki *et al* [16] was found to complicate fitting and yield a less appropriate fit at high ϕ.

8.3 The LAGB Vortex Channelling Dip

8.3.1 Experimental Observation

Measurements were performed on a number of GB and IG tracks for 4.9°, sample pk2. Figure 8.6 shows a typical measurement of $J_c(\phi)$ recorded for both GB and IG. The smooth variation described by equation 8.2 can be seen in the IG trace, dipping to a minimum at the GB intrinsic position and a maximum at the force free position. A marked difference, however, may be seen in the GB behaviour. At *high angles*, $|\phi| > \phi_K$, the $J_c^{GB}(\phi)$ curve follows that of $J_c^{IG}(\phi)$, but at a lower magnitude of J_c. At *lower angles*, $\phi < \phi_K$, a pronounced dipping of the $J_c^{GB}(\phi)$ curve away from $J_c^{IG}(\phi)$ is found to occur. The result is that the $J_c^{GB}(\phi = 0°)$ minimum is almost an order of magnitude smaller than the $J_c^{IG}(\phi = 0°)$ minimum. The presence of this dip may be attributed to a pronounced channelling effect associated with flux alignment to the LAGB plane.

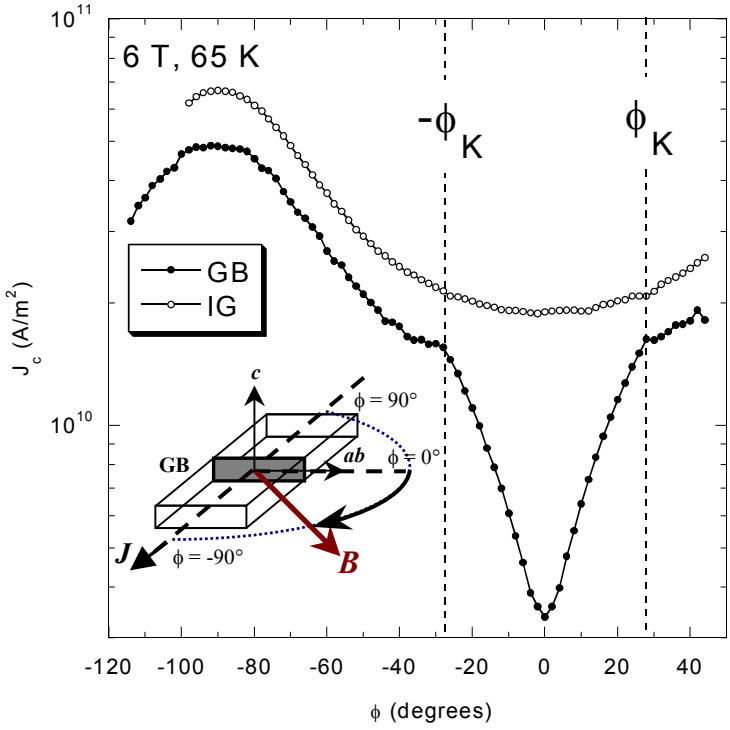

Figure 8.6. $J_c(\phi)$ measurements on GB and IG tracks on sample pk2, a 4.9° boundary. The inset gives the rotation geometry, which occurs in the *ab*-plane. For field $-\phi_K < \phi < \phi_K$ the GB trace exhibits a large channelling minimum as field aligns to the LAGB. Both track widths are $w = 9.8$ μm and $Q = 2.4$.

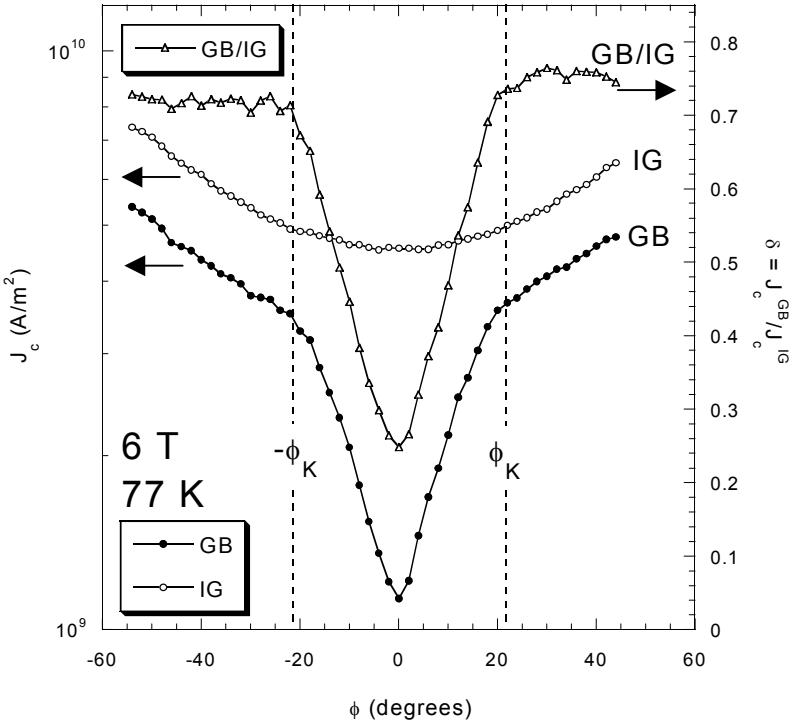

Figure 8.7. $J_c(\phi)$ recorded at 6 T, 77 K plotted for GB and IG on the left hand scale. The transparency ratio $\delta(\phi) = J_c^{GB}/J_c^{IG}$ is plotted on the right hand scale. Drastically reduced $\delta(\phi)$ is found for $-\phi_K < \phi < \phi_K$.

Figure 8.7 shows a close up of the channelling region at 6 T and 77 K, where $J_c(\phi)$ is plotted on the left hand axis and the ratio $\delta(\phi) = J_c^{GB}/J_c^{IG}$ is plotted on the right hand axis. For $|\phi| > \phi_K$ the ratio $\delta(\phi)$ remains approximately constant $\delta(\phi) \sim 0.7 - 0.8$, reflecting the same dependence on ϕ for IG and GB. For $-\phi_K < \phi < \phi_K$ ($|\phi| < \phi_K$) however, the ratio becomes angle dependent and drops off to $\delta(\phi) \sim 0.2 - 0.3$.

8.3.2 LAGB ϕ Channelling Model

It is proposed that the drop in $J_c^{GB}(\phi)$ over the angular extent $-\phi_K < \phi < \phi_K$ represents the presence of a strong channelling effect, reminiscent of that seen by Oussena *et al* for a twinning array [9]. The treatment that follows is an application of their analysis to a LAGB.

For field applied along the direction of the boundary ($\phi = 0°$), flux at the LAGB is channelled in the *c*-direction. This is due to the local reduction in $J_c = j_c^{GB}$ (see chapter 6) at the interface *and* a Lorentz force acting parallel to the defect plane. Dissipation will only occur at the GB as vortices in the banks remain pinned because local $j_c^{IG} > j_c^{GB}$. As the applied field is rotated in the *ab*-plane away from the GB, a kinked vortex structure develops as illustrated in figure 8.8 for a single vortex at an angle $\phi < \phi_K$. J_c of the track is now determined by the channelling of vortex segments that reside within the LAGB plane. The segments are of a length $L_K < w$ (where w is the track width) that decreases with increasing ϕ. Finally, at ϕ_K, $L_K = 0$, and a

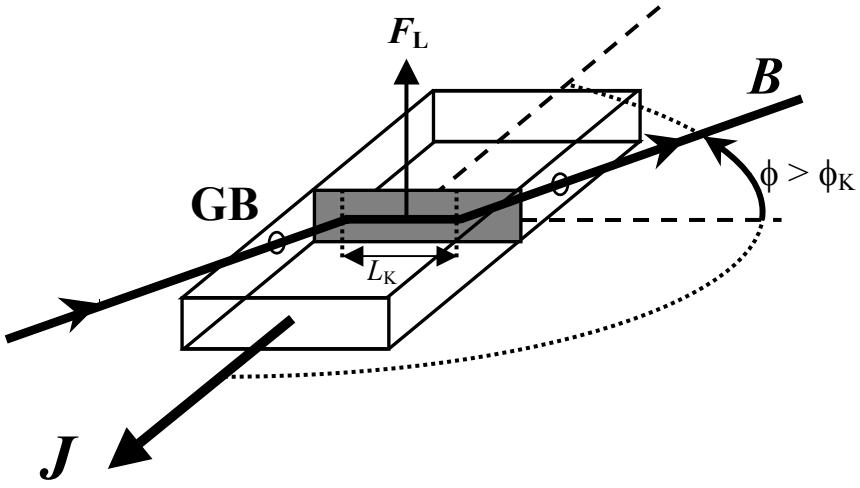

Figure 8.8. Possible vortex kinking occurring at the LAGB for angle of applied flux $\phi > \phi_K$. A vortex segment of length L_K resides within the LAGB.

rectilinear vortex structure is regained [11]. It is expected from studies on twins [17] that kinks will actually organise into chains so the LAGB will still be fully occupied but now by numerous vortex segments. This possible scenario is illustrated in figure 8.9.

The channel produced by the LAGB will become less effective if vortices are only partly trapped in such a manner. For field at an angle $\phi < \phi_L$, the whole length of vortices will be trapped, ($L_K = w$) which will experience a pinning force $f_{GB}(\phi < \phi_L) = f_{GB}(0°)$. Accordingly, for $\phi < \phi_L$ no change in J_c^{GB} should be observed with ϕ, as vortices remain locked in position. ϕ_L is not experimentally observed in the LAGB channelling results, but this may be partly due to the resolution of the measurements; steps of 2° in ϕ were performed across the whole scan range and so a lock-in angle of $\phi_L \sim 1°$ or less could exist. For simplicity, and due to the lack of its observation, for this treatment the magnitude of ϕ_L is assumed to be zero.

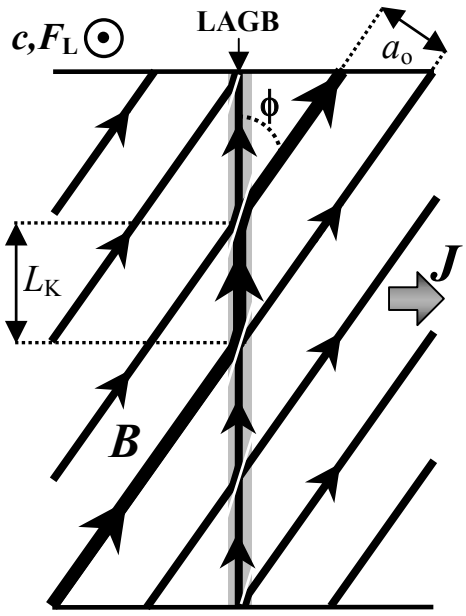

Figure 8.9. Proposed arrangement of kinked vortices at the LAGB for flux applied at $-\phi_K < \phi < \phi_K$. Multiple segments of length L_K lead to full occupation of the LAGB – bold vortex is highlighted as an example (after [17]).

For $0° < \phi < \phi_K$ segments of vortex within the GB will experience an increased pinning force, as they constitute part of a vortex structure that partly resides in the relatively strongly pinned IG regions. As ϕ increases, the length of the trapped segments decreases and so the average pinning force per unit length on the segments will increase. This explains the increase of $J_c^{GB}(\phi)$ with increasing ϕ (for $\phi \leq \phi_K$) as a transition from GB to IG dominated

dissipation. The increase in pinning force with rotation may be modelled as a function of the fractional change in segment length $\delta L_K/L_K$ as,

$$f_{GB}(\phi) - f_{GB}(0°) = -\left[f_{IG} - f_{GB}(0°)\right]\frac{\delta L_K}{L_K} \tag{8.3}$$

where f_{IG} is the pinning force in the IG regions. We can estimate $\delta L_K/L_K$ as a function of ϕ by using a geometrical argument. From figure 8.9, we can say that (for small angles) $a_o = \phi L_K$, and by differentiating we find $\delta L_K = -(a_o/\phi^2)\delta\phi = -L_K\delta\phi/\phi$. This gives us the result that $\delta L_K/L_K = -\delta\phi/\phi = -\phi/\phi_K$, where we have used $\delta\phi/\phi \sim \phi/\phi_K$. This is sensible, as at $\phi = \phi_K$ we find $\delta L_K/L_K = -1$, corresponding to a 100% change in segment length (from finite to zero). In addition, at ϕ_K both sides of equation 8.3 become equal to $f_{IG} - f_{GB}(0°)$, where we have used the relation $f_{GB}(\phi_K) = f_{IG}$.

Using equation 8.3 we can investigate the predicted dependence of the *relative decrease* in $J_c^{GB}(\phi)$. In a similar manner to Oussena *et al* we define this simply as,

$$\Delta_R = \frac{J_c(\phi) - J_c(\phi_K)}{J_c(\phi_K) - J_c(0°)} \tag{8.4}$$

which equals -1 at the dip minimum and 0 for $\phi \geq \phi_K$. We can approximate equation 8.4 by replacing J_c with relevant pinning forces and then substituting with equation 8.3 to find,

$$\Delta_R \approx \frac{f_{GB}(\phi) - f_{IG}}{f_{IG} - f_{GB}(0°)} = -\left(\frac{\delta L_K}{L_K}\right) - 1 = \left(\frac{\phi}{\phi_K}\right) - 1 \tag{8.5}$$

The result is a predicted linear increase of Δ_R with angle ϕ up to ϕ_K, at which point the IG properties of the LAGB track take over and determine the vortex pinning force.

The magnitude of ϕ_K as calculated by Blatter *et al* [11] is expected to be temperature independent and vary with GB pinning potential as

$$\phi_K \propto \varepsilon_{GB}^{1/2} \tag{8.6}$$

For higher fields however, an additional decrease was expected for a twin array, as a function of twin plane spacing and a_o [11]. As will be shown in the next sections, for a LAGB in the *ab* scan geometry, ϕ_K is found to be both extremely temperature and field dependent.

8.3.3 Temperature Dependence

An example of the temperature dependence of ϕ_K and the channelling effect is shown in figure 8.10 for an applied flux density of 6 T. Also plotted is an example IG trace recorded at

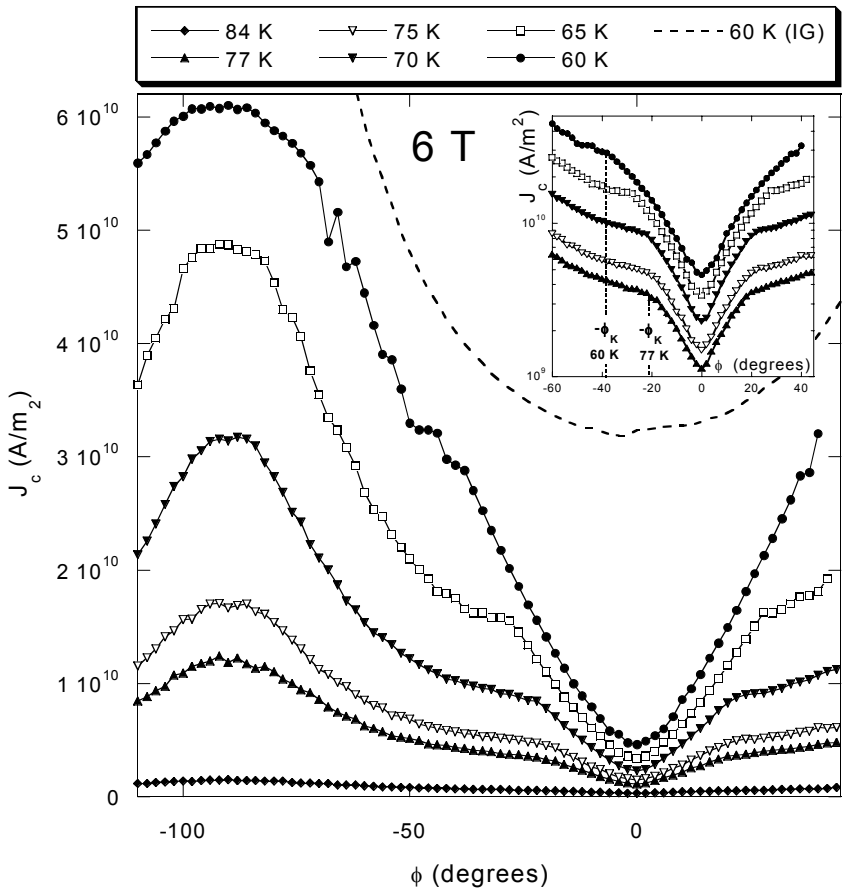

Figure 8.10. Temperature dependence of $J_c^{GB}(\phi)$ for an applied field of 6 T. $J_c^{IG}(\phi)$ is also plotted at 60 K for comparison. The inset shows the 60 to 77 K curves on a logarithmic plot. As temperature increases, ϕ_K decreases (marked for 60 K and 77 K). Both GB and IG tracks are w = 9.8 μm wide.

6 T, 60 K for comparison. As temperature decreases, both the magnitudes of $J_c(|\phi| > \phi_K)$ and of ϕ_K can be seen to increase significantly. As will be discussed in section 8.4, it is thought that the increase in width is due to the temperature dependence of the LAGB pinning potential ε_{GB}, in equation 8.6.

The temperature dependence of the transparency parameter $\delta = J_c^{GB}/J_c^{IG}$, for the data in figure 8.10 is shown in figure 8.11. Error bars of ± 10% are plotted for example on the 60 K trace, assuming ± 5% errors in both track width and film thickness[#]. There are three interesting features on this plot. The first is that for $|\phi| > \phi_K$ the value $\delta \sim 0.7 - 0.8$ appears to be temperature independent. Secondly, at ϕ_K the onset of the channelling effect is manifest as a very sharp decrease in $\delta(\phi)$ at a temperature dependent value of ϕ_K. Finally the transparency obtained for fields aligned with the LAGB is seen also to be temperature dependent, increasing from 0.15 to 0.25 as T is increased. In this $\phi = 0°$ position, the whole length of vortices reside within the LAGB plane - the segment length becomes equal to track width, $L_K = w$. The increase in δ with temperature can be ascribed therefore to the reduction in dimensionality of thermal fluctuations. This agrees well with the increase in δ at higher

[#] Fractional errors were combined in quadrature to give a ±7% error in J_c and ±10% error in the ratio δ.

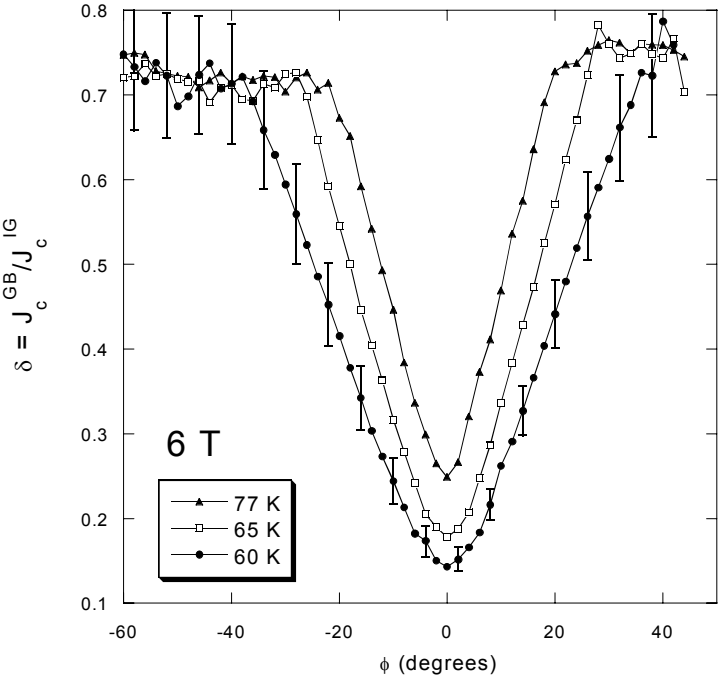

Figure 8.11. $\delta(\phi) = J_c^{GB}/J_c^{IG}$ measured at 6 T for various temperatures (data from figure 8.10). Error bars are plotted assuming ±5% track width and film thickness uncertainty (Q = 2.4, see section 4.2.5).

temperatures observed in section 7.2.3 for fields applied along the *c* axis (θ = 0°). The main difference is that in this *ab* geometry, no accommodation to the LAGB dislocation structure is possible, and the increase in δ is solely due to dimensionality effects. The increased value of B_{irr} for field applied along the *ab*-plane also rule out any contribution to the increase of $\delta = J_c^{GB}/J_c^{IG}$ due to a vanishing J_c^{IG} [18].

The effect of the degree of vortex alignment with the LAGB on the temperature dependence of $J_c^{GB}(\phi,T)$ is investigated further in figure 8.12. For various values of φ rotation, measurements of $J_c(T)$ were taken. The plots highlight the reduced temperature dependence for field applied along the LAGB plane in a similar result to that found in figure 8.3 for a twin array. As applied field is rotated out of the plane the kinked vortex structure develops, and a stronger dependence on temperature is obtained. This is due to a lessening in importance of the 2-Dimensional pinning effect, as kink segments L_K tend to zero in length. At φ = -48°, the temperature dependence can be seen to be identical to that obtained for an IG track also -48°, but scaled by a factor δ = 0.7 (see open symbols). It should be noted that the plot of figure 8.12 is also influenced by the temperature dependence of the channelling dip width, $\phi_K(T)$. The effect of this may be seen on the φ = -24° plot; for temperatures $T < \sim 70$ K, the curve probes the kinked vortex state and a reduced temperature dependence is found; for $T > \sim 70$ K the channelling width increases beyond φ = -24°, and a transition to a stronger dependence can be seen.

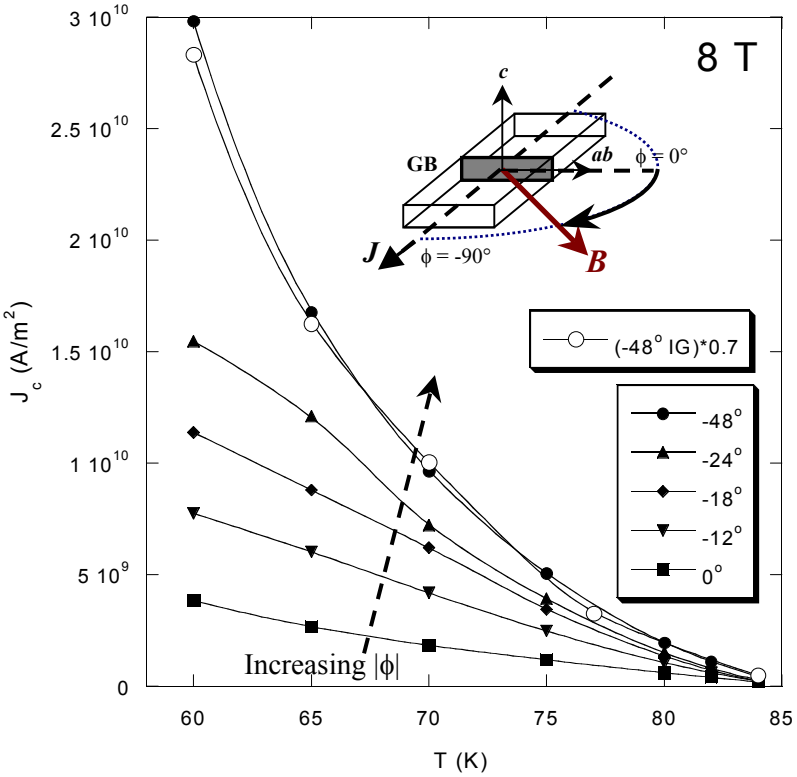

Figure 8.12. $J_c^{GB}(T)$ for different values of ϕ at 8 T. As field is rotated out of the pk2 LAGB plane, the temperature dependence of J_c^{GB} increases. By ϕ = -48°, the dependence matches that measured in an IG track at ϕ = -48° scaled by δ = 0.7. Lines are a guide to the eye.

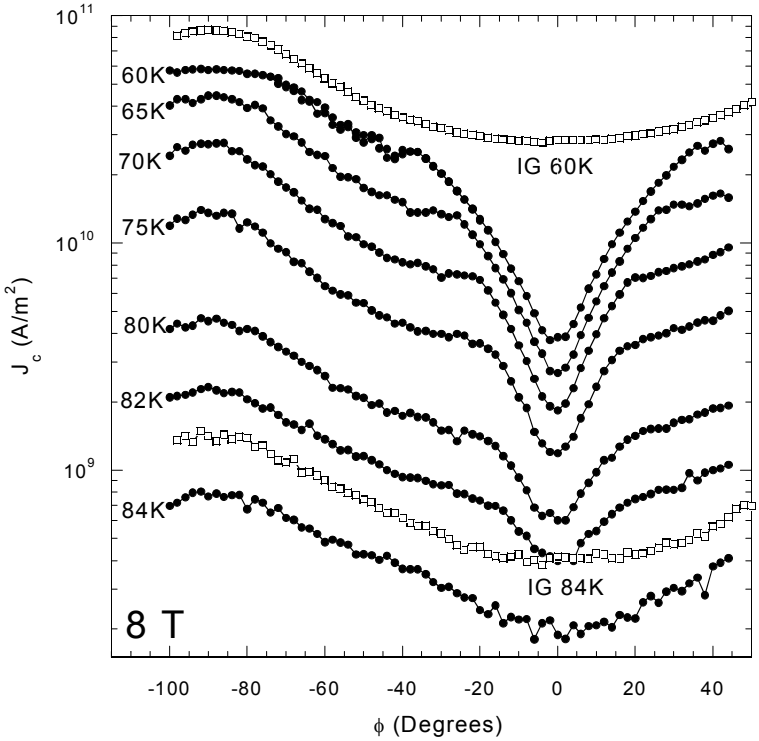

Figure 8.13. $J_c(\phi)$ measurements at 8 T for increasing temperature up to 84 K. Destruction of the channelling dip occurs at higher temperature as the effectiveness of the channel becomes reduced. IG plots at 60 K and 84 K are shown for comparison (open symbols).

The high field, high temperature structure of the channelling dip can be seen more clearly in figure 8.13. The figure shows LAGB ϕ scans at 8 T for temperatures up to 84 K. With increasing temperature, the reduction in ϕ_K previously mentioned can be seen. For sufficiently large T however, the dip becomes smeared and disappears at 84 K. This is probably due to the approach of the irreversibility line; the channel will become less effective as J_c^{IG} approaches J_c^{GB}. The V-I characteristics at 84 K, 8 T were found to display power law-like nature, indicating proximity to B_{irr}, but still possessed negative curvature on a double logarithmic plot – signifying they were measured below B_{irr} [19]. Such V-I curvature is to be expected, as E-fields will become less localised, increasing creep effects (chapter 6).

8.3.4 Field Dependence

Figure 8.14 shows the development of the channelling dip at 75 K for field magnitudes ranging from 1 T to 8 T. As with increasing temperature, increasing the applied field leads to a reduction in the channelling width, ϕ_K. An IG trace recorded at 2 T is also shown for comparison. At 8 T, the channelling dip is seen as a very marked drop in J_c^{GB} for fields closely aligned to the LAGB, with $\phi_K \sim 20°$. As field is decreased, ϕ_K increases and the dip expands to dominate an increasing region of the $J_c(\phi)$ scan, where at 2 T, $\phi_K \sim 40°$. For 1 T applied field, the kink in $J_c^{GB}(\phi)$ disappears, implying that channelling of some description occurs up to the force free peak itself.

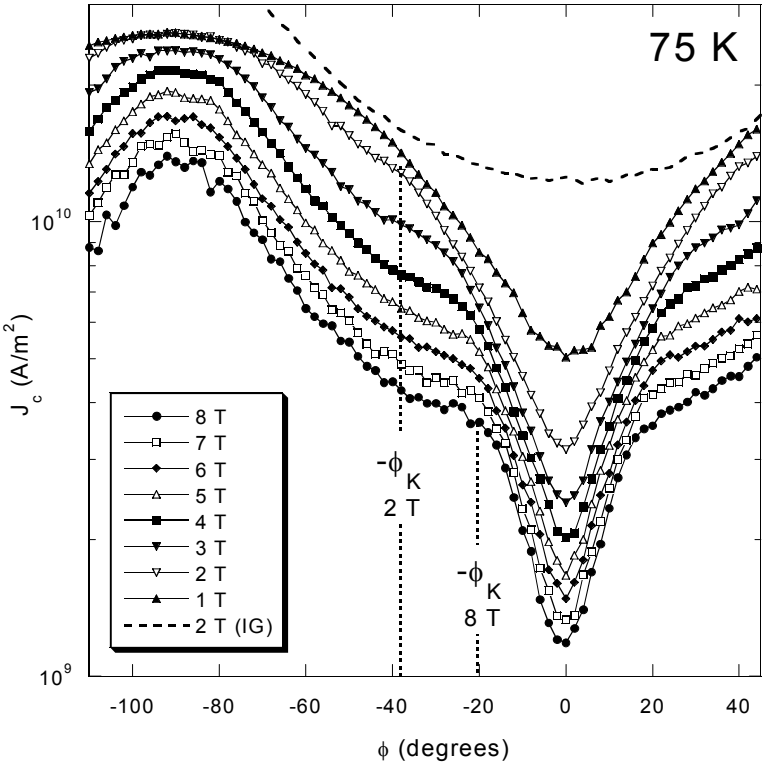

Figure 8.14. Field dependence of $J_c^{GB}(\phi)$ at 75 K compared to a $J_c^{IG}(\phi)$ trace at 2 T. ϕ_K decreases with increasing field as indicated at 2 T and 8 T. Both GB and IG tracks are $w = 9.8$ μm wide, $Q = 2.4$.

The field dependence of the transparency, $\delta(B)$, is shown in figure 8.15(b) for the ϕ-scans performed at 65 K and 2-8 T plotted in 8.15(a). As can be seen, for $|\phi| > \phi_K$ the result that $\delta \sim 0.7$ - 0.8 appears field (as well as temperature) independent. This is more evidence that beyond the angular range of channelling effects, J_c^{GB} reflects the behaviour of J_c^{IG}. Only for the 2 T scan, for which no break off in channelling effects may be seen, does δ vary at high angles. In addition, it should be noted that the value of $\delta(\phi = 0°)$ is also approximately constant with field, unlike its temperature dependence.

One possible cause of a decrease in ϕ_K with field could be due to a decrease in vortex segment length within the LAGB with increasing B. This is because, for a given angle ϕ, a decrease in $a_o(B) \sim \phi L_K$ (see figure 8.9) occurs. As will be shown in section 8.4 however, a more quantitative link may be made between ϕ_K and the magnitude of the IG critical current, which is believed to stem from the field dependence of $\varepsilon_{GB}(B)$.

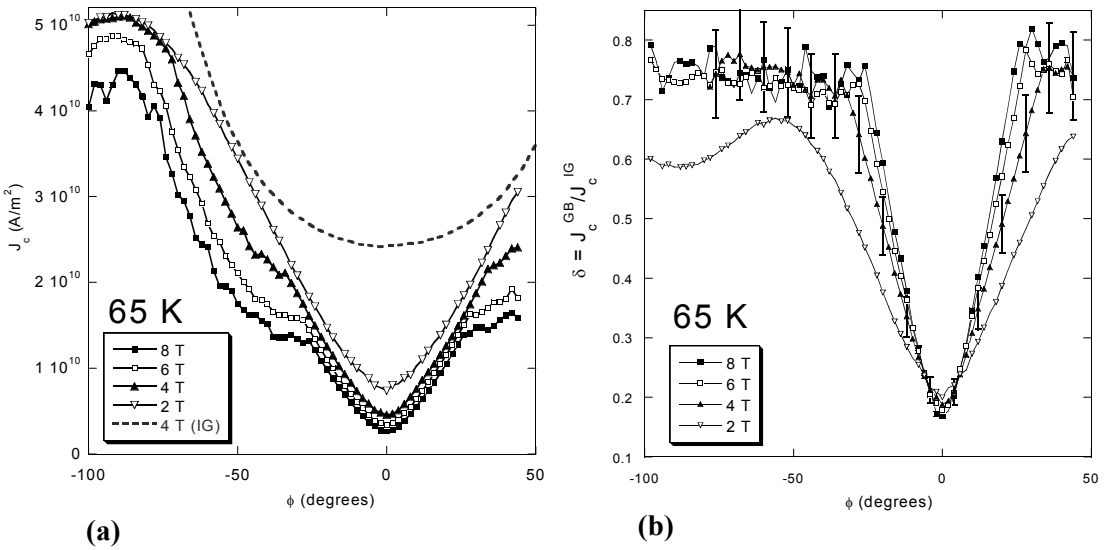

Figure 8.15. (a) $J_c^{GB}(\phi)$ measured at 65 K for various fields and (b) the field dependence of the ratio $\delta(\phi) = J_c^{GB}/J_c^{IG}$. $\delta(B)$ is approximately independent of field at $\phi = 0°$ and $\phi > \phi_K$ except at low field.

8.3.5 Track Variability

It should be noted that although similar behaviour was measured for all GB and IG tracks on sample pk2, the value of $\delta(\phi)$ for $|\phi| > \phi_K$ was found to vary slightly. For one track, IG3, the ratio was found to be $\delta(\phi) \sim 1$. This can be seen in figure 8.16, where the results of tracks IG3, IG2 and GB3 are plotted at 77 K and 4 T. All possessed the same track width $w = 9.8$ μm, and the IG tracks were both of the same length ($Q = 2.4$). The difference in behaviour may be attributed to the variability of the properties of the IG film across the sample. Error bars are plotted assuming the ± 5% variation in film thickness and ± 5% error in

track size previously stated. The consequence of $\delta(\phi) = 1$ for fields away from the GB plane is an effectively transparent interface. Credence, however, is lent to the appropriate value being $\delta(\phi) \sim 0.7$ - 0.8, as the tracks IG3 and GB3 that produce this ratio were found to possess the same J_c and *V-I* above the merging field *B** (see chapters 6 and 7) - this is indicative of the fact that both tracks possess IG regions with the same superconducting properties.

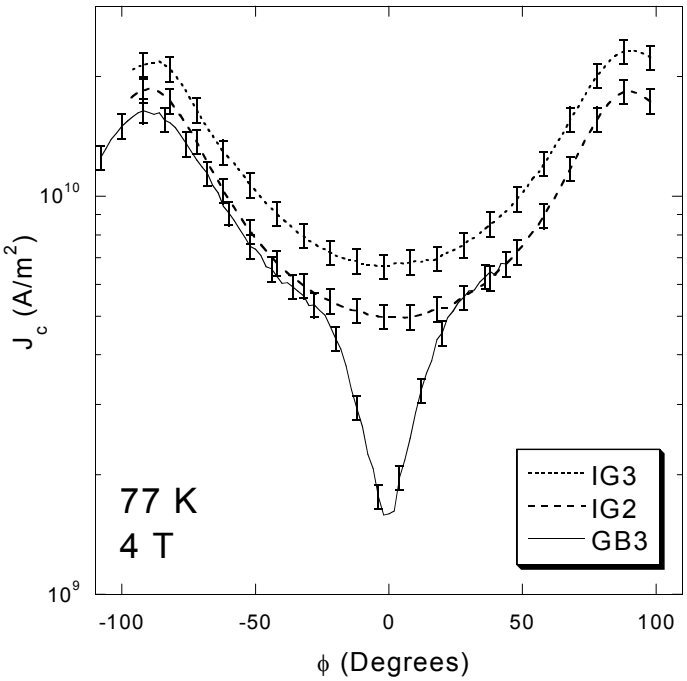

Figure 8.16. $J_c(\phi)$ measurements taken from three tracks, GB3 (line), IG2 (dashed) and IG3 (dotted). Error bars of ± 7 % (± 5 % in track with and film thickness) are plotted.

8.4 Scaling of Channelling Data – the Dependence of ϕ_K on J_c

In order to investigate the dependence of the channelling dip on *B* and *T*, and to test the validity of equation 8.5, the background Lorentz force variation (section 8.2) must first be removed. This was performed in the following manner, an example of which is shown in figure 8.17 for 2 T and 75 K. The background variation was taken to be that measured in the IG track (open circles) which was scaled onto $J_c^{GB}(\phi)$ at $|\phi| > \phi_K$ (black line) using the factor $\delta = 0.8$ (see inset figure 8.17). Where no comparable IG scan was available, the model of section 8.2 was used – which proved fine for $\phi < 70°$. We then subtract the fitted curves value at $\phi = 0°$ from itself, resulting in just the additional J_c expected to occur solely due to the reduction in Lorentz force (black crosses). The final step was to simply subtract this variation from the measured $J_c^{GB}(\phi)$ trace giving the variation in J_c^{GB} only due to the channelling interaction (black squares). The results show an approximate linear increase in $J_c^{GB}(\phi)$ with ϕ up to ϕ_K as predicted by equation 8.5. For $|\phi| > \phi_K$ figure 8.17 shows a constant $J_c^{GB}(\phi)$

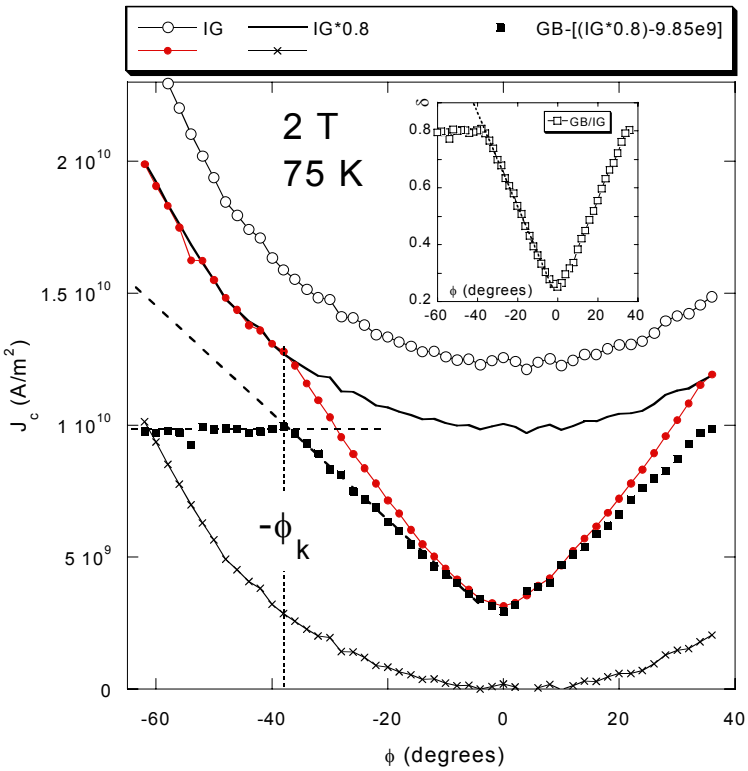

Figure 8.17. Process by which the background Lorentz variation was subtracted from $J_c^{GB}(\phi)$ for 2 T, 75 K - see text for explanation. The inset shows $\delta(\phi) = J_c^{GB}/J_c^{IG}$. After removal of the variation an approximate linear increase in J_c^{GB} with ϕ is found within the channelling dip and a constant $J_c^{GB}(|\phi| > \phi_K)$.

consistent with the collinear vortex structure – no segments kink into the LAGB and no channelling occurs. This is in agreement with the fact that at ϕ_K, $f_{GB}(\phi_K) = f_{IG}$, which was assumed to be independent of angle in section 8.3.2.

After following the above procedure to remove the effects of Lorentz force modulation, the remaining data was normalised to obtain the relative decrease Δ_R, defined by equation 8.4. The results are plotted in figure 8.18(a) for three channelling minima recorded at 60 K, 65 K and 77 K in an applied flux density of 6 T. The linear increase in Δ_R as field rotates away from the LAGB agrees well with equation 8.5, but deviates at low temperatures and small ϕ. This deviation is possibly associated with the method used to remove the Lorentz force variation, which assumed vortices lay in the same direction as the applied field – in fact, kinked vortices deviate from the applied field direction by an amount dependent upon the angle of application, ϕ. However, this appears only to be problematic for large segment size L_K occurring at small ϕ.

In a remarkably similar result to that obtained by Oussena *et al* [9], the curves of figure 8.18(a) can be accurately scaled onto each other by simply plotting Δ_R against $\phi/[J_c^{GB}(\phi_K)]^{1/2}$. The results are shown in figure 8.18(b).

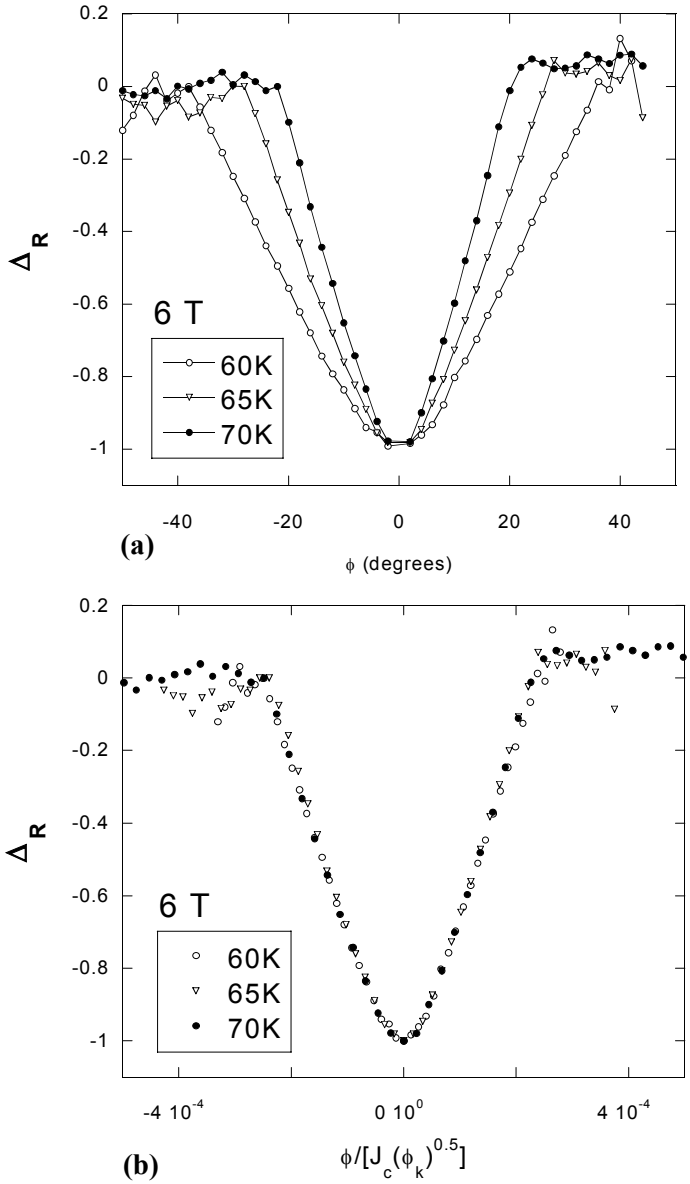

Figure 8.18.(a) The relative decrease Δ_R calculated using equation 8.4 for channelling dips measured at 6 T, for various temperatures. Dashed lines indicate approximate linear dependences of Δ_R on ϕ. (b) Scaling of the curves in (a) by plotting Δ_R against $\phi/[J_c^{GB}(\phi_K)]^{1/2}$ (see text).

As ϕ_K is dependent on the magnitude of J_c^{GB} at ϕ_K, a similar scaling result is expected if we vary the value of J_c^{GB} by changing the magnitude of applied field instead of temperature. Normalised plots of Δ_R with ϕ are shown in figure 8.19(a) for ϕ-scans taken at 65 K, 2 T, 4 T and 8 T. The plots all scaled well by again plotting Δ_R against $\phi/[J_c^{GB}(\phi_K)]^{1/2}$ in figure 8.19(b).

Scaling was found to break down at low temperatures and fields, where no ϕ_K could be identified, and at high fields and temperatures when the channelling dip begins to vanish.

The channel scaling implies the dependence

$$\phi_K \propto [J_c^{GB}(\phi_K)]^{1/2} \tag{8.7}$$

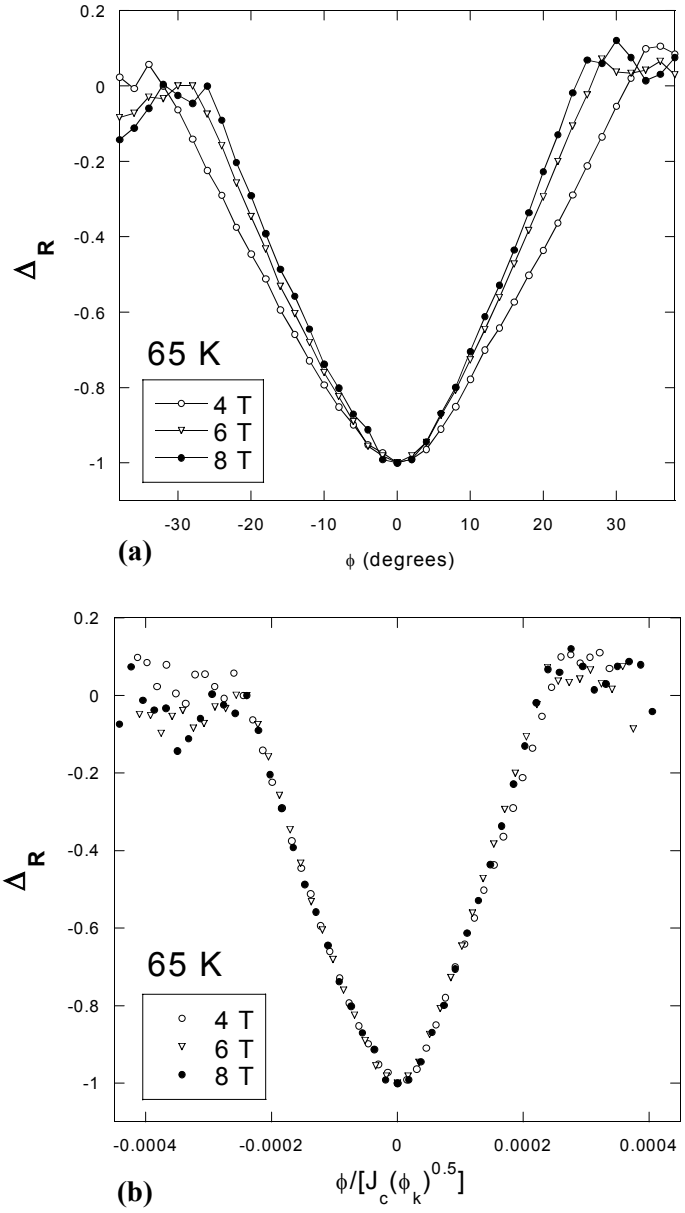

Figure 8.19.(a) The relative decrease Δ_R calculated using equation 8.4 for channelling dips measured at 65 K, for various applied fields. (b) Scaling of the curves in (a) by plotting Δ_R against $\phi/[J_c^{GB}(\phi_K)]^{1/2}$ (see text).

Attempts at scaling using a dependence other than the square root of equation 8.7 proved unsuccessful.

Within the model of section 8.3.2, the angle ϕ_K marks the point at which the pinning force $f_{GB}(\phi)$ becomes equal to the angular independent f_{IG} (where $f_{GB}(0°) < f_{IG}$). Evidence that the IG regions of the GB track do indeed determine J_c^{GB} for $|\phi| > \phi_K$ has been presented in sections 8.3.3 and 8.3.4. The measurements show that for angles greater than ϕ_K, $J_c^{GB}(\phi,B,T)$ varies proportionally to $J_c^{IG}(\phi,B,T)$ – in other words for $|\phi| > \phi_K$, $\boldsymbol{J_c^{GB}(\phi,B,T) = \delta J_c^{IG}(\phi,B,T)}$, where the value of $\delta \sim 0.7 - 0.8$ is independent of field, temperature and angle. For $|\phi| < \phi_K$, δ becomes extremely temperature, field and angle dependent.

The fact that measurements show proportionality rather than $J_c^{GB} = J_c^{IG}$ for $\phi > \phi_K$ may indicate two possible factors. Firstly, the difference may arise from a variability in IG properties across the film. As the error bars on plot 8.11 show, however, a ± 5% error in track width and film thickness is not sufficient to account for the difference alone.

Secondly, the difference may represent the insulating nature of the LAGB dislocation core array. Even for $|\phi| > \phi_K$, where no kinking into the LAGB is expected, and as such no channelling, the dislocation cores still represent an impediment to the supercurrent through a reduction in the effective cross sectional area (section 3.5). The factor $\delta = 0.7 - 0.8$ may therefore represent the channel model parameter δ_c, which gives the J_c^{GB} reduction from J_c^{IG} *solely* due to the cross section reduction. Although vortices are not channelled along the GB in the same manner at $|\phi| > \phi_K$ as for $|\phi| < \phi_K$, it is still reasonable to expect J_c^{GB} to be reduced - as the collinear vortex will still be depinned at the GB first, but resultant dragging will move the rest of the vortex. The same dragging will occur in the kinked vortex state, but J_c^{GB} will be further reduced by the channelling of vortex segments along the LAGB defect plane.

Oussena *et al* [9] explained the $\phi_K \propto [J_c^{GB}(\phi_K)]^{1/2}$ dependence by considering the work of Nelson and Vinokur [20]. Vortices which experience a Lorentz force *perpendicular* to a twin plane can become unpinned, forming loops extending a distance $l_\perp$ from the boundary. Nelson and Vinokur showed that $l_\perp \propto 1/J$, with J the driving current density producing the Lorentz force. By assuming vortex confinement to $l_\perp$ and not the potential barrier width, d_{eff}, they renormalized ε_{TP} (in equation 8.6 for a twin) by a factor $d_{eff}/l_\perp$, obtaining $\phi_K \propto (\varepsilon_{TP} d_{eff}/l_\perp)^{1/2} \propto [\Delta M(\phi_K)]^{1/2}$. This treatment would appear to be invalid for the transport geometry of figure 8.1. The driving Lorentz force is always parallel or anti parallel to the *c* direction, pushing vortices *along* the LAGB, not *out* as required by the Oussena *et al* model.

An alternate cause of the square root dependence can be found when one considers that the pinning potential ε_{GB} is related to the relative magnitudes of $J_c^{GB}(\phi = 0°)$ [or local j_c^{GB}] and J_c^{IG} [or local j_c^{IG}]. It may be roughly estimated therefore that the ratio $\varepsilon_{GB} \propto (J_c^{IG} - J_c^{GB})/J_c^{GB} = (J_c^{IG}/J_c^{GB}) - 1$. As $J_c^{IG} > J_c^{GB}$, and J_c^{GB} has a much weaker temperature dependence than J_c^{GB}, we can say to a first approximation that $\varepsilon_{GB} \propto J_c^{IG}$. Combined with equation 8.6, this assumption naturally leads to the fact that $\phi_K \propto (\varepsilon_{GB})^{1/2} \propto [J_c^{IG}(\phi_K)]^{1/2} \propto [J_c^{GB}(\phi_K)]^{1/2}$.

8.5 The *V-I* Characteristic and LAGB Channelling

Channelling along a LAGB is manifest in the two key measurements of (1) the *V-I* characteristic and its linear nature, and (2) the channelling minimum in $J_c^{GB}(\phi)$ with angle of

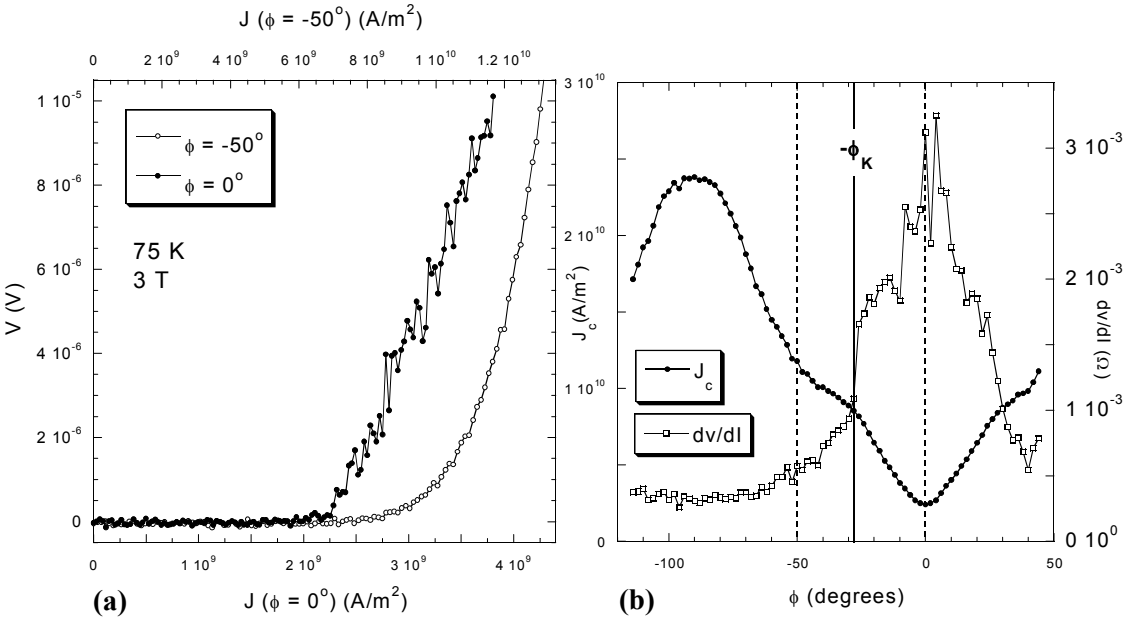

Figure 8.20.(a) *V-J* characteristics recorded at $\phi = 0°$ (bottom scale) and $\phi = -50°$ (top scale) at 75 K, 3 T. (b) $J_c^{GB}(\phi)$ plotted on the left hand scale and d*V*/d*I* on the right. The dashed lines indicate the angles at which the *V-J*s of (a) were taken.

applied field, ϕ. As discussed in chapter 6, for fields applied parallel to the *c*-axis, the *V-I* of a LAGB displays characteristic linearity and featuring. This linearity is well explained within a viscous flux flow (VFF) model, in which high LAGB *E*-fields push the *E-J* characteristics out of the creep dominated region and into the viscous regime. It will be shown in this section that both of these manifestations of flux channelling are closely linked.

Figure 8.20(a) shows the key result, *V-J*s taken from the LAGB track at angles $\phi = 0°$ and $\phi = -50°$ for 3 T and 75 K. At $\phi = 0°$ (bottom scale), the *V-J* is seen to possess a noisy linear behaviour, typical of the *V-J*s measured in chapter 6 and well interpreted in terms of viscous flux flow. Such *V-J*s were recorded at all angles of external field to the *c*-axis (section 9.3.6), provided the field was aligned within the LAGB i.e. $\phi = 0°$ or 180°. For field applied at an angle $|\phi| > \phi_K$ the *V-J* transition is found to be significantly different. An example at $\phi = -50°$ is plotted on the top scale of figure 8.20(a), demonstrating a curved nature reminiscent of flux creep rounding. This is consistent with a transition from a VFF determined *V-J* for fields aligned with the LAGB, and a creep dominated *V-J* for fields applied at an angle where no vortex kinking, and hence channelling is observed. The positions at which the measurements were taken are indicated by dashed lines in figure 8.20(b), which plots $J_c^{GB}(\phi)$ on the left hand scale and d*V*/d*I* (measured at $V_c^{GB} = 1\ \mu V$) on the right hand scale. The magnitude of d*V*/d*I* is seen to peak about $\phi = 0°$, consistent with the transition to flux flow resistivity.

For $|\phi| > \phi_K$, our model predicts dissipation determined by the IG regions of the track which can be seen qualitatively in the curvature of figure 8.20(a). The next step was to perform a direct comparison between the IG and GB *V-J* characteristics measured at $|\phi| > \phi_K$. An

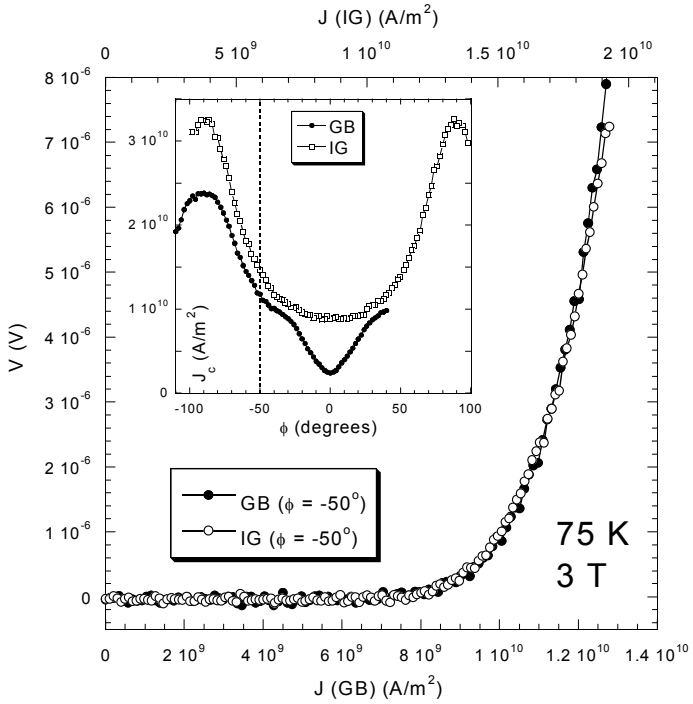

Figure 8.21. *V-J* curves taken at ϕ = -50°, 75 K and 3 T for both IG (open circles, top scale) and GB (filled circles bottom scale). The curves map onto each other and are displaced in *J* by a factor $\delta \sim 0.7$. The inset shows $J_c(\phi)$ for GB and IG and the location (dashed line) at which the *V-J*s were taken.

example is shown in figure 8.21 where GB and IG curves are plotted on the bottom and top scales respectively for ϕ = -50° at 3 T, 75 K (Q = 2.4, see section 6.6). In agreement with the J_c results of sections 8.3 and 8.4, the *V-J* characteristics map perfectly onto each other after a multiplication in *J* by a factor $\delta \sim 0.7$. This is yet more strong evidence that the same dissipative mechanism determines $J_c^{GB}(|\phi|>\phi_K)$ and J_c^{IG}.

The increase in GB d*V*/d*J* seen in figure 8.19(b) can also be compared directly to that

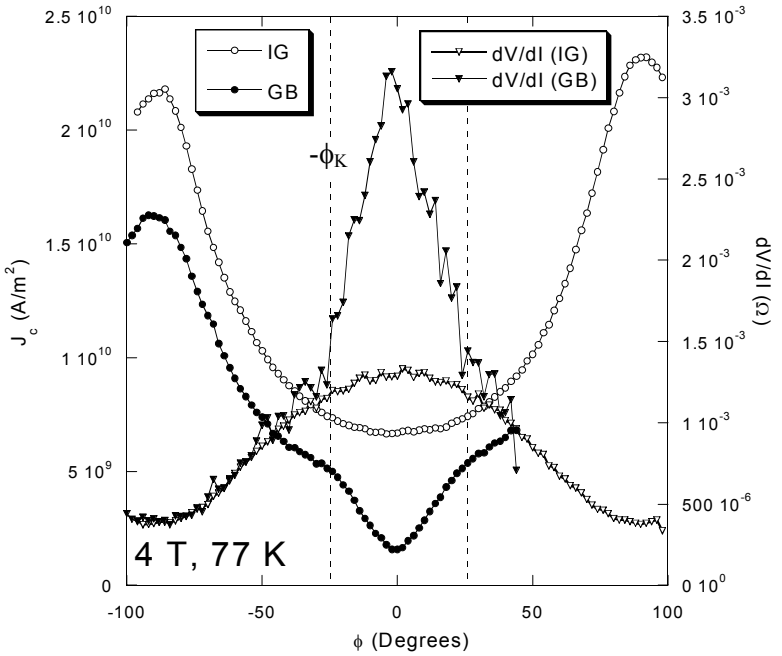

Figure 8.22. $J_c(\phi)$ for GB and IG at 4 T, 77 K plotted on the left hand scale (circles) and corresponding d*V*/d*I* (see text) on the right hand scale (triangles). d*V*/d*I*(GB) increases above d*V*/d*I*(IG) for $|\phi| < \phi_K$.

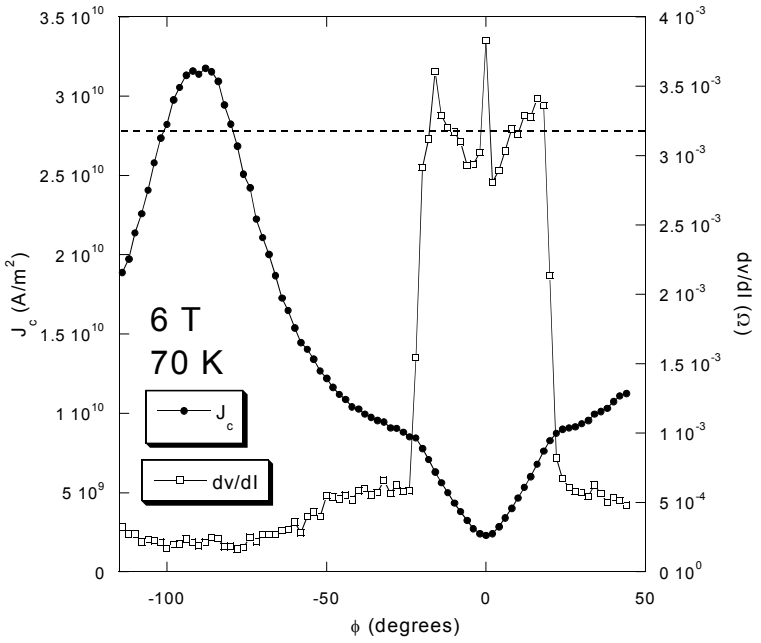

Figure 8.23. Example of lower temperature $J_c^{GB}(\phi)$ (left hand scale) and dV/d$I(\phi)$ (right hand scale) dependence at 6 T, 70 K. An almost discontinuous jump occurs at $\pm\ \phi_K$ to an approximate 3-3.5 $\times 10^{-3}$ Ω level (dashed line).

measured on an IG track. An example is shown in figure 8.22 for both GB and IG at 4 T and 77 K. On the left hand scale is plotted $J_c(\phi)$, showing a large channelling dip for $-25 < \phi < 25°$ in the GB trace. On the right hand scale is plotted the *V-I* characteristic gradient, dV/dI, for GB and IG tracks taken at comparable voltage criteria $V_c^{IG} = 2.4 V_c^{GB} = 2.4$ μV (see section 4.2.5). For $|\phi| > \phi_K$ both GB and IG gradients are seen to be very similar, which corresponds to the similar *V-I* characteristics. The GB gradient, however, diverges from that recorded for the IG track at $\pm\ \phi_K$, increasing to a maximum for $\phi = 0°$. As ϕ rotates in to the LAGB, *E*-fields increase as dissipation becomes more localised to the LAGB. The result is an increase of gradient as the viscous regime is accessed.

Although the change in dV/d$I(\phi)$ that occurs at $\pm\ \phi_K$ appears as a smooth onset in figure 8.22, it can, at lower temperatures, become an almost discontinuous jump. An example is shown in figure 8.23 at 6 T, 70 K. The commencement of vortex kinking into the GB results in a pronounced step up in dV/dI, over a range of just $\Delta\phi \sim 4°$, to an approximate plateau value of 3 - 3.5 $\times 10^{-3}$ Ω. For field rotation within the *ab*-plane of IG material, the flux flow resistivity is expected to be independent of angle as $B_{c2} \neq B_{c2}(\phi)$ (see equation 2.16). Accordingly, the fact that ρ_f is expected to strongly influence dV/dI over the angular range $-\phi_K < \phi < \phi_K$, may account for the plateau behaviour of figure 8.23.

In general however, *V-I* characteristics are only found to be linear for very close alignment of field to the boundary. Curvature is introduced more often in a gradual manner with rotation until at $\pm\ \phi_K$ an IG like rounding is found. As such, the shape of the dV/dI plot is found to be

influenced by the voltage criterion at which it is taken. An example of this behaviour is shown in figure 8.24 at 8 T and 80 K, where $J_c^{GB}(\phi)$ (left hand scale) and dV/dI (right hand scale) were extracted at 1, 4 and 8 μV respectively. The profile of dV/dI can be seen to transform from a peak at low criterion to a trough at high criterion. The increased V-I linearity for fields along the GB results in a reduced dependence of dV/dI on voltage criterion when compared to the curved characteristics at greater angles of ϕ.

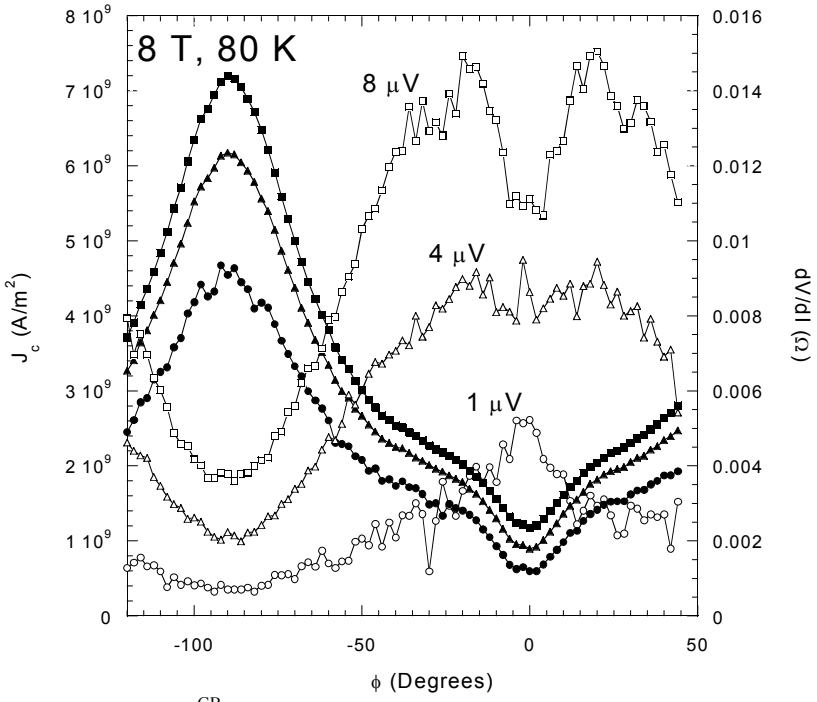

Figure 8.24. Dependence of $J_c^{GB}(\phi)$ (filled symbols) and dV/d$I(\phi)$ (open symbols) on the voltage criterion at which they are assessed: 1 μV (circles), 2 μV (triangles) and 8 μV (squares) at 8 T, 80 K. As criterion is increased a peak at $\phi = 0°$ can turn into a trough due to the relative linearity of the $\phi = 0°$ V-Js.

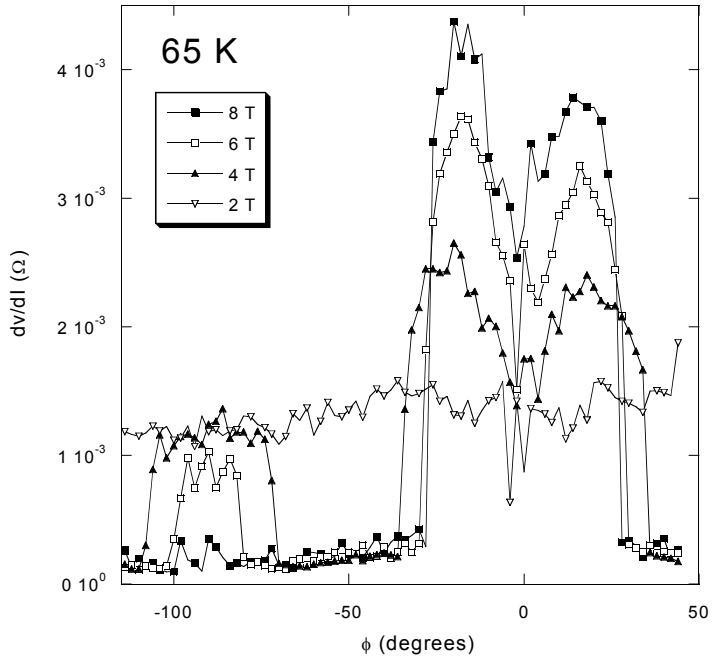

Figure 8.25. LAGB dV/d$I(\phi)$ for various fields at 65 K. At lower field and temperature there develops a gradient jump around the force free peak.

Finally, another effect has been detected in the dV/d$J(\phi)$ plots taken at lower temperatures. The jump in dV/dI found at $\pm \phi_K$ is accompanied by an additional jump that occurs close to the force free peak, and develops with decreasing field. An example is plotted in figure 8.25, at 65 K. As the effect occurs for $|\phi| > \phi_K$, it may be attributed to the IG properties of the LAGB track. However, similar jumps in dV/dI were not observed in scans on IG tracks at the same temperature and field. Only by lowering the temperature further were upturns found near the IG force free peak, at 60 K and 2 T. These were not discontinuous jumps as seen in the GB measurements however. It is possible the presence of the LAGB may exacerbate this effect, even if it is intrinsically an intragranular one.

8.6 Channelling for Field directed Out of the *ab*-plane

The measurements performed in this chapter have so far concentrated on field rotation within the *ab*-plane, at $\theta = 90°$ to the *c*-axis. This section, however, presents measurements taken of $J_c^{GB}(\phi)$ at various angles θ to the *c* direction. This is in order to chart the development of the channelling dip and provide a link with the $J_c^{GB}(\theta)$ rotation results of section 9.4. Figure 8.26 shows measurements performed at 4 T, 75 K for $\theta = 90°$ (in the *ab*-plane), 85°, 75° and 45°.

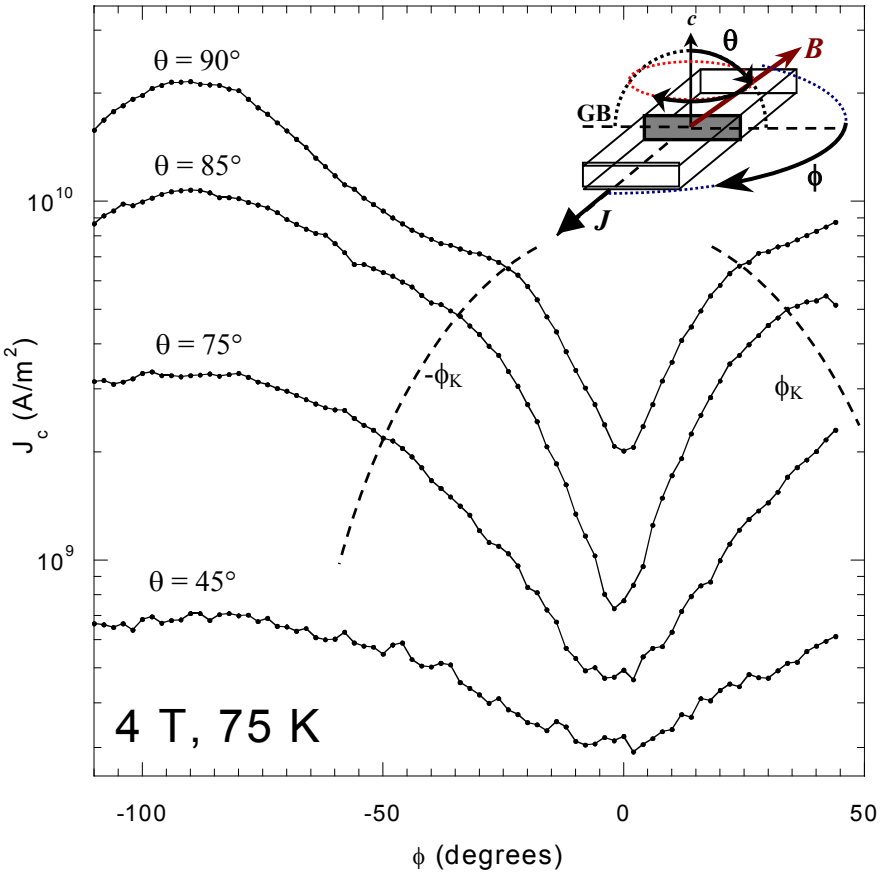

Figure 8.26. $J_c^{GB}(\phi)$ measurements performed at various angles θ to the *c*-axis. Field rotation within the *ab*-plane corresponds to $\theta = 90°$ (see inset for geometry of scans). The kinking angle ϕ_K is seen to increase for field rotation out of the *ab*-plane.

As θ is decreased from 90°, the magnitude of the background variation is seen to decrease. This is because the force free regime ($B \parallel J$) is not fully accessed and the Lorentz force variation over the scan is reduced – indeed, at θ = 0°, $J_c^{IG}(\phi)$ should yield a flat line and be independent of ϕ. Interestingly, as the field rotations move out of the *ab*-plane (towards θ = 0°) the magnitude of ϕ_K is seen to increase, as indicated by the dashed lines. The increase in ϕ_K occurs despite a reduction in $J_c^{GB}(\phi_K)$ magnitude. The position of ϕ_K also becomes less well defined with decreasing θ, and by θ = 45° no clear sign of ϕ_K can be seen in the $J_c^{GB}(\phi)$ measurement.

The increase in ϕ_K is likely to be due to the relative 'straightness' or linearity of the LAGB plane along the *ab*-plane (length = track width, *w*) and along the *c*-axis (length = film thickness, t_f). The TEM measurements on sample pk2 in chapter 5 reveal that the boundary plane in the direction of film growth can deviate significantly from the *c* axis and displays a typical meandering behaviour. For field along the GB in the *ab*-plane, the boundary is measured to depart from ideal linearity by up to 250 nm (meander), which for a 5 μm track represents only a 5 % deviation. For field along the GB in the *c* direction, the boundary deviates from linearity by 100 nm (or more), which for a film thickness of 145 nm represents a 70 % deviation. The result is that as θ decreases from 90°, the boundary length in the direction of the external field decreases, increasing the relative importance of the GB meander. The spread in angle that the GB makes to the *c*-axis correspondingly results in a *larger* spread in angle over which vortices will be, and can be, aligned to the defect plane. This will shift ϕ_K to larger values as seen in figure 8.26.

This result agrees well with the angular measurements of $J_c^{GB}(\theta)$ performed in section 9.4, in which field is also scanned out of the GB plane, but by rotating field away from the *c*-axis (in θ) towards ***J***. As for rotations in $J_c^{GB}(\phi)$, the $J_c^{GB}(\theta)$ measurements also reveal a kinking angle, at θ_K, the magnitude of which is found to be much greater than ϕ_K (see figures 9.28 and 9.29). This greater magnitude is due to the same mechanism described above – the increased importance of meander on vortex alignment.

8.7 Vortex Channelling at an Artificial Channel

Measurements in the ϕ-scan geometry were also performed on the artificial vortex channel (AC) created by locally thinning a line across an IG track (see section 4.1.7). The cross sectional reduction was expected to result in vortex channelling, as it represents a linearly correlated, non weak-linked defect. Signs of such channelling were indeed found in the angular scans of $J_c(\phi)$, denoted $J_c^{AC}(\phi)$. Although the magnitude of the effect is much smaller

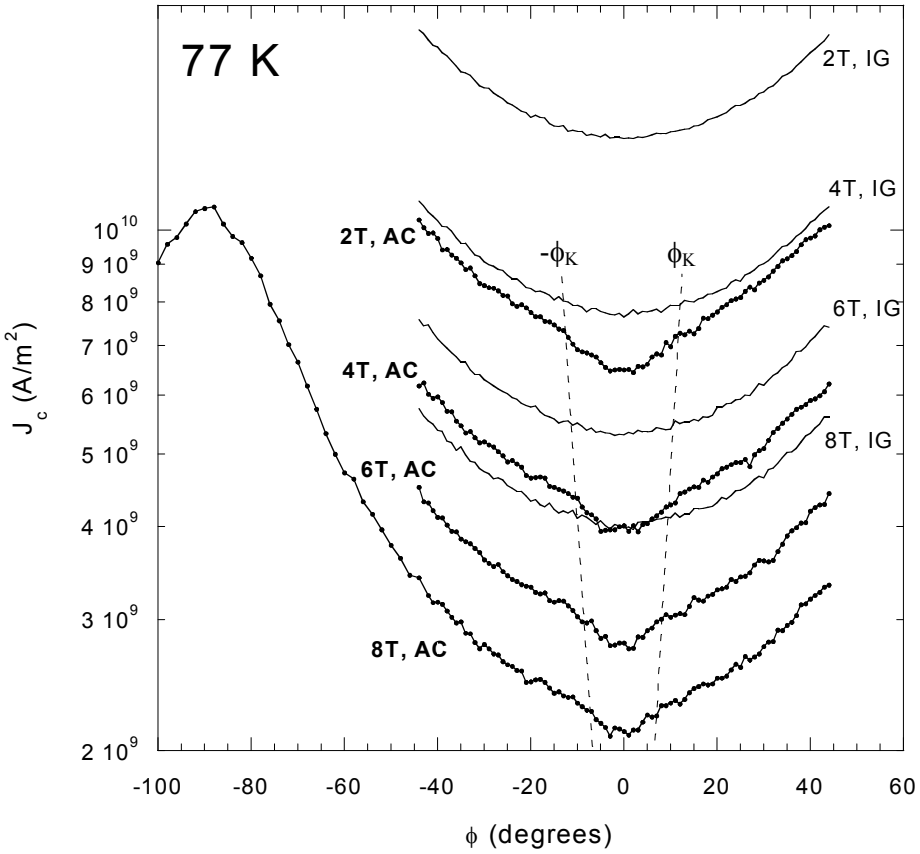

Figure 8.27. $J_c(\phi)$ measurements performed on the artificial FIB milled channel (termed AC) (circles) and on a reference IG track (lines) at 77 K for various applied fields. By comparison to the IG results, a channelling dip similar to that observed for LAGB pk2 (4.9°) can be seen for angles close to $\phi = 0°$. The dashed lines indicate the field dependence of ϕ_K. Track widths are w = 10 μm (IG), 6 μm (AC).

than that seen in the 4.9° LAGB (pk2), its presence indicates similarity in electronic behaviour.

Measurements on the AC are shown in figure 8.27, taken at 77 K for various applied fields. For reference, measurements on an IG track were also performed (of the same length as the AC track; $Q = 1$), which show the typical smooth variation about $\phi = 0°$ indicative of Lorentz force modulation. The AC scans however, show a small dip at $\phi = 0°$ for fields aligned with the channel. Consistent with the LAGB results, the width of the channelling region decreases with increasing field, as indicated by the dashed lines.

As opposed to the very noticeable LAGB dip, the AC dip represents only a small perturbation. It becomes more evident however when one investigates the ϕ dependence of the ratio $\delta(\phi) = J_c^{AC}/J_c^{IG}$. An example is shown in figure 8.28 for 2 T and 77 K, where $J_c(\phi)$ is plotted on the left hand axis and $\delta(\phi)$ on the right hand axis. For $|\phi| > \phi_K$, an almost constant $\delta(\phi) \sim 0.55$ is found. Taking the ratio above ϕ_K to imply cross sectional reduction (see section 8.4), this implies that local to the AC, film thickness is ~55% of the total IG film thickness, or 127 nm (t_f = 230 nm). If true, this represents a greater cross sectional reduction than that

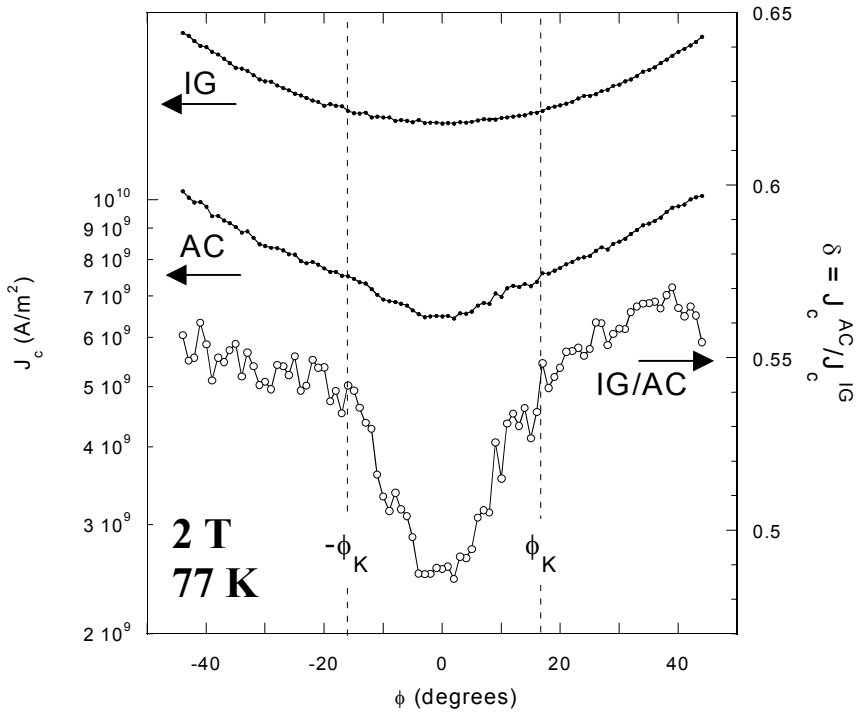

Figure 8.28. $J_c(\phi)$ plotted for AC and IG AT 2 T, 77 K on the left hand scale and $\delta(\phi) = J_c^{AC}/J_c^{IG}$ on the right hand scale. The decrease in δ for $|\phi| < \phi_K$ emphasises the small channelling dip.

observed for a 4.9° LAGB where local to the GB an effective area of ~ 70 – 80% film thickness is found.

For $-\phi_K < \phi < \phi_K$ a dip to less than $\delta(\phi) \sim 0.5$ is observed in figure 8.28, where $\phi_K \sim 16°$ and $J_c^{AC}(\phi_K) \sim 7.5 \times 10^9$ A/m^2. However, LAGB sample pk2 yielded $\phi_K = 38°$ and $J_c^{GB}(\phi_K) = 1.02 \times 10^{10}$ A/m^2 at 77 K, 2 T. Assuming a $\phi_K \propto J_c(\phi_K)^{1/2}$ dependence, the decrease in J_c^{AC} from J_c^{GB} is not sufficient to account for the reduction in ϕ_K alone (a factor of ~ 0.8 is predicted).

The reduced magnitudes of both ϕ_K and the depth of the channelling dip are likely to be due to the relatively large effective width $d_{eff} \sim 50$ - 70 nm across the channel. The result is a smeared AC pinning potential for vortices to align to, which is on a scale much greater than the core size. In addition, the large d_{eff} will reduce the effect of vortex core elongation, which acts to enhance the effectiveness of the vortex channel by reducing the pinning of vortices in the planar defect.

The reduced effectiveness of the AC channelling is also evident in the *V-I* characteristics obtained for applied field lying along the plane of the defect at $\phi = 0°$. Example *V-J* curves are shown in figure 8.29 at 2 T, 77 K for field applied at $\phi = 0°$ and (beyond ϕ_K) at $\phi = -44°$. Plotted on the lower axis, the characteristic at $\phi = 0°$ is slightly less curved that at $\phi = -44°$

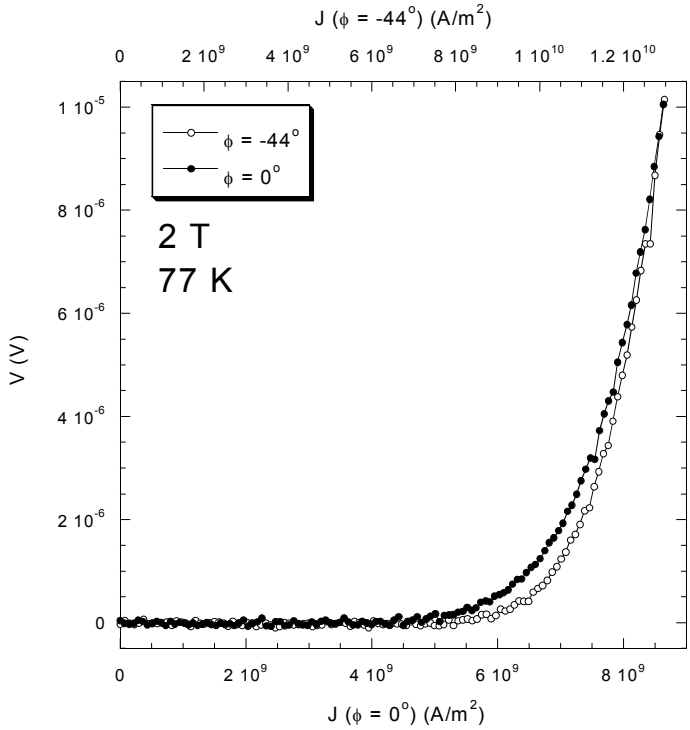

Figure 8.29. *V-J* characteristics recorded for applied field at $\phi = 0°$ (bottom scale) and $\phi = -44°$ (top scale) at 2 T, 77K for the artificial channel. Both characteristics display pronounced curvature, although at $\phi = 0°$ to a slightly lesser extent.

plotted on the upper axis. Both display significant rounding however, which is indicative of the reduced *E*-fields at the artificial channel when compared to an LAGB.

8.8 Summary and Discussion

This section has presented measurements of the LAGB electronic properties as external applied field is rotated within the *ab*-plane of the sample. The marked reduction in $J_c^{GB}(\phi)$ for fields aligned with the boundary plane indicates vortex channelling along the boundary plane. This behaviour has been shown to closely match that observed by Oussena *et al* [9] for single domain twin arrays in YBCO. Simple modification of a model predicting vortex kinking to twin boundaries has well described the channelling minimum observed on LAGB ϕ-scans. The scaling of channelling minima also implies a kinking angle dependence $\phi_K \propto [J_c^{GB}(\phi_K)]^{1/2}$. Within the dip J_c^{GB} varies linearly with ϕ, and with a reduced temperature dependence due to reduced dimensionality. Outside the dip, J_c^{GB} is controlled directly by J_c^{IG}, the properties of the IG sections of the LAGB track.

More significantly, the deleterious effects of the LAGB on current transport are found to be mitigated significantly by simple rotation of the applied field to angles $|\phi| > \phi_K$. This may well explain the large J_c values obtained for coated conductor tapes in field applied along the *ab*-plane [21,22,23]; the external field will not, in general, be well aligned with the network of

LAGB planes which are randomly directed in the tape. As such, a significant number of planes within the conductor will experience an applied field at an angle $|\phi| > \phi_K$.

More precisely, the current density ***J*** will no longer be perpendicular to each individual LAGB in the coated conductor (as it is in figure 8.1). The probable effect of such a non-perpendicular geometry in an isolated current track is depicted schematically in figure 8.30. As the inset shows, the LAGB plane is shifted by an amount $\Delta\phi_{GB}$ from the $\phi = 0°$ position, resulting in an equivalent shift in the position of the channelling minimum. Hence, in general the channelling minima will not be fully accessed for field applied along a coated conductor *ab*-plane at $\phi = 0°$. This will appreciably increase both the individual LAGB transparency and the total critical current of the tape.

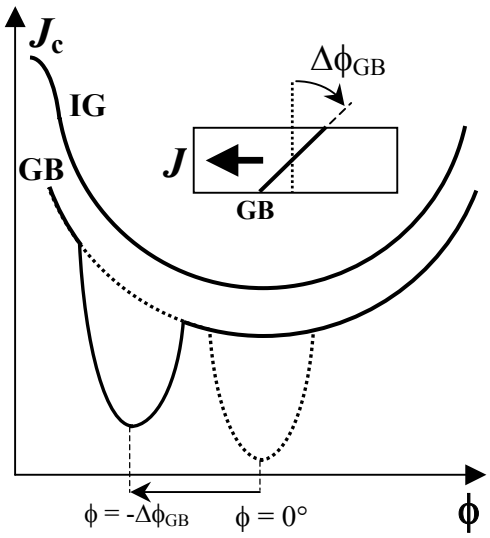

Figure 8.30. Schematic of the possible effect on $J_c^{GB}(\phi)$ for a LAGB at an angle $90°-\Delta\phi_{GB}$ to ***J*** (as shown in the inset). Dotted lines represent the GB at $\phi = 0°$.

Finally, evidence has also been found linking the $J_c^{GB}(\phi)$ channelling dip with the *linear* LAGB *V-I* characteristic. This strongly supports the interpretation of the linear *V-I* in terms of viscous flux flow channelling as detailed in chapter 6.

8.9 References

[1] K.E. Gray, M.B. Field and D.J. Miller, *Phys. Rev. B* **58** 9543 (1998)

[2] A. Díaz, L. Méchin, P. Berghuis, and J. E. Evetts, *Phys. Rev. B* **58**, R2960 (1998)

[3] A. Gurevich, M.S. Rzchowski, G. Daniels, S. Patnaik, B.M. Hinaus, F. Carllo, F. Tafuri and D.C. Larbalestier, *Phys. Rev. Lett.* **88**, 97001 (2002)

[4] A. Díaz, L. Méchin, P. Berghuis, and J. E. Evetts, *Phys. Rev. Lett.* **80**, 3855 (1998)

[5] W.K. Kwok, U. Welp, D.W. Crabtree, K.G. Vandervoot, R. Hulscher, J.Z. Lu, *Phys. Rev. Lett*. **64**, 966 (1990)

[6] G.A. Jorge and E. Rodriguez, *Phys. Rev. B* **61**, 103 (2000)

[7] J.N. Li, A.A. Menovsky and J.J.M. Franse, *Phys. Rev. B* **48**, 6612 (1993)

[8] M. Oussena, P.A.J de Groot, S.J. Porter, R. Gagnon and L. Taillefer, *Phys. Rev. B* **51**, 1389 (1995)

[9] M. Oussena, P.A.J. de Groot, K. Deligiannis, A.V. Volkozub, R. Gagnon and L. Taillefer, *Phys. Rev. Lett.* **76**, 1559 (1996)

[10] Z.W. Lin, G.D. Gu, A.S. Mahmoud and G.J. Russell, *Physica C* **349**, 95 (2001)

[11] G. Blatter, M.V. Feigel'man, V.B. Geshenkbein, A.I. Larkin and V. M. Vinokur, *Rev. Mod. Phys*. **66**, 1125 (1994)

[12] S. Sanfilippo, A. Sulpice, O. Laborde, D. Bourgault, Th. Fournier and R. Tournier, *Phys. Rev. B* **58**, 15189 (1998)

[13] P.H. Kes, 'Flux Pinning and the Summation of Pinning Forces', *Concise Encyclopedia of Magnetic and Superconducting Materials*, Ed. J.E. Evetts, Oxford, Pergamon (1992)

[14] A.A. Zhukov, G.K. Perkins, J.V. Thomas, A.D. Caplin, H. Kupfer and T. Wolf, *Phys. Rev. B* **56**, 3481 (1997)

[15] M. Tachiki and S. Takahashi, *Solid State Communications* **70**, 291 (1989b)

[16] T. Nishizaki, F. Ichikawa, T. Fukami, T. Aoimine, T. Terashima and Y. Bando, *Physica C* **204**, 305 (1993)

[17] T. Hwa, D. Nelson and V.M. Vinokur, *Phys. Rev. B* **48**, 1167 (1993)

[18] S.K. Gupta, S. Sen, J.C. Vyas, S.P. Pai, R. Pinto, V.C. Sahni, *Physica C* **324**, 137 (1999)

[19] N.F. Heinig, R.D. Redwing, I-Fei Tsu, A. Gurevich, J.E.Nordman, S.E. Babcock and D.C. Larbalestier, *Appl. Phys. Lett* **69**, 577 (1996)

[20] D.R. Nelson and V.M. Vinokur, *Phys. Rev. B* **48**, 13060 (1993)

[21] Y. Yamada, S. Beom, T. Araki, Y. Takahashi, T. Yuasa, H. Kurosaki, I. Hirabayashi, Y. Iijima and K. Takeda, *Physica C* **357**, 1007 (2001)

[22] J. Coulter, J.O. Willis, M.M. Mann, P.C. Dowden, S.R. Foltyn, P.N. Arendt, J.R. Groves, R.F. DePaula, M.P. Maley and D.E. Peterson, IEE Trans. Appl. Supercond. 9, 1487 (1999)

[23] A. Vostner, H.W. Weber, H.C. Freyhardt, A. Usoskin, J. Dzick and J. Knoke, *IEEE Trans. Appl. Supercond.* **11**, 2715 (2001)

9 LAGB $J_c(\theta)$ Measurements

This section presents the results of $J_c^{GB}(\theta)$ measurements, in which the applied magnetic field is rotated away from the *c*-axis of a LAGB track. The two main scans involve rotation of field within the LAGB plane and rotation out of the LAGB plane. Although both involve the channelling of vortices along the LAGB, the former reveals a $J_c^{GB}(\theta)$ maximum for field aligned with the boundary dislocations. The field and temperature dependence of this LAGB pinning peak is presented and investigated. At lower fields and temperatures a pronounced angular hysteresis is observed, which is modelled in terms of flux trapping within the intragranular regions of the LAGB track. In a result similar to that of chapter 8, measurements involving field rotation out of the plane are interpreted in terms of vortex channelling behaviour and a transition from kinked to collinear structure.

9.1 Introduction

As introduced in chapters 3 and 8, the pinning and channelling properties of an arrangement of defects can be investigated through the dependence of J_c on the angle of applied magnetic field, $\boldsymbol{H}_{app} = \boldsymbol{B}_{app}/\mu_o$. For field aligned with such defects an anomaly in J_c is expected. This chapter will show that for a track containing a LAGB, the observed anomaly depends upon the experimental scan geometry: whereas rotation of field within the *ab*-plane results in a channelling dip (see chapter 8), rotation of field within the LAGB *defect* plane can produce a

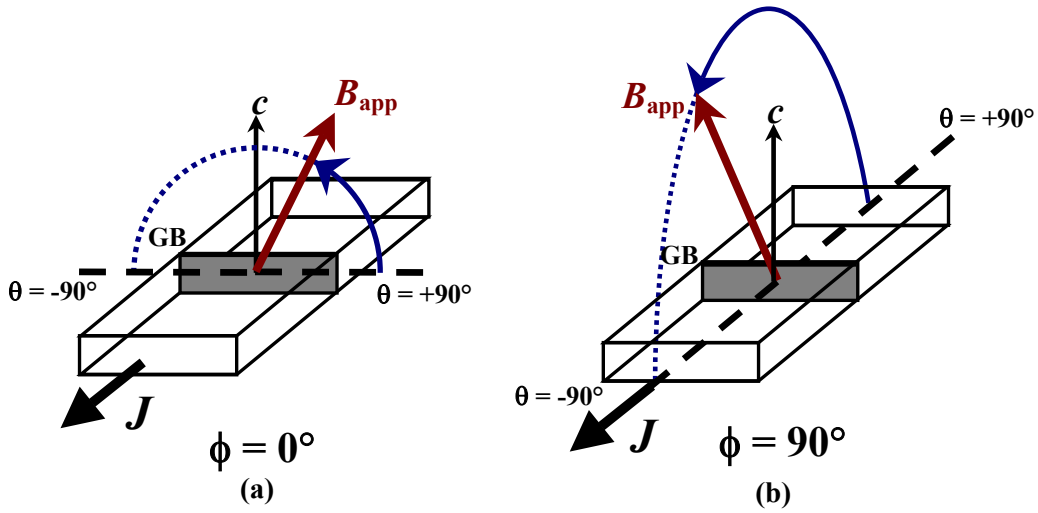

Figure 9.1. Experimental θ rotation geometries investigated in this chapter, for (a) rotation of the external field within the LAGB plane (at ϕ = 0°), and (b) rotation of the external field out of the LAGB plane (at ϕ = 90°).

pinning peak – the LAGB pinning peak. This latter geometry forms one of two types of field scan performed in this chapter, both of which are shown in figure 9.1 Applied field is rotated in θ for (a) ϕ = 0° corresponding to a field scan *within* the LAGB plane, and (b) ϕ = 90° corresponding to a field scan *out* of the LAGB plane. For a scan within the LAGB plane, the Lorentz force $F_L = J \times B$, is constant in magnitude over the scan, but varies in direction. For a scan rotating field out of the LAGB plane, the Lorentz force is varied in magnitude in a manner equivalent to that described in chapter 8 for a field rotation towards the force free peak from within the *ab*-plane.

9.2 Previous Work

To the Author's knowledge, no measurements on a LAGB sample performed in the geometry of figure 9.1(b) exist in the literature. However, the first experiments involving angular field scans within a LAGB plane (figure 9.1(a)) were performed by Díaz *et al* [1] on a 4° thin film YBCO grain boundary. They found the surprising result that as applied field was rotated within the plane of the LAGB, $J_c^{GB}(\theta)$ displayed a maximum for field aligned with the *c*-axis, θ = 0°. The same experiment performed on an intragranular track showed no maximum. The $J_c(\theta)$ profiles Díaz *et al* obtained for GB and IG tracks are shown in figures 9.2(a) and (b) respectively, for various applied fields at 77 K. In both figures, the intrinsic pinning peak can be seen at θ = 90°. As previously discussed (section 2.7), it is termed 'intrinsic' because it is thought due to the anisotropic and layered nature of YBCO. The additional peak at θ = 0° in the GB measurement provided clear evidence that flux pinning can occur at LAGBs, which were previously thought of as only current limiting defects. The pinning maximum is attributed to the strong pinning of vortices to the LAGB dislocation array, as on average such dislocations also run parallel to the *c* direction for a [001]-tilt misorientation (chapter 3).

As figure 9.2(a) shows, the LAGB peak was found to vanish at a field of 5 T and 77 K. This suppression of $J_c^{GB}(\theta)$ can be directly correlated with the crossing of the irreversibility line in the grains of the LAGB track, as presented in chapter 7 for $J_c^{GB}(B,\theta = 0°)$ measurements, and chapter 6 for *V-I* measurements. Above the merging field, B^*, dissipation in the IG regions of the LAGB track dominates the electronic response, and J_c^{GB} reflects the intragranular J_c^{IG}. This can be interpreted in the normalised plots of figure 9.2(d) and (e) which show scans within the GB plane at 77 K and 60 K respectively. Unlike at 77 K, at 60 K no suppression of the pinning peak occurred up to 7 T due to the increased irreversibility line and enhanced $B^* >> 7$ T. In fact, at 60 K, the LAGB peak *increases* in magnitude with increasing field relative to the intrinsic peak. The field and temperature dependence of the LAGB peak, and the angular dependence of $B^*(\theta)$ will be further probed in the next section.

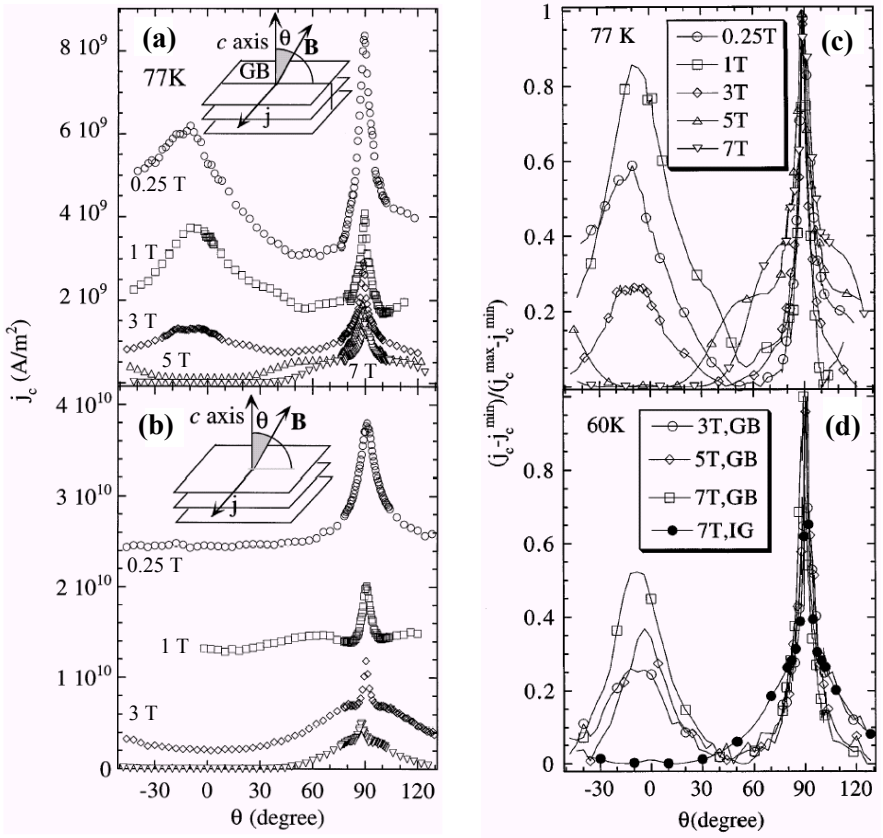

Figure 9.2. The results of Díaz *et al* [1] for field rotation within the LAGB plane, showing $J_c(\theta)$ measured at 77 K for (a) the GB track, and (b) an IG track at various fields. Normalised $J_c(\theta) = (J_c - J_c^{min})/(J_c^{max} - J_c^{min})$ is also shown for the GB track at (c) 77 K, and (d) 60 K.

Pinning peaks in $J_c(\theta)$ are not restricted to measurements on current tracks containing artificial LAGBs however. In the pioneering work of Roas *et al* [2], a peak in $J_c(\theta)$ was also observed for field parallel to the *c*-axis of a thin film YBCO (IG) track at low fields and high temperatures. This peak was attributed to vortex pinning at twin boundaries and stacking faults. Similar peaks at $\theta = 0°$ were observed in the angular measurements of Pan *et al* on thin film YBCO [3]. The fact that such IG peaks are also observed does not lessen the importance of the LAGB pinning peak. Firstly, Díaz *et al* found no peak for $B \parallel c$ in their comparative IG track at the same B and T. Secondly, the LAGB pinning peak at $\theta = 0°$ only represents the behaviour of flux lines *local* to the LAGB. For the $\phi = 0°$ scan geometry, vortices lie within the LAGB plane over the whole angular scan range and, because $J_c^{GB} < J_c^{IG}$, flux lines residing in the IG regions of the LAGB track are firmly pinned. For example, for a track of width 10 μm and at 1 T, this means that $J_c^{GB}(\theta)$ reflects the pinning of only 200 vortices at the LAGB dislocation array - assuming the initial depinning of a single vortex row. In this manner, $J_c^{GB}(\theta)$ directly probes the pinning properties of the LAGB dislocation structure.

The effectiveness of pinning to dislocations is now well recognised. Strong vortex pinning to linearly correlated dislocations has already been found to directly result in the high critical

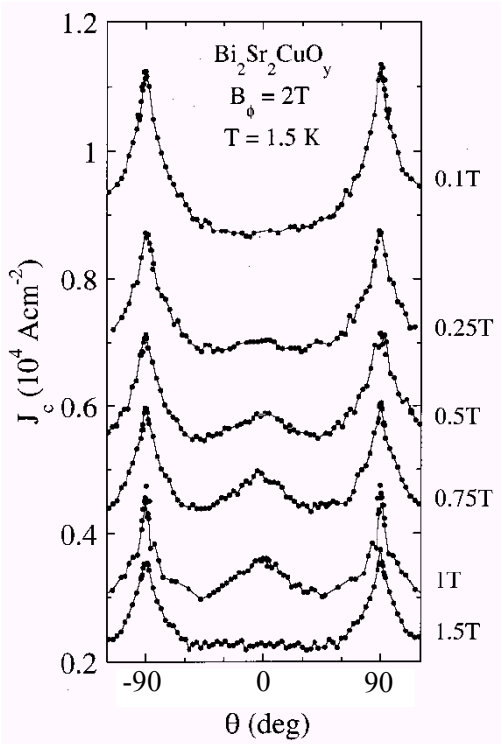

Figure 9.3. $J_c(\theta)$ measured on thin film $Bi_2Sr_2CuO_y$ irradiated to produce columnar defects along the *c*-axis ($\theta = 0°$) [5].

currents measured for thin film YBCO [4]. The interpretation of the LAGB pinning peak in terms of dislocation pinning is therefore a natural one. This assumes a *modulation* of the order parameter along the LAGB due to the regularly spaced dislocation cores, not a continuous insulating or normal layer at the interface as found for higher angle boundaries. As such it is expected that the presence of the pinning peak will be a signature of only lower angle misorientations.

Similarity may also be found between the LAGB pinning peak and the $J_c(\theta)$ measurements performed by Pomar *et al* [5] on thin films of $Bi_2Sr_2CuO_y$ ($T_c = 4$ K) after irradiation by 1 GeV Pb ions. The irradiation produced columnar defects (CDs) along the *c*-direction with a matching field of $B_\phi = 2$ T. For field rotation perpendicular to the transport current ($\phi = 0°$) they found an enhancement in $J_c(\theta)$ for fields aligned with the CDs. The $J_c(\theta)$ measurements they took at 1.5 K are shown in figure 9.3 at 1.5 K for various fields. Despite the disparity in matching fields for a 4° LAGB dislocation array (70 T) and the Pomar *et al* experiment, qualitatively similar behaviour may be seen with the results of figures 9.2.

It should be noted that such irradiation has been found to enhance the YBCO irreversibility line [6]. As discussed above and in chapter 7 however, the observation of such an effect for and LAGB track would be masked by dissipation in the intragranular regions.

9.3 Scanning Field Within the GB Plane: $J_c^{GB}(\theta, \phi = 0°)$

9.3.1 The LAGB Pinning Peak

Field sweeps were performed within the LAGB plane of samples ranging in misorientation from 3.8° (s2) to 4.9° (pk2), in the geometry of figure 9.1(a) for a wide range of temperature (5 - 77 K) and field (up to 8 T). Comparative measurements were also made on tracks patterned in the IG regions of each film. The measurements confirm the existence of the LAGB pinning peak, only previously observed by Díaz *et al* [1].

An example $J_c^{GB}(\theta)$ scan is shown in figure 9.4 for sample s2 at 8 T, 60 K. Enhancements in $J_c^{GB}(\theta)$ can be seen for fields aligned both along the *c*-axis ($\theta = 0°$), and the *ab*-plane

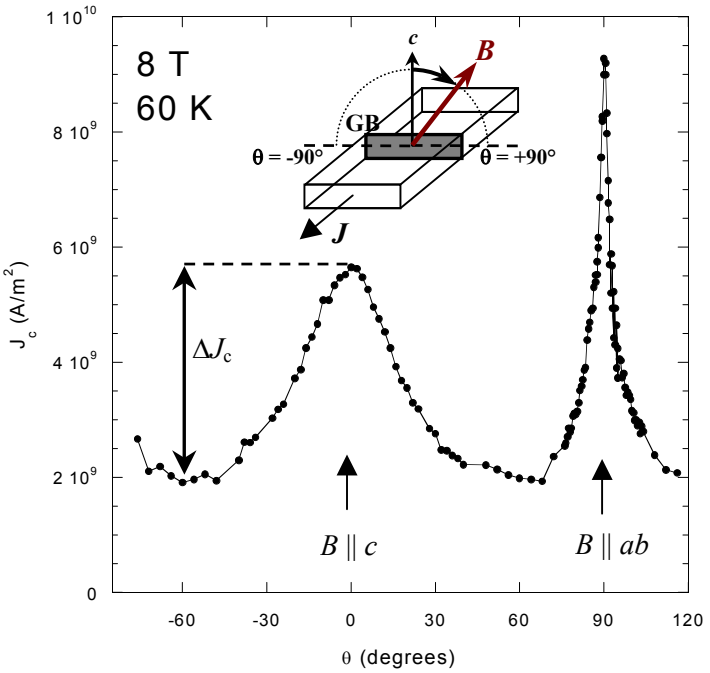

Figure 9.4. $J_c^{GB}(\theta, \phi = 0°)$ recorded at 8 T, 60 K, for rotation in the plane of a 3.8° LAGB ($\phi = 0°$) as shown in the inset. In addition to the intrinsic peak for $B \parallel ab$, an additional peak of magnitude ΔJ_c is observed for $B \parallel c$, when field is aligned along the GB dislocations. Track width $w = 5.5$ μm.

($\theta = 90°$). These anomalies can be interpreted as representing the effects of pinning to the LAGB dislocation array and the intrinsic mechanism respectively.

The behaviour of the GB track may be contrasted to that recorded on an IG track in the same geometry - an example of $J_c^{IG}(\theta)$ and $J_c^{GB}(\theta)$ both recorded at 8 T, 40 K is shown in figure 9.5(a) for sample s2. No equivalent peak at $\theta = 0°$ can be seen in the IG trace, a result found to be true for all comparative IG traces recorded. The effect of the LAGB pinning peak on the transparency $\delta(\theta) = J_c^{GB}/J_c^{IG}$ is shown in figure 9.5(b) for the traces in figure 9.5(a). As can be seen, the peak at $\theta = 0°$ in $J_c^{GB}(\theta)$ is highlighted in $\delta(\theta)$, to the extent that in this example it

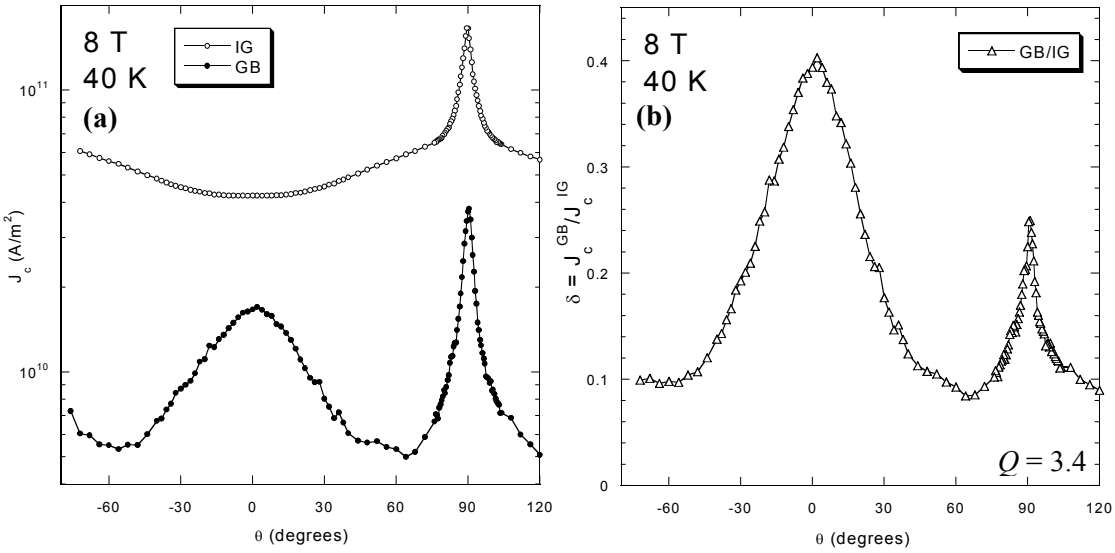

Figure 9.5.(a) $J_c(\theta, \phi = 0°)$ recorded at 8 T, 40 K for a GB (filled circles) and comparative IG track (open circles). (b) Transparency ratio $\delta(\theta) = J_c^{GB}/J_c^{IG}$ of the scans in (a). $w = 5.5$ μm (GB), 9.1 μm (IG).

exceeds the peak found at $\theta = 90°$.

The results of this chapter (and chapters 6 and 8) strongly suggest that channelling of vortices is always found to occur for fields sufficiently aligned with LAGB plane. In the scan geometry of this section (9.3), field is *always* aligned to the defect plane (although not to the dislocations). This means that vortices are channelled at the LAGB over the whole angular range of the measurement. This can be seen in figure 9.5(b), as $\delta < 1$ over the whole scan, indicating that J_c^{GB} represents the depinning and channelling of only those flux lines local to the LAGB. The peak observed for $\theta = 0°$ therefore represents the maximum pinning of vortices attained by alignment to the dislocation array, but *within* an easy flow channel – i.e. even at the LAGB pinning peak $J_c^{GB}(\theta) < J_c^{IG}(\theta)$.

9.3.2 Sample Dependence

The LAGB pinning peak was found to occur to varying degrees in all GB samples measured. Figure 9.6 shows a comparison of $J_c^{GB}(\theta)$ curves obtained at 4 T and 60 K for three samples: s2 (3.8°), 773c (4.0°) and pk2 (4.9°). All three exhibit a peak at $\theta = 0°$, but for the larger misorientation sample pk2, the pinning peak is reduced from that seen for s2 and 773c.

Figure 9.7 compares the normalised $J_c(\theta) = (J_c - J_c^{min})/(J_c^{max} - J_c^{min})$ for s2 and pk2 at 4 T, 60 K. Such a normalisation probes the dependence of the $\theta = 0°$ peak relative to the intrinsic ($\theta = 90°$) peak. It can be seen that sample pk2 possesses a smaller LAGB peak than s2 and, as shown in the inset, a reduced transparency $\delta(\theta)$ for all θ. This is consistent with the smaller channel widths (section 3.5) and increased vortex elongation effects (section 3.8) for the

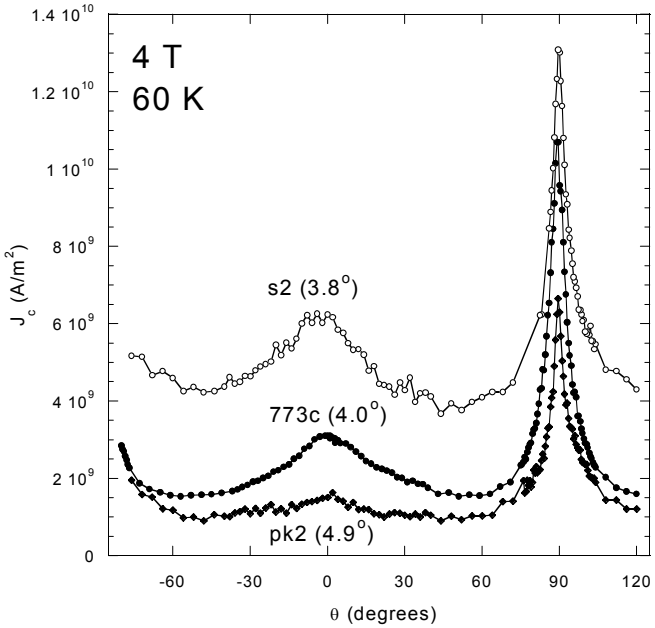

Figure 9.6. $J_c^{GB}(\theta)$ scans within the LAGB plane ($\phi = 0°$), recorded at 4 T, 60 K for three samples s2 (3.8°), 773c (4.0°) and pk2 (4.9°). The magnitide of the LAGB pinning peak is reduced with increasing misorientation.

larger pk2 misorientation. In particular, the reduced LAGB pinning peak for pk2 indicates that the pinning effect is indeed characteristic of lower angle GBs, in which the dislocations are sufficiently separated and sufficiently large (r_d decreases with increasing θ_m – see section 3.3) to afford pinning of vortices that are sufficiently non-deformed. The next section details the field and temperature dependence of $J_c(\theta)$ observed for samples pk2 and s2, and discusses factors that could affect the LAGB peak magnitude in more depth.

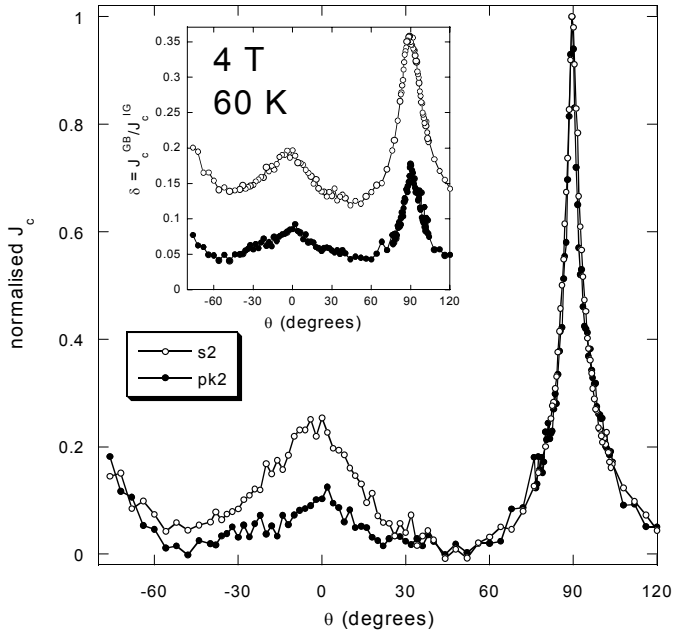

Figure 9.7. Normalised $J_c^{GB}(\theta) = (J_c - J_c^{min})/(J_c^{max} - J_c^{min})$ for pk2 (4.9°) and s2 (3.8°) recorded at 4 T, 60 K, for $\phi = 0°$. The inset also shows the transparency $\delta(\theta) = J_c^{GB}/J_c^{IG}$ for both samples. Track widths are w = 9.8 μm (pk2), 9.1 μm (s2).

9.3.3 Field Dependence

9.3.3.1 Observation

An example of the field dependence of $J_c^{GB}(\theta)$ and $J_c^{IG}(\theta)$ at 40 K is shown in figure 9.8(a) and (b) respectively. The pinning peak at $\theta = 0°$ in $J_c^{GB}(\theta)$ is found to be absent at lower fields, but gradually increases in definition with increasing field. The development of the peak can be contrasted with the comparatively featureless IG scans in figure 9.8(b). The low field $J_c^{GB}(\theta)$ scans also possess both a characteristic sloping and a larger degree of noise than the higher field measurements. The *noise* can be directly attributed to the low field noise observed in the LAGB *V-I* characteristic used to experimentally measure J_c^{GB} (see section 6.5) - as field increases, noise in both the *V-I* and in $J_c^{GB}(\theta)$ decrease. The *slope* can be explained in terms of flux trapping in the grains of the LAGB track - as will be discussed in detail in section 9.3.5, this effect is associated with a characteristic angular hysteresis.

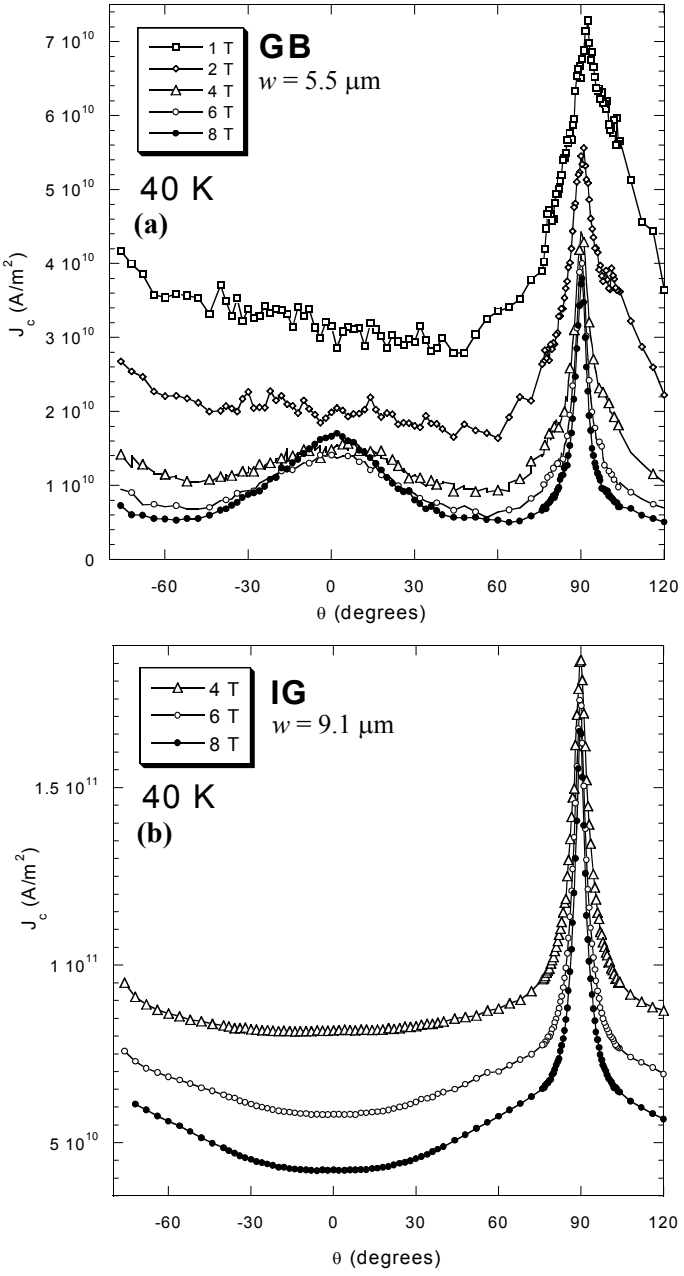

Figure 9.8.(a) $J_c^{GB}(\theta)$ and (b) $J_c^{IG}(\theta)$ recorded at 40 K and various applied field on sample s2 for $\phi = 0°$.

The relative increase in the LAGB peak with field is charted in figure 9.9, which plots the normalised $J_c = (J_c - J_c^{min})/(J_c^{max} - J_c^{min})$ for various fields at 60 K. With increasing field the transition can be seen from noisy and flat, to smooth and well defined.

For sufficiently low temperatures, however, the increase in the LAGB pinning peak with field is not only seen as relative to the intrinsic peak. For example, at 8 T the maximum of the LAGB peak in figure 9.8(a) is seen to exceed that at 6 T and 4 T, an effect that can be correlated to the increase in $J_c^{GB}(B, \theta = 0°)$ seen at high fields in figure 7.8. In addition, the *magnitude* of the LAGB peak, ΔJ_c, (measured from the peak maximum to the minimum that occurs on either side - see figure 9.4) is *also* found to increase with field. This can be seen in

figure 9.10, plotting ΔJ_c with field from 77 K to 10 K. The inset (log-linear axes) shows that an approximate *exponential* increase of ΔJ_c with field occurs for lower temperatures and higher fields.

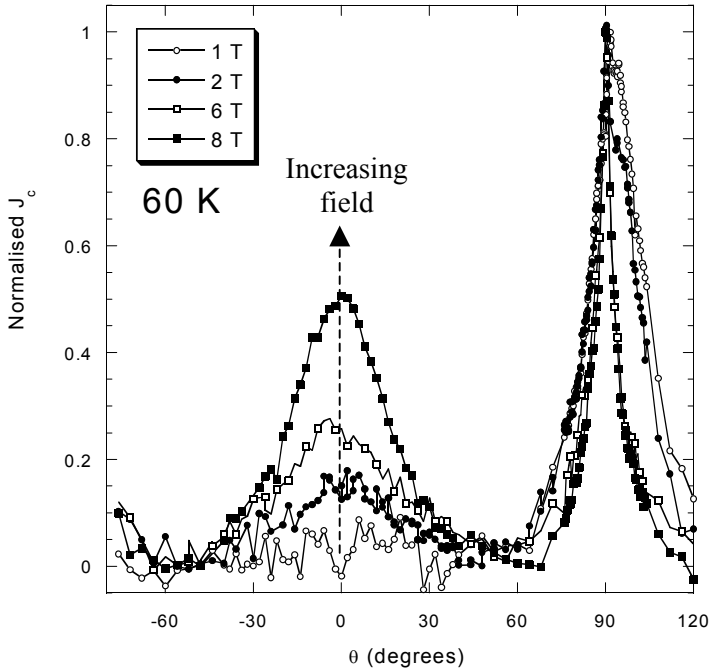

Figure 9.9. Normalised $J_c^{GB}(\theta, \phi = 0°)$ at 60 K for sample s2. The LAGB pinning peak increases relative to intrinsic peak with increasing field.

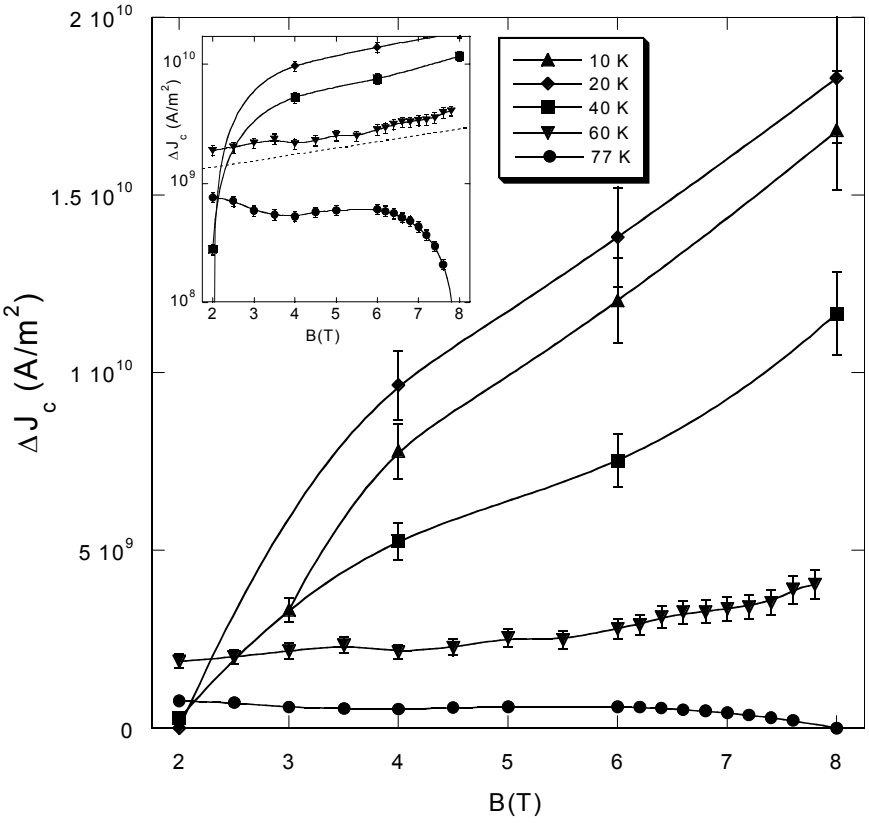

Figure 9.10. $\Delta J_c(B)$ at various temperatures for sample s2 (10% errors estimated). An approximately exponential increase in ΔJ_c with field is found for $T < 77$ K, as seen on the log plot inset. A fit to the 60 K curve gave $\Delta J_c \propto \exp[0.12B/B_o]$ (dashed line), where $B_o = 8.33$. Solid lines are a guide to the eye.

9.3.3.2 $J_c^{GB}(\theta)$ Limitation by $J_c^{IG}(\theta)$

As figure 9.10 shows, at higher temperatures ΔJ_c *decreases* with field. This is particularly clear in the inset plot at 6 T, 77 K. As discussed in section 9.2, the enhancement of $J_c^{GB}(\theta)$ at $\theta = 0°$ is effectively masked at high T, as B_{irr}^{IG} is approached and $J_c^{IG}(\theta)$ tends to zero. The resultant merging of GB and IG properties at B^* (as seen in $J_c(B)$ in section 7.1) is revealed particularly well in the angular measurement of $J_c^{GB}(\theta)$ and $J_c^{IG}(\theta)$. An example of this is shown in figure 9.11 for sample s2 at 8 T, 77 K. The LAGB peak is directly suppressed by IG dissipation and limited to $J_c^{GB}(\theta) = J_c^{IG}(\theta)$ over an angular range $|\theta| < 25°$. This range corresponds to $B > B^*(\theta)$. The peak disappears over the range as J_c^{GB} probes dissipation across the whole LAGB track, not solely at the LAGB dislocation array. Further rotation towards the *ab*-plane ($\theta = 90°$) results in $J_c^{GB}(\theta) < J_c^{IG}(\theta)$, due to an increasing $B^*(\theta)$. This agrees well with the fixed angle $J_c(B)$ measurements of figure 7.13.

The same behaviour is observed for sample pk2 (inset of figure 9.11), but the sample's reduced grain irreversibility line exaggerates the effect at 77 K, 8 T; while a LAGB peak may

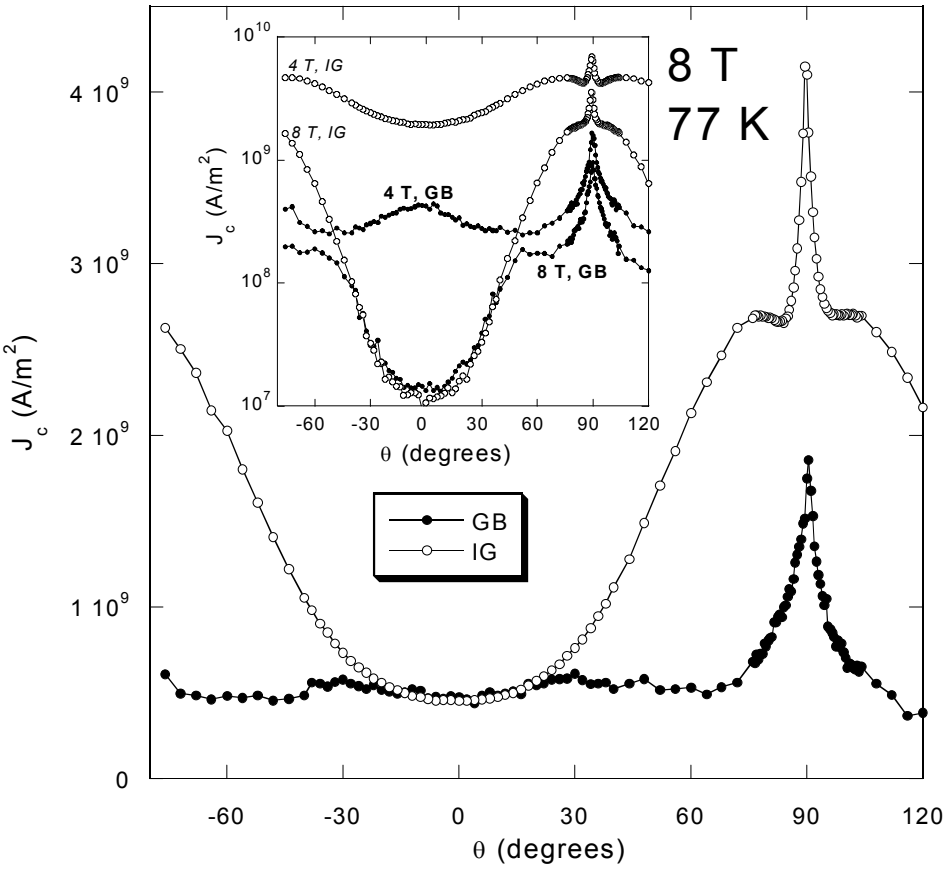

Figure 9.11. $J_c(\theta, \phi = 0°)$ recorded at 8 T, 77 K, for GB and IG tracks of sample s2. The LAGB pinning peak is supressed as dissipation ensues in the intragranular regions. Inset shows GB and IG $J_c(\theta)$ measured on sample pk2 at 4 T and 8 T, 77 K. As pk2 possesses a lower B_{irr}^{IG} than s2 the the peak suppression is more marked at 8 T. Q = 3.4 (s2), 2.4 (pk2). All track widths are ~ 10μm, except the s2 GB with w = 5.5 μm

be seen at 4 T, a large suppression is seen at 8 T due to a corresponding suppression of $J_c^{IG}(\theta)$. It is an important conclusion that such dips in $J_c^{GB}(\theta)$ at high field and temperature do not represent channelling dips as seen for field scans in the *ab*-plane (chapter 8). They merely represent the angular dependence of $B_{irr}^{IG}(\theta)$ and $B^*(\theta)$. This can also be contrasted with the theory of Pomar *et al* [5] that the onset of vortex interaction and collective effects suppress the pinning peak at high fields in an irradiated sample.

9.3.3.3 Field Dependence Mechanisms: $\Delta J_c(B)$

For lower fields and temperatures, such that $B < B^*(T)$, there are a number of factors that may influence the magnitude of the LAGB pinning peak with field. These are discussed below.

- **Vortex Matching**

Assuming the peak is due solely to vortex pinning by GB dislocations, the increase in its magnitude with field can be explained in terms of the large dislocation matching field B_ϕ. As discussed in section 7.1.3, for a 3.8° LAGB we find $B_\phi = 72$ T. Even at 8 T, where the vortex spacing $a_o = 17.7$ nm, there are still 3.7 dislocations per vortex core along a 10 μm long boundary. Diminished matching effects could also help explain the smaller LAGB peak observed for sample pk2; the larger matching field of pk2 (B_ϕ = 118 T) may lead to a reduction in the matching enhancement (see section 7.1.3).

The increase in the pinning peak magnitude with field may also be correlated to the increase in the ratio $\delta(B) = J_c^{GB}/J_c^{IG}$ seen at higher fields for B parallel to c. For sample s2, this

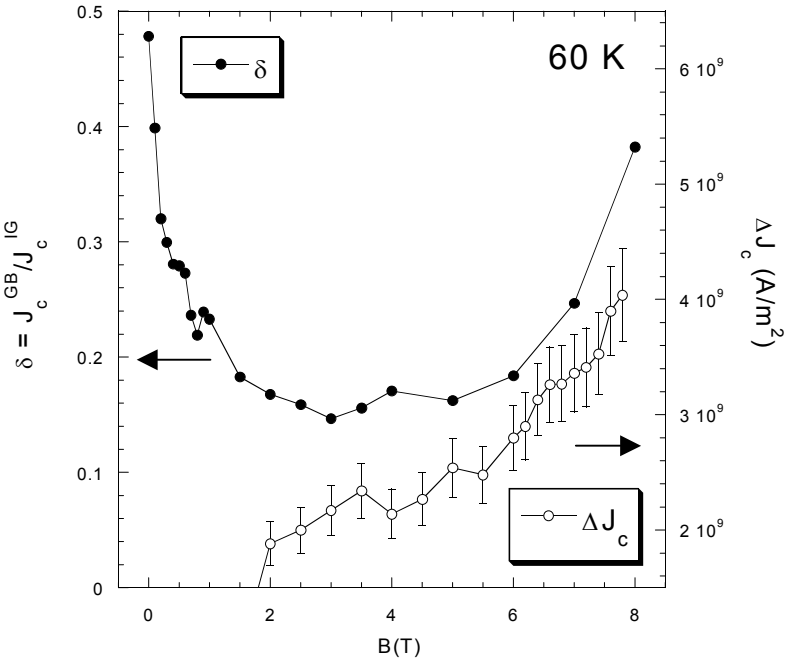

Figure 9.12. $\delta(B,\theta = 0°) = J_c^{GB}/J_c^{IG}$ measured on sampke s2 at 60 K plotted on the left hand scale (see section 7.1.4). The right hand scale shows the pinning peak magnitude, $\Delta J_c(B)$ extracted at 60 K from figure 9.10.

increase in δ is also accompanied by an increase in the absolute value of J_c^{GB}. Figure 9.12 plots $\delta(B, \theta = 0°)$ on the left hand axis, and $\Delta J_c(B)$ on the right hand axis at 60 K for s2. The increase of *both* ΔJ_c and $\delta(B)$ with field is evidence that increased LAGB pinning is linked to an increased angular pinning peak. This is consistent with a vortex-matching mediated increase in J_c^{GB} with field.

- **Core effects**

The effectiveness of vortex pinning to a dislocation will depend upon the relative sizes of vortex and dislocation cores. Both are expected to vary with field and temperature. As already discussed in section 7.2.3, the dislocation radius (r_d) may vary with B and T, and in doing so alter the GB transparency. The vortex core size has also been measured by Sonier *et al* [7] to increase with decreasing field and increasing temperature. For example at 0 K (extrapolated), the vortex core radius varies from $l \sim 20$ nm at 2 T to $l \sim 100$ nm at 0 T (at 1.5 T, l decreases from ~ 70 nm at 85 K to ~ 40 nm at 20 K). Such an effect may strongly influence the effectiveness of dislocations as linearly correlated pinning sites, especially when combined with the elongation of vortices expected at the LAGB. As calculated by Gurevich *et al*, pinning will fall off linearly with decreasing r_d, as $l > r_d$ (see section 3.8.3). Accordingly, a fall off in the LAGB pinning peak with decreasing field may well be expected.

- **Vortex Accommodation**

Lack of an angular LAGB pinning peak need not necessarily mean a lack of effective LAGB pinning. In practice, the presence of a peak at $\theta = 0°$ will depend on the relative field dependences of $J_c^{GB}(\theta = 0°)$ and $J_c^{GB}(\theta = 90°)$. If the low field intrinsic pinning is much stronger than LAGB pinning, then the latter could be effectively masked.

Experiments on irradiated material have shown a similar low field lack of directional pinning about the defect direction [8,9]. In the low field limit ($< 0.1H_{c1}$) Klein *et al* [8] found that instead of a *unidirectional* enhancement of $J_c(\theta)$ for field along the CDs, an *isotropic* enhancement was obtained. The effect was described in terms of a 'flux flop' phenomenon, whereby below a crossover field, vortices flop towards the CDs even when misaligned.

Accommodation of vortices to the LAGB *defect plane* is indeed thought to occur in such a manner for rotation of the applied field out of the plane - as detailed in chapter 8. It is therefore possible that enhanced vortex accommodation to LAGB *dislocations* occurs at low fields, resulting in an isotropic dependence of $J_c^{GB}(\theta, \phi = 0°)$ around $\theta = 0°$. The isotropic pinning state found by Klein *et al* [8] and Hardy *et al* [9], however, only spanned a very small field range $B < 1$ mT.

- **Vortex End Effects**

Another possible cause of a low field isotropic dependence of $J_c^{GB}(\theta)$ is the fact that for fields applied at an angle to the YBCO film, distortion of the flux line occurs over a length scale of $l_p = a_o/(\pi\Gamma)$ [10]. Flux lines within this region are perpendicular to the sample surface as sketched in figure 9.13. This is as a result of both the anisotropy of the material - current around a vortex line will tend to flow in the CuO_2 planes - and the limitation of circulating vortex supercurrents to *within* the sample. For very thin films, such an effect will result in flux lines parallel to the *c*-axis irrespective of the external field direction. For both s2 and pk2 films ($t_f \sim 150$ nm) at 1 T, the length of vortex line always parallel to *c* will be $2a_o/(t_f\pi\Gamma) \sim (6.4\text{ nm})/(150\text{ nm}) = 4$ %. At 0.1 T, this increases to 14 %. Lower fields can therefore increasingly produce a lack of angular variation about $\theta = 0°$ due to a deviation of the vortex and external field directions.

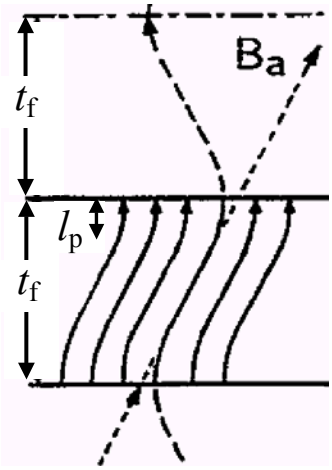

Figure 9.13. Flux lines in a sample of thickness t_f in an applied flux density B_a. A region of length *l* is found over which lines are perpendicular to the surface [10].

To summarise this section, the increase of the pinning peak at $\theta = 0°$ with field is most likely to be due to increased matching effects, leading to enhanced pinning. This agrees with the increase in J_c^{GB} seen for s2 at high fields. With decreasing field, the pinning peak disappears, either due to ineffective pinning or a deviation of vortex direction from field direction.

9.3.4 Temperature Dependence

9.3.4.1 Observation

An example of the temperature dependence of $J_c^{GB}(\theta, \phi = 0°)$ is shown for sample s2 in figure 9.14(a) for an applied flux density of 8 T. The peak at $\theta = 0°$ is present at all temperatures down to 10 K - apart from 77 K which, as discussed in section 9.3.3, is due to intragranular dissipation in the LAGB track. Comparative plots of $J_c^{IG}(\theta)$ are shown in figure 9.14(b), showing no maximum at $\theta = 0°$ over a similar temperature range (40 K to 77 K). In order to probe the temperature dependence further, figure 9.15 shows the data of figure 9.14(a) plotted in normalised form, $J_c^{GB} = (J_c - J_c^{min})/(J_c^{max} - J_c^{min})$. An example normalised IG scan is also plotted at 40 K for comparison. As temperature increases, the LAGB peak is also seen to increase relative to the intrinsic peak, until its destruction at 77 K.

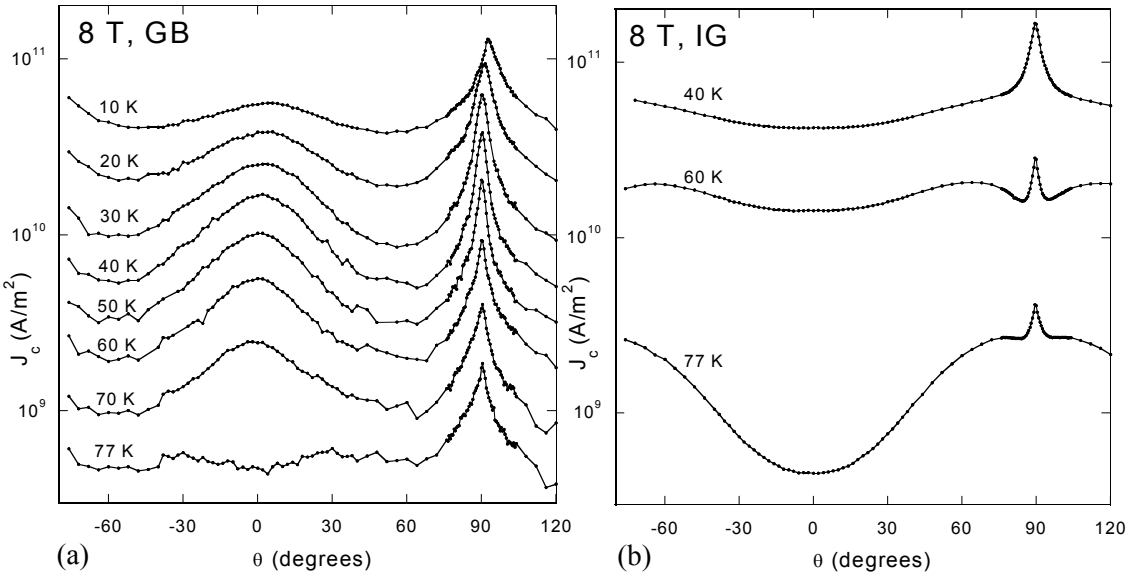

Figure 9.14. Temperature dependence of $J_c(\theta)$ measured at 8 T and on (a) LAGB and (b) IG tracks in sample s2 (3.8°) for rotation within the LAGB plane ($\phi = 0°$). w = 5.5 μm (GB), 9.1 μm (IG).

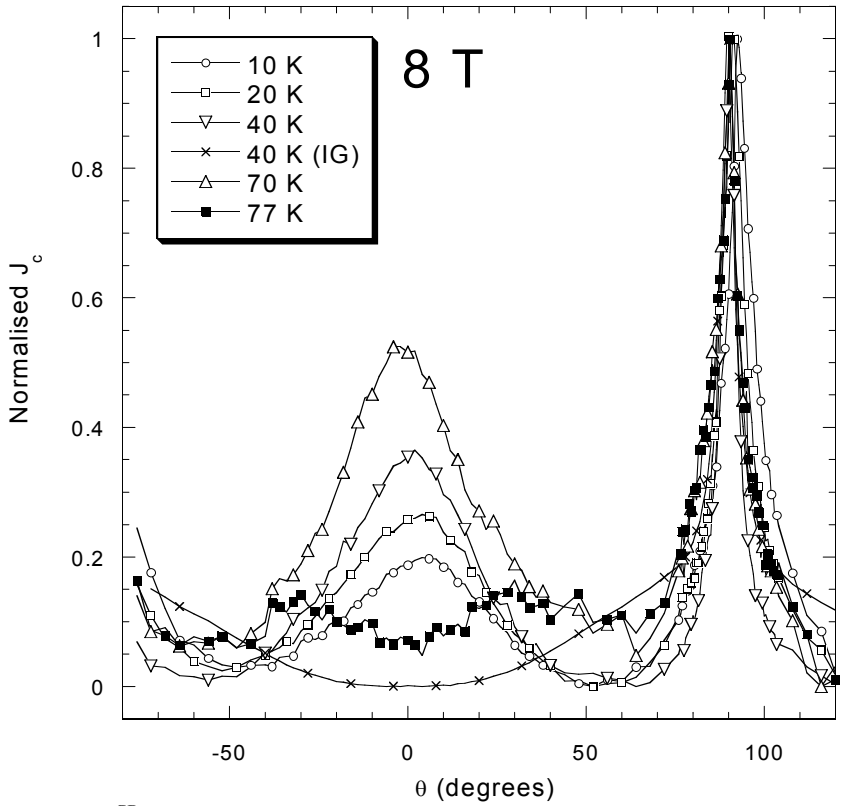

Figure 9.15. The $J_c^{GB}(\theta)$ data of figure 9.14 plotted in normalised form (see text), showing the development of the peak at $\theta = 0°$ at 8 from 10 K to 77 K. Normalised $J_c^{IG}(\theta)$ at 40 K is also plotted.

The temperature dependence of $\delta(\theta)$ is shown in figure 9.16 for sample pk2 at 4 T. A peak at $\theta = 0°$ exists in $\delta(\theta)$ at all temperatures measured down to 30 K. With increasing temperature the magnitude of both the LAGB and intrinsic peaks increases. As discussed in depth in section 7.2.3, this can be related to both the proximity of B_{irr}^{IG} and an increase in pinning at

the LAGB - as thermal fluctuations become more prominent and dimensionality reduction becomes more important.

Figure 9.17 shows the dependence of the peak magnitude ΔJ_c on temperature for fields of 2 T to 8 T for sample s2. With decreasing temperature, ΔJ_c is seen to increase smoothly. However, below what appears to be a field dependent temperature T_L, ΔJ_c starts to decrease again; for a 2 T scan, no peak at $\theta = 0°$ is found at temperatures less than 40 K. Traces

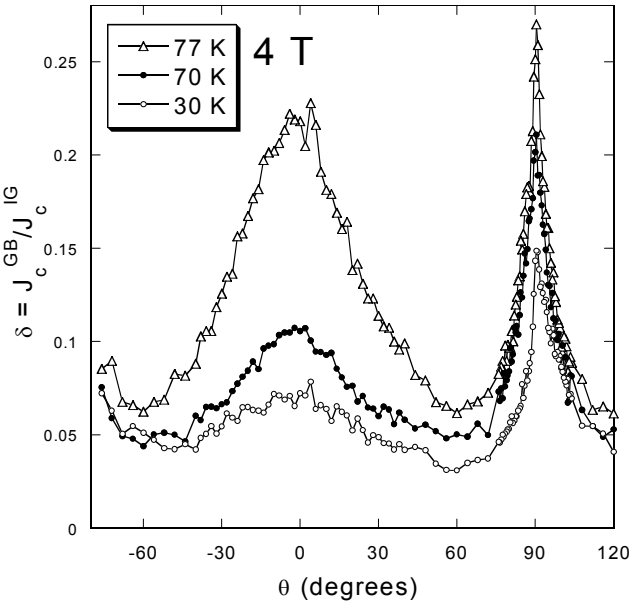

Figure 9.16. Temperature dependece of $\delta(\theta) = J_c^{GB}/J_c^{IG}$ at 4 T for sample pk2 (4.9°). The peak at $\theta = 0°$ develops with temperature due to the proximity of B_{irr}^{IG} and GB pinning ($Q = 2.4$).

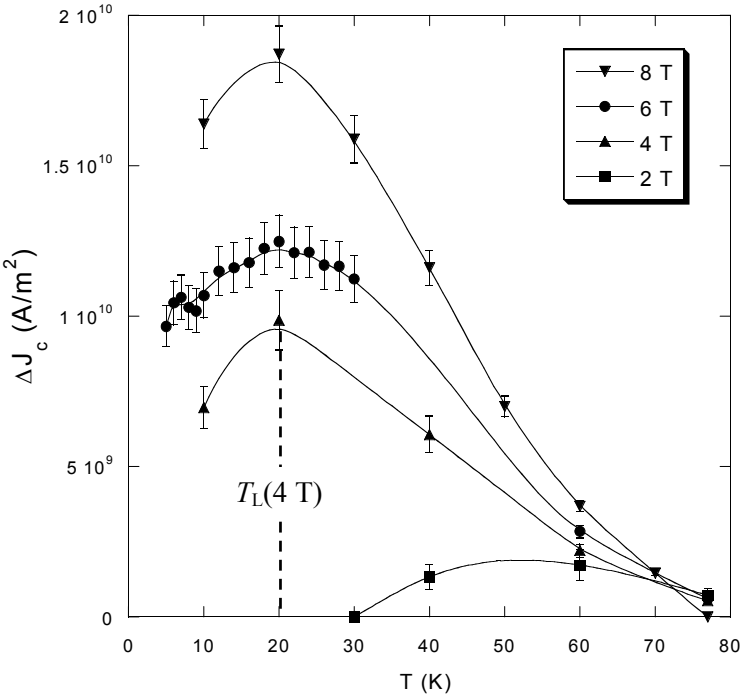

Figure 9.17. The dependence of the peak magnitude ΔJ_c on temperature for fields of 2, 4, 6 and 8 T for sample s2. Below T_L (similar for 4-8 T) ΔJ_c drops off with decreasing field. Errors of 5% (8 T) to 30 % (2 T) are estimated, and solid lines are a guide to the eye.

recorded at $T < T_L$ not only possessed reduced ΔJ_c, but at lower fields ($B <$ ~3 T for pk2) they developed a cusp at $\theta = 0°$. This will be presented and addressed in section 9.3.5, and is associated with the hysteretic behaviour also seen at low temperatures.

9.3.4.2 LAGB Pinning Model

A simple model, first proposed by Andres Díaz [11], has been developed to describe the observed temperature dependence of the LAGB pinning peak. The model is based on the pinning of individual vortices to the dislocation cores that constitute the LAGB. Both vortex and dislocation cores are assumed to a first approximation to be cylinders of radius $\xi_{ab}(T)$ and r_d respectively. The total pinning energy is therefore taken to be close to the value given by the condensation energy, $E_c(T) = B_c^2(t)/2\mu_o$ (equation 2.1) where $t = T/T_c$. We may estimate the vortex pinning force density (N/m^3) as

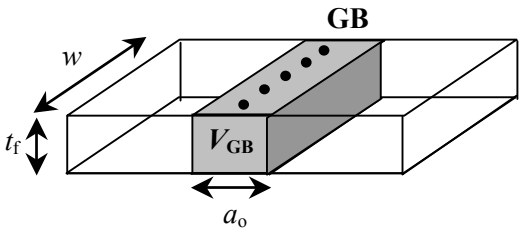

Figure 9.18. LAGB volume, $V_{GB} = a_o w t_f$, containing a line of $N_v = w/a_o$ vortices.

$$F_p = \frac{E_c(t)}{\xi_{ab}(t)} = \frac{B_c^2(t)}{2\mu_o \xi_{ab}(t)} \tag{9.1}$$

In order to calculate the elementary pinning force per vortex, f_p, the relevant vortex volume must be used (V) where, $f_p = F_p V$ (in Newtons). This has been estimated by assuming that a single line of vortices are pinned at the boundary. Above J_c^{GB} this line will be depinned and flow along the boundary, leading to dissipation over a width a_o (one vortex lattice space) as described in chapter 6 and sketched in figure 9.18. The volume of dissipation above J_c^{GB} is therefore $V_{GB} = a_o w t_f$. If $a_o > D$ (the dislocation spacing) we may say that the number of vortices pinned $N_v = w/a_o$. The vortex volume can therefore be estimated as

$$V = V_{GB}/N_v = a_o^2 t_f \tag{9.2}$$

Common temperature dependences for the critical field and coherence lengths are $B_c(t) = B_c(0)(1\text{-}t^2)$ and $\xi_{ab} = \xi_{ab}(0)(1 - t)^{-1/2}$ [12], which when substituted into 9.1 give

$$f_p = F_p V = \frac{B_c^2(0) a_o^2 t_f}{2\mu_o \xi_{ab}(0)} (1-t^2)^2 (1-t)^{1/2} = A(1-t^2)^2 (1-t)^{1/2} \tag{9.3}$$

where equation 9.2 has been used and A will be constant for a given field.

The next step was to compare the pinning force temperature dependence predicted by equation 9.3 with the results measured on the LAGB samples. In order to do this, the enhancement to pinning due to vortex alignment with the dislocation cores was assumed to be

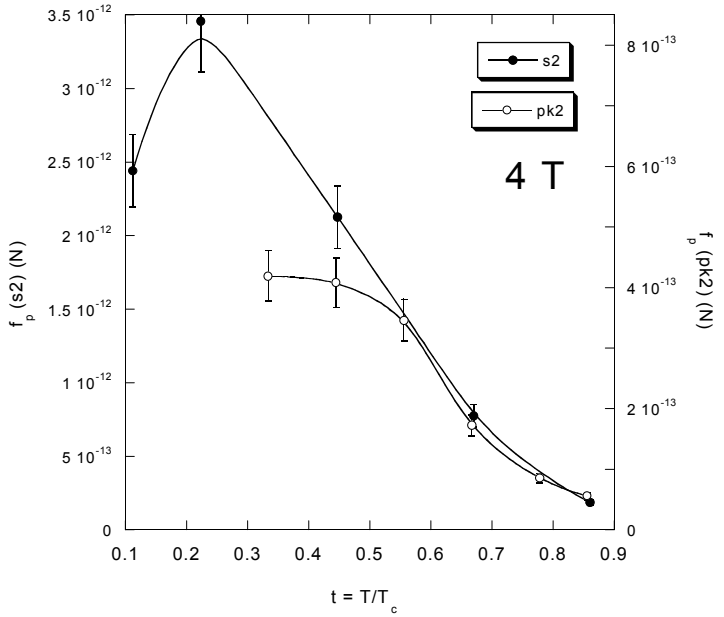

Figure 9.19. $f_p(t)$ extracted from sample s2 (left hand scale) and pk2 (right hand scale) at 4 T. Pinning is reduced for 4.9° sample pk2 over 3.8° s2, $f_p(\text{pk2}) < f_p(\text{s2})$.

$F_p = \Delta J_c B$, using the enhancement of J_c^{GB} seen about $\theta = 0°$ (see figure 9.4). The pinning force is therefore extracted as

$$f_p = F_p V = \Delta J_c B V = \Delta J_c B a_o^2 t_f = \frac{2}{\sqrt{3}} \Delta J_c \Phi_o t_f \qquad (9.4)$$

where equation 2.10 has been used to substitute for a_o.

Figure 9.19 shows a comparison of $f_p(t)$ extracted using equation 9.4 from sample s2 (left axis) and pk2 (right axis) at 4 T. Although a qualitatively similar behaviour is found for both LAGBs, the magnitude of the pinning force for the higher misorientation pk2 (4.9°) is reduced by a factor of ~ 4 from that of s2 (3.8°). Interestingly, the fall off of $\Delta J_c(t)$ and $f_p(t)$ at T_L also occurs at a much higher temperature for pk2.

The appropriateness of the predicted $f_p(t)$ of equation 9.3 is explored in figure 9.20, which shows the $\Delta J_c(T)$ data of figure 9.17 also converted using equation 9.4. The ΔJ_c axis (left hand scale) is effectively transformed by a factor $(2/\sqrt{3})\Phi_o t_f$, to give $f_p(t)$ plotted on the right hand axis. Subsequent fits of equation 9.3 are shown on the figure as dashed lines. For such a basic model the fits appear extremely good for the 4 T, 6 T and 8 T curves. The fits diverge from the measured data only at low temperatures, where the marked fall off in f_p and ΔJ_c can be seen below T_L.

The fall off of ΔJ_c has two possible sources. Firstly, as discussed in section 9.3.3.3, with decreasing temperature vortex cores *increase* in size and dislocation cores *decrease* in size. It

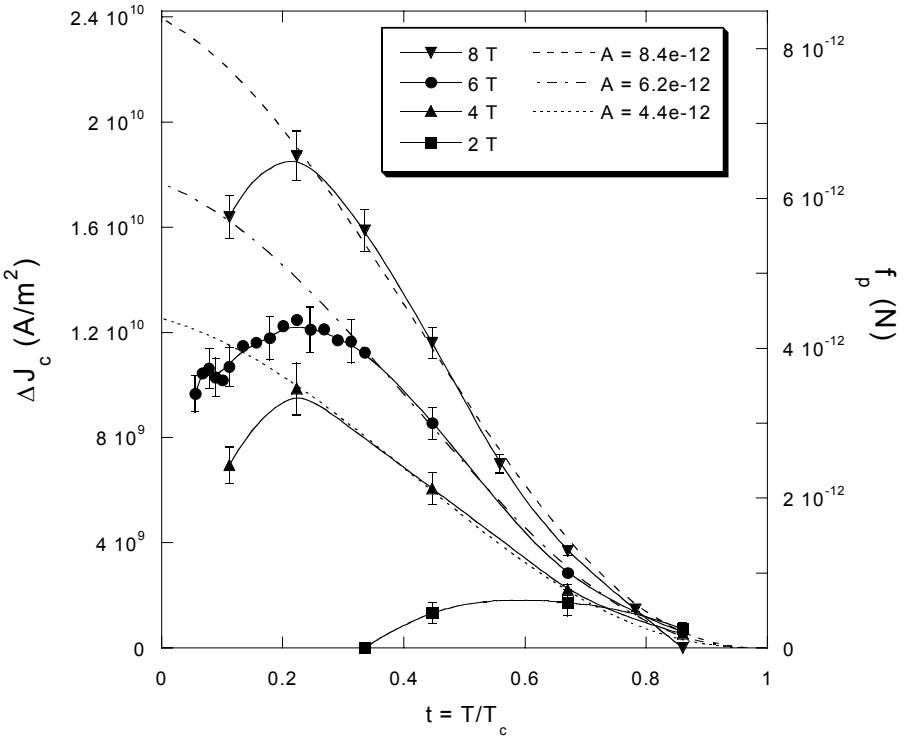

Figure 9.20. The $\Delta J_c(t)$ data of figure 9.17 (left hand scale) with reduced temperature $t = T/T_c$ for fields of 2 to 8 T, and the corresponding pinning force, f_p, calculated using equation 9.4 (right hand scale). Fits to equation 9.3 are also indicated. Solid lines are a guide to the eye.

is possible that the drop off is associated with a decrease in effective pinning. This agrees with the higher temperature fall off of $f_p(t)$ for pk2 – dislocation strain fields are smaller for increased misorientations. Alternatively, the decrease could mark the onset of the isotropic pinning enhancement predicted by Klein *et al* [8]. However, this effect was found to be absent in their single crystal YBCO samples below $T = 60$ K.

It should be noted that as field increases, the fitting parameter A as extracted from the data is also found to increase. However, as $A \propto a_o^2 \propto 1/B$ (equation 9.3) it is expected that A should *decrease* with field. This is a consequence of the calculation of vortex volume using the field dependent variables V_{GB} and N_v. The use of a constant V_{GB} alone would not alter this result and an additional modification, using $V = \pi\xi^2(t)t_f$, yielded a poor fit to the data.

9.3.5 LAGB Angular Hysteresis

9.3.5.1 Observation

At low temperatures and fields the angular scans of $J_c^{GB}(\theta)$ performed for rotation of applied field within the LAGB plane are found to display a marked hysteresis. The effect is visible as a clear shift in the position of the *intrinsic* pinning peak as a function of the direction of field rotation (θ^+ or θ^-). In this work, the effect is termed angular hysteresis and is found to become increasingly pronounced at both low field and low temperature. Similar measurements taken

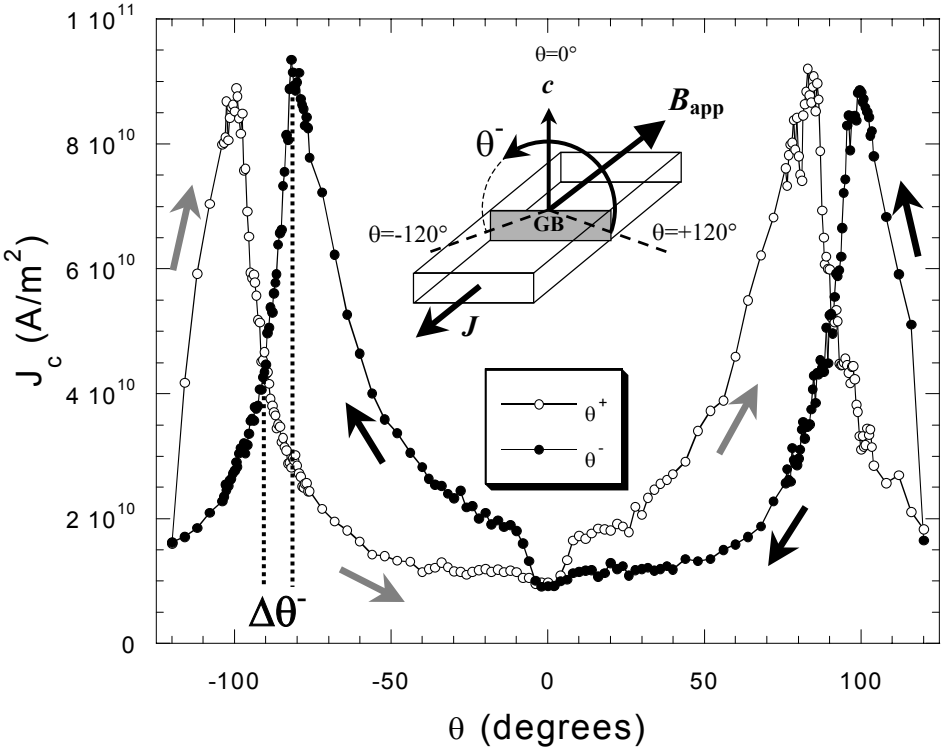

Figure 9.21. Angular measurement of $J_c^{GB}(\theta^+)$ and $J_c^{GB}(\theta^-)$ for sample pk2 at 2 T, 10 K. Pronounced hysteresis in $J_c^{GB}(\theta)$ with scan direction (θ- and θ^-) is visible as a shift in the intrinsic peak away from $\theta = \pm 90°$. Track width $w = 5.5$ μm. The inset shows the experimental geometry.

on intragranular tracks displayed no hysteresis, suggesting the effect is associated with the presence of the grain boundary. It is proposed that the angular hysteresis is linked to both the LAGB 'static' hysteresis measured in section 7.1.6 and the history dependent enhancement of flux at the LAGB - directly measured in section 5.3 by MO. These results confirm and greatly extend the low field (up to 1 T) angular measurements of Grimaldi *et al* [13] taken at only 65 K on a 5° LAGB.

A typical example of the angular hysteresis in $J_c^{GB}(\theta)$ observed is shown in figure 9.21, a $J_c^{GB}(\theta, \phi = 0°)$ profile taken at 10 K and 2 T for sample pk2. The intrinsic peaks are shifted away from $\theta = \pm 90°$ by an amount $\Delta\theta$, the sign of which is seen to depend upon the scan direction, θ^+ (giving $\Delta\theta^+$, a negative shift) or θ^- (giving $\Delta\theta^-$, a positive shift). The scale of the effect is such that at $\theta = -80°$, $J_c(\theta^-)$ is over 3 times that of $J_c(\theta^+)$. The dip in J_c at $\theta = 0°$ will be discussed in the next section, and is found to develop below T_L (section 9.3.4) when the LAGB pinning peak drops off in magnitude.

At both high T and high B, angular hysteresis is found to be suppressed. Plots of $J_c^{GB}(\theta^-)$ about the $\theta = -90°$ intrinsic peak are shown in figure 9.22(a) for pk2 as a function of applied field at 10 K. Although decreasing with field, hysteresis is still present at 8 T, 10 K. The temperature dependence of $J_c(\theta^-)$, also for pk2, is shown in 9.22(b) at 1 T. Hysteresis is not

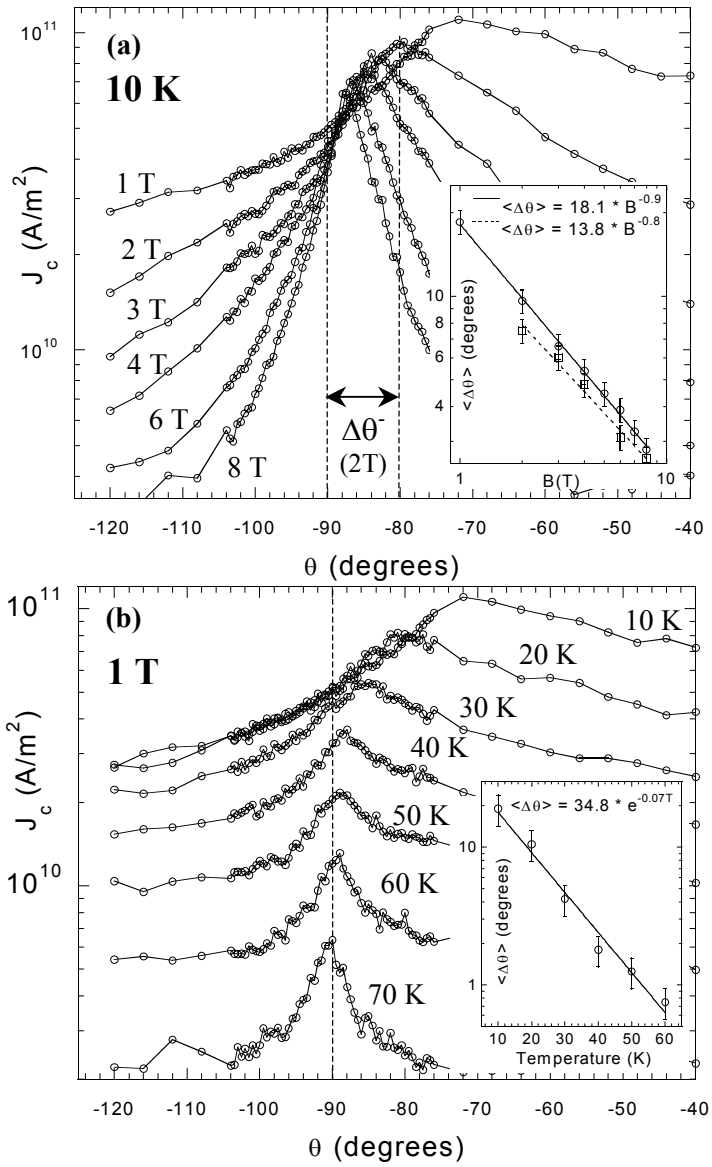

Figure 9.22.(a) Applied field and (b) temperature dependence of $J_c^{GB}(\theta^-)$ for pk2 for the θ = -90° intrinsic peak. Insets show the average intrinsic shift $\langle\Delta\theta\rangle = (|\Delta\theta^+|+|\Delta\theta^-|)/2$, as a function of field and temperature, including power law and exponential fits to B and T respectively (for s2, track width is also w = 5.5 μm and data is plotted as squares).

observable, within noise limits, for $T \geq 70$ K at 1 T. Similar scans on IG tracks of s2 show no detectable hysteresis, although direct comparison at *low* temperatures of IG $J_c(\theta)$ was not possible due to excessive contact heating.

9.3.5.2 Angular Hysteresis Model

It is proposed that LAGB *angular* hysteresis is linked to the LAGB *'static'* hysteresis in $J_c^{GB}(B, \theta = 0°)$ presented in section 7.1.6. Such static hysteresis is in turn almost certainly due to the history dependent flux enhancement directly measured to exist at the LAGB using the magneto-optic technique in section 5.3. Larger flux densities are experienced at the LAGB as the applied field parallel to *c* is ramped up (leading to lower J_c^{GB}), than when being ramped

down (leading to higher J_c^{GB}), in a model first proposed for polycrystalline material [14]. Angular hysteresis, also observed in Bi-2223 tapes [15,16], can be well explained within this linear, flux trapping (FT) model by recognising that the component of $\boldsymbol{B}_{app}$ perpendicular to the *ab*-plane ($B_\perp$) varies in magnitude as the external field is rotated. Rotation away from the *c*-axis (see figure 9.23) induces a reverse (-ve, or along the -*c* direction) flux, $\boldsymbol{B}_{rev}$, in the LAGB that must now be added *vectorially* to the applied field to obtain the local (net) flux direction, $\boldsymbol{B}_{GB} = \boldsymbol{B}_{app} + \boldsymbol{B}_{rev}$. It is at the intrinsic position, where J_c^{GB} varies rapidly with angle, that such small changes in the applied field direction result in large changes in J_c^{GB} magnitude. The induced flux and the vectorial addition that occurs during a $J_c^{GB}(\theta^+)$ measurement is sketched in figure 9.23. The intrinsic position is shifted towards $\theta = 0°$ as the net flux at the LAGB becomes aligned with the *ab*-plane for $\theta < 90°$.

More generally, the magnitude and sign of the induced LAGB flux component is determined by the flux profile within the neighbouring IG region. As discussed in section 5.3 and sketched in figure 5.15, whether the IG flux profile is paramagnetic or diamagnetic depends sensitively on the external field history. Just a small change $B_\perp$ is expected to switch flux profiles and reverse the sign of the LAGB flux component. Consequently, just a small reversal in the *direction* of field scan (from θ^+ to θ^-) will switch the grain magnetisation from paramagnetic to diamagnetic and change the sign of the LAGB flux component. Thus, a corresponding switch from $J_c^{GB}(\theta^+)$ to $J_c^{GB}(\theta^-)$ should also be observed over the same small

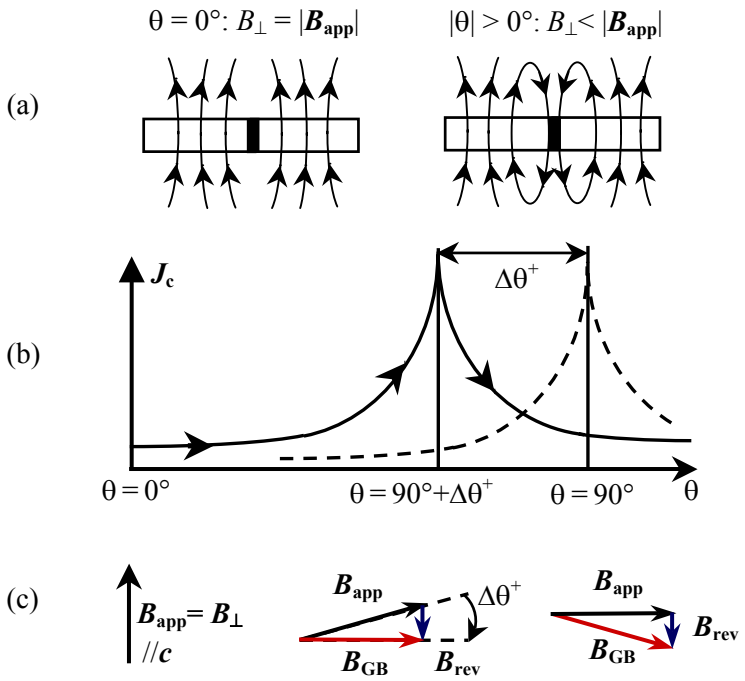

Figure 9.23.(a) Schematic diagram of the induced LAGB reverse flux as the field perpendicular to the *ab*-plane ($B_\perp$) is ramped down by rotation of the applied field, $\boldsymbol{B}_{app}$. (b) Schematic LAGB $J_c^{GB}(\theta^+)$ scan depicting hysteretic shifting of the intrinsic peak ($\Delta\theta^+$ is negative). The dotted line shows the unshifted peak position. (c) The corresponding vectorial addition of $\boldsymbol{B}_{app}$ and the induced LAGB reverse flux density, $\boldsymbol{B}_{rev}$, to give the *net flux direction*, $\boldsymbol{B}_{GB}$, at the angles marked in (b) during the θ^+ rotation.

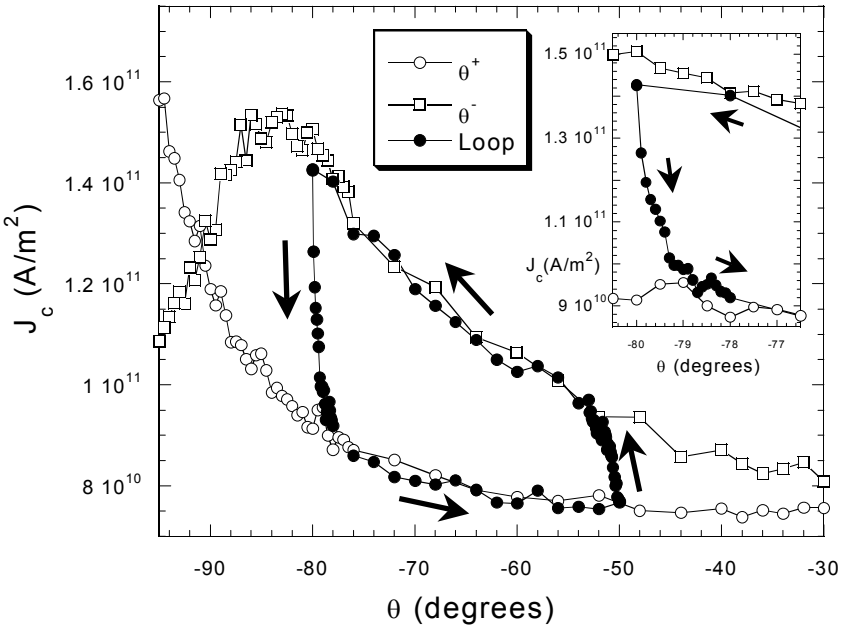

Figure 9.24. $J_c^{GB}(\theta^+)$, $J_c^{GB}(\theta^-)$ and a loop measured between θ = -50° and -80° for s2 at 2 T, 10 K. A sharp angular transition between the two scan directions can be seen, as the inset shows in more detail at θ = -80°.

change in angle. This is indeed what we find, figure 9.24 showing $J_c^{GB}(\theta^+)$, $J_c^{GB}(\theta^-)$ and a $J_c^{GB}(\theta)$ loop measured between θ = -50° and θ = -80° for sample s2 at 2 T, 10 K. The switch from $J_c^{GB}(\theta^+)$ to $J_c^{GB}(\theta^-)$ occurs within approximately 2-3° at θ = -80° (see inset of figure 9.24), and within 4° at θ = -50°, corresponding to a field change parallel to *c* of, $\Delta B_\perp = 0.10$ T and 0.11 T respectively.

In order to confirm this as the correct order of field change required to switch the IG magnetisation we used a Quantum Design SQUID magnetometer to perform *M-H* loop

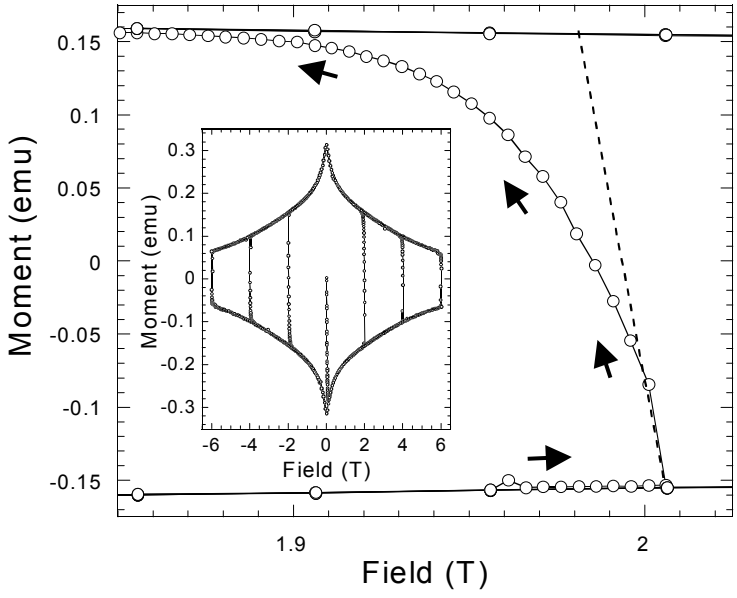

Figure 9.25. *M-H* loops measured for thin film YBCO sample 1277 (size 3 mm^2) in a perpendicular field, shown for 2, 4 and 6 T turning fields in the inset. The main plot shows the 2 T transition from $-M$ to $+M$ in more detail (dashed line shows initial transition slope).

measurements on a thin film YBCO sample in perpendicular field. The *M-H* loops are plotted in the inset of figure 9.25 for turning fields of 2 T, 4 T and 6 T at 10 K. They display an initial sharp transition in field to a negative maximum (demagnetising effects mean that the theoretical $M = -H$ is not observed), followed by a slow increase associated with mixed state flux penetration. At the turning fields the sharp switch from $-M$ to $+M$ can be seen to occur over a relatively small field range compared to the applied field magnitude. The main plot in figure 9.25 shows the 2 T turn in more detail. The full transition occurs in approximately 0.15 T, agreeing well with the value extracted from our angular measurements and the MO measurements of section 5.3. Although measured on a 3 mm^2 sample, it can be shown that this value would only be expected to halve for a 10 μm wide track [17,18].

The FT model also explains the development of the characteristic cusp in $J_c^{GB}(\theta)$ that occurs as field sweeps across $\theta = 0°$ from a particular direction (see figure 9.21). It simply marks a switch from paramagnetic to diamagnetic IG flux profile, as $B_\perp$ switches from increasing to decreasing. As such, a few degrees beyond the $\theta = 0°$ point the LAGB flux component switches sign from +ve to –ve, shifting the $J_c^{GB}(\theta)$ curve upwards as net flux at the GB is reduced.

As the IG flux profile slope is roughly a function of J_c in the critical state [19], one *may* expect angular hysteresis to scale with J_c. The insets of figure 9.22(a) and (b) show rough power law and exponential scaling of $<\Delta\theta>$ (averaged over $\Delta\theta^+$ and $\Delta\theta^-$) with B and T respectively. As an approximation to the dependence of $J_c^{IG}(B,\theta = 0°)$ (chapter 7) this tends to support the FT model. The insets also show that hysteresis is less pronounced for the smaller misorientation boundary, s2 (3.8°), consistent with the reduced degree of flux focussing expected at the GB.

More important evidence of the validity of the angular FT model is found in a direct comparison to the hysteretic 1-Dimensional static measurement of $J_c^{GB}(B,\theta = 0°)$ in figure 7.14. Figure 9.26 plots the data of figure 7.14, along with both $J_c^{GB}(\theta^+)$ and $J_c^{GB}(\theta^-)$ as a function of the component of field perpendicular to the *a-b* planes, $J_c^{GB}(B_\perp = B_{app}\cos\theta)$. In terms of an angular measurement, the static $J_c^{GB}(B,\theta = 0°)$ curve represents a scan starting at $\theta = -90°$ ($B_\perp = 0$ T), rotating in θ^+ to $\theta = 0°$ ($B_{app} = B_\perp = 2$ T), then rotating back in θ^- until $B_\perp = 0$ T and $\theta = -90°$ again. Both curves can be seen to agree qualitatively, displaying similar hysteretic behaviour and possessing characteristic peaks [14] at low field (~0.2 - 0.3 T). For an angular scan this peak corresponds to intrinsic pinning, net flux lying along the *a-b* plane. For the static scan, it corresponds to maximum cancellation of $B_\perp$ and the LAGB flux component, indicating a B_{rev} of approximately - 0.2 to - 0.3 T.

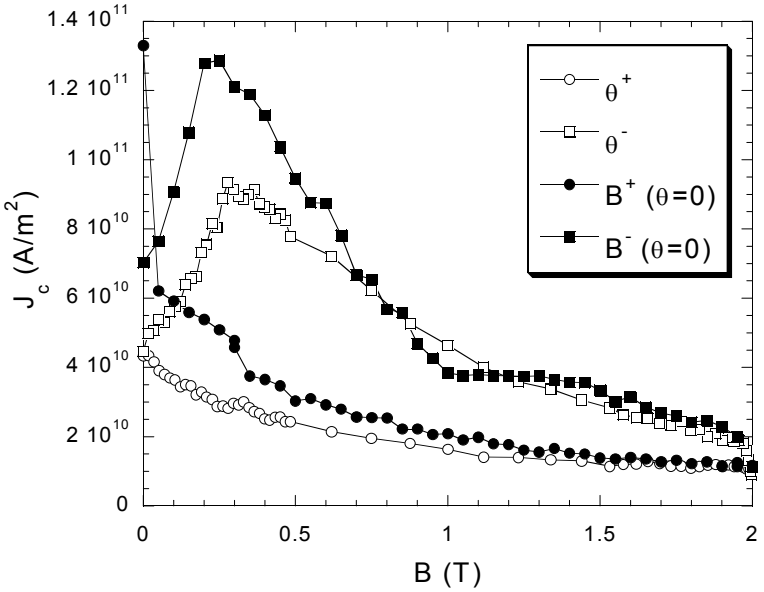

Figure 9.26. Static $J_c^{GB}(B, \theta = 0°)$ measurement of figure 7.14 (up to 2 T) for increasing (B^+) and decreasing (B^-) field for sample pk2 at 10 K (filled symbols). This is compared to the angular measurement $J_c^{GB}(B_\perp = B_{app}\cos\theta)$ for $B_{app} = 2$ T for the same sample (open symbols).

The MO imaging of section 5.3 has measured the magnitude and sign of the GB flux enhancement on a square of 250 μm^2 in sample pk2 at 4.2 K. An applied flux density of 93 mT (approximately the total penetration field for the IG region) resulted in a flux density locally at the LAGB of $B_{GB} = 165$ mT ± 15%. Saturation of the MO active layer at these relatively high fields means that the additional flux in the LAGB could be up to $B_{rev} = 91$ mT, approximately 0.1 T. This is on the same order as the 0.2 to 0.3 T predicted above, and indicates that significant additional components of flux can exist at a thin film LAGB.

Quantitatively, the curves of figure 9.26 can be seen to diverge in J_c^{GB} magnitude. This is primarily ascribed to the failure of the FT model to account for the fact that, in YBCO, J_c is not just a function of the *c*-axis component of magnetic field. The shoulder in J_c^{GB} observable from 1 to 1.5 T in the static measurement is also interesting and may be due to commensurability effects associated with the vortex lattice and LAGB channel [20]. It should be noted that this effect (flux line shear) is also another possible cause of hysteretic behaviour in $J_c(B)$ curves.

9.3.6 The *V-I* Characteristic

The *V-I* characteristic over the whole course of the $J_c^{GB}(\theta, \phi = 0°)$ scan was found to display linearity indicative of viscous channelling (see chapter 6). This is due of the fact that vortices remain locked into the GB defect plane over the scan range, resulting in localised dissipation and flux flow at the boundary (see section 9.3.1). However, GL theory predicts a decrease in the flux flow resistivity with angle of applied field in an anisotropic material. According to

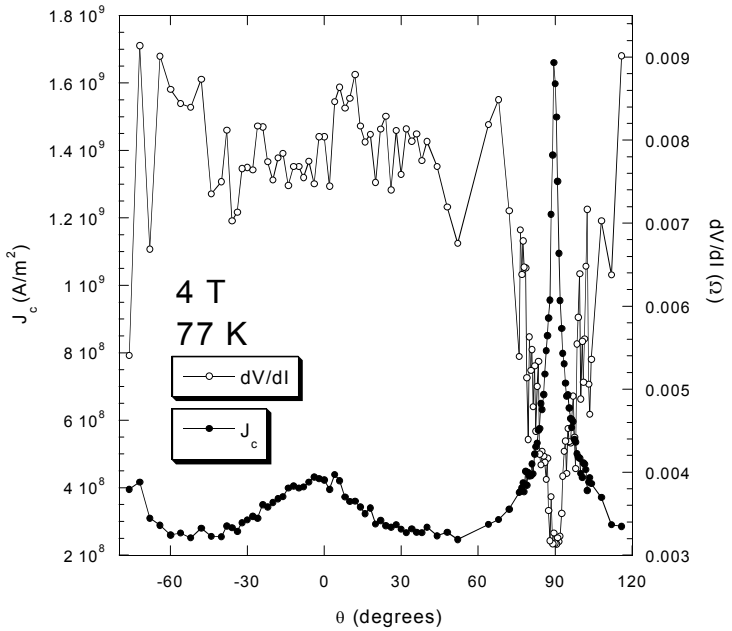

Figure 9.27. $J_c^{GB}(\theta)$ (left scale) and dV/dI(θ) (right scale) extracted from pk2 as a function of θ at 77 K, 4 T (w = 9.8 μm).

equation 2.16, $\rho_f \propto 1/B_{c2}(\theta)$, which combined with the scaling law of equation 2.21 predicts that $\rho_f(\theta) = \varepsilon_\theta \rho_f^c$, where ρ_f^c represents the flux flow resistivity for a vortex *lying* along the *c*-axis and *moving* along the *ab*-plane. Comparing values at θ = 0° and 90° this means that we expect $\rho_f^{ab}/\rho_f^c = 1/\Gamma$ = 0.14 - 0.2, where Γ = 5 – 7 (ρ_f^{ab} stands for vortices *lying* along the *ab*-plane and *moving* in the *c*-direction). A more detailed analysis by Hao and Clem [21] for flux flow in HTS materials yielded the only slightly different result of $\rho_f^{ab}/\rho_f^c = 4/(3\Gamma)$.

Figure 9.27 shows an example of dV/dI as a function of θ, extracted at a 1 μV criterion from the LAGB of pk2 at 77 K, 4 T. Also plotted is the corresponding $J_c^{GB}(\theta)$. The large degree of noise seen in dV/dI(θ) is associated with the *V-I* noise discussed in section 6.5, and makes determination of the precise θ dependence difficult. The ratio ρ_f^{ab}/ρ_f^c = [dV/dI(90°)]/[dV/dI(0°)] ~ 0.38 ± 0.05. If the *V-I* gradient is simply proportional to ρ_f, this reduction in gradient is less than that predicted above.

One reason why the expected reduction is not observed may lie in the stronger interaction between flux lines lying along the *ab*-plane (increased viscosity and shear modulus, c_{66}). This may result in increased vortex dragging effects causing additional rows to begin flowing along the GB above a certain current, increasing the *V-I* gradient (section 6.4). In this manner, the reduced ρ_f for field along the *ab*-plane may be expected to produce the same *V-I* kinking observed at lower temperatures for $B \parallel c$ presented in chapter 6. Although no clear kinks in the *V-I* characteristic were found at θ = 90° (4 T, 77 K), multiple kinking may result in curvature as opposed to clear gradient jump (section 6.6). It should be noted signs of *V-I*

structure indicative of a change in the number of channelled vortex rows *can* be seen in the measurements of Díaz *et al* at 60 K, for field parallel to the *ab*-plane [22].

9.4 Scanning Field Out of the GB Plane: $J_c^{GB}(\theta, \phi = 90°)$

9.4.1 Vortex Channelling

Measurements of $J_c^{GB}(\theta)$ were also performed for field rotation out of the LAGB plane ($\phi = 90°$), a geometry shown in figure 9.1(b). Unlike field scans within the plane (described in section 9.3), in this measurement vortices are rotated out of the boundary plane and towards the force free configuration. In this respect the scan is similar to $J_c^{GB}(\phi)$ described in chapter 8 for rotation in the *ab*-plane. The main difference is that $J_c^{GB}(\theta)$ includes an additional modulation due to the anisotropy between the *c* and *ab* directions.

Example measurements of $J_c^{GB}(\theta,\phi = 90°)$ and $J_c^{IG}(\theta,\phi = 90°)$ taken at 4 T, 77 K on sample pk2 are shown in figure 9.28. The GB trace is seen to be relatively featureless and almost independent of angle around the $\theta = 0°$ position, unlike the $J_c^{GB}(\theta,\phi = 0°)$ scans performed within the plane (figure 9.4). Although $J_c^{GB} < J_c^{IG}$ at low θ, as field rotates to high angles a transition in behaviour may be seen. For $|\theta| > \sim 80°$ the $J_c^{GB}(\theta)$ and $J_c^{IG}(\theta)$ curves are seen to almost merge and display the same dependence on θ. This is shown more clearly in the logarithmic plot in the inset of figure 9.28.

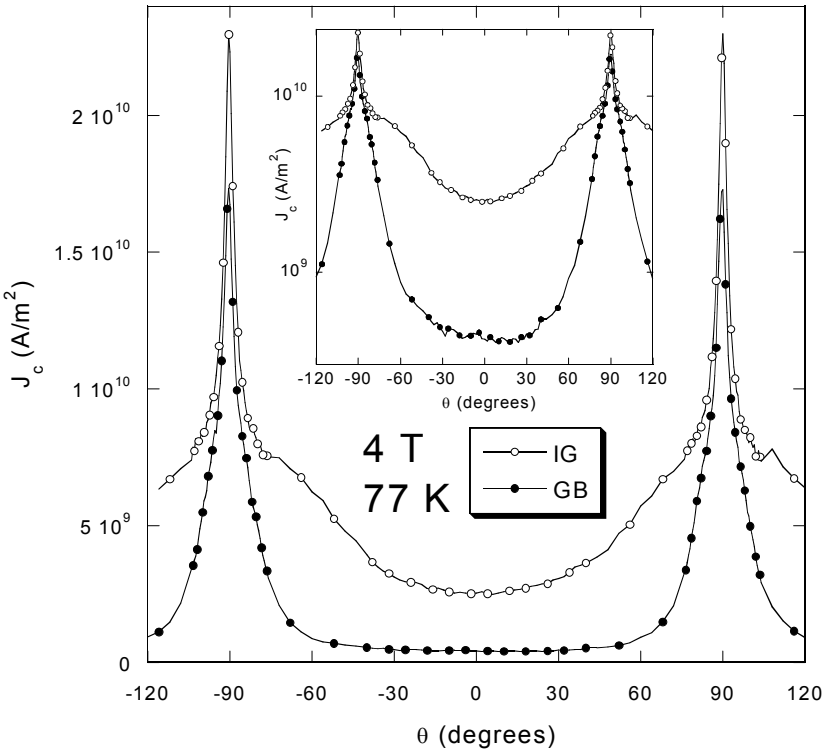

Figure 9.28. $J_c(\theta)$ measured for rotation at $\phi = 90°$, for GB and IG at 4 T, 77 K for sample pk2. The inset plots the same data on a log scale. Both tracks are $w = 9.8$ μm wide, and $Q = 1.4$.

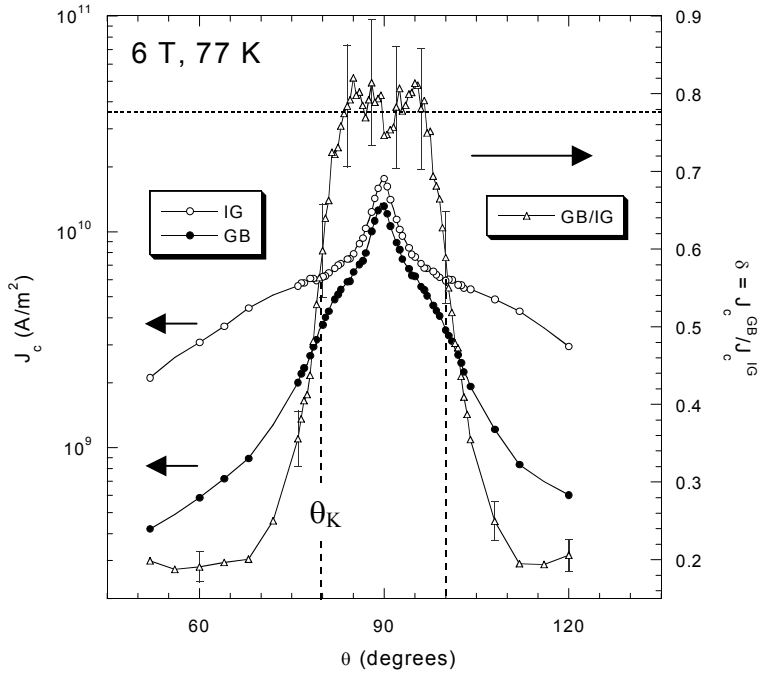

Figure 9.29. Close up of the behaviour of $J_c^{GB}(\theta)$ and $J_c^{IG}(\theta)$ for $\phi = 90°$, at 6 T, 77 K near the force free peak (left hand scale). Also plotted is $\delta(\theta) = J_c^{GB}/J_c^{IG}$ showing a transition to $\delta(\theta) \sim 0.8$ for $\theta > \theta_K$ (dashed line). Errors of ± 10% are estimated in $\delta(\theta)$.

This is a very similar result to that obtained in chapter 8 for ϕ above the vortex kinking angle, ϕ_K. Instead of ϕ_K found for a $J_c^{GB}(\phi)$ scan, we now see θ_K for a $J_c^{GB}(\theta)$ scan. The similarity of the result can be further explored by plotting the transparency ratio $\delta(\theta) = J_c^{GB}/J_c^{IG,}$ as seen in figure 9.29 for a scan taken at 6 T, 77 K. At $\theta_K \sim 80°$ the curves J_c^{GB} and J_c^{IG} (plotted on the left hand axis) close together, leading to a corresponding leap in $\delta(\theta)$ to approximately 0.8. We see that $\delta(\theta)$ remains ~0.8 across the force free peak, except for θ within a few degrees of 90°. The fact that $J_c^{GB}(\theta) = 0.8J_c^{IG}(\theta)$ for $\theta > \theta_K$ is exactly as found in chapter 8 for $\phi > \phi_K$. We may therefore interpret θ_K as the transition from a kinked vortex structure, in which vortex segments are still aligned with the LAGB, to a collinear structure, in which vortices are fully aligned with the external field. For $\theta < \theta_K$, channelling of vortex segments occurs along the LAGB plane in the *ab* direction. For $\theta > \theta_K$ no channelling occurs and dissipation is dominated by the IG properties of the LAGB track.

In this $J_c^{GB}(\theta,\phi = 90°)$ geometry we find a much larger vortex kinking angle than found at equivalent *B* and *T* in chapter 8, where $\theta_K(77\text{ K}, 4\text{ T}) \sim 80° >> \phi_K$ (4 T, 77 K) = 26°. As discussed in depth in section 8.6, this is likely to be due to an increase in the relative importance of GB meander on vortex alignment for the $J_c^{GB}(\theta)$ scan. The boundary plane of sample pk2 in the direction of growth is measured to deviate from $\theta = 0°$ (*c*-axis) by up to 45° in places (section 5.3) due to the multiple meander mechanism (section 3.4). As a fraction of

the GB length, such a deviation is much more important for field along the *c*-axis (t_f = 145 nm) than for field along the *ab*-plane (w = 9.8 μm here). As such, it is entirely possible that vortex accommodation to areas of the LAGB plane occurs over an extended range of angles in θ. This is backed by the measurements of section 8.6; rotating in ϕ at an angle θ < 90° (field no longer lying fully in the *ab*-plane) resulted in an *increased* magnitude of ϕ_K (see figure 8.26) over the ϕ = 90° value. The measurement of figure 9.28 represents a cut across figure 8.26 – it involves sitting at ϕ = ± 90° in figure 8.26 and moving across the $J_c^{GB}(\phi)$ curves along the J_c axis.

The relative independence of $J_c^{GB}(\theta)$ about θ = 0° could therefore be interpreted in terms of vortices locked in to the defect plane, an effect not seen in the $J_c^{GB}(\phi)$ measurements. As θ is rotated further away from θ = 0°, $J_c^{GB}(\theta)$ increases due to three effects (a) a reduction in the driving Lorentz force (b) a reduction in the vortex segment length L_K within the plane, which increases the pinning force per unit length on each segment, and (c) an increase in pinning due to the intrinsic effect; either to the layered *ab*-planes or via the anisotropic GL theory.

9.4.2 Field Dependence

Figure 9.30 shows the field dependence of $J_c^{GB}(\theta,\phi = 90°)$ at a temperature of 77 K. Also plotted is $J_c^{IG}(\theta,\phi = 90°)$ at 2 T, 77 K for comparison. It can be seen that $J_c^{GB}(\theta = 0°)$ has a stronger dependence on field than $J_c^{GB}(\theta = 90°)$ over the field range 2 – 6 T.

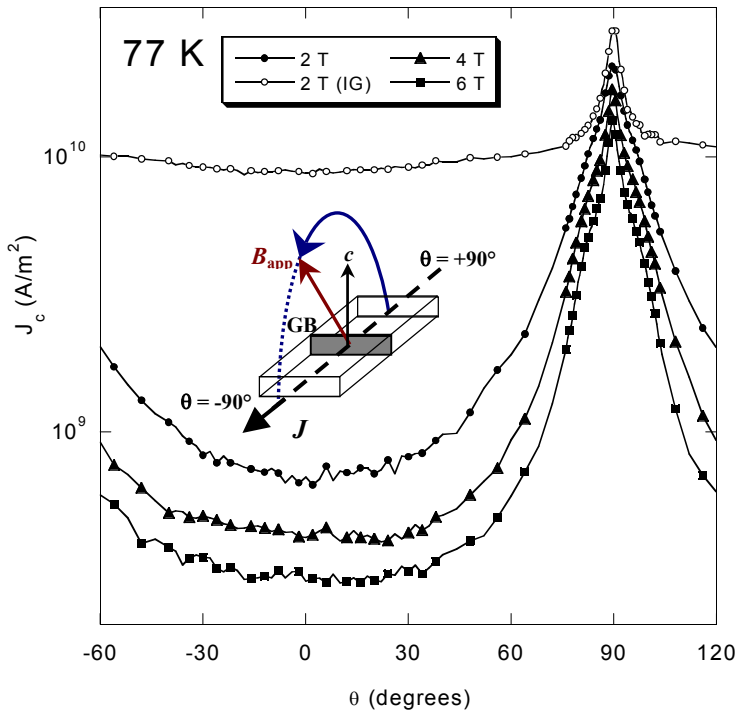

Figure 9.30. Field dependence of $J_c^{GB}(\theta)$ for rotation out of the GB plane (ϕ = 90°) at 77 K. Also plotted is $J_c^{IG}(\theta)$ recorded at 2 T, 77 K. Inset shows scan geometry.

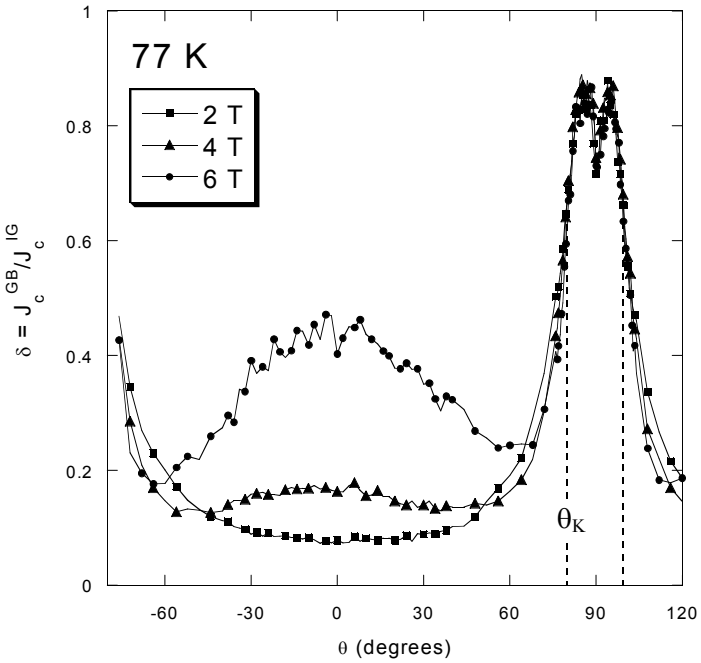

Figure 9.31. Field dependence of the transparency $\delta(\theta) = J_c^{GB}/J_c^{IG}$ for the data of figure 9.28. Notable features include the fact that θ_K appears relatively field independent, and the development of a peak at $\theta = 0°$ ($O = 1.4$).

The corresponding field dependence of $\delta(\theta)$ is explored in figure 9.31 for the data of figure 9.30. As field is increased, a peak in $\delta(\theta)$ is seen to develop about $\theta = 0°$. This is due to the relatively weak dependence of $J_c^{GB}(\theta)$ on angle in this position, as discussed in the previous section. The peak is enhanced for higher fields due to the suppression of $J_c^{IG}(\theta)$ by the proximity of B_{irr}^{IG}. The figure also shows that the magnitude of θ_K is found to vary only very weakly with field, as opposed to the strong field dependence found for ϕ_K in section 8.3.4. As ϕ_K was found to scale with $[J_c^{GB}(\phi_K)]^{1/2}$, a similar dependence for θ_K would explain this field invariance – as noted above, J_c^{GB} varies only weakly with field near the nominal force free position. The value of $\delta(\theta > \theta_K) \sim 0.8$ is seen to be independent of field in figure 9.31, as expected in the channelling model of chapter 8. Deviation does occur, however, for fields close to $\theta = 90°$ where a dip develops with increasing B.

It should be noted that unlike the scans of section 9.3.5, no angular hysteresis was found in the $J_c^{GB}(\theta,\phi = 90°)$ measurements. There is no intrinsic reason, however, why such hysteresis should not be observed in $\phi = 90°$ angular scans. The lack of observation is likely to be because measurements in this geometry were restricted to high temperatures (77 K) where hysteretic effects are suppressed.

9.4.3 The *V-I* Characteristic

More evidence of a transition from vortex channelling to IG determined dissipation at θ_K can be found in the nature of the *V-I* characteristics during the $J_c^{GB}(\theta,\phi = 90°)$ measurement. As

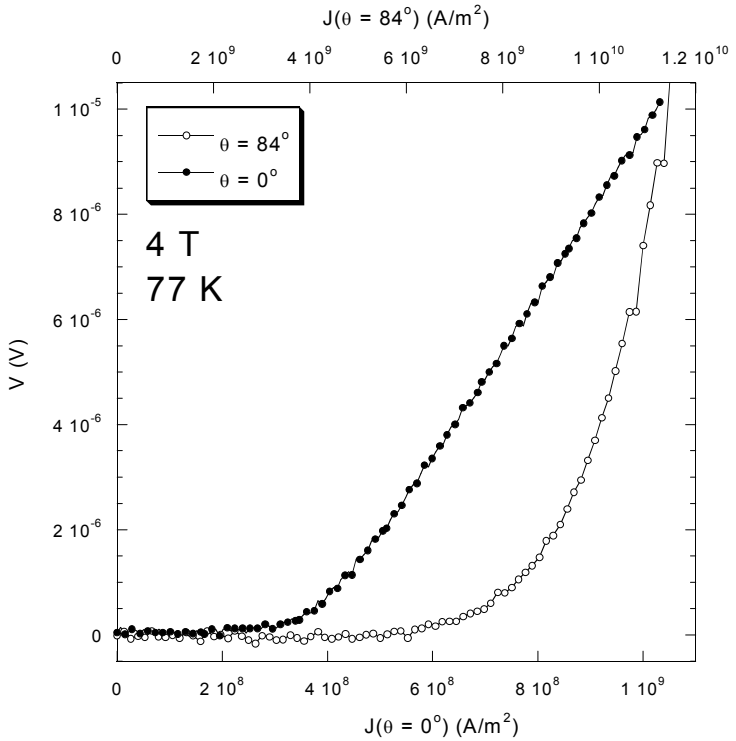

Figure 9.32. *V-I* characteristics taken at θ = 0° (plotted on the lower scale) and θ = 84° (plotted on the upper scale) during the 4 T $J_c^{GB}(\theta,\phi = 90°)$ scan of figure 9.28. The change from linear to curved for $\theta > \theta_K \sim 80°$ is evidence the transition from kinked to collinear vortices.

field rotates in θ out of the GB plane (nominally at θ = 0°) a transition occurs in *V-I* nature, from linear to curved. This behaviour is also observed for rotation out of the GB in ϕ, as presented in section 8.5. The onset of such curvature indicates that flux flow, and dissipation, is no longer localised to the GB. Figure 9.32 compares *V-J* curves taken at θ = 0° ($< \theta_K$) and θ = 84°, ($> \theta_K \sim 80°$). The relatively linear, VFF dominated *V-J* obtained for field at θ = 0° contrasts markedly with the creep dominated *V-I* obtained at θ = 84°, where no channelling is expected to occur.

Figure 9.33 emphasises the transition at θ_K by plotting $dV/dI(\theta)$ for both GB and IG tracks at 77 K, 4 T. Gradients were taken at comparative voltage criterions simply determined by the track lengths, where $V_c^{IG} = 1.4 V_c^{GB} = 1.4$ μV (see section 4.2.5). This figure shows a remarkable similarity in behaviour with that shown in figure 8.22 for rotation out of the GB in ϕ. As also found for $\phi > \phi_K$, for $\theta > \theta_K$ the gradients of both GB and IG *V-I* characteristic become very similar, indicating the near identical *V-I* characteristics which are only a factor of $\delta(\theta) = 0.8$ displaced apart in *J*. Both figure 9.33 and 8.22 show that within the channelling dominated angular range ($\theta < \theta_K$, $\phi < \phi_K$) the GB gradient is significantly larger than that in the IG track – indicative of the domination of flux flow resistivity over flux creep mentioned above (chapter 6).

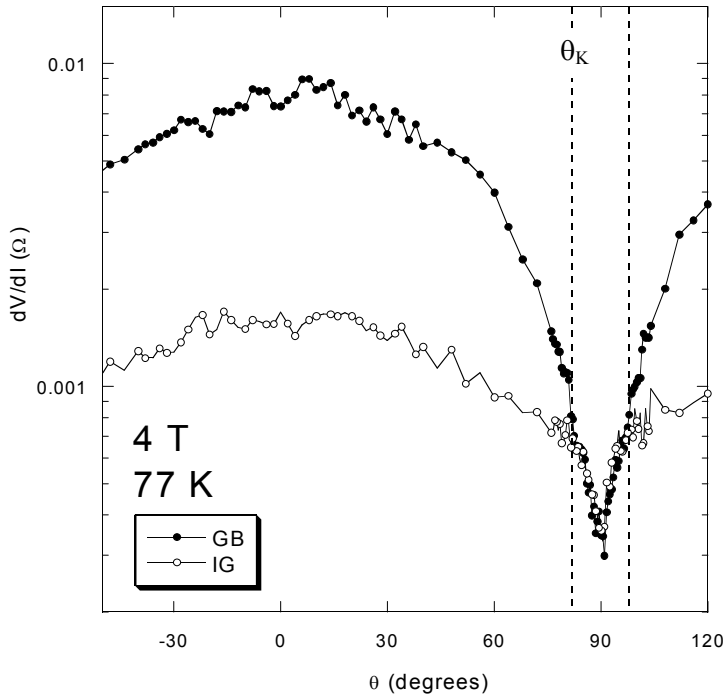

Figure 9.33. dV/dI measured during a 77 K, 4 T $J_c(\theta)$ measurement on both GB and IG track. For $\theta > \theta_K$ dV/dI curves effectively merge indicating the similar dissipative mechanisms for both GB and IG tracks in the collinear vortex state (Q = 1.4).

9.5 Summary

This chapter has shown that for field rotation *within* the plane of the LAGB ($\phi = 0°$) measurements probe a dissipative regime determined by vortex channelling over the whole scan range. An enhancement of $J_c^{GB}(\theta)$ about $\theta = 0°$ is interpreted in terms of pinning of vortices within the easy flow channel to the LAGB dislocation array. A simple core pinning model was found to fit the temperature dependence of the LAGB pinning peak well, except at low temperatures and low fields where the $J_c^{GB}(\theta)$ peak falls off in magnitude. This may be due to either vortex end effects, a fall off in pinning effectiveness or enhanced vortex accommodation resulting in an isotropic $J_c^{GB}(\theta)$ enhancement.

$J_c^{GB}(\theta,\phi = 0°)$ is also found to display pronounced hysteresis with the direction of rotation of the external applied field. This is linked to flux trapping within the grains, resulting in an *additional* flux component through the LAGB that must be vectorially summed with the applied field. This can lead to internal fields aligned with the *a-b* plane for external fields up to 20° away from 90° (10 K, 1 T). The model also accounts for the appearance of a low temperature cusp in $J_c^{GB}(\theta,\phi = 0°)$ at $\theta = 0°$.

For field scans *out* of the LAGB plane ($\phi = 90°$), the $J_c^{GB}(\theta)$ curves have been interpreted in terms of a transition from kinked and channelled vortices, to collinear vortices at an angle θ_K.

This is very similar behaviour to that observed scanning out of the GB in the *ab*-plane (chapter 8). The increased kinking angle (80°) indicates the distorted nature of the GB in the *c*-direction on the scale of the film thickness.

9.6 References

[1] A. Díaz, L. Méchin, P. Berghuis, and J. E. Evetts, *Phys. Rev. Lett.* **80**, 3855 (1998)

[2] V. Roas, L. Schultz and G. Saemann-Ischenko, *Phys. Rev. Lett*. **64**, 479 (1990)

[3] V.M. Pan, V.S. Flis, V.A. Komashko, O.P. Karasevska, V.L. Svetchnikov, M. Lorenz, A.N. Ivanyuta, G.A. Melkov, E.A. Pashitskii and H.W. Zandbergen, *IEEE Trans. Appl. Supercond.* **11**, 3960 (2001)

[4] B. Dam, J.M. Huijbregtse, F.C. Klaassen, R.C.F. van der Geest, G. Doornbos, J.H. Rector, A.M. Testa, S. Freisem, J.C. Martinez, B. Stauble-Pumpin and R. Griessen, *Nature* (London) **399**, 439 (1999)

[5] A. Pomar, L. Martel, Z.Z. Li and H. Raffy, *Phys. Rev. B* **63**, 134525 (2001)

[6] L. Civale, A.D. Marwick, T.K. Worthington, M.A. Kirk, J.R. Thompson, L. Krusinelbaum, Y. Sun, J.R. Clem and F. Holtzeberg *Phys. Rev. Lett.* **67**, 648 (1991)

[7] J.E. Sonier, R.F. Kiefl, J.H. Brewer, D.A. Bonn, S.R. Dunsiger, W.N. Hardy, R. Liang, R.I. Miller, D.R. Noakes and C.E. Stronach, *Phys. Rev. B* **59**,R729 (1999)

[8] L. Klein, E.R. Yacoby, Y. Wolfus, Y. Yeshurun, L. Burlachkow, B. Ya Shapiro, M. Konczykowski, F. Holtzberg, *Phys. Rev. B* **47**, 12349 (1993)

[9] V. Hardy, A. Wahl, S. Hebert, A. Ruyter, J. Provost, D. Groult and Ch. Simon, *Phys. Rev B* **54**, 656 (1996)

[10] E.H. Brandt, *Phys. Rev. B* **48** 6699 (1993)

[11] A. Díaz, *Private Communication* (1999)

[12] M. Tinkham, *Introduction to Superconductivity*, 2nd Edition, McGraw-Hill, New York (1996); J. R. Waldram, *Superconductivity of Metals and Cuprates*, IoP Publishing, London, (1996)

[13] G. Grimaldi, V. Boffa, G. Celentano, F. Fabbri, U. Gambardella, S. Pace and T. Petrisor, *IEEE Trans. Appl. Supercond.* **11**, 3776 (2001)

[14] J.E. Evetts and B.A. Glowacki, *Cryogenics* **28**, 641 (1988)

[15] M. Rábara, T. Takeuchi, K. Miya, *Physica C* **313**, 213 (1999)

[16] F. Warmont and H. Jones, *Supercond. Sci. Technol.* **14**, 145 (2001)

[17] C. Jooss, A. Albrecht, H. Kuhn, S. Leonhardt and H. Kronmuller, *Rep.Prog. Phys.* **65**, 651 (2001)

[18] C. Jooss, University of Goettingen, *Private Communication* (2002)

[19] C. P. Bean, Rev. Mod. Phys. **36,** 31 (1964)

[20] A. Pruymboom, P. H. Kes, E. van der Drift, and S. Radelaar, *Phys. Rev. Lett*. **60**, 1430 (1988).

[21] Z. Hao and J.R. Clem, *IEEE Trans. Magn*. **27**, 1086 (1991)

[22] A. Díaz, L. Méchin, P. Berghuis, and J. E. Evetts, *Phys. Rev. B* **58**, R2960 (1998)

APPENDIX A – Misorientation Types

In general, YBCO grain boundaries can consist of a mixture of three types of misorientation, termed [001]-tilt, [100]-tilt and [100]-twist, shown in figure B.1(a). The same sharp dependence of J_c^{GB} on misorientation as found for [001]-tilt (see figure 3.2) is *also* found for [100]-tilt and [100]-twist, as shown in figure B.1(b). Although for symmetric [001]-tilt boundaries, the dislocation structure may be described by a *single* set of dislocations, mixed boundaries can require several independent sets of dislocations.

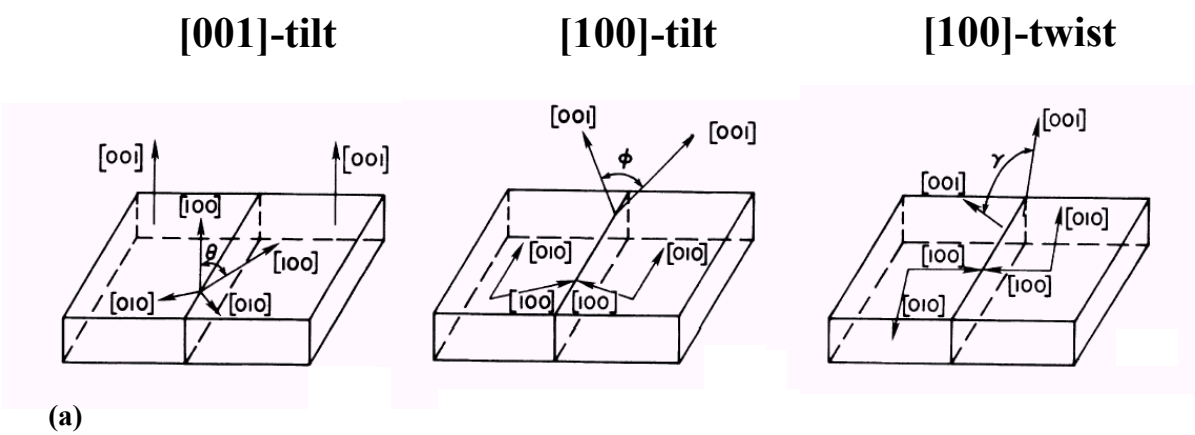

(a)

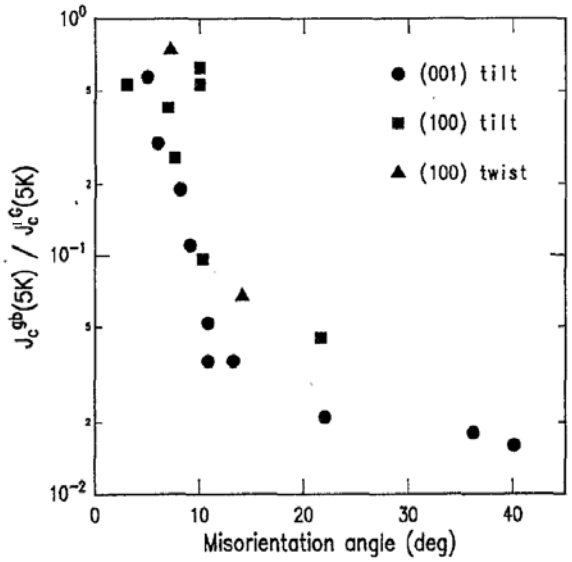

(b)

Figure B.1.(a) Three different GB misorientation types, and (b) the dependence of J_c^{GB}/J_c^{IG} with absolute misorientation angle. The main tilt components of each misorientation data point are labelled. Data from Dimos *et al*, reference [3] in chapter 3.

APPENDIX B - List of Samples Investigated

The samples investigated (through various techniques) during this work are listed in the table below. Films were all deposited at the University of Cambridge (IRC in Superconductivity and Department of Materials Science). Bicrystal misorientations are quoted as supplied.

Sample Name	Sample Type	Substrate Source	Method	Deposited By
s2	4° Bicrystal Thin Film	Shinkosha	PLD	F. Kahlmann
pk2	4° Bicrystal Thin Film	Pi-Kem	PLD	F. Kahlmann
773c	4° Bicrystal Thin Film	Crystal	Sputtered	V. Tsaneva
773b	4° Bicrystal Thin Film	Crystal	PLD	F. Kahlmann
773d	4° Bicrystal Substrate	Crystal	NA	NA
640a2	2° Bicrystal Thin Film	Crystal	PLD	F. Kahlmann
1277	Single Crystal Thin Film	Pi-Kem	PLD	F. Kahlmann
1237b	Single Crystal Thin Film	Pi-Kem	PLD	F. Kahlmann
1181	Single Crystal Thin Film	Crystal	PLD	F. Kahlmann

Sample Name	Misorientation			Details	Source
s2	3.8°			PLD	F. Kahlmann
pk2	4.9°			PLD	F. Kahlmann
773c	4.0°	0.2°	0.3°	Sputtered	V. Tsaneva
773b	4°	/	/		
s4					
1277				PLD	F. Kahlmann
1237				PLD	F. Kahlmann
640					

APPENDIX C – Partial Vortex Row Modification to the VFF Model

We assume there exist two regions, I and II, both of which possess the same minimum j_c^{GB} at the interface (see inset of figure C1). Above j_{c1}, a single line of vortices flow along the GB and through both regions. Above j_{c2}, however, a second row of vortices flow only along region II interface as it possesses a wider effective J_c profile than region I. This is illustrated schematically in figure C1, where the current density through regions I and II is J_I and J_{II} respectively.

Conservation of vortices necessitates that

$$v_f = v_{f1} + v_{f2} \tag{C.1}$$

This is also arrived at by using the fact that the voltage drop across the GB must be constant along its entire length, giving $\Delta V = E\delta = \delta v_f B$, where δ is the perpendicular width of each row ($\sim a_o$). If we assume that each row flows with its own J_c value, we can also use the fact that $(J - J_c)\Phi_o = \eta v_f$ (see equation 2.13). For example, row 2 in region II flows at v_{f2} and satisfies the equation, $J_{II} - j_{c2} = \eta v_f$. Substituting for v_f, v_{f1} and v_{f2} using equation 2.13 results in the equation for J_I in terms of J_{II},

$$J_I = 2J_{II} - j_{c2} \quad \text{for } J_{II} > j_{c2} \qquad \text{and} \qquad J_I = J_{II} \quad \text{for } J_{II} < j_{c2} \tag{C.2}$$

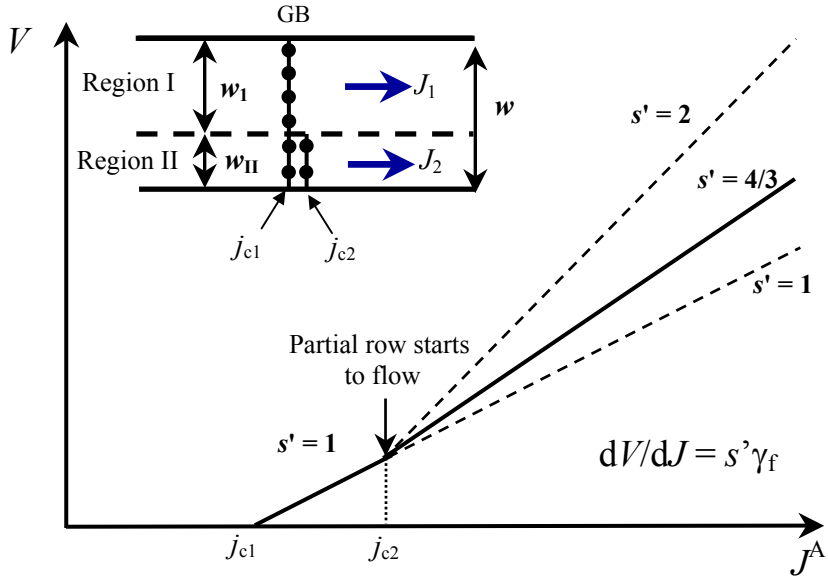

Figure C.1. Sketch of the gradient kink expected for partial rows starting to flow at $J^A = j_{c2}$ for $w_I = w$ (s' = 1), $w_I = 0$ (s' = 2) and $w_I = w_{II}$ (s' = 4/3). Inset shows the geometry, where $s = 2$ for region II.

Differentiating equation C.2 we find that $dJ_I/dJ_{II} = 2$ for $J_{II} > j_{c2}$. The result of this is that as soon as the second row starts to flow, any further increase in current is diverted through region I and is twice that through region II. As such, a percolative behaviour is to be expected of an inhomogeneous LAGB with a varying J_c profile – current will be diverted preferably to regions with fewer rows flowing.

In order to deduce the effect on dV/dJ of the flow of partial rows of vortices we also need to use the fact that

$$w = w_I + w_{II} \tag{C.3}$$

and that the total current is $I = J_I t w_I + J_{II} t w_{II}$, giving the averaged track current density,

$$J^A = \frac{I}{wt} = (J_I - J_{II})\left(\frac{w_I}{w}\right) + J_{II} \tag{C.4}$$

By substituting for J_I in this equation from equation C.2, J^A as a function of J_{II} can be found. Differentiating this expression with respect to J_{II} yields, $dJ^A/dJ_{II} = (w^I/w) + 1$. And so we can deduce the 'measured' dV/dJ^A across the composite structure as,

$$\frac{dV}{dJ^A} = \frac{dJ^A}{dJ_{II}}\frac{dJ_{II}}{dJ^A} = \frac{w}{w_I + w}\frac{dV}{dJ_{II}} = \gamma_f\, s'(J) \qquad \text{where} \qquad s'(J) = \frac{2w}{(w_I + w)} \tag{C.5}$$

where the fact that in region II, $dV/dJ_{II} = s\gamma_f = 2\gamma_f$ has been used and γ_f is, as defined in equation 6.7, related to the flux flow resistivity. Now the gradient may step in a non-integer multiple $s'(J)$ of γ_f dependent upon the relative lengths of regions I and II. For example,

for $w_I = w$, s' = 1 and $dV/dJ^A = \gamma_f$.

for $w_I = 0$, s' = 2 and $dV/dJ^A = 2\gamma_f$

for $w_I = w/2 = w_{II}$, s' = 4/3 and $dV/dJ^A = (4/3)\gamma_f$

These cases are sketched in figure C.1, and could explain the non-integer kinking seen in figures 6.9 and 6.10.

APPENDIX D - Publications

M.J. Hogg, F. Kahlmann, E.J. Tarte, Z.H. Barber and J.E. Evetts, "Vortex Channeling and the Voltage-Current Characteristics of $YBa_2Cu_3O_7$ Low-Angle Grain Boundaries", *Appl. Phys. Lett.* **78**, 1433 (2001)

M.J. Hogg, F. Kahlmann, Z.H. Barber and J.E. Evetts, "Angular Hysteresis in the Critical Current of $YBa_2Cu_3O_7$ Low-Angle Grain Boundaries", *Supercond. Sci. Technol.* **14**, 647 (2001)

J.E. Evetts, **M.J. Hogg**, B.A. Glowacki, N.A. Rutter and V.N. Tsaneva, "Current Percolation and the *V-I* transition in $YBa_2Cu_3O_7$ Bicrystals and Granular Coated Conductors", *Supercond. Sci. Technol.* **12**, 1050 (1999)

T. Nurgaliev, V.N. Tsaneva, T.I. Donchev. Z.H. Barber, E.J. Tarte, M.G. Blamire, **M.J. Hogg**, J.E. Evetts, M. Taslakov, S. Miteva, A.Y. Spasov, G. Ovsyannikov, Z.G. Ivanov, H. Nilsson, "Characterization of YBCO Thin Films for Microwave Applications", *Physica C*, in press (2002)


For Emily, whenever I may find her.

M.J. Hogg, F. Kahlmann, E.J. Tarte, Z.H. Barber, J.D. Durrell and J.E. Evetts, "Vortex Channelling and Pinning at $YBa_2Cu_3O_7$ Low-Angle Grain Boundaries", in preparation